frontiers | Research Topics

Cardiovascular engineering

Edited by
Christopher T. Nguyen, Marianne Schmid Daners, Ellen T. Roche, Caglar Ozturk and Xuanhe Zhao

Published in
Frontiers in Cardiovascular Medicine

ISSN 1664-8714
ISBN 978-2-83250-920-3
DOI 10.3389/978-2-83250-920-3

About Frontiers

Frontiers is more than just an open access publisher of scholarly articles: it is a pioneering approach to the world of academia, radically improving the way scholarly research is managed. The grand vision of Frontiers is a world where all people have an equal opportunity to seek, share and generate knowledge. Frontiers provides immediate and permanent online open access to all its publications, but this alone is not enough to realize our grand goals.

Frontiers journal series

The Frontiers journal series is a multi-tier and interdisciplinary set of open-access, online journals, promising a paradigm shift from the current review, selection and dissemination processes in academic publishing. All Frontiers journals are driven by researchers for researchers; therefore, they constitute a service to the scholarly community. At the same time, the *Frontiers journal series* operates on a revolutionary invention, the tiered publishing system, initially addressing specific communities of scholars, and gradually climbing up to broader public understanding, thus serving the interests of the lay society, too.

Dedication to quality

Each Frontiers article is a landmark of the highest quality, thanks to genuinely collaborative interactions between authors and review editors, who include some of the world's best academicians. Research must be certified by peers before entering a stream of knowledge that may eventually reach the public - and shape society; therefore, Frontiers only applies the most rigorous and unbiased reviews. Frontiers revolutionizes research publishing by freely delivering the most outstanding research, evaluated with no bias from both the academic and social point of view. By applying the most advanced information technologies, Frontiers is catapulting scholarly publishing into a new generation.

What are Frontiers Research Topics?

Frontiers Research Topics are very popular trademarks of the *Frontiers journals series*: they are collections of at least ten articles, all centered on a particular subject. With their unique mix of varied contributions from Original Research to Review Articles, Frontiers Research Topics unify the most influential researchers, the latest key findings and historical advances in a hot research area.

Find out more on how to host your own Frontiers Research Topic or contribute to one as an author by contacting the Frontiers editorial office: frontiersin.org/about/contact

Cardiovascular engineering

Topic editors

Christopher T. Nguyen — Cleveland Clinic, United States
Marianne Schmid Daners — ETH Zürich, Switzerland
Ellen T. Roche — Massachusetts Institute of Technology, United States
Caglar Ozturk — Massachusetts Institute of Technology, United States
Xuanhe Zhao — Massachusetts Institute of Technology, United States

Citation

Nguyen, C. T., Daners, M. S., Roche, E. T., Ozturk, C., Zhao, X., eds. (2022). *Cardiovascular engineering*. Lausanne: Frontiers Media SA.
doi: 10.3389/978-2-83250-920-3

Table of contents

frontiers | Frontiers in Cardiovascular Medicine

TYPE Editorial
PUBLISHED 21 November 2022
DOI 10.3389/fcvm.2022.1089794

OPEN ACCESS

EDITED AND REVIEWED BY
Junjie Xiao,
Shanghai University, China

*CORRESPONDENCE
Christopher T. Nguyen
nguyenc6@ccf.org

SPECIALTY SECTION
This article was submitted to General Cardiovascular Medicine, a section of the journal Frontiers in Cardiovascular Medicine

RECEIVED 04 November 2022
ACCEPTED 10 November 2022
PUBLISHED 21 November 2022

CITATION
Ozturk C, Schmid Daners M, Zhao X, Roche ET and Nguyen CT (2022) Editorial: Cardiovascular engineering. *Front. Cardiovasc. Med.* 9:1089794. doi: 10.3389/fcvm.2022.1089794

Editorial: Cardiovascular engineering

Caglar Ozturk[1], Marianne Schmid Daners[2], Xuanhe Zhao[3,4], Ellen T. Roche[1,3] and Christopher T. Nguyen[5,6,7,8,9]*

[1]Institute for Medical Engineering and Science, Massachusetts Institute of Technology, Cambridge, MA, United States, [2]Product Development Group Zurich, Department of Mechanical and Process Engineering, ETH Zurich, Zurich, Switzerland, [3]Department of Mechanical Engineering, Massachusetts Institute of Technology, Cambridge, MA, United States, [4]Department of Civil and Environmental Engineering, Massachusetts Institute of Technology, Cambridge, MA, United States, [5]Cardiovascular Innovation Research Center, Heart Vascular and Thoracic Institute, Cleveland Clinic, Cleveland, OH, United States, [6]Cardiovascular Research Center, Massachusetts General Hospital, Charlestown, MA, United States, [7]Martinos Center for Biomedical Imaging, Massachusetts General Hospital, Charlestown, MA, United States, [8]Department of Diagnostic Radiology Imaging, Imaging Institute, Cleveland Clinic, Cleveland, OH, United States, [9]Department of Cardiovascular and Metabolic Sciences, Lerner Research Institute, Cleveland Clinic, Cleveland, OH, United States

KEYWORDS

cardiovascular engineering, cardiovascular disease, cardiovascular devices, computational modeling, cardiovascular biomechanics, cardiac imaging, heart failure

Editorial on the Research Topic
Cardiovascular engineering

Cardiovascular disease remains the leading cause of death worldwide, despite significant advances in medical technology and in our knowledge of the disease and the treatment (1, 2). Over the last two decades, we have seen remarkable development in the fields of technology, healthcare, and the biological sciences. Since the cardiovascular field has progressed so rapidly, it is essential that each major innovation must function increasingly better than current technologies to have a long-lasting impact. The combination of exploding knowledge and recent advances in biology, medicine, imaging, and engineering have all helped foster a creative and unique environment for cardiovascular engineering.

Given the complexity of cardiovascular physiology, this field of study must encompass a wide range of research, from basic to translational, and aim to create diagnostic strategies, interventions, and biomedical devices that employ engineering principles and methods for cardiovascular disease. This special issue focuses on recent developments, reviews, and applications in cardiovascular engineering, incorporating topics such as mechanical assist devices, medical imaging, cardiovascular biomechanics, and biomaterials. In this editorial article, we provide a summary of the featured work in this issue.

Several groups focused on mechanical circulatory support (MCS) devices, such as ventricular assist devices (VADs) and total artificial hearts (TAHs) to advance existing knowledge and technological solutions for cardiovascular disease. Two papers

shed novel light on the role of artificial pulsatility in continuous-flow support devices. Fang et al. assessed the impact of pulsatility using rotor speed modulation sequences in the HeartMate 3. The authors conducted a comprehensive computational fluid dynamics investigation on the washout performance with a particular focus on slow washout regions as an indicator of elevated risk of in-pump thrombus formation. The findings suggested that artificial pulsatility mostly enhances the washout of the flow separation region distal of the outflow cannula curvature. Furthermore, a physiological data-driven iterative learning controller has been introduced by Magkoutas et al.. Their controller effectively tracks predefined pump flow trajectories, and aims to generate a physiologically relevant, pulsatile, and treatment-driven response for continuous-flow VADs. This is a significant advancement over continuous-flow VADs and speed-based controllers, and opens up new opportunities in the management of continuous-flow VAD therapy since patient-specific preload sensitivity may be chosen directly based on clinical feedback.

Fox et al. have emphasized the need for effective therapeutic options for infants and children. Their research focused on developing a novel, continuous-flow, magnetically levitated TAH that may be used as a therapeutic option for high-risk pediatric patients with heart failure. This detailed work on a magnetically levitated prototype, which included computational analysis, *in vitro* hydraulic testing and hemolytic assessment revealed promising hydraulic performance characteristics, supporting the pulmonary and systemic circulation adequately in a hybrid design configuration.

Besides MCS, a number of groups demonstrated innovative preclinical disease models as a testbed to drive cardiovascular engineering design, testing, and validation. Malone et al. developed a new bench top mechanical circulatory loop (MCL) that can model the normal heart function and heart failure with preserved ejection fraction (HFpEF)—a multifactorial type of heart failure with multiple phenotypes. Their MCL features two independently controlled cardiac chambers which can be altered to limit diastolic filling to mimic the severity of HFpEF and can accurately simulate the diastolic hemodynamics of the left atrium and left ventricle. In addition, a patient-specific lumped parameter model of HFpEF was developed and a prototype of a soft robotic extra-aortic counterpulsation device was created to investigate the physiological implications of varying operating conditions by Arduini et al.. Briefly, they investigated the feasibility of patient-specific testing of novel cardiac support devices using lumped parameter computational models based on clinical hemodynamic data. Although the advantages of counter-pulsation therapy are not yet totally elucidated, the framework provided in this study stimulate future research into the efficacy of counter-pulsation therapy as a treatment for patients with HFpEF.

Kolli et al. created an *in vitro* experimental flow loop employing patient-specific 3D-printed coronary arteries as a proxy for invasive cardiac catheterization laboratory measurements. In this pilot study, they evaluated coronary artery ischemia using an *in vitro* method, combination of non-invasive coronary CT angiography and 3D printing based fractional flow reserve (FFR). When compared to invasive FFR approach, their 3D printing based non-invasive environment showed a strong correlation and a consistency, paving the way for a non-invasive diagnostic technique that can eventually substitute invasive FFR.

Exarchos et al. describe research supporting the hypothesis that micro-structured surfaces with anisotropic topographies can enhance long-term endothelialization of cardiovascular implants (CVIs). Describing recent efforts to modify the surfaces of various CVIs, including stents, grafts, valves, and VADs, they discuss the associated advances and challenges that have been encountered during their clinical translation. In their original research article, the authors show that anisotropic topographies on micro-structured surfaces could restore the monolayer integrity of senescent endothelial cells, enhances cell alignment, and promote proliferation.

Regarding cardiac magnetic resonance imaging (MRI) approaches, a deep learning method for fully automatic strain analysis (termed DeepStrain) based on cine-MRI images was introduced by Morales et al.. The authors aimed to explore whether DeepStrain may identify asymptomatic dysfunction in young adults with cardiac risk factors such as obesity, hypertension, and type 2 diabetes mellitus. Reference strain values for asymptomatic LV diastolic and systolic dysfunction in various young adult populations have been presented using a fully automatic strain analysis software.

What's more, Huh et al. presented a novel 4D spatiotemporal reconstruction process for dynamically acquired single photon emission computed tomography data. Since cardiac deformation and respiration both reduce the quality of the reconstructed image, the authors developed an algorithm to reconstruct the dynamic sequence of independent respiratory and cardiac phases and tested it using the data generated from a Monte Carlo simulation.

In summary, this specific Research Topic on cardiovascular engineering provides a platform to exhibit a variety of original research, methods and review articles on recent scientific advances in cardiovascular implants, computational modeling, imaging, and *in vitro* simulators for pediatric and adult patients. We appreciate the efforts of all authors for helping make this such a fruitful special issue.

Author contributions

CO drafted the Editorial manuscript. MSD, XZ, ETR, and CTN revised it for interpretation and content. All authors contributed to the article and approved the submitted version.

Conflict of interest

The authors declare that the research was conducted in the absence of any commercial or financial relationships that could be construed as a potential conflict of interest.

Publisher's note

All claims expressed in this article are solely those of the authors and do not necessarily represent those of their affiliated organizations, or those of the publisher, the editors and the reviewers. Any product that may be evaluated in this article, or claim that may be made by its manufacturer, is not guaranteed or endorsed by the publisher.

References

1. Abou-Saleh H, Zouein FA, El-Yazbi A, Sanoudou D, Raynaud C, Rao C, et al. The march of pluripotent stem cells in cardiovascular regenerative medicine. *Stem Cell Res Ther.* (2018) 9:201–31. doi: 10.1186/s13287-018-0947-5

2. McClellan M, Brown N, Califf RM, Warner JJ. Call to action: urgent challenges in cardiovascular disease: a presidential advisory from the American Heart Association. *Circulation*. (2019) 139:e44–54. doi: 10.1161/CIR.0000000000000652

frontiers in Cardiovascular Medicine

ORIGINAL RESEARCH
published: 11 March 2022
doi: 10.3389/fcvm.2022.775780

Insights Into the Low Rate of In-Pump Thrombosis With the HeartMate 3: Does the Artificial Pulse Improve Washout?

*Peng Fang[1,2], Jianjun Du[1], Andrea Boraschi[2], Silvia Bozzi[3], Alberto Redaelli[3], Marianne Schmid Daners[4], Vartan Kurtcuoglu[2], Filippo Consolo[5,6] and Diane de Zélicourt[2]**

[1] School of Mechanical Engineering and Automation, Harbin Institute of Technology, Shenzhen, Shenzhen, China, [2] The Interface Group, Institute of Physiology, University of Zurich, Zurich, Switzerland, [3] Department of Electronics, Information and Bioengineering, Politecnico di Milano, Milano, Italy, [4] Product Development Group Zurich, Department of Mechanical and Process Engineering, ETH Zurich, Zurich, Switzerland, [5] Anesthesia and Intensive Care, IRCCS San Raffaele Scientific Institute, Milano, Italy, [6] Università Vita Salute San Raffaele, Milano, Italy

While earlier studies reported no relevant effect of the HeartMate 3 (HM3) artificial pulse (AP) on bulk pump washout, its effect on regions with prolonged residence times remains unexplored. Using numerical simulations, we compared pump washout in the HM3 with and without AP with a focus on the clearance of the last 5% of the pump volume. Results were examined in terms of flush-volume (V_f, number of times the pump was flushed with new blood) to probe the effect of the AP independent of changing flow rate. Irrespective of the flow condition, the HM3 washout scaled linearly with flush volume up to 70% washout and slowed down for the last 30%. Flush volumes needed to washout 95% of the pump were comparable with and without the AP (1.3–1.4 V_f), while 99% washout required 2.1–2.2 V_f with the AP vs. 2.5 V_f without the AP. The AP enhanced washout of the bend relief and near-wall regions. It also transiently shifted or eliminated stagnation regions and led to rapid wall shear stress fluctuations below the rotor and in the secondary flow path. Our results suggest potential benefits of the AP for clearance of fluid regions that might elicit in-pump thrombosis and provide possible mechanistic rationale behind clinical data showing very low rate of in-pump thrombosis with the HM3. Further optimization of the AP sequence is warranted to balance washout efficacy while limiting blood damage.

Keywords: left ventricular assist device (LVAD), computational fluid dynamics (CFD), HeartMate 3 (HM3), pump thrombosis, washout, rotational speed modulation, wall shear stress (WSS)

OPEN ACCESS

Edited by:
Ryo Torii,
University College London,
United Kingdom

Reviewed by:
Jonathan Grinstein,
University of Chicago, United States
Katharine Fraser,
University of Bath, United Kingdom

***Correspondence:**
Diane de Zélicourt
diane.dezelicourt@physiol.uzh.ch

Specialty section:
This article was submitted to General Cardiovascular Medicine, a section of the journal Frontiers in Cardiovascular Medicine

Received: *14 September 2021*
Accepted: *02 February 2022*
Published: *11 March 2022*

Citation:
Fang P, Du J, Boraschi A, Bozzi S, Redaelli A, Schmid Daners M, Kurtcuoglu V, Consolo F and de Zélicourt D (2022) Insights Into the Low Rate of In-Pump Thrombosis With the HeartMate 3: Does the Artificial Pulse Improve Washout? Front. Cardiovasc. Med. 9:775780. doi: 10.3389/fcvm.2022.775780

INTRODUCTION

Heart failure is a rapidly expanding and lethal cardiovascular disease with a 30% 1-year mortality rate in older adults (1). Left ventricular assist devices (LVADs) offer a lifesaving option for patients with advanced heart failure, restoring the cardiac output their heart can no longer provide (2). Over the past decades, LVADs have evolved from bridge-to-transplant to destination therapy and have become a viable alternative to heart transplantation with comparable outcomes (3–5). However, patients with LVAD still suffer from high complication rates, including thrombosis, bleeding, and strokes (4), which have at least in part been attributed to the hemodynamics of the implanted pump (6–8).

The HeartMate 3 (HM3) (Abbott, Chicago, Illinois, USA) has attracted attention due to its remarkably low rate of in-pump thrombosis (0 and 1.1% at 6 and 24 months after implantation, respectively) (9) compared to earlier devices such as the HeartMate II (HMII) (Abbott, Chicago, Illinois, USA) or to the HeartWare ventricular assist device (HVAD) (Medtronic, Minneapolis, Minnesota, USA) that showed a 10.7 and 6.4% rate of pump exchange due to pump thrombosis at 2 years, respectively (10). Distinctive features of the HM3 include a fully magnetically levitated rotor, large secondary flow paths, and its operative regime with the artificial pulse (AP) rotor speed modulation sequence (11–13). With a 2,000-rpm decrease in rotor speed followed by a 4,000-rpm increase before returning to baseline within the span of 350 ms, the AP entails a large and rapid change in rotor speed with the set goal to improve washout (11, 13). Accordingly, potential beneficial effects of the AP in terms of pump thrombogenicity have been suggested (14). However, whether the AP plays a role in the very low rate of clinically observed in-pump thrombosis or whether these may be solely due to the pump geometrical features remains unclear.

Previous studies assessing the impact of rotor speed modulation sequences have suggested that these may enhance arterial pulsatility via transient loading of the left ventricle (15). In the registry to evaluate the heartWare left ventricular assist system (ReVOLVE) study, patients with HVAD with the Lavare Cycle enabled showed significantly lower rates of strokes than those without, but the rate of in-pump thrombosis was unchanged (16). In line with these observations, experimental and computational fluid dynamics (CFD) studies suggested that, while the Lavare Cycle might improve ventricular washout (16), it did not have a significant impact on the HVAD flow fields or pump washout (17). As the AP is an inherent component of the HM3 system and cannot be switched off, isolated impact of the AP cannot be assessed clinically, requiring *in-vitro* or *in-silico* approaches. Our earlier study in the area suggested that under the tested conditions, the AP did not improve overall pump washout, defined as the time required for 95% of the blood present in the HM3 at a given time point to exit the pump (17, 18). Washout of the remaining 5% was not in the scope of those studies. However, in terms of in-pump thrombosis, understanding the distribution and clearance rate of the last 5% of so-called "old blood" remaining in the pump is of prime interest, as these 5% are the ones with the longest residence time. While it may be inferred that by alternating flow disturbances (which may increase mixing) and sudden acceleration (which may then increase washout), the AP may help in the clearance of otherwise hard-to-clear fluid regions; no study has investigated its actual contribution to improving internal pump hemodynamics and limiting the risk of in-pump thrombosis. Furthermore, because the AP duration (0.35 s) is on the same order as the characteristic 95% washout time (∼0.3 s at 5 L/min) (17), a time-dependent understanding of the HM3 washout pattern is warranted.

In this study, we conduct a comprehensive investigation of the effect of the AP on the washout in the HM3, with a focus on slow washout regions as a surrogate marker of elevated risk of in-pump thrombus formation. In detail, we analyze wall shear stress (WSS) patterns, regions of flow stasis, clearance times, and clearance patterns for five different reference time points, providing a better understanding of the effect of the AP on bulk and local washout. Results are analyzed in terms of both the washout time and nondimensional flush volume, defined as number of times the pump was flushed with new blood, providing insights into the effect of the AP and associated rotor acceleration and deceleration independent of the pump flow rate.

MATERIALS AND METHODS

Computational Methods

Numerical simulations of the blood flow within the HM3 with and without the AP were conducted in STAR-CCM+ (Siemens, Munich, Germany). The HM3 pump geometry and mesh were obtained from Boraschi et al. (17). The mesh contained 10 million polyhedral grid elements, including an 8-element boundary layer along the rotor, a 10-element boundary layer along the stator, and local mesh refinement where needed. Unsteady Reynolds-averaged Navier–Stokes simulations were conducted using implicit second-order temporal and spatial discretization, Menter's Shear Stress Transport (SST) k-ω turbulent modeling, dynamic time-stepping (programmed to correspond to 2° of rotation per time step), and a 10^{-5} convergence criterion for the residual error. Blood was considered as an incompressible Newtonian fluid ($\rho = 1,050\ kg/m^3$ and $\mu = 3.5$ mPa · s). For regional analysis, the pump fluid volume was divided into three parts: the inflow cannula, the pump core, and the outflow cannula (**Figure 1**). More detailed information on the HM3 geometry, grid independence tests, validation, and computational methods can be found in our previous studies (17, 18).

Simulation Scenarios and Boundary Conditions

To isolate the impact of the AP, we compared the results obtained with the AP virtually turned on or off. For both the

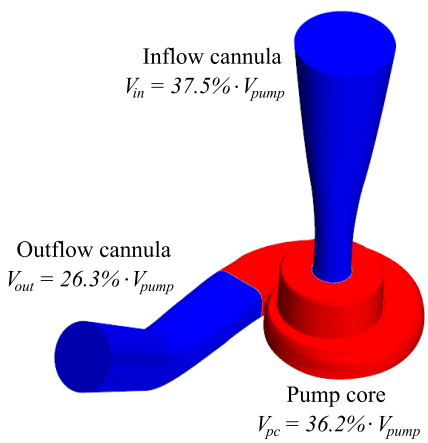

FIGURE 1 | Visualization of the domain splitting retained for analysis by parts. V_{pump} is the pump volume and V_{in}, V_{pc}, and V_{out} are the volumes of the inflow cannula, pump core, and outflow cannula, respectively.

conditions, inlet and outlet pressure boundary conditions were obtained from a lumped parameter model (19) representing the cardiovascular system of an average patient with LVAD—with a heart rate of 91 bpm, end-diastolic left ventricular volume of 345 ml, and ejection fraction of 10.3% prior to LVAD implantation (20), implanted with the HM3 LVAD. Dynamic hydraulic properties of the HM3 were derived from (21). To assess the effect of the AP in isolation, residual left ventricular pulsatility was turned off for these simulations and the baseline set-speed of the AP defined according to (17, 18) aiming to achieve a clinically relevant mean pump flow of 5 L/min over the 0.35 s of the AP duration. The resulting rotational speed sequence for the AP scenario entailed a baseline set-speed of 5,650 rpm, a low-speed phase at 3,650 rpm for 0.15 s, and a high-speed phase at 7,650 rpm for 0.2 s (**Figure 2A**). The pump pressure head varied between 59.0 and 81.2 mm Hg over the AP cycle (**Figure 2B**). Time-dependent rotational speed and pump pressure head derived from the lumped parameter model were imposed as boundary conditions for the CFD simulations. In the baseline scenario with the AP virtually turned off, the pump was operated at the same rotational speed and pressure as during the baseline conditions of the AP scenario, namely, 5,650 rpm and 71.6 mm Hg, respectively.

Finally, we further simulated a low-flow condition (3,600 rpm, 3.5 L/min) and a high-flow condition (7,600 rpm, 8.6 L/min) to assess the dependence of the baseline washout on the pump flow rate and rotational speed.

Data Analysis

Volume Washout

To investigate volume washout, we quantified the clearance of a passive "old blood" scalar (OBS) by pure advection:

$$\rho \frac{\partial [OBS]\left(\vec{x}, t\right)}{\partial t} + \rho \nabla \cdot \left(\vec{u} \cdot [OBS]\right) = 0 \qquad for\ t > t_i \quad (1)$$

where t is time, $\vec{x}$ is the position vector, $[OBS]$ is the OBS concentration, ρ is the blood density, $\vec{u}$ is the blood velocity, and t_i is the OBS scalar initialization time. The initial scalar concentration, $[OBS]_0$, was set to 100% and $[OBS]$ is set to zero at the inflow. The 7 cm extension of the outlet allows for adequate handling of reverse flow during the AP without influence of the outlet boundary condition on the OBS concentration within the pump. For the AP, we studied the washout of five OBS (denoted AP1 through AP5) with initialization times chosen such that the residual fraction of OBS was around 5, 10, 25, 50, and 100% at the beginning of the AP, respectively.

Residual Fraction of OBS

We define the OBS residual fraction, *rOBS*, as:

$$rOBS\,(t) = \frac{1}{V \cdot [OBS]_0} \cdot \int_V [OBS]\,(t) \cdot \partial\, V \quad (2)$$

where V is the integration volume. Unless otherwise specified, rOBS refers to the residual OBS concentration in the whole pump.

Flush Volume

To assess whether the differences in pump washout solely relate to differences in pump flow rate or whether the acceleration and deceleration imparted by the AP provide further advantages, we define the nondimensional flush volume, V_f, associated with each OBS as:

$$V_f(t, t_i) = \frac{1}{V_{pump}} \int_{t_i}^{t} Q\,(\tau) \partial \tau \quad (3)$$

where t_i is the OBS initialization time, V_{pump} is the pump volume, and Q is the signed pump flow rate. Q is positive when new blood flows from the ventricle toward the aorta and Q is negative when the flow reverses and old blood flows back from the outlet graft into the pump. V_f describes the number of times the pump was flushed with new blood since OBS initialization.

Reference OBS Residual Fraction

To provide a reference for pump washout rates, we define for each OBS a reference OBS residual fraction for the whole pump,

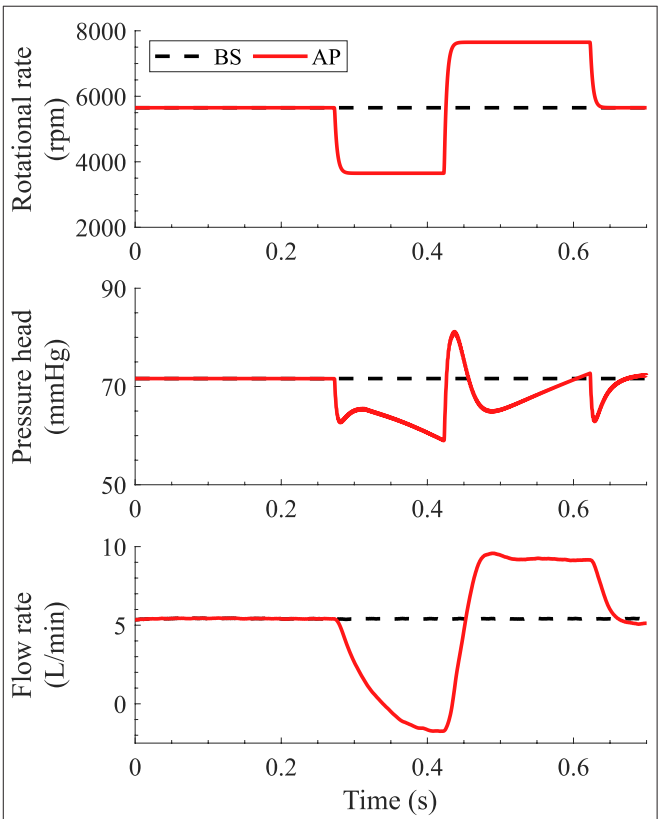

FIGURE 2 | Pump rotational speed **(A)**, pump pressure head **(B)** and pump flow rate **(C)** during the artificial pulse and under baseline conditions. The pump pressure head associated with the different conditions was obtained from the lumped parameter heart-pump interaction model as described in Simulation Scenarios and Boundary Conditions. Rotational speed and pressure head are imposed as boundary conditions in the computational fluid dynamics (CFD) simulations, while the pump flow rate is a result of the CFD simulations.

$rOBS_{ref}$, assuming perfect flushing of the old blood by the new one:

$$rOBS_{ref}\,(t, t_i) \;=\; 1 \;-\; V_f\,(t, t_i) \tag{4}$$

With the above definition $rOBS_{ref} = 0\%$ when $V_f = 1$, i.e., the old blood would be entirely washed out after flushing the pump with once its volume of new blood.

Wall Shear Stress

Finally, to evaluate the effect of the AP on surface washout, we compared WSS patterns across conditions. We monitored instantaneous WSS variation at selected locations in area of flow stagnation along the top and bottom of the casing (see **Supplementary Figure S1** for the location of the monitoring points).

RESULTS

Overall old Blood Scalar Washout With and Without AP

For all the tested conditions, the residual OBS concentrations, rOBS, initially closely follow the associated reference curves, $rOBS_{ref}$ (**Figure 3B**). The difference between simulated and reference residual concentrations is below 0.001% down to rOBS = 50% for baseline and AP1–4 and below 2% down to rOBS = 30% for all the tested conditions (**Supplementary Material S2**). For the first 70% of the pump volume, OBS clearance initially scales almost one-to-one with the overall flush volume, so that all the curves initially collapse onto one another when plotted against V_f (**Figure 3D**). The same pattern is observed under the high- and low-flow conditions (**Supplementary Material S3**).

Under the simulated conditions, the low-speed phase of the AP leads to a transient flow reversal (**Figure 3A**) associated with an increase in all the rOBS (**Figure 3B**, AP1–5). This translates into a "shark fin" feature in **Figure 3D** because the net V_f, decreases for negative pump flow rates, reflecting backflow of old blood from the outflow graft into the pump. Flow reversal does not lead to a "shark fin" feature for $rOBS_{AP4}$ and $rOBS_{AP5}$, as the curves follow the reference washout curve, $rOBS_{ref}$, during that phase.

Taken together, the alternating low- and high-speed phases of the AP translate into prolonged 95% washout times compared to baseline (**Figure 3C** and **Table 1**). However, depending on the initialization time considered, the mean pump flow rate during the washout period changes as well, decreasing from 5.42 L/min at baseline to 4.94 L/min for AP5 and 4.25 L/min for AP1 (**Table 1**). Accounting for the effect of flow rate, flush volumes required to reach 95% washout are comparable across conditions, ranging between 1.3 and 1.4, with the exception of AP1 for which the AP started just before the retained rOBS = 5% assessment cutoff ($rOBS_{AP1} = 5.9\%$ at AP start, **Table 1**). In contrast, the number of flush volumes required to reach 99% washout decreases from 2.5 at baseline to 2.1–2.2 with the AP or under high-flow condition.

Clearance Modes

Looking at the distribution of regions with high to low OBS concentration as washout progresses (**Figure 4**), different phases can be identified. At first, the sum of fluid volumes with ≥1% OBS decreases rapidly. The pump volume can be broadly categorized into regions with >80% OBS and regions with <1% OBS (dark red and white areas in **Figure 4**), suggesting that old blood is replaced almost one-to-one by new blood in the main flow paths. In the second phase, the decline in rOBS given in **Figure 3** is no longer associated with a net increase in regions with new blood only ([OBS] < 1%, white areas), but rather by mixing of old and new blood within the pump core and the outlet downstream. At baseline, the sum of fluid volumes with [OBS] > 1% remains relatively stable between $V_f = 0.55$ and $V_f = 1.4$ only decreasing from 66 to 60%, corresponding approximately to the combined pump core and outlet volumes (63%, horizontal white line in **Figures 4A,B**). Mixing phases between old and new blood are manifest by the appearance of fluid fractions with intermediate concentrations. The sum of fluid regions with [OBS] > 1% declines steeply after the residual OBS concentration in the core pump drops below 1% ($V_f = 1.8$, **Figures 4B1, 5B1**) and mixed blood is pushed toward the outlet. The same is observed for higher concentration bands. For example, the sum of fluid volumes with [OBS] > 50% declines steeply after the residual OBS concentration in the core pump drops below 50% ($V_f = 0.56$). The last phase is characterized by a drastic reduction of the clearance rate of all the concentration bands, testifying for the presence of fluid regions with prolonged residence times. While the overall rOBS is reduced to 5% with 1.4 flush volumes at baseline (**Table 1**) with only 4% of the pump volume having OBS concentrations higher than 20% (**Figure 4B**), it takes an additional 1.1 flush volumes to reduce both of these to 1%.

Due to the flow reversal, the low-speed phase of the AP (illustrated by dotted lines in **Figure 4**) leads to backflow of mixed old and new blood back from the outflow graft into the pump illustrated by the increase in fluid volumes containing low to medium OBS concentrations ($1 \leq [OBS] \leq 50\%$). The flow reversal still benefits the clearance of regions with high OBS concentrations with a continuous decline of the pump volume with [OBS] ≥ 50% (**Figure 4B**). The high-speed phase leads to a faster and deeper reduction of regions of high OBS concentration than at baseline. The sum of the regions with more than 20% OBS accounts for <1% of the pump volume already at $V_f = 1.85$ for AP1 vs. 2.5 for baseline (**Figure 4B**).

Old Blood Scalar Clearance per Part

Figure 5 shows the OBS washout for the three pump parts individually (see **Supplementary Figures 4, 5** for the complete set of results including the flow sensitivity study). The residual OBS concentration in the inflow cannula initially decays linearly, as only little mixing occurs in that part, and drops below 1% within 1 flush volume (**Figure 5A1**). OBS in the near-wall regions (here defined as <40 μm away from the walls) accounts for the majority of the OBS left in the inflow cannula after $V_f = 1$ (**Figure 5A2**) and is only slowly washed out. In the pump core, the residual OBS concentration follows an exponential

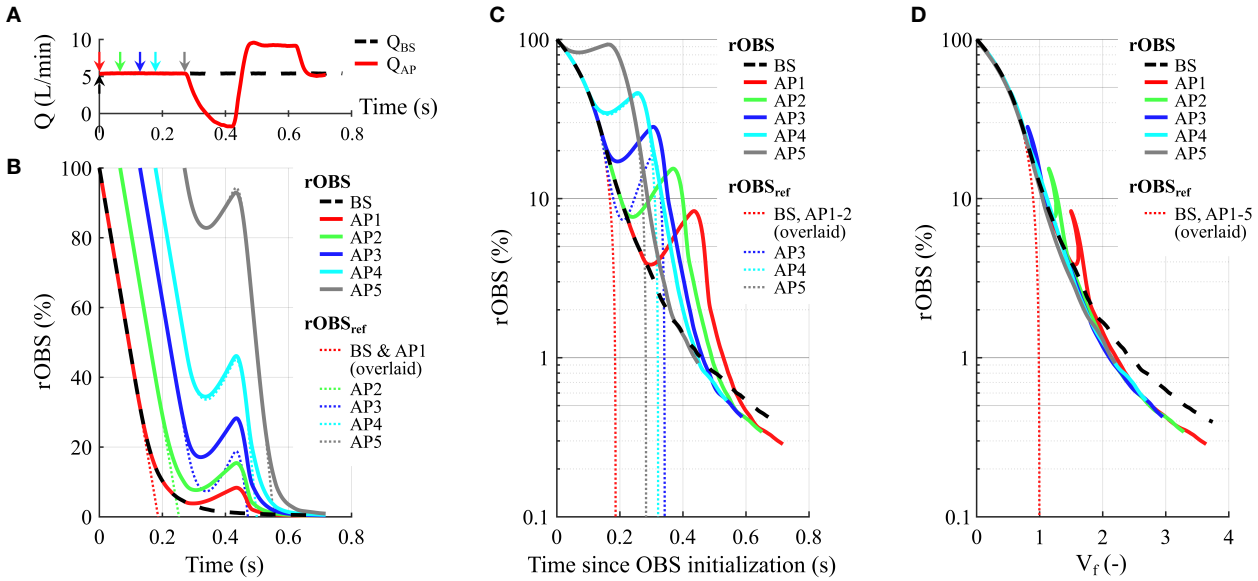

FIGURE 3 | Effect of the artificial pulse (AP) on the residual fraction of old blood scalar (rOBS). **(A)** Pump flow rate under baseline condition (BS) and with the AP. Arrows illustrate the different OBS initialization times using the same color coding as in **(B–D)**. Specifically, we consider one OBS for baseline (BS initialized in $t = 0$, black dashed arrow) and five different OBS initialization times with the AP (AP1–5, full colored arrows). **(B)** rOBS as a function of time (thick lines). For each OBS, the thin dotted lines illustrate the temporal evolution of the reference residual OBS concentration, $rOBS_{ref}$, providing a reference for the best possible washout given the pump flow rate. **(C)** rOBS as a function of time since initialization. A logarithmic scale is used to visualize differences for rOBS below 5%. 99% washout times for BS and AP3–5 are comparable despite the AP flow reversal and reduced flush volume for AP3–5 as illustrated by the longer $rOBS_{ref}$ clearance times (thin dotted lines). **(D)** rOBS as a function of the flush volume, V_f. Per definition, all the $rOBS_{ref}$ curves are overlaid depicting the best case scenario where one flush volume suffices to clear the pump. The "shark fin" feature corresponds to the AP flow reversal. The rotor acceleration and high-speed phase accelerate OBS washout for an equivalent flush volume as illustrated by the faster decline of rOBS for AP1–5 compared to baseline. The rOBS time course for all the simulated scenario, including high- and low-flow conditions, is given in **Supplementary Material S3**.

TABLE 1 | 95 and 99% washout times for different old blood scalars considered in the study.

Old blood scalar	rOBS at AP start (%)	95% washout time		99% washout time		
		Time (s)	V_f (–)	Time (s)	V_f (–)	$\overline{Q_{99\%}}$ (L/min)
Baseline	–	**0.26**	1.4	0.46	2.5	5.42
AP1	5.9	0.26 (1st), 0.47 (2nd)	1.4 (1st), 1.7 (2nd)	0.53	2.2	4.25
AP2	11.9	0.41	1.4	0.49	2.1	4.39
AP3	24.5	0.38	1.4	0.46	2.1	4.60
AP4	56.9	0.36	1.4	0.45	2.1	4.84
AP5	100.0	0.31	**1.3**	**0.44**	2.1	4.94
Low flow	–	0.41	1.3	0.72	2.4	3.50
High flow	–	0.17	1.3	0.27	2.1	8.60

Minimum washout times are marked in bold.
$\overline{Q_{99\%}}$: Time-average of the pump flow rate between OBS injection time and the 99% washout time.

decay, consistent with mixing, reaching 99% clearance within 1.5 flush volumes from the point at which new blood reached the pump core (**Figure 5B1**). Remaining OBS in the pump core is below 0.1% by $V_f = 3.5$, with good clearance of the near-wall regions (**Figure 5B2**). OBS clearance is the slowest in the outflow cannula, requiring 3.1 flush volumes from the point at which new blood reached the outlet to drop below 1% at baseline (**Figure 5C1**). The OBS secluded in the near-wall regions (**Figure 5C2**) accounts for <10% of the OBS remaining in the outflow cannula after $V_f = 2.0$, suggesting other slow clearance regions.

Compared to baseline, the AP leads to a transient increase in rOBS in the different pump parts followed by a faster and deeper OBS clearance during the acceleration phase (leading to the aforementioned "shark fin" feature, **Figures 5A1–C1**). By reverting flow direction along the walls, flow reversal favors clearance of the near-wall regions consistent with the decay of high volume with high OBS concentrations noted in **Figure 4**.

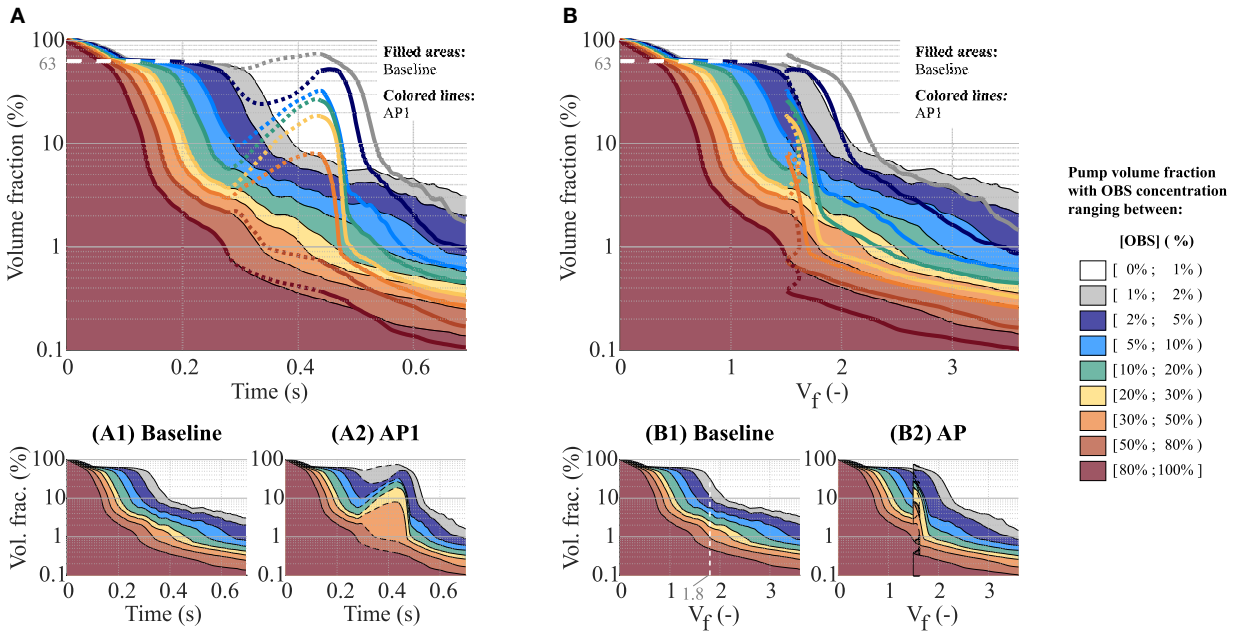

FIGURE 4 | Effect of the AP on the fraction of the pump volume with high to low OBS concentrations as a function of time **(A,A1,A2)** and flush volume **(B,B1,B2)**. **(A1,A2,B1,B2)** show the results for baseline and AP1 individually. The dashed contour lines highlight the low-speed phase of the AP, which, due to the associated flow reversal, leads to a transient decrease in the net flush volume, V_f **(B2)**. **(A,B)** To ease the comparison between baseline and AP1, **(A,B)** show the superposition of **(A1,A2,B1,B2**), respectively. The colored areas depict the results under baseline conditions [corresponding to **(A1,B1)**, respectively], while the thick colored lines correspond to AP1 [corresponding to **(A2,B2)**, respectively]. Here again, the dashed lines highlight the low-speed phase of the AP. Note that, for all the panels, a logarithmic scale is used for the Y-axis.

The cumulative effect of the low- and high-seed phases is negligible in the pump core and strongest in the outflow cannula. After $V_f = 2.0$, rOBS in the outflow cannula is 1–1.5% lower with the AP than at baseline (**Figure 5C1**) and rOBS values in the near-wall regions of the inflow and outflow cannula are 5–12% lower than at baseline (**Figures 5A2,C2**). Improved near-wall washout accounts for more than 50% of the benefit observed in the inflow cannula, but only for 10–20% of the benefit noted in the outflow cannula.

Washout of the Secondary Flow Paths of the Pump Core

As also noted in previous publications (17, 18), a region of low velocity forms centrally below the rotor during forward flow (**Figures 6A1,B1,D1**). The low-speed phase of the AP eliminates this low velocity region (**Figure 6C1**). The overall increase in OBS caused by the flow reversal is quickly counteracted during the high-speed phase (**Figure 6D2**). However, it is noteworthy that this flow stagnation region is unstable even at baseline (with a spatial shift between A1 and B1 for example) and, thereby, not associated with prolonged OBS residence times.

In the secondary flow path (**Figure 7**), the net flow direction is from the outer casing toward the center. A stagnation point forms on the upper surface of the rotor where a delicate balance between centrifugal force and pressure difference is achieved. Modulation of the rotor speed induces a spatial shift of that stagnation point. The formation of Taylor–Couette–Poiseuille flow pattern, common in rotating machinery (22, 23), along the outer casing, is also of note. Their spatial frequency is directly modulated by the rotor velocity.

We monitored WSS close to the two above noted stagnation regions (**Figure 8**). Centrally under the rotor, WSS oscillates between 0.19 and 15.57 Pa at baseline, in line with the unstable stagnation point location noted above. These WSS increase over 100 Pa (maximum 576.20 Pa) during the flow reversal (**Figure 6C1**) and return close to their baseline value during the high-speed phase of the AP because the stagnation region remains in the same location as at baseline. In the mid-radial location of the upper surface of the rotor, maximum WSS reaches 41.49 Pa at baseline and vary from 8.63 to 100.50 Pa during the AP deceleration and acceleration phases. For both the baseline and AP, the WSS direction is mainly concentrated between 300 and 330°.

Effect of the AP on Outlet Clearance

The bend relief and resulting curvature of the HM3 outflow lead to the formation of a flow separation (**Figure 9A**), which accounts for the majority of the OBS remaining in the outlet by $V_f = 2.0$. By increasing mixing during the low-speed phase and then quickly removing mixed blood during the acceleration, the AP improves washout of the bend relief (**Figure 9B**) and generally reduces OBS concentrations in the outlet (**Figures 5C1,C2**).

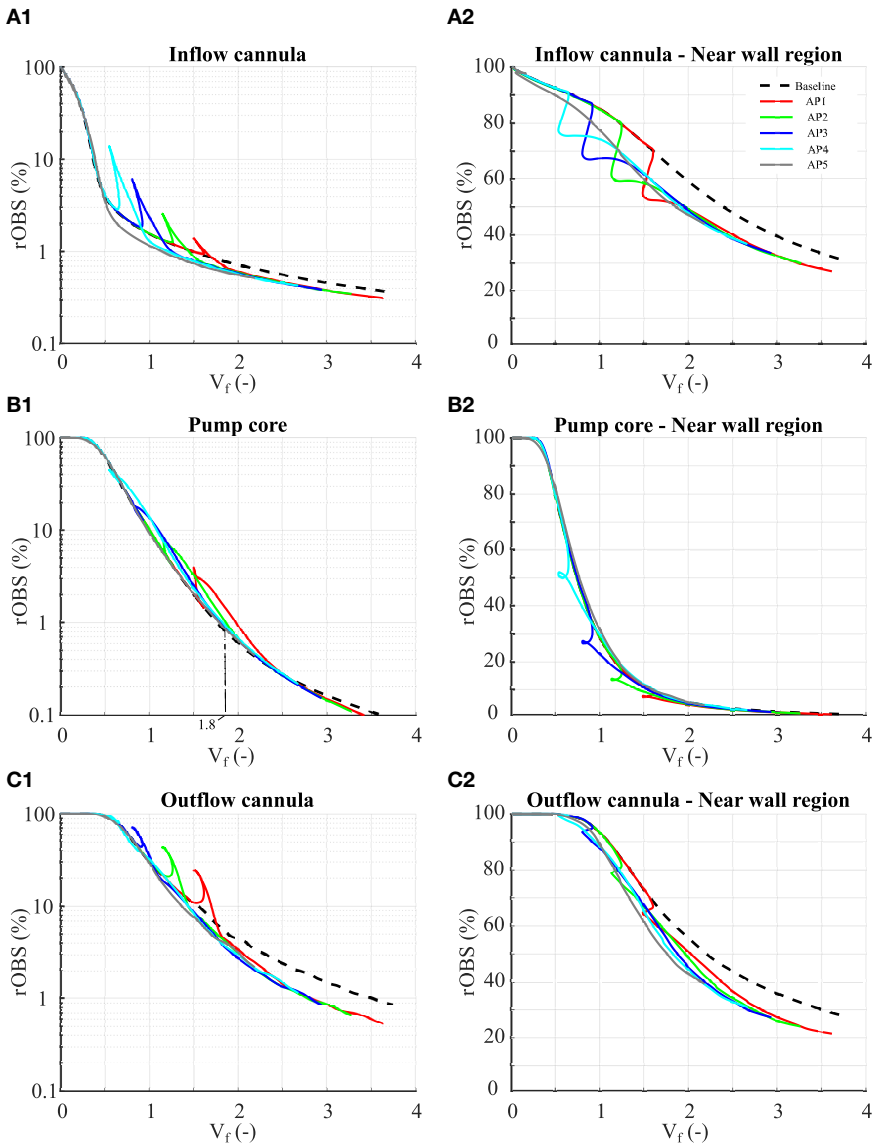

FIGURE 5 | Residual OBS concentrations in the inflow cannula **(A1–A2)**, pump core **(B1–B2)**, and outflow cannula **(C1–C2)**. Definition of the different parts is given in **Figure 1. (A1–C1)** Residual OBS concentrations for the each pump part. Note that the results are plotted using a logarithmic scale for the residual OBS concentrations. **(A2–C2)** Residual OBS concentration in the vicinity of the pump surfaces ($\leq$40 μm away from the walls). In total, these near-wall regions occupy 0.92% of the whole pump volume, 0.62% of the inlet, 1.44% of the pump core, and 0.71% of the outlet volumes.

DISCUSSION

Left ventricular assist device thrombogenicity depends on multiple factors including patient-specific characteristics (24) as well as pump implantation configurations (25, 26), postimplant patient management strategies (27), and the pump internal flow fields (6), which, in turn, affect blood cell and protein residence times and shear stress exposure. Aiming at providing mechanistic insights into the low occurrence of the HM3 in-pump thrombosis and at isolating the contribution of the AP from that of the HM3 internal design, we used CFD simulations coupled with passive scalar advection to assess the effects of the AP on the volume and surface washout of the HM3. Of specific interest was: (i) the clearance of the last 5 to 1% of residual OBS concentration, taken as indicative of regions of prolonged residence times and (ii) the clearance of the pump internal surfaces to assess the effect of the AP in mitigating the risk of thrombus formation and/or deposition inside the pump.

Different measures of scalar washout and residence time have been studied to compare the performances across different pumps or flow conditions. Molteni et al. (28) compared the outlet scalar washout of the CentriMag (Abbott, Chicago, Illinois, USA), HVAD, and the HMII for pump flow rates ranging between 1 and 5 L/min. After normalization for the effect of pump

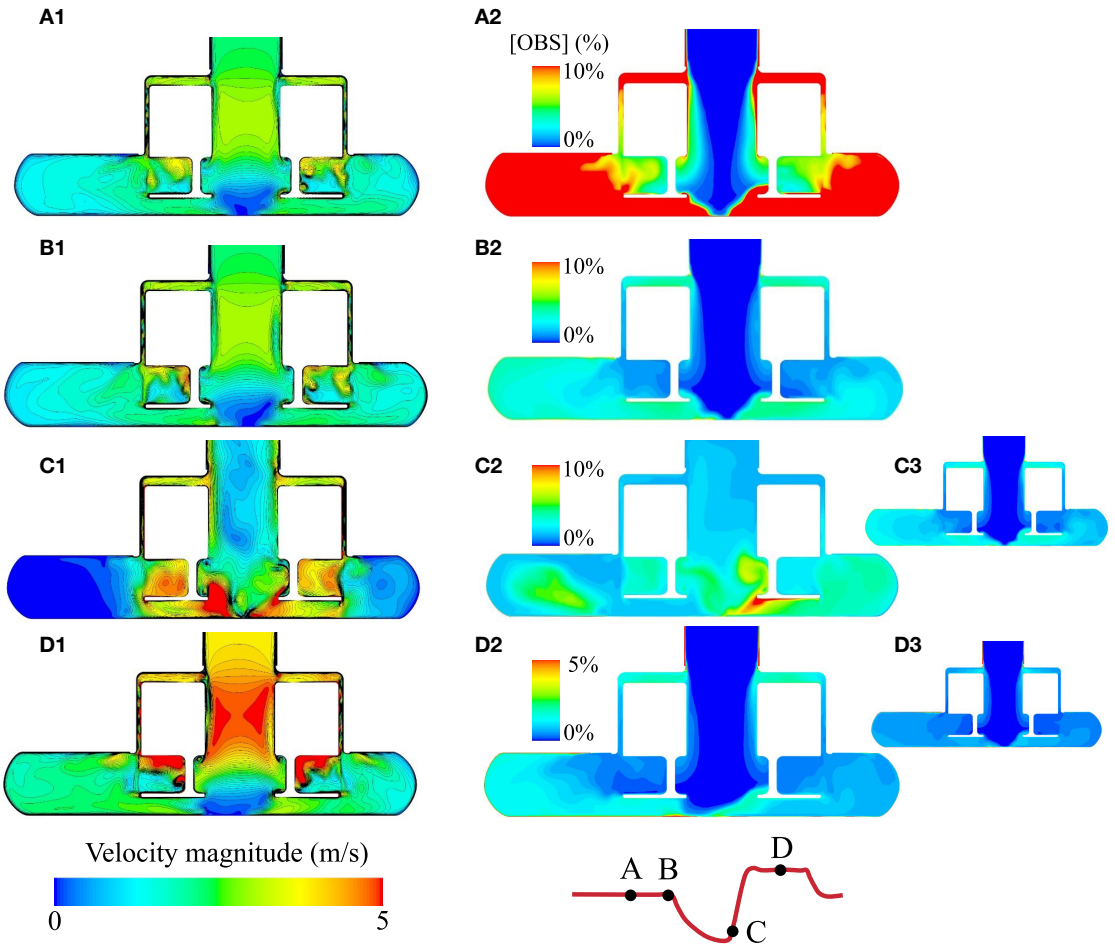

FIGURE 6 | Comparison of the instantaneous velocity fields and evolution of the OBS concentrations in the pump core during the AP1 scenario. **(A1–D1)** Instantaneous velocity fields in the HM3 pump core for the four instants illustrated on the flow curve with the pump operating at baseline speed (5,650 rpm, instants A and B), low speed (3,650 rpm, instant C), and high speed (7,650 rpm, instant D). For AP1, the time points A, B, C, and D correspond to $V_f = 0.9$, 1.4, 1.5, and 2.0, respectively. **(A2–D2)** OBS concentrations at instants A, B, C, and D for the AP1 scenario. OBS concentrations are expressed as a percentage of the initial concentration $[OBS]_0$. rOBS over the core pump for the AP1 scenario is 14.0, 2.6, 4.0, and 0.9% at the instants A, B, C, and D, respectively. **(C3,D3)** OBS concentrations in the pump core for $V_f = 1.5$ and 2.0 under baseline conditions, corresponding to the same flush volumes as instants C and D for AP1. Note that instants A and B apply to the baseline scenario as well, as the pump is operating under the set baseline speed at those time points.

priming volume and flow rate, the time required for the residual OBS concentration at the pump outlet to drop below 50, T50, corresponded to 0.76–0.94 flush volumes for all the pumps and all the flow conditions. Time required to reduce the residual outlet OBS concentration to 5%, T05, showed higher variations, corresponding to 1.8–2.2 flush volumes for the HMII up to 2.6–2.8 in the HVAD and CentriMag. Deriving the outlet scalar washout from our results (**Supplementary Material S4**), the T50 in the HM3 under the baseline, high-, and low-flow conditions corresponded to 0.9 flush volumes for all the three conditions, while T05 ranged between 1.6 and 1.7. Zhang et al. (29) reported average residence times of 0.12, 0.20, and 0.18 s at the outlet of the CH-ventricular assist device (CH-VAD) (CH Biomedical Incorporation, Suzhou, China), HVAD, and the HM II for a pump flow rate of 4.5 L/min. A similar metric can be derived from the washout plots under constant operating conditions (**Supplementary Material S5**), yielding average residence times of 0.28, 0.18, and 0.11 s under the low-flow, baseline, and high-flow conditions, respectively. These average residence times correspond to 0.97 flush volumes for all the three conditions. By investigating the performance of the HVAD under different constant operating conditions, Granegger et al. (30) reported that the 90% washout time, defined as the time required to reduce the residual old blood concentration within the pump from 100% down to 10%, was 0.3 s at 5 L/min and 0.6 s at 2.5 L/min, scaling inversely with the flow rate. Mean blood transit times reported by Bourque et al. (11) for the HM3 also followed a perfect inverse-proportional relationship with the pump flow rate, with values of 0.587, 0.219, and 0.118 s at 2.0, 5.4, and 10.0 L/min, respectively. Similarly, in this study, the 95% washout of the HM3, defined as the number of flush volumes required to reduce the residual old blood concentration in the pump from 100 down to 5%,

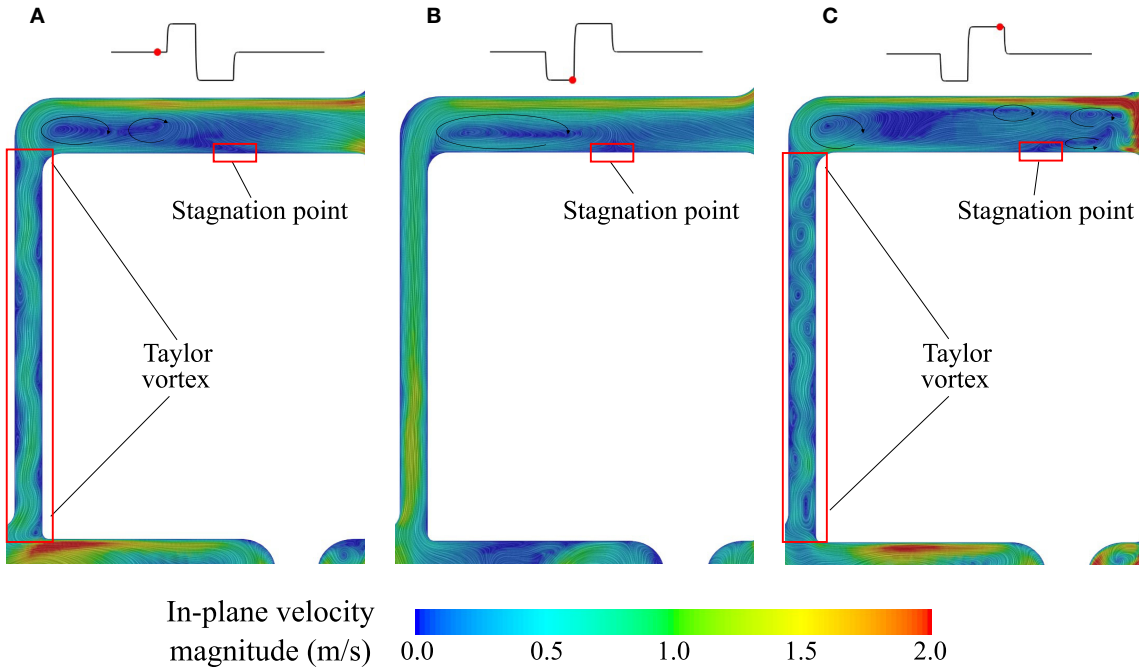

FIGURE 7 | Velocity field in the secondary flow path. **(A)** Baseline, **(B)** Low-speed phase of the AP, and **(C)** High-speed phase of the AP.

was comparable across tested conditions. Whether the AP was turned on or off, 95% washout was achieved within 1.3–1.4 flush volumes. Similar results were obtained by Boraschi et al. (17) under a different baseline condition, wherein the 95% washout time was 0.29 s at 5 L/min, translating to 1.4 flush volumes, a performance which appears reasonable when compared to the best possible scenario wherein 95% washout would be achieved in exactly 0.95 flush volumes. Altogether, despite the large and rapid changes in both the flow rate and rotor speed imparted by the AP, washout dynamics down to 95% pump washout are only marginally affected when normalizing for the effect of flow rate. Similarly, average residence times were primarily dictated by the flow rate, corresponding to the time to drive approximately one flush volume of blood through the pump. This suggest that, overall, the 95% washout is primarily determined by the pump flow, while the acceleration and deceleration rates of the rotor and flow only have a marginal effect. These further point to a predominant role of the pump internal design and smaller role of the AP at least for the washout of main flow paths.

On the other hand, the AP showed to be of advantage for the 99% washout of the HM3. At baseline, reducing the rOBS concentration down to 1%, i.e., achieving 99% washout, required 2.5 flush volumes, a stark increase compared to the 1.4 flush volumes required for the 95% washout. When accounting for differences in flow rate, 99% washout was faster with the AP than without for all the considered injection times ($V_f = 2.1$–2.2), suggesting that the AP may help clear harder to wash fluid regions. This is of interest, as fluid regions with prolonged high OBS concentrations pinpoint areas with prolonged residence times, which although the exact thresholds remain elusive and no doubt contributes to increased risk of platelet aggregation and deposition.

Closer investigation of the pump clearance suggests that the AP may be beneficial for the clearance of the near-wall regions in the inlet and outlet as well as of the flow separation downstream of the bend relief. It is not unexpected that curvature—which is needed to connect the pump to the aorta—may lead to flow separation (**Figure 9**). In the HM3, part of that curvature is already included within the outflow cannula by the bend relief. The AP benefits the clearance of that specific region, increasing mixing during the low-flow phase followed by rapid clearance during the high-speed phase. Whether such effect would also benefit graft washout downstream of the pump remains to be demonstrated. Clearance of the outflow graft, which has until now received little attention, may be a relevant topic to pursue in the future, especially since these grafts are also prone to thrombus formation (31).

In contrast to the inlet and outlet cannulas, washout of the HM3 pump core benefitted only minimally from the AP (**Figure 5**), pointing to a primary role of the rotor and volute design in the observed volume washout rates despite the large changes in local flow structures imparted by the AP. Specific design features of the HM3 pump core include no central post and large gaps. Consistent with the results of Fang et al. (32) and Wiegmann et al. (18), the absence of central post leads to the formation of a flow stagnation region centrally below the rotor under baseline conditions. This stagnation region was completely eradicated by flow reversal during the low-speed phase of the AP. In the top gap, the competing effect of centrifugal forces and pressure gradients leads to a complex alternation

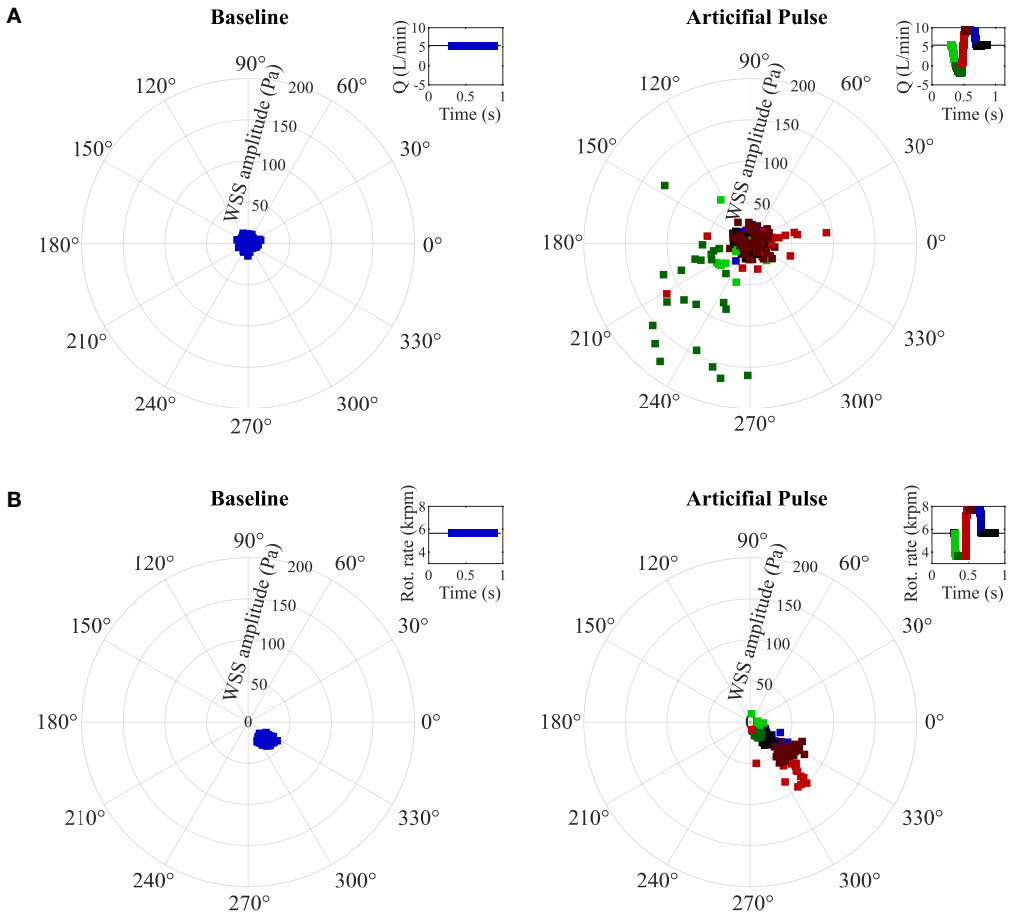

FIGURE 8 | Wall shear stress on the central points of **(A)** the bottom of casing and **(B)** the top of casing within secondary flow path. Five outliers in **(A)** (with WSS higher than 200 Pa) are not shown. WSS: wall shear stress (see **Supplementary Material S1** for the location of the WSS monitoring points).

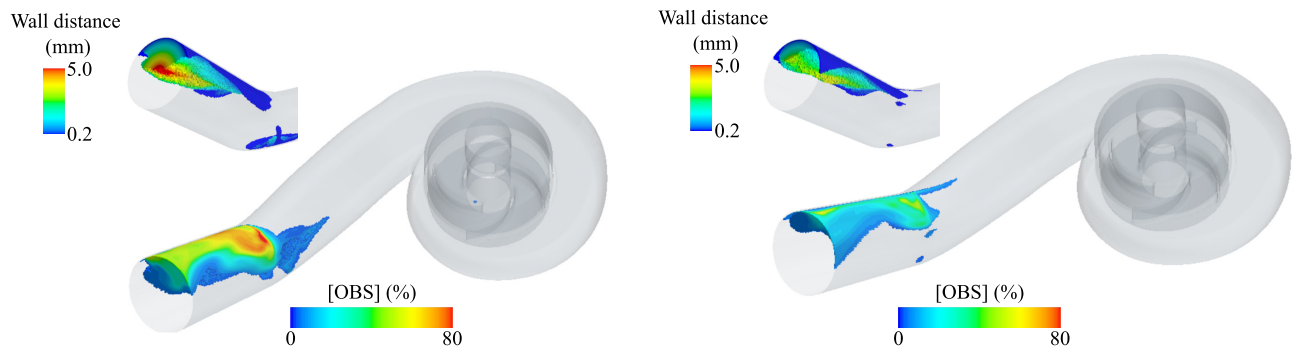

FIGURE 9 | Fluid volumes in the HeartMate 3 (HM3) pump core and outlet cannula with residual OBS concentrations over 5% after flushing the pump with two times its blood volume ($V_f = 2.0$) without AP [**(A)**, baseline conditions] and with AP [**(B)**, AP1 scenario]. At $V_f = 2.0$, the average residual OBS concentration is 1.7 and 1.5% in the core pump for the Baseline and AP1 scenario, respectively, and is 4.5% at baseline and 3.5% for AP1 in the outlet cannula. For ease of visualization, only fluid volumes with [OBS] $\geq$ 5% and more than 200 μm away from the pump surfaces are shown. Apart from a small region under the rotor at baseline, no 5% OBS isovolume are identified in the pump core at that instance. The insets show the 5% OBS isovolumes in the outflow cannula color coded by wall distance to highlight the penetration depth of that region under baseline conditions and the effect of the AP on its clearance.

of recirculation regions and the formation of a stagnation point along the upper surface of the rotor. By changing the rotor speed, the AP again favors spatial shift of the stagnation points and mixing, which may theoretically be advantageous for washout. However, the noted stagnation regions are not stable even under constant operating conditions. rOBS concentration centrally under the rotor is already below 1% after 1.4 flush volumes at baseline. Bottom, side, and top secondary flow paths, although cleared at a slower rate than the main flow path, do not display isolated pockets of high rOBS values (**Figures 6D2,D3**), suggesting adequate washout for all the considered conditions.

Besides OBS washout (or volume washout), the impact of the AP on WSS is of interest, as it directly impacts surface washout. WSS provides an indication of near-wall blood velocity and regions of low WSS (<0.3 or 1 Pa) have been associated with an increased risk for clot deposition (33, 34). Jamiolkowski et al. (35) further reported that wall shear rates above 1,000 s^{-1} [corresponding to WSS of 3 Pa (36) with viscosity used in their study] were related to decreased thrombus stability and more embolization events. Within the stagnation region centrally below the rotor, maximum WSS reached 15.6 Pa at baseline, which is already one order of magnitude higher than reported cutoff values for clot deposition or thrombi destabilization and up to 576 Pa during the AP, over two orders of magnitude higher than reported thresholds. The high WSS value and changing WSS direction observed in the HM3 pump core are, therefore, likely to further contribute to the very low rate of in-pump thrombosis noted in patients with the HM3. However, further studies would be needed to determine whether such high WSS and WSS gradients are required to that end or whether the same objective may be achieved with already lower values. Whether periodic surface clearance, as imparted by the AP, enhances the risk of secondary thromboembolic events caused by the detachment of small thrombi formed on the pump surface also warrants further investigation.

Finally, the above noted benefits of the AP in terms of volume and surface washout also come at the cost of an abrupt increase in fluid shear stresses throughout the pump volume. As discussed by Wiegmann et al. (18) and Boraschi et al. (17), the rotor acceleration and high-speed phase of the AP increase fluid shear stresses and turbulence levels. In both the studies, the stress-exposure profiles of particles flowing through the pump during the AP shifted toward longer exposure time to supraphysiological stresses combined with rapid fluctuations in experienced shear stresses, both of which were experimentally found to contribute to platelet activation (7). The high stresses imparted by the AP may, therefore, contribute to the still relevant rates of strokes in patients implanted with the HM3 (9). Elevated fluid shear stresses and turbulence have also been associated with the degradation of von Willebrand factor (vWF) multimeres (37) that are essential for hemostasis. Clinically, although at a lower extent compared to the HeartMate II, vWF deficiency (38, 39) and bleeding rates (42.9%) (9) remain high with the HM3. A rationale revision of the AP speed modulation sequence for lower shear stress exposures may be, therefore, an interesting avenue to pursue to reduce its intrinsic prothrombotic profile and limit bleeding complications. Of note, lowering shear stress generated by the pump during the AP might reinforce the clinical reliability of new antithrombotic strategies—lower anticoagulation target (40) or aspirin-free regimen (39, 41, 42), which showed improved hemocompatibility-related outcomes in patients with HM3.

This study has limitations. Blood was simplified to an incompressible Newtonian fluid, excluding particles and semisolid components, such as cells, proteins, and lipoproteins. The HM3 geometry was scanned from an explanted pump. Therefore, we cannot exclude small differences to the actual geometry. Furthermore, the HM3 features textured blood-contacting surfaces, which were not taken into account in this study, but have been assumed, also contribute to enhanced antithrombogenic properties (11). Residual cardiac contractility was not simulated, meaning that we neglected the impact of cardiac pulsatility on internal pump hemodynamics, which is expected to influence washout time because of its influence on the mean pump flow. However, as changes imparted by the residual (low) cardiac contractility of patients with end-stage heart failure are smoother and of lower amplitude than those imparted by sudden changes characteristics of the AP, we expect the normalized behavior to be well captured by the conditions investigated here. The HM3 only allows to increase/decrease the pump rotational speed by a 100-rpm step and an "unphysical" baseline rotational speed of 5,650 rpm was used. This choice was dictated by the numerical problem, specifically by the need to target clinically relevant flow conditions. In detail, according to the patient characteristics of our lumped parameter model of the cardiovascular system, this value allowed us to achieve a mean pump flow rate of about 5 L/min with the AP. On the other hand, results of the simulations where the high- and low-flow conditions were imposed (**Supplementary Materials S3–S5**) suggest that this 50-rpm difference is unlikely to significantly affect the results. Finally, exact biological thresholds (e.g., WSS needed to prevent deposits on pump surfaces) are unknown. The forces required for the removal of deposits on blood-contacting surfaces depend on the thrombus stability, size, and shape as well as on the surface properties. Further fundamental studies are warranted to evaluate the influence of WSS on deposit removal and blood damage.

CONCLUSION

In summary, the AP did not affect the 95% washout, suggesting the dominant role of pump flow rate. The AP helped in clearing regions with prolonged exposure times, particularly in the near-wall regions and bend relief. In contrast and as highlighted by earlier studies, the AP leads to an abrupt increase in turbulence and shear stress levels, which have been associated with higher platelet activation levels and blood damage. Altogether, these results provide a mechanistic rationale as to why the HM3 is associated with negligible rate of in-pump thrombosis, but still relevant rate of stroke. Further understanding of the biological effects of turbulence as well as of the WSS required to

prevent thrombus deposition may help to establish the costs and benefits of rotor accelerations such as those imposed during the AP and further optimize rotor speed modulation sequences. From this perspective, our numerical platform represents a valuable tool for the fine-tuning of rotor speed modulation sequences of current and future generations of LVADs.

DATA AVAILABILITY STATEMENT

The raw data supporting the conclusions of this article will be made available by the authors, without undue reservation.

AUTHOR CONTRIBUTIONS

PF and AB formalized the simulation methodology. PF conducted the simulations and performed the data analysis. MS, SB, and AR guided the data interpretation. PF, JD, DZ, and VK were involved in funding acquisition. FC and DZ conceived the study and DZ, JD, and VK directed the research. All the authors contributed to the manuscript and have approved the final version of the manuscript.

FUNDING

The authors gratefully acknowledge the financial support from the University of Zürich by contributing to the open access publication fees, the Shenzhen Science and Technology Innovation Foundation (Grant No. JCYJ20160427184134564 to JD), the National Natural Science Foundation of China (Grant No. U2141210 to JD), the China Scholarship Council (No. 202006120445 to PF), the Swiss National Science Foundation through the NCCR Kidney. CH (to VK), and the Stavros Niarchos Foundation (to VK). This study is a part of the Zurich Heart project under the umbrella of University Medicine Zurich.

SUPPLEMENTARY MATERIAL

The Supplementary Material for this article can be found online at: https://www.frontiersin.org/articles/10.3389/fcvm.2022.775780/full#supplementary-material

REFERENCES

1. Benjamin EJ, Virani SS, Callaway CW, Chamberlain AM, Chang AR, Cheng S, et al. Heart disease and stroke statistics - 2018 update: a report from the American Heart Association. *Circulation*. (2018) 137:e67–e492. doi: 10.1161/CIR.0000000000000558
2. Burkhoff D, Klotz S, Mancini DM. LVAD-induced reverse remodeling: basic and clinical implications for myocardial recovery. *J Card Fail.* (2006) 12:227–39. doi: 10.1016/j.cardfail.2005.10.012
3. Zimpfer D, Gustafsson F, Potapov E, Pya Y, Schmitto J, Berchtold-Herz M, et al. Two-year outcome after implantation of a full magnetically levitated left ventricular assist device: Results from the ELEVATE Registry. *Eur Heart J.* (2020) 41:3801–9. doi: 10.1093/eurheartj/ehaa639
4. Molina EJ, Shah P, Kiernan MS, Cornwell WK, Copeland H, Takeda K, et al. The Society of Thoracic Surgeons Intermacs 2020 Annual Report. *Ann Thorac Surg.* (2021) 111:778–92. doi: 10.1016/j.athoracsur.2020.12.038
5. Kirklin JK, Naftel DC, Pagani FD, Kormos RL, Stevenson LW, Blume ED, et al. Seventh INTERMACS annual report: 15,000 patients and counting. *J Hear Lung Transplant.* (2015) 34:1495–504. doi: 10.1016/j.healun.2015.10.003
6. Selmi M, Chiu WC, Chivukula VK, Melisurgo G, Beckman JA, Mahr C, et al. Blood damage in Left Ventricular Assist Devices: Pump thrombosis or system thrombosis? *Int J Artif Organs.* (2019) 42:113–24. doi: 10.1177/0391398818806162
7. Consolo F, Sheriff J, Gorla S, Magri N, Bluestein D, Pappalardo F, et al. High frequency components of hemodynamic shear stress profiles are a major determinant of shear-mediated platelet activation in therapeutic blood recirculating devices. *Sci Rep.* (2017) 7:1–14. doi: 10.1038/s41598-017-05130-5
8. Meyer AD, Rishmawi AR, Kamucheka R, Lafleur C, Batchinsky AI, Mackman N, et al. Effect of blood flow on platelets, leukocytes, and extracellular vesicles in thrombosis of simulated neonatal extracorporeal circulation. *J Thromb Haemost.* (2020) 18:399–410. doi: 10.1111/jth.14661
9. Mehra MR, Goldstein DJ, Uriel N, Cleveland JC, Yuzefpolskaya M, Salerno C, et al. Two-year outcomes with a magnetically levitated cardiac pump in heart failure. *N Engl J Med.* (2018) 378:1386–95. doi: 10.1056/NEJMoa1800866
10. Rogers JG, Pagani FD, Tatooles AJ, Bhat G, Slaughter MS, Birks EJ, et al. Intrapericardial left ventricular assist device for advanced heart failure. *N Engl J Med.* (2017) 376:451–60. doi: 10.1056/NEJMoa1602954
11. Bourque K, Cotter C, Dague C, Harjes D, Dur O, Duhamel J, et al. Design rationale and preclinical evaluation of the HeartMate 3 left ventricular assist system for hemocompatibility. *ASAIO J.* (2016) 62:375–83. doi: 10.1097/MAT.0000000000000388
12. Heatley G, Sood P, Goldstein D, Uriel N, Cleveland J, Middlebrook D, et al. Clinical trial design and rationale of the Multicenter Study of MagLev Technology in Patients Undergoing Mechanical Circulatory Support Therapy with HeartMate 3 (MOMENTUM 3) investigational device exemption clinical study protocol. *J Hear Lung Transplant.* (2016) 35:528–36. doi: 10.1016/j.healun.2016.01.021
13. Schmitto JD, Hanke JS, Rojas S V, Avsar M, Haverich A. First implantation in man of a new magnetically levitated left ventricular assist device (HeartMate III). *J Hear Lung Transplant.* (2015) 34:858–60. doi: 10.1016/j.healun.2015.03.001
14. Essandoh M, Essandoh G, Stallkamp ED, Perez WJ. Spectral doppler analysis of the HeartMate 3 left ventricular assist device inflow: new challenges presented by the artificial pulse technology. *J Cardiothorac Vasc Anesth.* (2018) 32:e4–5. doi: 10.1053/j.jvca.2018.07.005
15. Bourque K, Dague C, Farrar D, Harms K, Tamez D, Cohn W, et al. In vivo assessment of a rotary left ventricular assist device-induced artificial pulse in the proximal and distal aorta. *Artif Organs.* (2006) 30:638–42. doi: 10.1111/j.1525-1594.2006.00276.x
16. Zimpfer D, Strueber M, Aigner P, Schmitto JD, Fiane AE, Larbalestier R, et al. Evaluation of the HeartWare ventricular assist device Lavare cycle in a particle image velocimetry model and in clinical practice. *Eur J Cardio-thoracic Surg.* (2016) 50:839–48. doi: 10.1093/ejcts/ezw232
17. Boraschi A, Bozzi S, Thamsen B, Granegger M, Wiegmann L, Pappalardo F, et al. Thrombotic risk of rotor speed modulation regimes of contemporary centrifugal continuous-flow left ventricular assist devices. *ASAIO J.* (2020) Publish Ah:14–16. doi: 10.1097/MAT.0000000000001297
18. Wiegmann L, Thamsen B, de Zélicourt D, Granegger M, Boës S, Schmid Daners M, et al. Fluid dynamics in the HeartMate 3: influence of the artificial pulse feature and residual cardiac pulsation. *Artif Organs.* (2019) 43:363–76. doi: 10.1111/aor.13346
19. Colacino FM, Moscato F, Piedimonte F, Arabia M, Danieli GA. Left ventricle load impedance control by apical VAD can help heart recovery and patient perfusion: a numerical study. *ASAIO J.* (2007) 53:263–77. doi: 10.1097/MAT.0b013e31805b7e39

20. Gupta S, Woldendorp K, Muthiah K, Robson D, Prichard R, Macdonald PS, et al. Normalisation of haemodynamics in patients with end-stage heart failure with continuous-flow left ventricular assist device therapy. *Hear Lung Circ.* (2014) 23:963–9. doi: 10.1016/j.hlc.2014.04.259
21. Boës S, Thamsen B, Haas M, Schmid Daners M, Meboldt M, Granegger M. Hydraulic Characterization of Implantable Rotary Blood Pumps. *IEEE Trans Biomed Eng.* (2019) 66:1618–927. doi: 10.1109/TBME.2018.2876840
22. Poncet S, Viazzo S, Oguic R. Large eddy simulations of Taylor-Couette-Poiseuille flows in a narrow-gap system. *Phys Fluids*. (2014) 26:105108. doi: 10.1063/1.4899196
23. Taskin ME, Fraser KH, Zhang T, Gellman B, Fleischli A, Dasse KA, et al. Computational characterization of flow and hemolytic performance of the ultramag blood pump for circulatory support. *Artif Organs.* (2010) 34:1099–113. doi: 10.1111/j.1525-1594.2010.01017.x
24. Consolo F, Sferrazza G, Motolone G, Contri R, Valerio L, Lembo R, et al. Platelet activation is a preoperative risk factor for the development of thromboembolic complications in patients with continuous-flow left ventricular assist device. *Eur J Heart Fail.* (2018) 20:792–800. doi: 10.1002/ejhf.1113
25. May-Newman K, Moon J, Ramesh V, Montes R, Campos J, Herold B, et al. The effect of inflow cannula length on the intraventricular flow field: an in vitro flow visualization study using the evaheart left ventricular assist device. *ASAIO J.* (2017) 63:592–603. doi: 10.1097/MAT.0000000000000559
26. Ortiz S, Vu V, Montes R, May-Newman K. Left ventricular flow dynamics with the HeartMate3 left ventricular assist device. *ASAIO J.* (2021) Publish Ah:1–11. doi: 10.1097/MAT.0000000000001523
27. Hohner E, Crow J, Moranville MP. Medication management for left ventricular assist device thrombosis. *Am J Heal Pharm.* (2015) 72:1104–13. doi: 10.2146/ajhp140538
28. Molteni A, Masri ZP, Low KW, Yousef HN, Sienz J, Fraser KH. Experimental measurement and numerical modelling of dye washout for investigation of blood residence time in ventricular assist devices. *Int J Artif Organs.* (2018) 41:201–12. doi: 10.1177/0391398817752877
29. Zhang J, Chen Z, Griffith BP, Wu ZJ. Computational characterization of flow and blood damage potential of the new maglev CH-VAD pump versus the HVAD and HeartMate II pumps. *Int J Artif Organs.* (2020) 43:653–62. doi: 10.1177/0391398820903734
30. Granegger M, Thamsen B, Schlöglhofer T, Lach S, Escher A, Haas T, et al. Blood trauma potential of the HeartWare Ventricular Assist Device in pediatric patients. *J Thorac Cardiovasc Surg.* (2020) 159:1519–27.e1. doi: 10.1016/j.jtcvs.2019.06.084
31. Duero Posada VR. Outflow Graft Occlusion of the HeartMate 3 LVAD. *Circ Heart Fail.* (2017) 10:e004275. doi: 10.1161/CIRCHEARTFAILURE.117.004275
32. Fang P, Du J, Yu S. Effect of the center post establishment and its design variations on the performance of a centrifugal rotary blood pump. *Cardiovasc Eng Technol.* (2020) 11:337–49. doi: 10.1007/s13239-020-00464-0
33. Hochareon P, Manning KB, Fontaine AA, Tarbell JM, Deutsch S. Correlation of in vivo clot deposition with the flow characteristics in the 50 cc Penn State Artificial Heart: a preliminary study. *ASAIO J.* (2004) 50:537–42. doi: 10.1097/01.MAT.0000145694.40637.A0
34. Rayz VL, Boussel L, Ge L, Leach JR, Martin AJ, Lawton MT, et al. Flow residence time and regions of intraluminal thrombus deposition in intracranial aneurysms. *Ann Biomed Eng.* (2010) 38:3058–69. doi: 10.1007/s10439-010-0065-8
35. Jamiolkowski MA, Pedersen DD, Wu WT, Antaki JF, Wagner WR. Visualization and analysis of biomaterial-centered thrombus formation within a defined crevice under flow. *Biomaterials.* (2016) 96:72–83. doi: 10.1016/j.biomaterials.2016.04.022
36. Resnick N, Yahav H, Shay-Salit A, Shushy M, Schubert S, Zilberman LCM, et al. Fluid shear stress and the vascular endothelium: For better and for worse. *Prog Biophys Mol Biol.* (2003) 81:177–99. doi: 10.1016/S0079-6107(02)00052-4
37. Jhun CS, Siedlecki C, Xu L, Lukic B, Newswanger R, Yeager E, et al. Stress and Exposure Time on von Willebrand Factor Degradation. *Artif Organs.* (2019) 43:199–206. doi: 10.1111/aor.13323
38. Bansal A, Uriel N, Colombo PC, Narisetty K, Long JW, Bhimaraj A, et al. Effects of a fully magnetically levitated centrifugal-flow or axial-flow left ventricular assist device on von Willebrand factor: a prospective multicenter clinical trial. *J Hear Lung Transplant.* (2019) 38:806–16. doi: 10.1016/j.healun.2019.05.006
39. Consolo F, Marasi A, Valle P. Della, Mara A, Redaelli A, Zangrillo A, et al. Bleeding in patients with continuous-flow left ventricular assist devices : acquired von Willebrand disease or antithrombotics? *Eur J Cardiothorac Surg.* (2021) 00:1–8. doi: 10.1093/ejcts/ezab474
40. Netuka I, Ivák P, Tučanová Z, Gregor S, Szárszoi O, Sood P, et al. Evaluation of low-intensity anti-coagulation with a fully magnetically levitated centrifugal-flow circulatory pump—the MAGENTUM 1 study. *J Hear Lung Transplant.* (2018) 37:579–86. doi: 10.1016/j.healun.2018.03.002
41. Consolo F, Raimondi Lucchetti M, Tramontin C, Lapenna E, Pappalardo F. Do we need aspirin in HeartMate 3 patients? *Eur J Heart Fail.* (2019) 21:815–7. doi: 10.1002/ejhf.1468
42. Consolo F, Pozzi L, Pieri M, Della Valle P, Redaelli A, D'Angelo A, et al. Influence of different antithrombotic regimens on platelet-mediated thrombin generation in patients with left ventricular assist devices. *ASAIO J.* (2020) 66:415–22. doi: 10.1097/MAT.0000000000001064

Conflict of Interest: The authors declare that the research was conducted in the absence of any commercial or financial relationships that could be construed as a potential conflict of interest.

Publisher's Note: All claims expressed in this article are solely those of the authors and do not necessarily represent those of their affiliated organizations, or those of the publisher, the editors and the reviewers. Any product that may be evaluated in this article, or claim that may be made by its manufacturer, is not guaranteed or endorsed by the publisher.

frontiers | Frontiers in Cardiovascular Medicine

ORIGINAL RESEARCH
published: 11 April 2022
doi: 10.3389/fcvm.2022.831080

DeepStrain Evidence of Asymptomatic Left Ventricular Diastolic and Systolic Dysfunction in Young Adults With Cardiac Risk Factors

Manuel A. Morales[1,2†], Gert J. H. Snel[3†], Maaike van den Boomen[1,3,4], Ronald J. H. Borra[3,5], Vincent M. van Deursen[6], Riemer H. J. A. Slart[5,7], David Izquierdo-Garcia[1,2], Niek H. J. Prakken[3†] and Ciprian Catana[1*†]*

[1] Department of Radiology, Athinoula A. Martinos Center for Biomedical Imaging, Massachusetts General Hospital and Harvard Medical School, Boston, MA, United States, [2] Harvard-MIT Division of Health Sciences and Technology, Cambridge, MA, United States, [3] Department of Radiology, Medical Imaging Center, University Medical Center Groningen, University of Groningen, Groningen, Netherlands, [4] Cardiovascular Research Center, Massachusetts General Hospital and Harvard Medical School, Boston, MA, United States, [5] Department of Nuclear Medicine and Molecular Imaging, Medical Imaging Center, University Medical Center Groningen, University of Groningen, Groningen, Netherlands, [6] Department of Cardiology, University Medical Center Groningen, University of Groningen, Groningen, Netherlands, [7] Department of Biomedical Photonic Imaging, Faculty of Science and Technology, University of Twente, Enschede, Netherlands

OPEN ACCESS

Edited by:
Marianne Schmid Daners,
ETH Zürich, Switzerland

Reviewed by:
J. Paul Finn,
UCLA Health System, United States
Victor Ferrari,
Hospital of the University of Pennsylvania, United States

***Correspondence:**
Manuel A. Morales
mmorale5@bidmc.harvard.edu
Ciprian Catana
ccatana@mgh.harvard.edu

[†] These authors have contributed equally to this work and share first and last authorship

Specialty section:
This article was submitted to General Cardiovascular Medicine, a section of the journal Frontiers in Cardiovascular Medicine

Received: 07 December 2021
Accepted: 11 March 2022
Published: 11 April 2022

Citation:
Morales MA, Snel GJH, van den Boomen M, Borra RJH, van Deursen VM, Slart RHJA, Izquierdo-Garcia D, Prakken NHJ and Catana C (2022) DeepStrain Evidence of Asymptomatic Left Ventricular Diastolic and Systolic Dysfunction in Young Adults With Cardiac Risk Factors. Front. Cardiovasc. Med. 9:831080. doi: 10.3389/fcvm.2022.831080

Purpose: To evaluate if a fully-automatic deep learning method for myocardial strain analysis based on magnetic resonance imaging (MRI) cine images can detect asymptomatic dysfunction in young adults with cardiac risk factors.

Methods: An automated workflow termed DeepStrain was implemented using two U-Net models for segmentation and motion tracking. DeepStrain was trained and tested using short-axis cine-MRI images from healthy subjects and patients with cardiac disease. Subsequently, subjects aged 18–45 years were prospectively recruited and classified among age- and gender-matched groups: risk factor group (RFG) 1 including overweight without hypertension or type 2 diabetes; RFG2 including hypertension without type 2 diabetes, regardless of overweight; RFG3 including type 2 diabetes, regardless of overweight or hypertension. Subjects underwent cardiac short-axis cine-MRI image acquisition. Differences in DeepStrain-based left ventricular global circumferential and radial strain and strain rate among groups were evaluated.

Results: The cohort consisted of 119 participants: 30 controls, 39 in RFG1, 30 in RFG2, and 20 in RFG3. Despite comparable (>0.05) left-ventricular mass, volumes, and ejection fraction, all groups (RFG1, RFG2, RFG3) showed signs of asymptomatic left ventricular diastolic and systolic dysfunction, evidenced by lower circumferential early-diastolic strain rate (<0.05, <0.001, <0.01), and lower septal circumferential end-systolic strain (<0.001, <0.05, <0.001) compared with controls. Multivariate linear regression showed that body surface area correlated negatively with all strain measures (<0.01), and mean arterial pressure correlated negatively with early-diastolic strain rate (<0.01).

Conclusion: DeepStrain fully-automatically provided evidence of asymptomatic left ventricular diastolic and systolic dysfunction in asymptomatic young adults with overweight, hypertension, and type 2 diabetes risk factors.

Keywords: deep learning, myocardial strain, young adults, risk factors, cardiac MRI, left ventricular dysfunction

INTRODUCTION

Worldwide shifts toward sedentary lifestyles and suboptimal diets have led to increased prevalence of global obesity and obesity-related comorbidities such as hypertension (1, 2). Both conditions alone are strong independent risk factors for type 2 diabetes mellitus (T2DM) (3), and increased cardiovascular morbidity and mortality (4). Obesity, hypertension, and T2DM interact synergistically to influence cardiac remodeling, resulting in a markedly heightened risk of cardiovascular disease and heart failure when these risk factors co-cluster (5). Further, links have been made between these risk factors and the increased incidence of heart failure in the young (6). The manifestations of heart failure could be preceded by asymptomatic left ventricular diastolic dysfunction (ALVDD), a silent disease whose development and progression are stimulated by comorbidities, specially obesity, hypertension, and T2DM (7). Strain and strain rate (SR) imaging have emerged as promising technologies for the assessment of myocardial deformation and earlier detection of asymptomatic dysfunction. Indeed, a recent echocardiography strain study reported ALVDD in young adults with obesity, as evidenced by reduced diastolic SR (8). Other studies in older adults have shown that asymptomatic left ventricular systolic dysfunction (ALVSD) can coexist with ALVDD even when ejection fraction is preserved, and this is associated with adverse long-term prognosis (9, 10). Thus, strain imaging tools could provide a sensitive and comprehensive evaluation of left ventricular (LV) function complementary to ejection fraction. Further, identification of both ALVDD and ALVSD at the onset of non-specific symptoms could represent the earliest opportunity for diagnosis and treatment (7, 9).

Echocardiographic examinations can be non-diagnostic or have inconclusive findings, especially in obese patients (11). In such cases, cardiac magnetic resonance imaging (MRI) plays an important complementary role and is often requested as it provides the most accurate and reproducible assessment of cardiac function, structure, and myocardial tissue properties (12). Cardiac MRI feature tracking methods requiring only clinically standard cine images could offer advanced strain readouts as well, providing additional information about the underlying biomechanical motion without modifications to the imaging protocol. In addition, cine-based strain analysis has been used to detect ALVDD and ALVSD in older adults (13–15). Nevertheless, feature tracking is a time-consuming process that requires considerable training and expertise to perform. Semi-automatic methods are available in commercial software. However, manual correction of tracked myocardial boundaries is still often required, which results in operator-related discrepancies in strain measures (16). Alternatively, we have shown that myocardial deformation can be automatically quantified from short-axis cine-MRI images using convolutional neural networks (17). Further, we have developed and validated a deep learning method for fully-automatic strain analysis (i.e., DeepStrain) based on cine-MRI images (18). DeepStrain showed significant differences among patients with known cardiac disease. However, characterization of asymptomatic dysfunction is potentially more difficult compared to older populations, since they are less likely to have obvious clinical or imaging signs of cardiac disease during examination (19). Indeed, few cardiac MRI strain studies have focused on younger populations with cardiac risk factors, yet identification and characterization of ALVDD and ALVSD in this population is of clinical and public health importance since young adults have a life-time risk of heart failure as high as 20%, and may benefit the most from earlier treatment (20).

Thus, we sought to evaluate if a fully-automatic deep learning method for myocardial strain analysis based on cardiac cine-MRI can detect asymptomatic dysfunction in asymptomatic young adults with overweight, hypertension, and T2DM cardiac risk factors.

MATERIALS AND METHODS

Study Population

This prospective cross-sectional single-center study was approved by the local medical ethical committee, and conducted in accordance with the Declaration of Helsinki. Subjects aged 18–45 years were voluntarily recruited with public advertisements and signed informed consent before participation. Exclusion criteria were history or knowledge of cardiac disease, cardiac risk factors other than overweight, hypertension or T2DM, exercising >3 h/week (21), and contraindications to cardiac MRI. Presence of cardiac risk factors was checked using a medical questionnaire, and with measurements of weight, blood pressure and hemoglobin A1c (HbA1c). Overweight was defined as body mass index (BMI) $\geq$ 25 kg/m^2; hypertension was defined as either actively under pharmacological treatment or three consecutive blood pressure measurements $\geq$ 140/90 mmHg; T2DM was defined as either actively under pharmacological treatment or a HbA1c level $\geq$ 48 mmol/mol measured prior to the MRI exam. All subjects were classified into one of the following age- and gender-matched groups: controls including all subjects without risk factors; risk factor group 1 (RFG1)

Abbreviations: ALVDD, asymptomatic left ventricular diastolic dysfunction; ALVSD, asymptomatic left ventricular systolic dysfunction; ANOVA, analysis of variance; BMI, body mass index; MRI, magnetic resonance imaging; HbA1c, hemoglobin A1c; LV, left ventricular; RFG, risk factor group; SR, strain rate; T2DM, type 2 diabetes mellitus.

including all overweight subjects with neither hypertension nor T2DM; RFG2 including all hypertensive subjects without T2DM, regardless of the presence or absence of additional overweight; RFG3 including all subjects with T2DM, regardless of the presence or absence of additional overweight or hypertension (**Figure 1**).

MRI Acquisition

All subjects underwent cardiac MRI using a 3 Tesla (T) scanner (MAGNETOM Prisma, Siemens Healthineers, Erlangen, Germany) with a 60-element phased-array body coil. Experienced operators used a retrospective electrocardiogram (ECG)-gated steady-state free precession sequence to acquire short-axis cines covering the heart from atria to ventricular apex during a series of breath-holds. Each cine contained 25 cardiac phases with 6 mm slice thickness, and 4 mm interslice gaps. Short-axis acquisition parameters were: repetition time 38.92–44.52 ms, echo time 1.15–1.31 ms, flip angle 43–46°, field of view 300–453 × 225–453 mm^2, acquisition matrix 256 × 192–256.

DeepStrain Analysis

The DeepStrain workflow uses a pair of cine-MRI stacks at two different time frames (**Figure 2**). A cardiac segmentation network (CarSON) generated tissue labels for a single time frame. This was done for all time frames, and labels were used to calculate LV morphology and function. Since Lagrangian strain evaluates myocardial deformation with the end-diastolic phase as the reference, end-diastolic labels were used to construct the LV anatomical model required for strain analysis. A cardiac motion estimation network (CarMEN) was used to generate motion vectors using a pair of time frames concatenated along the channel dimension, which were used to calculate the Lagrangian strain (17). The first time frame was kept always at end-diastole, while the second frame was evaluated for all contracted phases. Per-voxel strain measures were combined with the LV labels to extract both global and regional circumferential and radial strain values. We evaluated global end-systolic strain, global systolic and early-diastolic SR, and regional end-systolic strain for each ventricular wall according to the American Heart Association polar map (22), i.e., anterior (regions 1, 7, and 13), septal (regions 2, 3, 8, 9, and 14), inferior (regions 4, 10, and 15), and lateral (regions 5, 6, 11, 12, and 16). The apex region 17 was excluded from the regional analysis but included in the global evaluation. The combined DeepStrain workflow was trained using short-axis cine-MRI data that was obtained using 1.5 T (Siemens Area, Siemens Medical Solutions, Germany) and 3.0 T scanners (Siemens Trio Tim, Siemens Medical Solutions, Germany). The data was collected from 150 subjects evenly divided into five groups, including healthy subjects and patients with hypertrophic cardiomyopathy, abnormal right ventricle, myocardial infarction with reduced ejection fraction, and dilated cardiomyopathy (23). DeepStrain automatically processed the data from each subject (∼25 frames) in <2.2 min on a 32GB RAM CPU. The model and pre-trained parameters were made freely available online.

Statistical Analysis

Demographic variables were expressed as mean ± standard deviation, and strain-related variables as mean [95% confidence interval]. Variables were tested for normality with a Shapiro-Wilk test and for homogeneity of variance using Levene's test. One-way

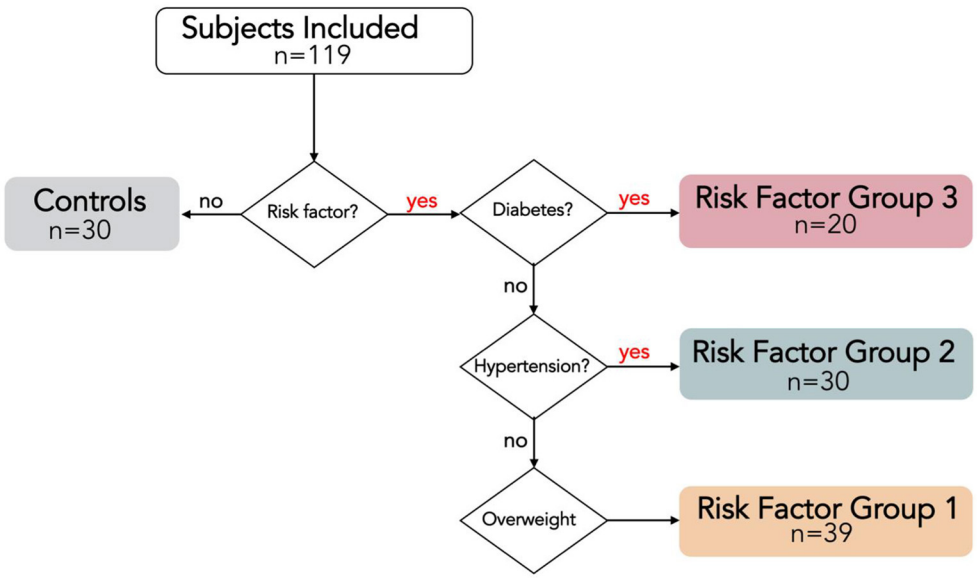

FIGURE 1 | Risk Factor Group (RFG) classifications visualized with a flow chart. RFG3 includes all type 2 diabetes mellitus (T2DM) subjects, regardless of the presence of hypertension or overweight. RFG2 includes all hypertensive subjects without T2DM, regardless of the presence of overweight. RGF1 includes all overweight subjects without hypertension and T2DM.

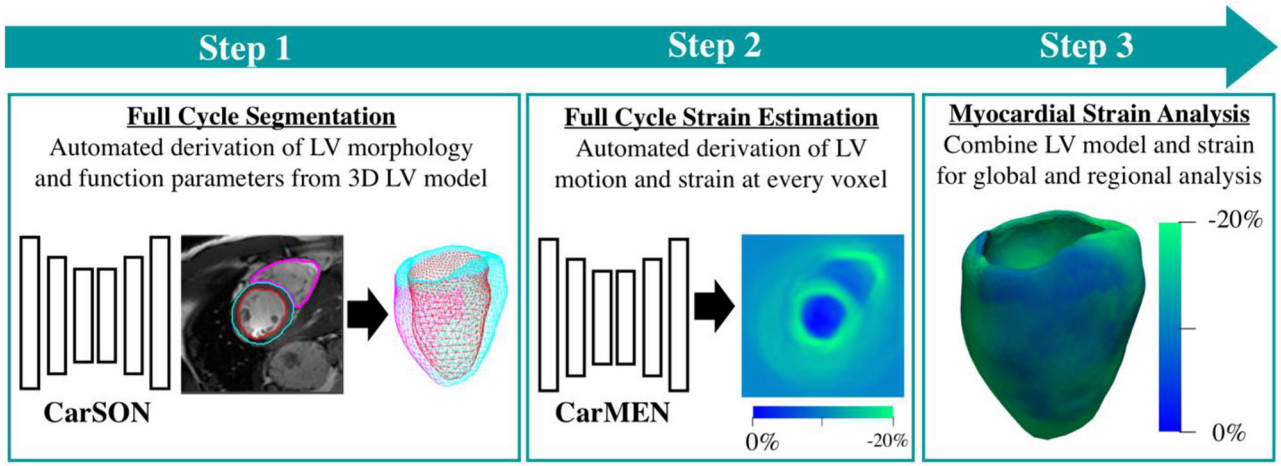

FIGURE 2 | DeepStrain workflow. The first step is segmentation of the left and right ventricular tissues. The second step is evaluation of left-ventricular motion. These two steps are performed using deep learning convolutional neural networks. These networks are combined into a single workflow for fast and automated strain analysis (third step).

analysis of variance (ANOVA) with *post-hoc* test by Bonferroni was used to examine differences among groups. Multivariate linear regression analysis was used to identify the independent association of the clinical variables body surface area, mean arterial pressure, and HbA1c on global strain measures. A p-value < 0.05 was considered statistically significant. Data were analyzed using Python (version 3.5, Python Software Foundation, www.python.org).

RESULTS

The study cohort consisted of 119 participants (35 ± 5 years, 50% male) including the control group with 30 subjects; RFG1 with 39 overweight subjects; RFG2 with 30 hypertensive subjects, including 13 (43%) with additional overweight; RFG3 with 20 T2DM subjects, including 11 (55%) with additional overweight, 1 (5%) with additional hypertension and 8 (40%) with both (**Table 1**). The ECG recorded during cardiac MRI showed regular cardiac rhythm in all subjects. Mean heart rate of RFG3 was significantly higher compared to controls ($p < 0.001$). Furthermore, there were no significant differences between groups in LV mass, volumes, and ejection fraction (**Supplementary Table 1**).

Global Strain and Strain Rate

Comparisons of global end-systolic strain showed that there were no significant differences in circumferential and radial strains between groups, except for a significantly decreased radial strain in RFG1 (19.4% [18.0, 20.8]; $p < 0.05$) relative to controls (21.9% [20.7, 23.1]) (**Table 2**; **Figure 3**).

Global circumferential early-diastolic SR was significantly reduced in RFG1 (0.70 s^{-1} [0.64, 0.75]; $p < 0.05$), RFG2 (0.62 s^{-1} [0.56, 0.67]; $p < 0.001$), and RFG3 (0.62 s^{-1} [0.55, 0.68]; $p < 0.01$) relative to controls (0.81 s^{-1} [0.74, 0.89]) (**Table 2**; **Figure 4A**). Radial early-diastolic SR was also significantly reduced in RFG3 (−1.34 s^{-1} [−1.48, −1.19]; $p < 0.05$) compared to controls (−1.62 s^{-1} [−1.74, −1.51]) (**Figure 4B**). There were no significant differences between controls and RFGs in global systolic SR.

Body surface area was negatively associated with circumferential and radial end-systolic strain ($p < 0.001$; $p < 0.001$), early-diastolic SR ($p < 0.001$; $p < 0.01$), and systolic SR ($p < 0.001$; $p < 0.01$). Mean arterial pressure was negatively associated with early-diastolic circumferential SR ($p < 0.01$), while HbA1c was not significantly associated with strain measures (**Table 3**).

Regional Strain

Regional comparisons of end-systolic strain by wall showed significantly lower circumferential strain in the septal wall of RFG1 (−13.7% [−14.2, −13.3]; $p < 0.001$), RFG2 (−14.1% [−14.7, −13.5]; $p < 0.05$), and RFG3 (−12.9% [−13.6, −12.1]; $p < 0.001$) compared to controls (−15.1% [−15.6, −14.7]) (**Table 2**; **Figure 5A**). Notably, circumferential strain was significantly increased in the lateral wall of RFG1 (−17.7% [−18.1, −17.3]; $p < 0.01$), RFG2 (−18.1% [−18.5, −17.7]; $p < 0.001$), and RFG3 (−17.9% [−18.3, −17.4]; $p < 0.01$) compared to controls (−16.8% [−17.2, −16.5]). Radial strain was decreased in the anterior ($p < 0.01$), inferior ($p < 0.001$), and lateral ($p < 0.001$) walls of RFG1 and RFG3 compared to controls (**Figure 5B**).

DISCUSSION

DeepStrain analysis of standard short-axis cine-MRI images identified evidence of ALVDD and ALVSD in asymptomatic young subjects with at least one cardiovascular risk factor including overweight, hypertension, and T2DM, but without presence or history of cardiovascular disease. Despite comparable LV mass, volumes, and ejection fraction to controls, all

TABLE 1 | Clinical characteristics of controls and risk factor groups (RFG).

	Controls ($n = 30$)	RFG1 ($n = 39$)	RFG2 ($n = 30$)	RFG3 ($n = 20$)	*P*-value
Age (years)	34 ± 3	33 ± 6	36 ± 5	37 ± 5	0.051
Gender, male	16 (53)	19 (49)	14 (47)	10 (50)	0.964
Height (cm)	178 ± 7	175 ± 8	178 ± 10	174 ± 10	0.206
Weight (kg)	70 ± 9	94 ± 13***	82 ± 16*	98 ± 19***	<0.001
Body mass index (kg/m^2)	22 ± 2	30 ± 3***	25 ± 5***	32 ± 5***	<0.001
Body surface area (m^2)	1.9 ± 0.2	2.1 ± 0.2***	2.0 ± 0.2	2.2 ± 0.3***	<0.001
Heart rate (bpm)	61 ± 9	67 ± 11	68 ± 8	77 ± 8***	<0.001
Systolic blood pressure (mmHg)	117 ± 8	122 ± 8	138 ± 18	136 ± 12***	<0.001
Diastolic blood pressure (mmHg)	78 ± 5	81 ± 6	92 ± 11	89 ± 8***	<0.001
Hemoglobin A1c (mmol/mol)	33 ± 3	34 ± 3	32 ± 3	61 ± 17***	<0.001
Hypertension medication, yes	–	–	24 (80)	4 (20)	–
Type 2 diabetes medication, yes	–	–	–	20 (100)	–

*Data is presented as either mean ± standard deviation or number (percentage). P-value shows the one-way ANOVA test value between groups. post-hoc test by Bonferroni: *p < 0.05; ***p < 0.001 vs. controls.*

TABLE 2 | Left-ventricular strain in controls and risk factor groups (RFG).

	Controls	RFG1	RFG2	RFG3	*P*-value
Circumferential					
Global end-systolic strain (%)	−14.4 [−14.9, −14.0]	−14.4 [−15.0, −13.7]	−14.3 [−14.8, −13.7]	−14.2 [−14.9, −13.5]	0.964
Global early-diastolic strain rate (s^{-1})	0.81 [0.74, 0.89]	0.70 [0.64, 0.75]*	0.62 [0.56, 0.67]***	0.62 [0.55, 0.68]**	<0.001
Global systolic strain rate (s^{-1})	−1.00 [−1.09, −0.92]	−0.98 [−1.06, −0.90]	−0.99 [−1.10, −0.89]	−0.97 [−1.06, −0.88]	0.979
Regional end-systolic strain (%)					
Anterior	−12.5 [−12.8, −12.1]	−13.0 [−13.4, −12.5]	−13.0 [−13.4, −12.5]	−13.2 [−13.9, −12.6]	0.158
Septal	−15.1 [−15.6, −14.7]	−13.7 [−14.2, −13.3]***	−14.1 [−14.7, −13.5]*	−12.9 [−13.6, −12.1]***	<0.001
Inferior	−12.8 [−13.1, −12.5]	−13.4 [−13.8, −13.1]	−13.5 [−13.9, −13.1]	−13.0 [−13.5, −12.5]	0.058
Lateral	−16.8 [−17.2, −16.5]	−17.7 [−18.1, −17.3]**	−18.1 [−18.5, −17.7]***	−17.9 [−18.3, −17.4]**	<0.001
Radial					
Global end-systolic strain (%)	21.9 [20.7, 23.1]	19.4 [18.0, 20.8]*	21.6 [20.4, 22.6]	19.7 [17.7, 21.7]	0.021
Global early-diastolic strain rate (s^{-1})	−1.62 [−1.74, −1.51]	−1.42 [−1.54, −1.30]	−1.41 [−1.52, −1.30]	−1.34 [−1.48, −1.19]*	0.021
Global systolic strain rate (s^{-1})	1.51 [1.39, 1.63]	1.32 [1.19, 1.47]	1.52 [1.39, 1.66]	1.34 [1.20, 1.47]	0.088
Regional end-systolic strain (%)					
Anterior	21.3 [20.5, 22.2]	19.0 [18.1, 20.0]**	20.7 [19.9, 21.5]	18.4 [16.9, 19.7]**	<0.001
Septal	19.9 [19.2, 20.6]	19.7 [18.9, 20.4]	21.3 [20.6, 22.0]	18.9 [17.9, 19.9]	<0.001
Inferior	23.8 [22.9, 24.8]	20.4 [19.5, 21.3]***	24.1 [23.1, 25.1]	18.4 [16.5, 20.3]***	<0.001
Lateral	24.4 [23.7, 25.0]	20.9 [20.1, 21.7]***	23.9 [23.3, 24.5]	21.2 [19.8, 22.6]***	<0.001

*Data is presented as mean [95% confidence interval]. P-value shows the one-way ANOVA test value between groups. post-hoc test by Bonferroni: *p < 0.05; **p < 0.01; ***p < 0.001 vs. controls.*

RFGs showed impairment of LV circumferential early-diastolic SR as well as regional circumferential end-systolic strain. On multivariate linear regression analysis, body surface area correlated negatively with all strain measures, and mean arterial pressure was a negative correlate of circumferential early-diastolic SR. Our results are consistent with similar studies in older adults with similar risk factors. However, most studies have predominantly focused on one or two risk factors groups, which makes comparisons across the three groups difficult due to differences in software and operator. Our study is the first to report reference strain values across control, overweight, hypertension, and T2DM populations using a single user-independent, fully-automatic strain analysis software.

Asymptomatic Diastolic Dysfunction

The link from obesity, hypertension, and diabetes to diastolic dysfunction across multiple age groups has been well established in previous studies (4). For instance, a study in asymptomatic older adults recently reported a progressive decline in circumferential early-diastolic SR from controls to newly diagnosed T2DM to longstanding T2DM, and reduced radial early-diastolic SR in longstanding T2DM. This suggests

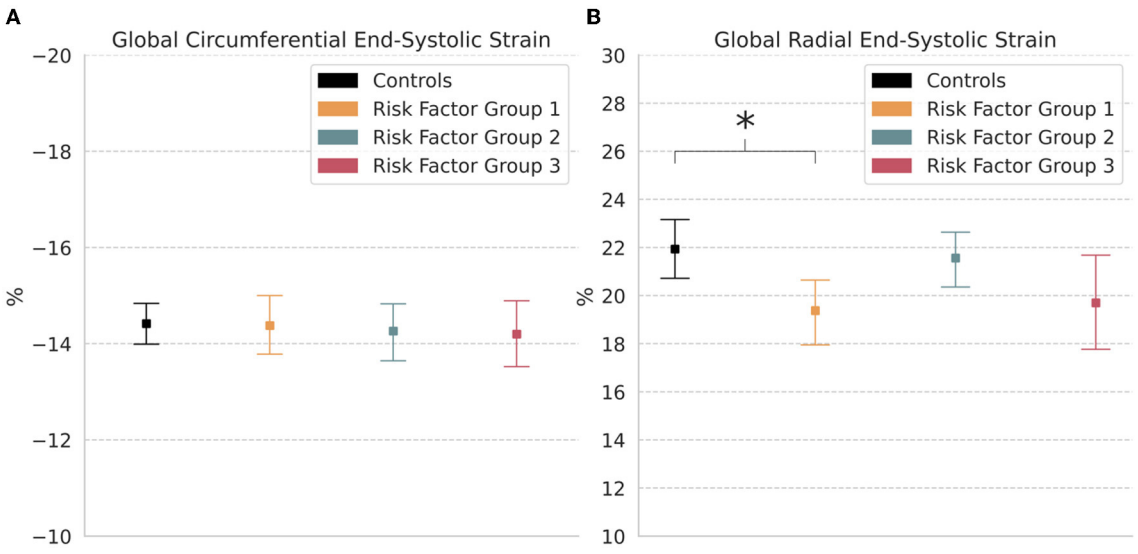

FIGURE 3 | Global strain. Measures of **(A)** Circumferential and **(B)** Radial end-systolic strain in controls and risk factor groups. Strain results are visualized as mean with 95% confidence interval. *post-hoc* test by Bonferroni: $^{*}p < 0.05$.

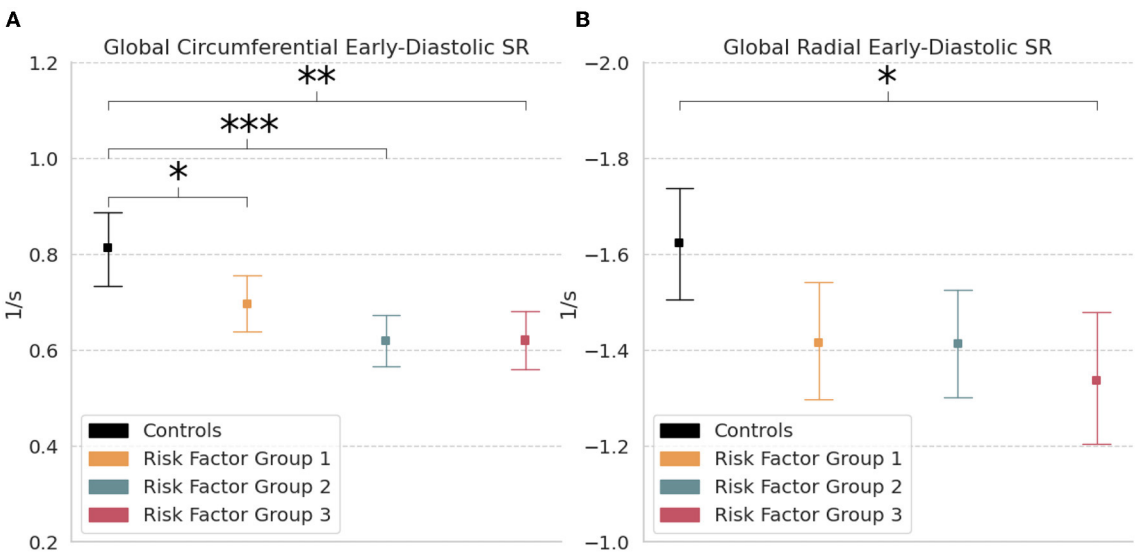

FIGURE 4 | Global strain rate. Measures of **(A)** Circumferential and **(B)** Radial early-diastolic strain rate (SR) in controls and risk factor groups. Strain results are visualized as mean with 95% confidence interval. *post-hoc* test by Bonferroni: $^{*}p < 0.05$; $^{**}p < 0.01$; $^{***}p < 0.001$.

asymptomatic diastolic dysfunction may occur early in the pathogenesis of T2DM, and accumulate gradually over time (13). However, data regarding diastolic dysfunction in younger (i.e., mean age < 45 years old) asymptomatic populations is limited. Echocardiography studies have reported reduced circumferential early-diastolic SR in obesity (8), and similar reductions have been documented in obese subjects using tagging-MRI (24). In this cine-MRI study, we showed that a significant reduction already exists in overweight subjects (i.e., RFG1), even when a lower BMI threshold of 25 kg/m^2 was used. Further, we found that both circumferential and radial early-diastolic SR were inversely associated with body surface area, which is an important finding because body surface area is a prognostic indicator of adverse outcomes in heart failure. In hypertensive subjects without diabetes, reduction in circumferential early-diastolic SR values proportional to standard echocardiography grading of diastolic function has also been reported (25). Similarly, our study showed these values were reduced in RFG2 relative to controls, and were inversely associated with mean arterial pressure. Taking both overweight and hypertension into consideration, these results are consistent with the observed benefits of weight reduction, namely reduced mean arterial pressure and improved diastolic

TABLE 3 | Independent correlates of global strain measures.

	End-systolic strain		Early-diastolic strain rate		Systolic strain rate	
	β	*P*-value	β	*P*-value	β	*P*-value
Circumferential						
Body surface area	−0.691	<0.001	−0.067	<0.001	−0.090	<0.001
Mean arterial pressure	−0.106	0.471	−0.046	0.007	0.020	0.383
Hemoglobin A1c	0.168	0.261	0.002	0.901	0.024	0.303
Radial						
Body surface area	−1.404	<0.001	−0.088	0.009	−0.112	0.003
Mean arterial pressure	0.407	0.264	−0.023	0.481	0.046	0.208
Hemoglobin A1c	−0.016	0.967	−0.013	0.691	−0.018	0.629

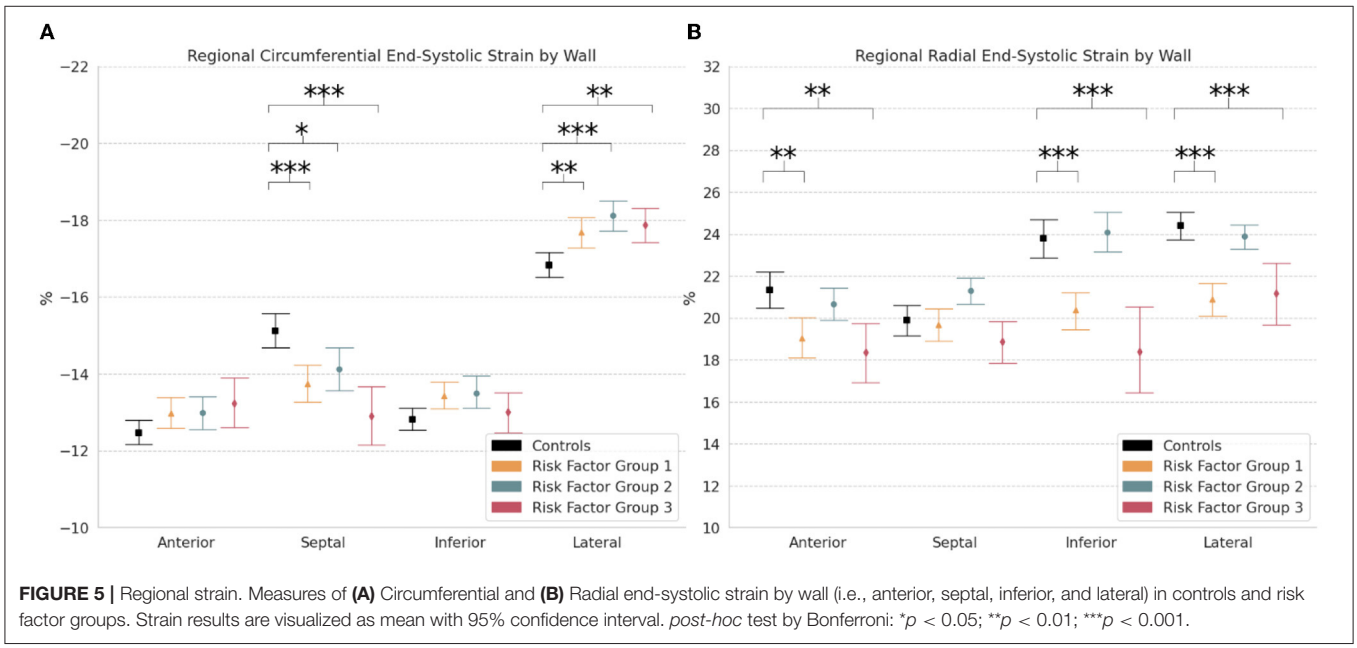

FIGURE 5 | Regional strain. Measures of **(A)** Circumferential and **(B)** Radial end-systolic strain by wall (i.e., anterior, septal, inferior, and lateral) in controls and risk factor groups. Strain results are visualized as mean with 95% confidence interval. *post-hoc* test by Bonferroni: $^{*}p < 0.05$; $^{**}p < 0.01$; $^{***}p < 0.001$.

parameters. In addition, since both obesity and hypertension are strong risk factors for T2DM, it is not surprising that circumferential and radial early-diastolic SR were significantly reduced in RFG3 compared to controls, which is consistent with previous studies in T2DM (8, 24). These results are evidence of ALVDD in young adults with overweight, hypertension, and T2DM, characterized by a progressive deterioration in early-diastolic SR from controls to RFG1 to RFG2 to RFG3. Thus, DeepStrain could become a useful tool in the evaluation of suspected diastolic dysfunction.

Asymptomatic Systolic Dysfunction

Multiple studies in older adults have reported reduced systolic strain with preserved ejection fraction in obesity, hypertension, and T2DM (10, 14, 15, 24, 26). For example, cardiac MRI studies measuring global circumferential end-systolic strain have reported a clear reduction in obesity (14), and progressive decline from controls to hypertension to hypertension with T2DM (15). Evidence of reduced systolic strain in younger asymptomatic populations is less clear. Studies in obese subjects have shown no significant differences in measures of global circumferential end-systolic strain relative to lean controls (8, 24, 27). Likewise, we found global circumferential end-systolic strain was preserved in overweight subjects relative to lean controls, but was negatively associated with increased body surface area. Our study showed radial and circumferential global strain values were preserved in RFG2 subjects, but were associated with increased mean arterial pressure. Conflicting results have been reported in T2DM. Haley et al. showed global circumferential end-systolic strain values were reduced in T2DM subjects relative to non-diabetic lean controls (8), whereas a more recent but smaller study by Khan et al. reported no significant differences in values between controls and T2DM subjects (24). We also found comparable values between controls and RFG3 subjects, and no association between strain and HbA1c levels, the latter consistent with the finding that HbA1c is not always associated with LV dysfunction. These discrepancies may be caused by differences between echocardiography, tagging- and cine-MRI imaging modalities, which could be exacerbated when differences in strain are less pronounced. With some

exceptions where the mean age was 43 years old (26), studies in younger populations have not reported radial strain, and to the best of our knowledge none of them has presented regional evaluations.

The typical progression from stage A heart failure (i.e., inclusion into a RFG) to symptomatic stage C heart failure begins with ALVDD, followed by ALVSD, overt systolic dysfunction, and finally by symptomatic heart failure (7, 9). Although the presence of ALVDD in all RFGs was clearly indicated by a reduction in global early-diastolic SR, the use of global systolic strain measures to establish the presence or absence of ALVSD was less conclusive in both our study and previous studies. Indeed, our finding that global circumferential strain is preserved may be explained by the small sample sizes and inability to achieve statistical significance in *post-hoc* analyses, but could also imply that global measures are less sensitive to subtle systolic dysfunction than regional measures, as previously shown for mild hypertension (28). In fact, accurate evaluation of regional strain is challenging but potentially very important as it could provide additional insights regarding early disease processes. For instance, asymmetric septal hypertrophy due to increased afterload has been considered a consequence of increased wall stress on the septum compared to the free lateral wall. This asymmetric response to stress results in reduced strain values in the septal wall and increased values in the lateral as reported in human and animal studies, which could be explained by a larger compensatory preload recruitment in the free wall compared to the septum (28, 29). Similar asymmetric strain alterations have been reported in patients with non-ischemic cardiomyopathy, and in these patients partial left ventriculectomy has been shown to normalize wall stress and improve septal strain (30). Further, septal-only fibrosis in non-ischemic cardiomyopathy has been documented to result in worse global circumferential strain relative to patients with free-wall only fibrosis, highlighting the need to identify both location and extent of deformation abnormalities (31). In line with these studies, we found significant regional alterations in circumferential end-systolic strain in asymptomatic young adults with overweight, hypertension, and T2DM, characterized by reduced septal strain and increased lateral strain. Thus, our regional analysis with DeepStrain provides evidence of the existence of heterogeneous strain alterations early in the disease process, although further studies are needed to assess regional strain alterations in non-ischemic patient populations.

DeepStrain-Based Analysis

To our best knowledge, the current study is the first to apply an end-to-end deep learning-based workflow for myocardial strain analysis detection of ALVDD and ALVSD in risk populations, an approach that offers several advantages over traditional techniques. Firstly, there are no explicit assumptions about myocardial tissue properties imbedded into the model (e.g., incompressible myocardium), which is common in conventional methods (32), while this might not always accurately reflect the underlying biomechanical motion (33). Secondly, analysis per subject was done two orders of magnitude faster than conventional methods (32). Thirdly, the open-source nature of the software enables the scientific community to easily apply our approach to other populations. Lastly, the purchase of commercially available software licenses whose accuracy depends on the segmentation procedure and vendor is not always an option for research groups (16), whereas open-source software provides key opportunities for cost reduction, clinical engagement in software development, and accelerated innovation.

The results presented in this study were based on cine-MRI images acquired using a 3.0 T MRI scanner with a custom 60-element coil. However, DeepStrain could potentially capture similar abnormalities using other clinical scanners. For instance, DeepStrain was trained using images acquired using both 1.5 T and 3.0 T MRI scanners (23), therefore our method could be applied to data acquired with both magnetic field strengths. Further, we previously demonstrated that our method can be applied to images collected with a different vendor using tagging-MRI as reference (32). In addition, we have reported high intra-scanner repeatability in strain measures in data acquired with a 6-channel body surface coil (18), therefore a custom 60-element coil might not be necessary to capture subclinical abnormalities.

The DeepStrain model used in this study was based on five populations covering a wide spectrum of cardiac anatomy and function, which reduces the bias toward a single heart condition. Specifically, the training cohort included groups with dilated and hypertrophic cardiomyopathy, myocardial infarction, and abnormal right ventricle. Obesity and obesity-related comorbidities often result in structural abnormalities such as LV hypertrophy, potentially leading to obesity cardiomyopathy, hypertensive heart disease or diabetic cardiomyopathy. Thus, the inclusion of the cardiomyopathy cohorts during training was particularly important. Nevertheless, in this study, the RFGs showed normal anatomy compared to the control group based on measures of volume and mass. Therefore, further validation in patients with more advanced cardiac diseases is necessary and might require additional training. In addition, validation in larger cohorts and comparisons to commercial software are necessary to further demonstrate the clinical utility of DeepStrain.

Study Limitations

DeepStrain currently does not support long-axis images, therefore longitudinal strain was not reported. From a technical perspective, a joint model that uses both short and long axis images would be needed to enforce consistency in the evaluated deformation. For instance, such model could be based on recently published cine-MRI data with both long and short axis views (34). The small participant numbers in the T2DM subgroup may hinder the reliability of the measured strain, especially for regional strain analysis. Since this was a cross-sectional study, we could not monitor the progression of subclinical dysfunction or link these findings to clinical outcomes. Further, two of the groups included in the study cohort had a mixture of risk factors, therefore the current study cannot separate the independent impact of each of the three risk factors.

CONCLUSIONS

In young adults with overweight, hypertension, and T2DM risk factors, early-diastolic SR suggested ALVDD, and regional alterations in end-systolic strain indicated ALVSD despite

preserved ejection fraction. These results demonstrate that the application of DeepStrain in routine cardiac MRI studies would fully-automatically offer useful information about the underlying biomechanical motion using standard short-axis cine-MRI data.

DATA AVAILABILITY STATEMENT

The raw data supporting the conclusions of this article will be made available by the authors, without undue reservation.

ETHICS STATEMENT

The studies involving human participants were reviewed and approved by Medical Ethical Committee of the University Medical Center Groningen (No. 2016/476). The participants provided their written informed consent to participate in this study.

AUTHOR CONTRIBUTIONS

MM contributed with implementation and analysis of strain methodology. GS, MB, and NP contributed with data acquisition. MM and GS analysed and interpreted that data and drafted the manuscript. All other authors revised the drafted manuscript, contributed critical intellectual content, and approved the final version of the manuscript.

FUNDING

This work was supported by the Dutch Heart Association (2016T042) and in part by the U.S. National Cancer Institute under Grant 1R01CA218187-01A1.

ACKNOWLEDGMENTS

We acknowledge the support of NVIDIA Corporation with the donation of the Titan X Pascal GPU used for this research.

SUPPLEMENTARY MATERIAL

The Supplementary Material for this article can be found online at: https://www.frontiersin.org/articles/10.3389/fcvm.2022.831080/full#supplementary-material

REFERENCES

1. Afshin A, Sur PJ, Fay KA, Cornaby L, Ferrara G, Salama JS, et al. Health effects of dietary risks in 195 countries, 1990–2017: a systematic analysis for the Global Burden of Disease Study 2017. *Lancet.* (2019) 393:1958–72. doi: 10.1016/S0140-6736(19)30041-8
2. Guthold R, Stevens GA, Riley LM, Bull FC. Worldwide trends in insufficient physical activity from 2001 to 2016: a pooled analysis of 358 population-based surveys with 1·9 million participants. *Lancet Glob Heal.* (2018) 6:e1077–86. doi: 10.1016/S2214-109X(18)30357-7
3. Petrie JR, Guzik TJ, Touyz RM. Diabetes, hypertension, and cardiovascular disease: clinical insights and vascular mechanisms. *Can J Cardiol.* (2018) 34:575–84. doi: 10.1016/j.cjca.2017.12.005
4. Mazloomzadeh S, Zarandi FK, Shoghli A, Dinmohammadi H. Metabolic syndrome, its components and mortality: a population-based study. *Med J Islam Repub Iran.* (2019) 33:11. doi: 10.47176/mjiri.33.11
5. von Jeinsen B, Vasan RS, McManus DD, Mitchell GF, Cheng S, Xanthakis V. Joint influences of obesity, diabetes, and hypertension on indices of ventricular remodeling: Findings from the community-based Framingham Heart Study. *PLoS One.* (2020) 15:e0243199. doi: 10.1371/journal.pone.0243199
6. Christiansen MN, Køber L, Weeke P, Vasan RS, Jeppesen JL, Smith JG, et al. Age-specific trends in incidence, mortality, and comorbidities of heart failure in Denmark, 1995 to 2012. *Circulation.* (2017) 135:1214–23. doi: 10.1161/CIRCULATIONAHA.116.025941
7. Kosmala W, Marwick TH. Asymptomatic left ventricular diastolic dysfunction: predicting progression to symptomatic heart failure. *JACC Cardiovasc Imaging.* (2020) 13:215–27. doi: 10.1016/j.jcmg.2018.10.039
8. Haley JE, Zhiqian G, Philip KR, Nicolas ML, Thomas KR, Lawrence DM, et al. Reduction in myocardial strain is evident in adolescents and young adults with obesity and type 2 diabetes. *Pediatr Diabet.* (2020) 21:243–50. doi: 10.1111/pedi.12961
9. Sara JD, Toya T, Taher R, Lerman A, Gersh B, Anavekar NS. asymptomatic left ventricle systolic dysfunction. *Eur Cardiol Rev.* (2020) 15:e13. doi: 10.15420/ecr.2019.14
10. Ng ACT, Bertini M, Ewe SH, van der Velde ET, Leung DY, Delgado V, et al. Defining subclinical myocardial dysfunction and implications for patients with diabetes mellitus and preserved ejection fraction. *Am J Cardiol.* (2019) 124:892–898. doi: 10.1016/j.amjcard.2019.06.011
11. Uppot RN. Technical challenges of imaging & image-guided interventions in obese patients. *Br J Radiol.* (2018) 91:20170931. doi: 10.1259/bjr.20170931
12. Shah RV, Abbasi SA, Kwong RY. Role of cardiac MRI in diabetes. *Curr Cardiol Rep.* (2014) 16:449. doi: 10.1007/s11886-013-0449-0
13. Liu X, Yang ZG, Gao Y, Xie LJ, Jiang L, Hu BY, et al. Left ventricular subclinical myocardial dysfunction in uncomplicated type 2 diabetes mellitus is associated with impaired myocardial perfusion: a contrast-enhanced cardiovascular magnetic resonance study. *Cardiovasc Diabetol.* (2018) 17:139. doi: 10.1186/s12933-018-0782-0
14. Homsi R, Yuecel S, Schlesinger-Irsch U, Meier-Schroers M, Kuetting D, Luetkens J, et al. Epicardial fat, left ventricular strain, and T1-relaxation times in obese individuals with a normal ejection fraction. *Acta radiol.* (2019) 60:1251–7. doi: 10.1177/0284185119826549
15. Kropidlowski C, Meier-Schroers M, Kuetting D, Sprinkart A, Schild H, Thomas D, et al. CMR based measurement of aortic stiffness, epicardial fat, left ventricular myocardial strain and fibrosis in hypertensive patients. *IJC Hear Vasc.* (2020) 27:100477. doi: 10.1016/j.ijcha.2020.100477
16. Lim C, Blaszczyk E, Riazy L, Wiesemann S, Schüler J, von Knobelsdorff-Brenkenhoff F, et al. Quantification of myocardial strain assessed by cardiovascular magnetic resonance feature tracking in healthy subjects—influence of segmentation and analysis software. *Eur Radiol.* (2021) 31:3962–72. doi: 10.1007/s00330-020-07539-5
17. Morales MA, Izquierdo-Garcia D, Aganj I, Kalpathy-Cramer J, Rosen BR, Catana C. Implementation and validation of a three-dimensional cardiac motion estimation network. *Radiol Artif Intell.* (2019) 1:e180080. doi: 10.1148/ryai.2019180080
18. Morales MA, van den Boomen M, Nguyen C, Kalpathy-Cramer J, Rosen BR, Stultz CM, et al. DeepStrain: a deep learning workflow for the automated characterization of cardiac mechanics. *Front Cardiovasc Med.* (2021) 8:730316. doi: 10.3389/fcvm.2021.730316
19. Wong CM, Hawkins NM, Jhund PS, Macdonald MR, Solomon SD, Granger CB, et al. Clinical characteristics and outcomes of young and very young adults with heart failure: the CHARM programme (candesartan in heart failure assessment of reduction in mortality and morbidity). *J Am Coll Cardiol.* (2013) 62:1845–54. doi: 10.1016/j.jacc.2013.05.072

20. Lloyd-Jones DM, Larson MG, Leip EP, Beiser A, D'Agostino RB, Kannel WB, et al. Lifetime risk for developing congestive heart failure: the framingham heart study. *Circulation.* (2002) 106:3068–72. doi: 10.1161/01.CIR.0000039105.49749.6F
21. Prakken NH, Velthuis BK, Teske AJ, Mosterd A, Mali WP, Cramer MJ. Cardiac MRI reference values for athletes and nonathletes corrected for body surface area, training hours/week and sex. *Eur J Cardiovasc Prev Rehabil.* (2010) 17:198–203. doi: 10.1097/HJR.0b013e3283347fdb
22. Cerqueira MD, Weissman NJ, Dilsizian V, Jacobs AK, Kaul S, Laskey WK, et al. standardized myocardial segmentation and nomenclature for tomographic imaging of the heart: a statement for healthcare professionals from the cardiac imaging committee of the council on clinical cardiology of the American heart association. *Circulation.* (2002) 105:539–42. doi: 10.1161/hc0402.102975
23. Bernard O, Lalande A, Zotti C, Cervenansky F, Yang X, Heng PA, et al. Deep learning techniques for automatic mri cardiac multi-structures segmentation and diagnosis: is the problem solved? *IEEE Trans Med Imaging.* (2018) 37:2514–25. doi: 10.1109/TMI.2018.2837502
24. Khan JN, Wilmot EG, Leggate M, Singh A, Yates T, Nimmo M, et al. Subclinical diastolic dysfunction in young adults with Type 2 diabetes mellitus: a multiparametric contrast-enhanced cardiovascular magnetic resonance pilot study assessing potential mechanisms. *Eur Heart J Cardiovasc Imaging.* (2014) 15:1263–9. doi: 10.1093/ehjci/jeu121
25. Sharif H, Ting S, Forsythe L, McGregor G, Banerjee P, O'Leary D, et al. Layer-specific systolic and diastolic strain in hypertensive patients with and without mild diastolic dysfunction. *Echo Res Pract.* (2018) 5:41–9. doi: 10.1530/ERP-17-0072
26. Liu H, Wang J, Pan Y, Ge Y, Guo Z, Zhao S. Early and quantitative assessment of myocardial deformation in essential hypertension patients by using cardiovascular magnetic resonance feature tracking. *Sci Rep.* (2020) 10:3582. doi: 10.1038/s41598-020-60537-x
27. Xu E, Kachenoura N, Della Valle V, Dubern B, Karsenty A, Tounian P, et al. Multichamber dysfunction in children and adolescents with severe obesity: a cardiac magnetic resonance imaging myocardial strain study. *J Magn Reson Imaging.* (2021) 54:1393–1403. doi: 10.1002/jmri.27796
28. Baltabaeva A, Marciniak M, Bijnens B, Moggridge J, He FJ, Antonios TF, et al. Regional left ventricular deformation and geometry analysis provides insights in myocardial remodelling in mild to moderate hypertension. *Eur J Echocardiogr.* (2008) 9:501–8. doi: 10.1016/j.euje.2007.08.004
29. Murai D, Yamada S, Hayashi T, Okada K, Nishino H, Nakabachi M, et al. Relationships of left ventricular strain and strain rate to wall stress and their afterload dependency. *Heart Vessels.* (2017) 32:574–83. doi: 10.1007/s00380-016-0900-4
30. Young AA, Dokos S, Powell KA, Sturm B, McCulloch AD, Starling RC, et al. Regional heterogeneity of function in nonischemic dilated cardiomyopathy. *Cardiovasc Res.* (2001) 49:308–18. doi: 10.1016/S0008-6363(00)00248-0
31. Csecs I, Pashakhanloo F, Paskavitz A, Jang J, Al-Otaibi T, Neisius U, et al. Association between left ventricular mechanical deformation and myocardial fibrosis in nonischemic cardiomyopathy. *J Am Heart Assoc.* (2020) 9:e016797. doi: 10.1161/JAHA.120.016797
32. Tobon-Gomez C, De Craene M, McLeod K, Tautz L, Shi W, Hennemuth A, et al. Benchmarking framework for myocardial tracking and deformation algorithms: an open access database. *Med Image Anal.* (2013) 17:632–648. doi: 10.1016/j.media.2013.03.008
33. Kumar V, Ryu AJ, Manduca A, Rao C, Gibbons RJ, Gersh BJ, et al. Cardiac MRI demonstrates compressibility in healthy myocardium but not in myocardium with reduced ejection fraction. *Int J Cardiol.* (2021) 322:278–83. doi: 10.1016/j.ijcard.2020.08.087
34. Campello VM, Gkontra P, Izquierdo C, Martin-Isla C, Sojoudi A, Full PM, et al. Multi-Centre, multi-vendor and multi-disease cardiac segmentation: the m&ms challenge. *IEEE Trans Med Imaging.* (2021) 40:3543–54. doi: 10.1109/TMI.2021.3090082

Conflict of Interest: The authors declare that the research was conducted in the absence of any commercial or financial relationships that could be construed as a potential conflict of interest.

frontiers | Frontiers in Cardiovascular Medicine

ORIGINAL RESEARCH
published: 30 June 2022
doi: 10.3389/fcvm.2022.909680

Improved Functional Assessment of Ischemic Severity Using 3D Printed Models

Kranthi K. Kolli[1], Sun-Joo Jang[1], Abdul Zahid[1], Alexandre Caprio[1], Seyedhamidreza Alaie[1], Amir Ali Amiri Moghadam[1], Patricia Xu[2], The CREDENCE Trial Investigators[†], Robert Shepherd[2], Bobak Mosadegh[1] and Simon Dunham[1]*

[1] Department of Radiology, Dalio Institute of Cardiovascular Imaging, Weill Cornell Medical College, New York, NY, United States, [2] Department of Mechanical and Aerospace Engineering, Cornell University, Ithaca, NY, United States

Objective: To develop a novel *in vitro* method for evaluating coronary artery ischemia using a combination of non-invasive coronary CT angiograms (CCTA) and 3D printing (FFR_{3D}).

Methods: Twenty eight patients with varying degrees of coronary artery disease who underwent non-invasive CCTA scans and invasive fractional flow reserve (FFR) of their epicardial coronary arteries were included in this study. Coronary arteries were segmented and reconstructed from CCTA scans using Mimics (Materialize). The segmented models were then 3D printed using a Carbon M1 3D printer with urethane methacrylate (UMA) family of rigid resins. Physiological coronary circulation was modeled *in vitro* as flow-dependent stenosis resistance in series with variable downstream resistance. A range of physiological flow rates (Q) were applied using a peristaltic steady flow pump and titrated with a flow sensor. The pressure drop (ΔP) and the pressure ratio (P_d/P_a) were assessed for patient-specific aortic pressure (P_a) and differing flow rates (Q) to evaluate FFR_{3D} using the 3D printed model.

Results: There was a good positive correlation ($r = 0.87$, $p < 0.0001$) between FFR_{3D} and invasive FFR. Bland-Altman analysis revealed a good concordance between the FFR_{3D} and invasive FFR values with a mean bias of 0.02 (limits of agreement: −0.14 to 0.18; $p = 0.2$).

Conclusions: 3D printed patient-specific models can be used in a non-invasive *in vitro* environment to quantify coronary artery ischemia with good correlation and concordance to that of invasive FFR.

Keywords: CCTA, radiology, 3D printing, *in vitro*, blood analog fluid, fractional flow reserve, catheterization

OPEN ACCESS

Edited by:
Caglar Ozturk, Massachusetts Institute of Technology, United States

Reviewed by:
Martin L. Tomov, Emory University, United States
Dong-Guk Paeng, Jeju National University, South Korea

****Correspondence:***
Kranthi K. Kolli
Kranthi.kolli@gmail.com

[†]A full list of investigators and their affiliations are available in the supplementary material

Specialty section:
This article was submitted to General Cardiovascular Medicine, a section of the journal Frontiers in Cardiovascular Medicine

Received: *31 March 2022*
Accepted: *25 May 2022*
Published: *30 June 2022*

Citation:
Kolli KK, Jang S-J, Zahid A, Caprio A, Alaie S, Moghadam AAA, Xu P, Shepherd R, Mosadegh B and Dunham S (2022) Improved Functional Assessment of Ischemic Severity Using 3D Printed Models. Front. Cardiovasc. Med. 9:909680. doi: 10.3389/fcvm.2022.909680

INTRODUCTION

Obstructive coronary artery disease (CAD) is one of the most common type of cardiovascular disease (1). The evaluation and diagnosis of CAD remains a challenging task. Anatomical and functional assessment through invasive coronary angiography (ICA) is the current reference standard to indicate the presence, location, and extent of a stenosis/obstruction. Stenoses that are

functionally significant (flow limiting/ischemia causing) need to be treated invasively to reduce CAD morbidity (2–5). On the contrary, invasive treatment of functionally non-significant stenoses may lead to harmful outcomes (3, 6). Thus, the independent evaluation of this disease either by non-invasive or invasive approaches is of utmost importance for the selection of appropriate and optimized therapeutic methods such as bypass surgery, stents or drug therapy while treating a patient.

Non-invasive imaging methods like coronary CT angiography (CCTA) not only help identify patients with suspected CAD, but also allow for visualization/quantification of the coronary artery stenosis (7). Although CCTA has high sensitivity in determining the functional significance of the stenosis and ruling out CAD, its corresponding specificity is lower (8–11). Hence, patients with obstructive CAD typically undergo an additional procedure like ICA to further determine the functional significance of the stenosis by invasively measuring the fractional flow reserve (FFR; ratio of average pressures distal [P_d] and proximal [P_a] to a stenosis at maximal hyperemia). FFR is the current clinical gold standard for both establishing the functional significance of a stenosis and also to guide its treatment. In order to reduce the number of unnecessary invasive procedures, non-invasive determination of the functional significance of stenoses based on CCTA images is being extensively investigated (12–14).

Recently, 3D printing, an additive manufacturing technique that enables direct fabrication of physical models based on digital objects of arbitrary geometry, has become more common; particularly for medical device and healthcare applications (15, 16). The purpose of this research is to develop a novel *in vitro* method to evaluate coronary artery ischemia using 3D printed coronary arteries whose 3D geometric features are derived from non-invasive coronary CT angiograms (CCTA). An *in vitro* flow circulation system representative of invasive measurements in a cardiac catheterization laboratory was developed to experimentally evaluate the hemodynamic parameters of pressure and flow across patient-specific 3D printed models. Our overall goal is to develop a novel non-invasive system for determining patient-specific thresholds of ischemia and to validate this system in a unique clinical trial of individuals with comprehensive physiologic measurements. In this pilot study, the concordance between the FFR values measured *in vitro* using 3D printed models (FFR_{3D}) and the gold standard (invasive FFR) is also examined.

METHODS

This study was performed as a prespecified secondary aim of the CREDENCE study, to investigate the mechanism by which plaque characteristics may impact fractional flow reserve *via* their material properties (17). An *in vitro* flow circulation system representative of invasive measurements in a cardiac catheterization laboratory was developed to experimentally evaluate the hemodynamic parameters of pressure and flow across a pilot cohort of twenty eight patient-specific 3D printed coronary artery models. Experiments were based on patient's image data and hemodynamic parameters, which were De-identified prior to study. The details of the study population and experimental setup are discussed below.

Study Patients

A random subset of twenty eight patients from the multicenter CREDENCE trial (Clinical Trials Gov., ID: NCT02173275) were included in this pilot study. The CREDENCE trial is a prospective, multicenter diagnostic derivation-validation controlled clinical trial that recruited 612 stable patients, without a prior diagnosis of CAD from 2014–2017. Patients were recruited across 17 centers in the Unites States, Netherlands, Japan, China, Latvia, Italy, and South Korea. The rationale and design of the CREDENCE trial has been described in a previous study (17). Briefly, enrolled patients underwent both CCTA and Myocardial perfusion imaging tests (MPI), followed by invasive coronary angiography (ICA) with FFR measurements in three epicardial coronary arteries. Eligibility criteria included referral to non-emergent ICA according to the American College of Cardiology/American Heart Association clinical practice guidelines for stable ischemic heart disease (18, 19). All the non-invasive and invasive imaging tests were interpreted blindly by core laboratories. The institutional review board of each enrolling site approved the study protocol and all patients provided written informed consent.

Image Acquisition

CCTA imaging was performed using a single or dual source CT scanner with at least 64-detector rows and a detector row width of $\leq$0.75 mm (17). Scans were performed retrospectively (65%), prospectively (27%), or with single-beat (8%) acquisitions. Sites were instructed to perform CCTA in accordance with quality standards set forth by the Society of Cardiovascular Computed Tomography (SCCT) guidelines (20). The CCTA images were exported into a DICOM (Digital Imaging and Communications in Medicine) format. Patient-specific 3D coronary artery models were then segmented from this CT volume data, in DICOM format, using Mimics image processing software (Mimics 18.0, Materialize, Leuven, Belgium).

Image Segmentation and 3D Printing of Coronary Vessel Models

In total, twenty eight patient-specific 3D coronary artery models [five right coronary artery (RCA), five left circumflex coronary artery (LCX) and 18 left anterior descending artery (LAD)] have been segmented from the CCTA images of 28 patients. Segmentation was performed by defining a range of thresholding value to obtain the segmentation mask of the region of interest (blood volumes for the aorta and coronary vessels) in Mimics (Mimics 18.0, Materialize, Leuven, Belgium). The thresholding value for the region of interest in general different for different patients but is within the range of soft tissue. After setting an optimal thresholding value, a region growing function was used to generate the coronary artery mask along with some unwanted mask (mask volumes unrelated to coronaries) which is later edited manually. This segmented mask was then assessed by an independent experienced cardiologist (SJ)

who is blinded to both CCTA and ICA results. A patient-specific 3D aorto coronary lumen surface model, from this final segmented mask, was saved in the Steriolithography (STL) geometric file format. The meshes were then moved to Geomagic^{TM} to simplify the mesh (by linear subdivision) and add smoothness to the mesh. The corresponding coronary vessel of interest (RCA/LCX and/or LAD) without branches, from this aorto-coronary surface geometry (lumen), was then: (i) extracted; (ii) thickened outwards by 1 mm from the lumen surface to represent arterial thickness; and (iii) coupled with appropriate barb fittings at its inlet and outlet in solid works (Dassault Systemes, France; **Figure 1A**). These coronary vessel models with barb fittings in STL geometric format were then printed using a Carbon M1 3D printer (Carbon Inc., California, United States) with urethane methacrylate (UMA) family of rigid resins. The Carbon M1 3D printer uses an additive manufacturing methodology called projection stereolithography apparatus (21) (SLA); which builds/fabricates models layer by layer using a curable photopolymer (liquid resin). Apart from the higher resolution, an additional advantage of using the SLA methodology to 3D print the coronary vessels is that there is no support material in the lumen that needs to be removed post-printing [for e.g., like in PolyJet printing method (22)]. Thus, 3D printing the models using an SLA methodology not only saves time (post-print cleaning), but also yields a smooth lumen surface in the 3D printed model, similar to that in the 3D geometric model.

In vitro Flow Circulation System

The coronary flow system, shown in **Figure 1B**, was used to perform the *in vitro* experiments under physiologic steady flow conditions of pressure and flow. The flow was maintained to be quasi-steady in the flow system and mean flow rate was used as the relevant maximum flow rate scale (perceived hyperemia). A 60:40 mixture (by volume) of distilled water and glycerol (Shelley Medical Imaging Technologies, Ontario), having a viscosity (4.5 cP) and density (1.04 g/cm^3) similar to that of blood was selected for use in the experiment as the Newtonian blood-analog fluid (BAF). Previous studies have shown that Newtonian assumption has lesser influence on flow field in medium to large sized arteries such as coronary artery (23–25).

A Cole-Parmer digital gear-drive pump (model # EW-74014-42) was used to impart and vary the flow rates in the flow system. The circulation system was modeled as a flow-dependent stenosis resistance (R_p) in series with an adjustable downstream resistance (R_d; needle valve [model # EW-06394-04]) (26). The corresponding electrical analog of the model is shown in **Figure 1C**. The fluid reservoir is open to atmosphere, thus assuming P_b in **Figure 1C** to be zero. The fluid reservoir, pump, 3D printed coronary vessel model and the needle valve were connected to form a closed loop using flexible Platinum-cured Silicone tubing.

Experimental Setup

In order to mimic the pressure measurement in a cardiac catheterization laboratory setting, a 5F diagnostic catheter was advanced proximal to the stenosis section through a cannula. The aortic pressure (P_a) was measured through a fluid-filled line connected to a Namic disposable transducer (Navilyst Medical) and the coronary guiding catheter. "A 0.014" pressure sensor-tipped guidewire, connected to a Volcano ComboMap machine (Volcano Corp.,), was set to zero, advanced *via* an introducer needle and a hemostatic valve through the diagnostic catheter. The pressure sensor-tipped guidewire was then calibrated, normalized to the diagnostic catheter, and advanced distal to the stenosis section. The pressure distal to the stenosis (P_d) was measured through this pressure sensor-tipped guidewire. Inlet flow rate into the stenosis test section was measured using a transit-time ultrasound clamp-on flow sensor (Transonic Inc.,TS410-ME4PXL).

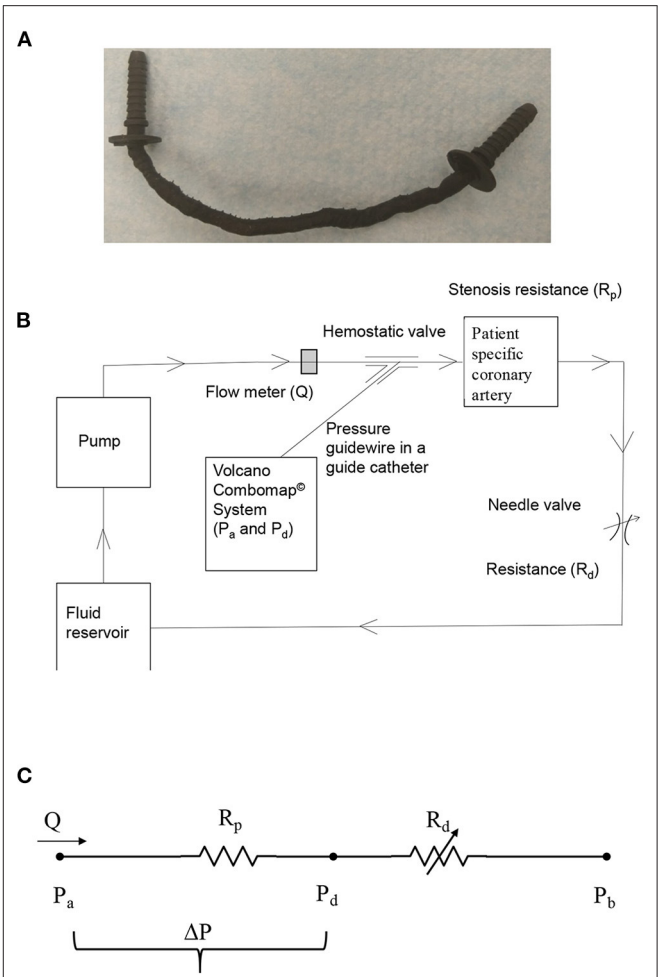

FIGURE 1 | (A) 3D printed patient-specific LAD coronary artery; **(B)** schematic of *in vitro* coronary flow-loop setup for FFR_{3D}; and **(C)** electrical analog model of the flow-loop with two resistances in series. R_p, stenosis resistance from the 3D printed model; R_d, coronary microvascular resistance; Q, flow through stenosed artery measured by the flowmeter; P_a, aortic pressure; P_d, pressure distal to the stenosis; $\Delta P = P_a - P_d$, pressure-drop across stenosis; P_b, coronary outflow pressure.

Experimental Protocol

The 3D printed patient specific coronary vessel models were fixed in the flow system one at a time, as shown in **Figure 1B**. The BAF was then allowed to circulate through the flow system for about 5 min prior to the experiment in order to achieve steady state conditions and care was taken so that the flow loop did not have any air-bubbles during the experiment. The aortic pressure (P_a) for each 3D printed model was maintained at a constant value as measured during invasive coronary angiography for the corresponding patient. This constant inlet aortic pressure (P_a) condition is achieved, under different flow rates, by varying the needle valve resistance (R_d) that mimicked adjustable microcirculatory resistance. The distal pressure (P_d) for each varying flow rate was measured only after pulling back the pressure guidewire into the diagnostic catheter, renormalizing and advancing across the stenosis, to avoid the effect of drift on the measurements. Three sets ($n = 3$) of experiments were carried out and the three pressure-flow data sets were averaged to obtain the pressure drop- flow rate (ΔP–Q; **Supplementary Figure 1**) for each. The pressure ratio (P_d/P_a) at differing prescribed flow rates (Q), applied to each of the 3D printed model was then assessed from the ΔP–Q curves (**Supplementary Figure 2**).

Determination of Hyperemic Flow

The physiological flow conditions like pharmacologically induced hyperemia are unknown in the *in vitro* experimental setup. However, the methodology for estimating *hyperemia* using maximal vasodilation-distal perfusion pressure plot (CFR-P_d) was previously proposed by Kirkeeide et al. (27) and reported in an *in vitro* setting by Sinha Roy et al. (28) assuming a resting blood flow rate of 50 mL/min for a 3 mm native diameter vessel. Utilizing this resting blood flow value, the hyperemic flow rates, Q_h, were obtained using the *intersection* of the (CFR-P_d) line and the experimental ΔP–Q curve (**Supplementary Figure 3**). The CFR-P_d line was a linear curve fit based on previously reported clinical data from 32 patients' (29) group with normal microvasculature. These patients had no evidence of myocardial infarction (MI), no left ventricular hypertrophy, no valvular heart disease, and a normal left ventricular ejection fraction. The *Y*-intercept of the CFR-P_d line is denoted as zero-flow mean pressure (P_{zf}), which represents the residual pressure at no flow. Physiologically realistic P_{zf} values of 20 mmHg, as reported in a previous clinical study (30, 31), were also used in the maximal vasodilation CFR-P_d line (**Supplementary Figure 3**). The distal bed-resistance (R_d) offered by the microvasculature to the flow can then be evaluated as below:

$$R_d = \frac{(P_d - P_{zf})}{Q_h} \quad (1)$$

Statistical Analysis

The association between FFR_{3D} and FFR was assessed by Bland–Altman plots with 95% limits of agreement and spearman correlation coefficient. The receiver operating characteristic (ROC) curve with a corresponding area under the ROC curve (AUC) was performed to assess the per-vessel discrimination of functional ischemia by FFR_{3D}, using invasive FFR $\leq$ 0.8 as the reference standard. Youden's index was used to determine the optimal threshold value of FFR_{3D}. Statistical analyses were performed using Medcalc (Ostende, Belgium) with p-value <0.05 considered to indicate a statistically significant result.

TABLE 1 | Baseline patient characteristics.

Characteristic	Data
Age (y)*	65.3 ± 8.3
Male-to-female ratio	21:7
Diabetes	7 (25%)
Hypertension	18 (64%)
Dyslipidemia	12 (43%)
Family history of CAD	10 (36%)
Past history of smoking	6 (21%)
>50% stenosis by CT	17 (61%)
Number of vessels (LAD/LCX/RCA)	18/5/5

Data are means ± standard deviation.

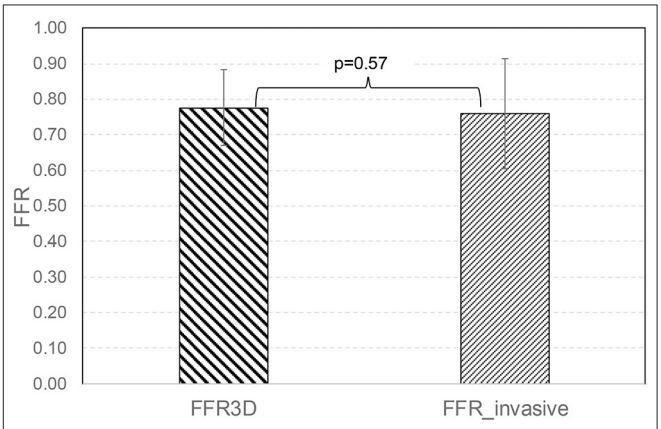

FIGURE 2 | Mean value comparison between FFR_{3D} and invasive FFR.

RESULTS

Baseline Patient Characteristics

The baseline clinical characteristics of the twenty eight patients/vessels (5 RCA, 5 LCX, and 18 LAD) are summarized in **Table 1**. The average age of the study population was at 65.3 ± 8.3 years. The prevalence of known cardiovascular risk factors among this cohort was 25% for diabetes, 64% for hypertension, 43% for Dyslipidemia, 36% for family history of CAD and 21% for past history of smoking. The study population consisted of intermediate coronary stenosis with a mean diameter stenosis of 53.7 ± 17.1% after quantitative CT measurements. Significant stenosis (>50 diameter stenosis) was observed in 61% of study population.

Correlation and Concordance Between FFR_{3D} (*in vitro*) and FFR (Invasive)

No significant difference was observed in the mean values between FFR3D and invasive FFR values (0.78 ± 0.11 and 0.76 ±

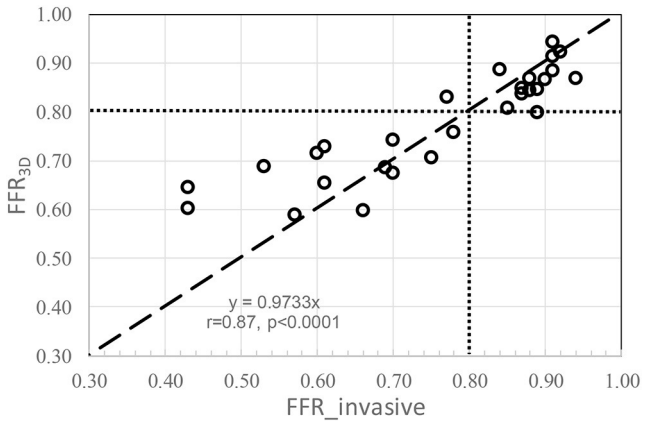

FIGURE 3 | Correlation between FFR_{3D} and invasive FFR (dotted lines represent an FFR value of 0.80).

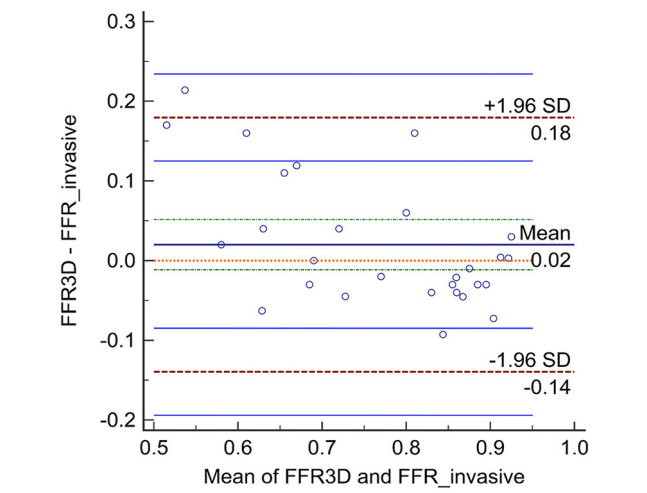

FIGURE 4 | Bland-Altman analysis between FFR_{3D} and invasive FFR.

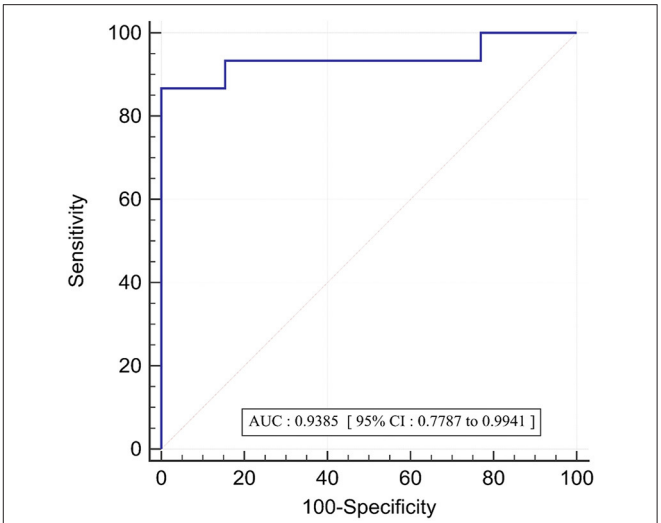

FIGURE 5 | ROC curve for the prediction of functionally significant stenoses (FFR<=0.80) by FFR_{3D}; AUC, area under the curve; ROC, receiver operating curve.

0.15, p=0.57; **Figure 2**). For these twenty eight models, there was also a good positive correlation as determined by the Spearman coefficient of correlation ($r = 0.87$, $p < 0.0001$; **Figure 3**) between the FFR_{3D} and invasive FFR. Further, Bland–Altman analysis (**Figure 4**) revealed a mean bias of 0.02 (limits of agreement: −0.14 to 0.18; $p = 0.2$), which was proportional to the average of FFR (Spearman $r = 0.42$; $p = 0.025$). Thus, suggesting that the concordance between FFR_{3D} and invasive FFR for the assessment of ischemic severity was good.

In the twenty eight vessels, there were 15 (54%) vessels with an invasive FFR $\leq$ 0.8 signifying the presence of ischemia. The area under the receiver operating curve with regards to discriminating ischemic lesions by FFR_{3D} at the invasive FFR threshold of 0.80 is displayed in **Figure 5**. ROC analysis for FFR_{3D} demonstrated an AUC of 0.94 (95% CI: 0.78–0.99; $p < 0.0001$). Youden's index testing establishes a threshold of $\leq$0.76 for FFR_{3D}, sensitivity = 86.7% (95% CI: 59.5–98.3), specificity = 100 % (95% CI: 75.3–100). This threshold value correctly classified 100% of vessels.

DISCUSSION

An *in vitro* experimental flow-loop was developed to model physiological coronary circulation in CCTA-derived *patient-specific 3D printed* coronary vessel geometry as a flow-dependent stenosis resistance (R_p) in series with a downstream resistance (R_d). The *in vitro* flow circulation system was representative of invasive measurements in a cardiac catheterization laboratory. In this pilot study, twenty eight CCTA-derived *patient-specific* 3D printed coronary vessels were integrated into this flow loop one at a time to estimate the FFR value *in vitro* (FFR_{3D}) and compare the same with the corresponding gold standard invasive FFR. We observed that the FFR values estimated from the 3D printed models *in vitro* (FFR_{3D}) correlated well ($r = 0.87$; $p < 0.0001$) with the corresponding invasive FFR values. More importantly, in this pilot study, Bland-Altman analysis revealed a good concordance between the FFR_{3D} and invasive FFR values with a mean bias of 0.02 (limits of agreement: −0.14 to 0.18).

Coronary artery disease (CAD) is one of the main causes of morbidity and mortality worldwide (1, 32, 33). Anatomical assessment through invasive coronary angiography (ICA) remains the gold standard for the diagnosis of CAD. Invasive measurement of fractional flow reserve (FFR); a physiological adjunct to functional stenosis severity when combined with the anatomical assessment from ICA was found to outperform the anatomical assessment alone for diagnosing and guiding treatment to CAD (34, 35). However, FFR is currently used to guide only about 6% of interventions performed in the United States (36) due to limiting factors like adenosine infusion, risk of complications due to invasiveness of using pressure wire

in distal vessels for e.g., vessel dissection (occurs in about 0.5% of the procedures) and patient-related contraindications (34, 37, 38) (hypotension, asthma, etc.). To overcome these limitations, there has been a recent interest in developing and using less invasive techniques for assessing both anatomy and physiology. CCTA imaging is one such non-invasive imaging modality that will allow for assessing both anatomy and physiology [for e g., using 3D lumen reconstruction and computational fluid dynamics [CFD]; FFR_{CT} (12–14)].

Conversely, for the first time, in this pilot study using CCTA images, we developed and evaluated a novel *in vitro* method to assess *physiological* ischemia from CCTA-derived and *3D printed* coronary arteries. Briefly, the programmatic workflow in the proposed methodology on a per-patient basis involves the following three steps: (i) semi-automatic segmentation of lumen from CCTA scans (about ∼ 40 min); (ii) 3D printing the segmented model (about ∼60 min); and (iii) plugging the 3D model into the existing flow loop to simulate patient-specific physiological conditions and estimate FFR_{3D} (about ∼10 min). Thus, currently the total time required to estimate FFR_{3D} from a CCTA scan is about 110 min (∼2 h). With the recent developments in automatic reconstruction of coronary arteries from CCTA using deep learning technology and also the advancements in additive manufacturing technology; we believe that we can further reduce the total estimated time to about from 40 to 30 min or even lower in future.

Comparison to FFR_{CT}

Using invasive FFR as a gold standard, the novel approach of combining CT scans and computational fluid dynamics (CFD) for estimating non-invasive FFR (FFR_{CT}) was first evaluated by Koo et al. (12) and Min et al. (13) in a cohort of 103 and 252 patients, respectively. Norgaard et al. (14) in a separate study also concluded that FFR_{CT} has high diagnostic performance when compared to invasive FFR and reported that mean time to computation of FFR_{CT} results was less than 4 h. It should be noted that both FFR_{CT} and FFR_{3D} use segmentation approaches as a first step to generate the lumen geometry from CCTA scans. On this patient-specific lumen geometry, FFR_{CT} uses CFD to solve the Navier-Stokes equations for fluid flow by estimating resting flow and assuming that microcirculation reacts predictably to the physiological condition of maximal hyperemia (39). FFR_{3D}, however, uses the 3D printed models to generate the characteristic non-linear ΔP–Q curves while accounting for the physiological phenomenon of coronary autoregulation and then estimates patient-specific hyperemic condition from these curves in confluence with the linear CFR-P_d line from previous clinical measurements (26). Moreover, the measurement uncertainty (from flow sensor and pressure wire) corresponding each data point in the non-linear ΔP–Q curve (**Supplementary Figure 1**) was also quantified using uncertainty analysis (40, 41). The uncertainty in pressure-ratio (P_d/P_a) and flow-ratio (Q/Q_b) values at each data point due to measurement errors were found to be within 1%. In addition to the above, although the shorter time required to estimate FFR_{3D} (from this pilot study) is advantageous, we believe that a future comprehensive study comparing both FFR_{3D} and FFR_{CT} is still warranted.

Comparison to Quantitative Flow Ratio

Recently, Tu et al. (42) proposed an alternative method, Quantitative flow reserve (QFR), of calculating FFR during in-procedure angiography (43). Briefly, the methodology involves: (i) generating a 3D vessel contour from 2D quantitative coronary angiography (QCA); (ii) followed by hyperemic flow estimation from Thrombolysis in Myocardial Infarction (TIMI) frame count using empirical relations; and (iii) utilization of CFD or simplified analytical equations to estimate QFR at hyperemia [median time for QFR estimation is 5 min (43)]. Tu et al. (42), in their initial study, reported that there was a strong correlation ($r = 0.81$; $p < 0.001$) between QFR and invasive FFR with a mean difference of 0.06 ($p = 0.054$). Similar to these results, our pilot study using 3D printing methodology (FFR_{3D}) also showed a strong correlation ($r = 0.87$; $p < 0.0001$) and a lower mean bias (0.02; $p = 0.2$) when compared to invasive FFR. Although there is a substantial gain in processing time for QFR (5 min) over FFR_{3D} (110 min), it should be noted that QFR is derived from: (i) 3D vessel contour derived from 2D angiograms as opposed to volumetric data used for geometry generation in FFR_{3D}; and (ii) hyperemia estimation from empirical equations as opposed to the physiological scenario of accounting for auto-regulation and micro-circulatory resistance in FFR_{3D}.

Potential Clinical Implications and Future Work

As mentioned previously, physiology-guided decision making using invasive FFR in conjunction with invasive coronary angiography can improve diagnosis and treatment of CAD. However, invasive FFR is currently used to guide only about 6% of interventions performed in the United States (36). One of the main reasons for this can be either the cost of pressure wire and/or the small risk of injuring vessels during pressure wire manipulation [for e g., Side branch dissection (37)]. Alternatively, a complete non-invasive diagnostic approach of combining both anatomy and physiology using CCTA scans and 3D printing (FFR_{3D}) will incur low cost and no risk of dissection.

Currently, the estimation of FFR_{3D} requires some user interaction during the three steps of segmentation, 3D printing and flow loop evaluation. Technological advancements in deep learning based segmentation approaches, 3D printing methodologies (and materials) and using pressure sensing taps on the 3D printed model for direct pressure measurement could further automate and expedite the entire workflow. Moreover, beyond the estimation of FFR_{3D} for CAD diagnosis; the 3D model could also be used for various pre-intervention planning approaches including: (i) estimating the length and type of stent needed to open the blockage; (ii) assessment of post-intervention hemodynamics after inserting a stent into the 3D model to open the vessel; and (iii) physiologically discriminate between focal and diffuse CAD by measuring the drop in pressure across a length of a vessel (i.e., pressure gradient) (44).

Assumptions

The wall of the stenosis geometry was assumed to be rigid in the *in vitro* experiment. A rigid wall approximation when compared to a compliant wall model is expected to provide a conservative estimate (45) (limiting case) of pressure drop as seen in hyperemia. However, further *in vitro* experiments with compliant stenosis models are needed for comparison. The resting blood flow was assumed to be a constant value of 50 mL/min in this study. Previously, in a preclinical study with anesthetized dogs, Gould et al. (46) reported that progressive reduction of coronary lumen has no effect on resting blood flow until the vessel is occluded by about 80–85% of the nominal vessel diameter. More recently, Nijjer et al. (47), in a large dataset of real-world patients, that underwent simultaneous intracoronary pressure and flow measurement, also reported that *resting flow is preserved* despite increasing stenosis severity owing to compensatory reduction in resting microvascular resistance.

The study involves predominantly focal lesions, and we assume that the side branch flow likely affects diffuse lesions differently than focal lesions. Gosling et al. (48), evaluated the effect of side branch flow on non-dimensional physiological flow indices and reported that there was no significant change/effect on the non-dimensional physiological indices (pressure based). The authors report that this phenomenon could be because side branch flow likely affects diffuse lesions differently than focal lesions. However, it should also be noted that in contrast to observations from this study, Sturdy et al. (49) and Vardhan et al. (50) reported that neglecting the side branches increased estimates of wall shear stress and pressure drop.

LIMITATIONS

Steady state average pressure and flow values were used in this *in vitro* experiment because FFR values are defined as the mean pressure ratios. Previously, Huo et al. (51), in an *in vitro* experiment compared pressure drop between pulsatile flow and steady-state flow. They reported that pressure drop across a stenosis remained relatively unchanged (<5%), provided that the mean value of the pulsatile flow rate (time-averaged over a cardiac cycle) equaled the steady state value. Nevertheless, we plan to extend the present work in the future to study the effects of unsteady pulsatile flow. The blood analog fluid used in the *in vitro* model has a Newtonian viscosity of 4.5 cP similar to normal blood viscosity data available in existing literature. The viscosity of blood changes with many factors, and may somewhat impact pressure drop due to variability in viscous losses.

This pilot study is limited by its small sample size. We only validated FFR_{3D} on patients with de novo lesions. Selection bias might be involved. Further, the experiments were conducted with *patient-specific* single coronary vessel models; thus neglecting the effect of branching/bifurcation, serial lesions or collateral flow, which may cause additional levels of pressure drop. Consequently, future studies in a large sample size using *patient-specific aorto-coronary 3D-printed* models that account for the presence of bifurcation and collateral flow should extend our current work.

CONCLUSION

In this study, an *in vitro* experimental flow loop using 3D-printed patient-specific coronary arteries was developed. The flow loop essentially modeled physiological coronary circulation, as flow-dependent stenosis resistance in series with a downstream resistance. The main finding of this study was that *3D printed patient-specific* models (FFR_{3D}) can be used in a *non-invasive in vitro* environment to quantify coronary artery ischemia with good correlation and concordance to that of invasive FFR.

COMPETENCY IN MEDICAL KNOWLEDGE

Invasive FFR is the current gold standard not only for evaluating the functional significance of a stenosis but also to guide treatment. In this pilot study, we developed a novel non-invasive diagnostic approach of combining both anatomy and physiology using CCTA scans and 3D printing (FFR_{3D}) to evaluate coronary artery ischemia. The FFR evaluated using 3D printed patient-specific models had a good correlation and concordance with invasive FFR.

TRANSLATIONAL OUTLOOK

Future studies in a large sample size using *patient-specific aorto-coronary 3D-printed* models that account for the presence of bifurcation and collateral flow are needed to extend our current work. Furthermore, the technological advancements in deep learning based segmentation approaches, 3D printing methodologies (and materials) and utilization of pressure sensing taps on the 3D printed model for direct pressure measurement could further automate and expedite the entire workflow while testing in a larger cohort.

DATA AVAILABILITY STATEMENT

The original contributions presented in the study are included in the article/**Supplementary Material**, further inquiries can be directed to the corresponding author/s.

ETHICS STATEMENT

The studies involving human participants were reviewed and approved by IRB, WCMC. *In vitro* experiments were based on patient's image data and hemodynamic parameters, which were deidentified prior to study. Written informed consent for participation was not required for this study in accordance with the National Legislation and the Institutional Requirements.

AUTHOR CONTRIBUTIONS

KK, SD, and BM: designed the study. KK, S-JJ, AZ, AC, SA, AM, PX, and RS: participated in segmenting the image data and 3D printing the *in vitro* models. KK, SA, and AM: *in vitro* experimental setup. KK: analyzed the data and drafted the

manuscript with all authors. All authors read and approved the final manuscript.

FUNDING

This manuscript was supported, in part, by grants from the National Institutes of Health, the National Heart Lung and Blood Institute (Grant Nos. R01 HL118019, R01 HL115150, and R21 HL132277), as well as from a generous gift from the Dalio Foundation.

SUPPLEMENTARY MATERIAL

The Supplementary Material for this article can be found online at: https://www.frontiersin.org/articles/10.3389/fcvm.2022.909680/full#supplementary-material

REFERENCES

1. Benjamin EJ, Virani SS, Callaway CW, Chamberlain AM, Chang AR, Cheng S, et al. Heart disease and stroke statistics-—2018 update: a report from the american heart association. *Circulation.* (2018) 137:e67–e492. doi: 10.1161/CIR.0000000000000573
2. Pijls NH, De Bruyne B, Peels K, Van Der Voort PH, Bonnier HJ, Bartunek JKJJ, et al. Measurement of fractional flow reserve to assess the functional severity of coronary-artery stenoses. *N Engl J Med.* (1996) 334:1703–8. doi: 10.1056/NEJM199606273342604
3. Pijls NH, Fearon WF, Tonino PA, Siebert U, Ikeno F, Bornschein B, et al. Fractional flow reserve vs. angiography for guiding percutaneous coronary intervention in patients with multivessel coronary artery disease: 2 year follow-up of the FAME (Fractional Flow Reserve Versus Angiography for Multivessel Evaluation) study. *J Am Coll Cardiol.* (2010) 56:177–84. doi: 10.1016/j.jacc.2010.04.012
4. Tonino PA, De Bruyne B, Pijls NH, Siebert U, Ikeno F. van' t Veer M, et al. Fractional flow reserve versus angiography for guiding percutaneous coronary intervention. *N Engl J Med.* (2009) 360:213–24. doi: 10.1056/NEJMoa0807611
5. van Nunen LX, Zimmermann FM, Tonino PA, Barbato E, Baumbach A, Engstrom T, et al. Fractional flow reserve vs. angiography for guidance of PCI in patients with multivessel coronary artery disease (FAME): 5 year follow-up of a randomized controlled trial. *Lancet.* (2015) 386:1853–60. doi: 10.1016/S0140-6736(15)00057-4
6. Pijls NH, Tanaka N, Fearon WF. Functional assessment of coronary stenoses: can we live without it? *Eur Heart J.* (2013) 34:1335–44. doi: 10.1093/eurheartj/ehs436
7. Budoff MJ, Dowe D, Jollis JG, Gitter M, Sutherland J, Halamert E, et al. Diagnostic performance of 64-multidetector row coronary computed tomographic angiography for evaluation of coronary artery stenosis in individuals without known coronary artery disease: results from the prospective multicenter ACCURACY (Assessment by Coronary Computed Tomographic Angiography of Individuals Undergoing Invasive Coronary Angiography) trial. *J Am Coll Cardiol.* (2008) 52:1724–32. doi: 10.1016/j.jacc.2008.07.031
8. Bamberg F, Becker A, Schwarz F, Marcus RP, Greif M, von Ziegler F, et al. Detection of hemodynamically significant coronary artery stenosis: incremental diagnostic value of dynamic CT-based myocardial perfusion imaging. *Radiology.* (2011) 260:689–98. doi: 10.1148/radiol.11110638
9. Danad I, Szymonifka J, Twisk JWR, Norgaard BL, Zarins CK, Knaapen P, et al. Diagnostic performance of cardiac imaging methods to diagnose ischaemia-causing coronary artery disease when directly compared with fractional flow reserve as a reference standard: a meta-analysis. *Eur Heart J.* (2016) 38:991–8. doi: 10.1093/eurheartj/ehw095
10. Ko BS, Cameron JD, Leung M, Meredith IT, Leong DP, Antonis PR, et al. Combined CT coronary angiography and stress myocardial perfusion imaging for hemodynamically significant stenoses in patients with suspected coronary artery disease: a comparison with fractional flow reserve. *JACC Cardiovascular Imaging.* (2012) 5:1097–111. doi: 10.1016/j.jcmg.2012.09.004
11. Meijboom WB, Van Mieghem CA, van Pelt N, Weustink A, Pugliese F, Mollet NR, et al. Comprehensive assessment of coronary artery stenoses: computed tomography coronary angiography versus conventional coronary angiography and correlation with fractional flow reserve in patients with stable angina. *J Am Coll Cardiol.* (2008) 52:636–43.
12. Koo BK, Erglis A, Doh JH, Daniels DV, Jegere S, Kim HS, et al. Diagnosis of ischemia-causing coronary stenoses by noninvasive fractional flow reserve computed from coronary computed tomographic angiograms. Results from the prospective multicenter DISCOVER-FLOW (Diagnosis of Ischemia-Causing Stenoses Obtained Via Noninvasive Fractional Flow Reserve) study. *J Am Coll Cardiol.* (2011) 58:1989–97. doi: 10.1016/j.jacc.2011.06.066
13. Min JK, Leipsic J, Pencina MJ, Berman DS, Koo BK, van Mieghem C, et al. Diagnostic accuracy of fractional flow reserve from anatomic CT angiography. *JAMA.* (2012) 308:1237–45. doi: 10.1001/2012.jama.11274
14. Norgaard BL, Leipsic J, Gaur S, Seneviratne S, Ko BS, Ito H, et al. Diagnostic performance of noninvasive fractional flow reserve derived from coronary computed tomography angiography in suspected coronary artery disease: the NXT trial (Analysis of Coronary Blood Flow Using CT Angiography: Next Steps). *J Am Coll Cardiol.* (2014) 63:1145–55. doi: 10.1016/j.jacc.2013.11.043
15. Mosadegh B, Xiong G, Dunham S, Min JK. Current progress in 3D printing for cardiovascular tissue engineering. *Biomed Mater.* (2015) 10:034002. doi: 10.1088/1748-6041/10/3/034002
16. Vukicevic M, Mosadegh B, Min JK, Little SH. Cardiac 3D printing and its future directions. *JACC Cardiovasc Imaging.* (2017) 10:171–84. doi: 10.1016/j.jcmg.2016.12.001
17. Rizvi A, Hartaigh BO, Knaapen P, Leipsic J, Shaw LJ, Andreini D, et al. Rationale and design of the credence trial: computed tomographic evaluation of atherosclerotic determinants of myocardial ischemia. *BMC Cardiovasc Disord.* (2016) 16:e190. doi: 10.1186/s12872-016-0360-x
18. Fihn SD, Blankenship JC, Alexander KP, Bittl JA, Byrne JG, Fletcher BJ, et al. 2014 ACC/AHA/AATS/PCNA/SCAI/STS focused update of the guideline for the diagnosis and management of patients with stable ischemic heart disease: a report of the American College of Cardiology/American Heart Association Task Force on Practice Guidelines, and the American Association for Thoracic Surgery, Preventive Cardiovascular Nurses Association, Society for Cardiovascular Angiography and Interventions, and Society of Thoracic Surgeons. *J Am Coll Cardiol.* (2014) 64:1929–49. doi: 10.1161/CIR.0000000000000095
19. Montalescot G, Sechtem U, Achenbach S, Andreotti F, Arden C, Budaj A, et al. 2013 ESC guidelines on the management of stable coronary artery disease: the task force on the management of stable coronary artery disease of the European Society of Cardiology. *Eur Heart J.* (2013) 34:2949–3003. doi: 10.1093/eurheartj/eht296
20. Leipsic J, Abbara S, Achenbach S, Cury R, Earls JP, Mancini GJ, et al. SCCT guidelines for the interpretation and reporting of coronary CT angiography: a report of the Society of Cardiovascular Computed Tomography Guidelines Committee. *J Cardiovasc Comput Tomogr.* (2014) 8:342–58. doi: 10.1016/j.jcct.2014.07.003
21. Tumbleston JR, Shirvanyants D, Ermoshkin N, Janusziewicz R, Johnson AR, Kelly D, et al. Continuous liquid interface production of 3D objects. *Science.* (2015) 347:1349–52. doi: 10.1126/science.aaa2397
22. Ionita CN, Mokin M, Varble N, Bednarek DR, Xiang J, Snyder KV, et al. Challenges and limitations of patient-specific vascular phantom fabrication using 3D polyjet printing. *Proc SPIE Int Soc Opt Eng.* (2014) 9038:90380M. doi: 10.1117/12.2042266
23. Min S, Kang G, Paeng DG, Choi JH. The reasons why fractional flow reserve and instantaneous wave-free ratio are similar using wave separation analysis. *BMC Cardiovasc Disord.* (2021) 21:e48. doi: 10.1186/s12872-021-01855-4
24. Liu H, Lan L, Abrigo J, Ip HL, Soo Y, Zheng D, et al. Comparison of newtonian and non-newtonian fluid models in blood flow simulation

in patients with intracranial arterial stenosis. *Front Physiol.* (2021) 12:e782647. doi: 10.3389/fphys.2021.782647
25. Johnston BM, Johnston PR, Corney S, Kilpatrick D. Non-newtonian blood flow in human right coronary arteries: steady state simulations. *J Biomech.* (2004) 37:709–20. doi: 10.1016/j.jbiomech.2003.09.016
26. Kolli KK, Min JK, Ha S, Soohoo H, Xiong G. Effect of varying hemodynamic and vascular conditions on fractional flow reserve: an *in vitro* study. *J Am Heart Assoc.* (2016) 5:e003634. doi: 10.1161/JAHA.116.003634
27. Kirkeeide RL, Gould KL, Parsel L. Assessment of coronary stenoses by myocardial perfusion imaging during pharmacologic coronary vasodilation. VII Validation of coronary flow reserve as a single integrated functional measure of stenosis severity reflecting all its geometric dimensions. *J Am Coll Cardiol.* (1986) 7:103–13. doi: 10.1016/S0735-1097(86)80266-2
28. Roy AS, Banerjee RK, Back LH, Back MR, Khoury S, Millard RW. Delineating the guide-wire flow obstruction effect in assessment of fractional flow reserve and coronary flow reserve measurements. *Am J Physiol Heart Circ Physiol.* (2005) 289:H392–7. doi: 10.1152/ajpheart.00798.2004
29. Wilson RF, Johnson MR, Marcus ML, Aylward PE, Skorton DJ, Collins S, et al. The effect of coronary angioplasty on coronary flow reserve. *Circulation.* (1988) 77:873–85. doi: 10.1161/01.CIR.77.4.873
30. Kitabata H, Imanishi T, Kubo T, Takarada S, Kashiwagi M, Matsumoto H, et al. Coronary microvascular resistance index immediately after primary percutaneous coronary intervention as a predictor of the transmural extent of infarction in patients with ST-segment elevation anterior acute myocardial infarction. *JACC Cardiovasc Imaging.* (2009) 2:263–72. doi: 10.1016/j.jcmg.2008.11.013
31. Van Herck PL, Carlier SG, Claeys MJ, Haine SE, Gorissen P, Miljoen H, et al. Coronary microvascular dysfunction after myocardial infarction: increased coronary zero flow pressure both in the infarcted and in the remote myocardium is mainly related to left ventricular filling pressure. *Heart.* (2007) 93:1231–7. doi: 10.1136/hrt.2006.100818
32. Mendis S, Davis S, Norrving B. Organizational update: the world health organization global status report on non-communicable diseases 2014; one more landmark step in the combat against stroke and vascular disease. *Stroke.* (2015) 46:e121–2. doi: 10.1161/STROKEAHA.113.003377
33. Roth GA, Abate D, Abate KH, Abay SM, Abbafati C, Abbasi N, et al. Global, regional, and national age-sex-specific mortality for 282 causes of death in 195 countries and territories, 1980–2017: a systematic analysis for the Global Burden of Disease Study 2017. *Lancet.* (2018) 392:1736–88. doi: 10.1016/S0140-6736(18)32203-7
34. Curzen N, Rana O, Nicholas Z, Golledge P, Zaman A, Oldroyd K, et al. Does routine pressure wire assessment influence management strategy at coronary angiography for diagnosis of chest pain? the RIPCORD study. *Circ Cardiovasc Interv.* (2014) 7:248–55. doi: 10.1161/CIRCINTERVENTIONS.113.000978
35. Toth GG, Toth B, Johnson NP, De Vroey F, Di Serafino L, Pyxaras S, et al. Revascularization decisions in patients with stable angina and intermediate lesions: results of the international survey on interventional strategy. *Circ Cardiovasc Interv.* (2014) 7:751–9. doi: 10.1161/CIRCINTERVENTIONS.114.001608
36. Wijns W, Kolh P, Danchin N, Di Mario C, Falk V, Folliguet T, et al. Guidelines on myocardial revascularization. *Eur Heart J.* (2010) 31:2501–55. doi: 10.1093/eurheartj/ehq277
37. Kumsars I, Narbute I, Thuesen L, Niemela M, Steigen TK, Kervinen K, et al. Side branch fractional flow reserve measurements after main vessel stenting: a Nordic-Baltic Bifurcation Study III substudy. *EuroIntervention.* (2012) 7:1155–61. doi: 10.4244/EIJV7I10A186
38. Park E, Price A, Vidovich MI. Adenosine-induced atrial fibrillation during fractional flow reserve measurement. *Cardiol J.* (2012) 19:650–1. doi: 10.5603/CJ.2012.0121
39. Min JK, Taylor CA, Achenbach S, Koo BK, Leipsic J, Norgaard BL, et al. Noninvasive fractional flow reserve derived from coronary ct angiography: clinical data and scientific principles. *JACC Cardiovasc Imaging.* (2015) 8:1209–22. doi: 10.1016/j.jcmg.2015.08.006
40. Kline SJ. Describing uncertainty in single sample experiments. *Mech Engineering.* (1953) 75:3–8.
41. Moffat RJ. Describing the uncertainties in experimental results. *Exp Therm Fluid Sci.* (1988) 1:3–17. doi: 10.1016/0894-1777(88)90043-X
42. Tu S, Barbato E, Köszegi Z, Yang J, Sun Z, Holm NR, et al. Fractional flow reserve calculation from 3-dimensional quantitative coronary angiography and timi frame count: a fast computer model to quantify the functional significance of moderately obstructed coronary arteries. *JACC Cardiovasc Imaging.* (2014) 7:768–77. doi: 10.1016/j.jcin.2014.03.004
43. Westra J, Tu S, Winther S, Nissen L, Vestergaard MB, Andersen BK, et al. Evaluation of coronary artery stenosis by quantitative flow ratio during invasive coronary angiography: The WIFI II Study (Wire-Free Functional Imaging II). *Circ Cardiovasc Imaging.* (2018) 11:e007107. doi: 10.1161/CIRCIMAGING.117.007107
44. Collet C, Sonck J, Vandeloo B, Mizukami T, Roosens B, Lochy S, et al. Measurement of hyperemic pullback pressure gradients to characterize patterns of coronary atherosclerosis. *J Am Coll Cardiol.* (2019) 74:1772–84. doi: 10.1016/j.jacc.2019.07.072
45. Siebes M, Campbell CS, D'Argenio DZ. Fluid dynamics of a partially collapsible stenosis in a flow model of the coronary circulation. *J Biomech Eng.* (1996) 118:489–97. doi: 10.1115/1.2796035
46. Gould KL, Lipscomb K, Hamilton GW. Physiologic basis for assessing critical coronary stenosis. Instantaneous flow response and regional distribution during coronary hyperemia as measures of coronary flow reserve. *Am J Cardiol.* (1974) 33:87–94. doi: 10.1016/0002-9149(74)90743-7
47. Nijjer SS, de Waard GA, Sen S, van de Hoef TP, Petraco R, Echavarria-Pinto M, et al. Coronary pressure and flow relationships in humans: phasic analysis of normal and pathological vessels and the implications for stenosis assessment: a report from the Iberian-Dutch-English (IDEAL) collaborators [published online 2015]. *Eur Heart J.* (2016) 37:2069–80. doi: 10.1093/eurheartj/ehv626
48. Gosling RC, Sturdy J, Morris PD, Fossan FE, Hellevik LR, Lawford P, et al. Effect of side branch flow upon physiological indices in coronary artery disease. *J Biomech.* (2020) 103:109698. doi: 10.1016/j.jbiomech.2020.109698
49. Sturdy J, Kjernlie JK, Nydal HM, Eck VG, Hellevik LR. Uncertainty quantification of computational coronary stenosis assessment and model based mitigation of image resolution limitations. *J Comput Sci.* (2019) 31:137–50. doi: 10.1016/j.jocs.2019.01.004
50. Vardhan M, Gounley J, Chen SJ, Kahn AM, Leopold JA, Randles A. The importance of side branches in modeling 3D hemodynamics from angiograms for patients with coronary artery disease. *Sci Rep.* (2019) 9:8854. doi: 10.1038/s41598-019-45342-5
51. Huo Y, Svendsen M, Choy JS, Zhang ZD, Kassab GS. A validated predictive model of coronary fractional flow reserve. *J R Soc Interface.* (2012) 9:1325–38. doi: 10.1098/rsif.2011.0605

Conflict of Interest: Dr. Min has served on the Scientific Advisory Board of Arineta and GE Healthcare; has received funding from the Dalio Foundation, the National Institutes of Health, and GE Healthcare; and has an equity interest in MDDX and Cleerly. Dr. Shaw receives funding from the National Institutes of Health. KK is an employee at Abbott. However, he was an employee of the Dalio Institute of Cardiovascular Imaging, Weill Cornell Medicine, at the time of both executing the study and writing the manuscript.

The remaining authors declare that the research was conducted in the absence of any commercial or financial relationships that could be construed as a potential conflict of interest.

Publisher's Note: All claims expressed in this article are solely those of the authors and do not necessarily represent those of their affiliated organizations, or those of the publisher, the editors and the reviewers. Any product that may be evaluated in this article, or claim that may be made by its manufacturer, is not guaranteed or endorsed by the publisher.

frontiers | Frontiers in Cardiovascular Medicine

ORIGINAL RESEARCH
published: 13 July 2022
doi: 10.3389/fcvm.2022.922387

Physiologic Data-Driven Iterative Learning Control for Left Ventricular Assist Devices

Konstantinos Magkoutas†, *Philip Arm*†, *Mirko Meboldt and Marianne Schmid Daners**

Product Development Group Zurich, Department of Mechanical and Process Engineering, ETH Zurich, Zurich, Switzerland

Continuous flow ventricular assist devices (cfVADs) constitute a viable and increasingly used therapy for end-stage heart failure patients. However, they are still operating at a fixed-speed mode that precludes physiological cfVAD response and it is often related to adverse events of cfVAD therapy. To ameliorate this, various physiological controllers have been proposed, however, the majority of these controllers do not account for the lack of pulsatility in the cfVAD operation, which is supposed to be beneficial for the physiological function of the cardiovascular system. In this study, we present a physiological data-driven iterative learning controller (PDD-ILC) that accurately tracks predefined pump flow trajectories, aiming to achieve physiological, pulsatile, and treatment-driven response of cfVADs. The controller has been extensively tested in an *in-silico* environment under various physiological conditions, and compared with a physiologic pump flow proportional-integral-derivative controller (PF-PIDC) developed in this study as well as the constant speed (CS) control that is the current state of the art in clinical practice. Additionally, two treatment objectives were investigated to achieve pulsatility maximization and left ventricular stroke work (LVSW) minimization by implementing copulsation and counterpulsation pump modes, respectively. Under all experimental conditions, the PDD-ILC as well as the PF-PIDC demonstrated highly accurate tracking of the reference pump flow trajectories, outperforming existing model-based iterative learning control approaches. Additionally, the developed controllers achieved the predefined treatment objectives and resulted in improved hemodynamics and preload sensitivities compared to the CS support.

Keywords: LVAD, heart failure, data driven control, iterative learning control, VAD physiological control, ventricular assist devices, ILC, pulsatile blood pump

OPEN ACCESS

Edited by:
Nicola Cosentino, Monzino Cardiology Center (IRCCS), Italy

Reviewed by:
Clemens Zeile, Otto von Guericke University Magdeburg, Germany
Audrey Adji, Victor Chang Cardiac Research Institute, Australia

***Correspondence:**
Marianne Schmid Daners
marischm@ethz.ch

†*These authors have contributed equally to this work*

Specialty section:
This article was submitted to General Cardiovascular Medicine, a section of the journal Frontiers in Cardiovascular Medicine

Received: *17 April 2022*
Accepted: *20 June 2022*
Published: *13 July 2022*

Citation:
Magkoutas K, Arm P, Meboldt M and Schmid Daners M (2022) Physiologic Data-Driven Iterative Learning Control for Left Ventricular Assist Devices. Front. Cardiovasc. Med. 9:922387. doi: 10.3389/fcvm.2022.922387

INTRODUCTION

The prevalence of advanced heart failure (HF), a complex heart syndrome that has long been associated with significant mortality and morbidity rates, has been continuously rising worldwide over the last decades (1–3). For the afflicted patients who account for approximately 1–2% of the general adult population, (3) heart transplantation (HT) is considered the gold standard therapy; however, despite the increased number of heart transplantations performed yearly, the number of recipients continues to significantly outpace the supply of donors (4).

An alternative surgical treatment to mitigate donors' shortage and allow better management of end-stage HF patients is the implantation of ventricular assist devices (VADs) (5, 6). VADs are

mechanical pumps that relieve the native heart and restore a fragment of the cardiac output. Their major deployment is complementary, serving as bridge to transplantation or bridge to recovery (7). However, recent studies have shown that VADs are increasingly used as destination therapy, achieving 1- and 2-year survival rates of 82.3 and 73.1%, respectively, which are comparable to HT (8, 9).

Since their initial approval, VADs have been evolved and matured, with the continuous flow turbodynamic VADs (cfVADs) superseding the bulky and failure-prone volume displacement, pulsatile VADs (10, 11). Despite the notably improved reliability and implantability, cfVADs are still associated with right-heart failure, gastrointestinal bleeding, hemorrhagic strokes, and aortic valve insufficiency, which reduce the survival rates and increase hospital readmissions (5, 12–14). These adverse events are often related to the inability of the currently used cfVADs to respond physiologically to the changing perfusion demands of the patients. To ameliorate this, various research groups have been investigating cfVAD control strategies that restore the physiological response of cfVADs (15, 16). The majority of these strategies aim to imitate the Frank-Starling mechanism (17) by adapting the rotational speed of the cfVAD based on feedback provided by hemodynamic parameters that act as preload surrogates (18–21). More complex strategies utilize norm-optimal iterative learning control (22, 23) to regulate the end-diastolic volume. They exploit the repetitive nature of the heart and, hence, use information of previous cycles to deduce the control input for the new cycle. These approaches are promising; however, their performance can be restricted by the accuracy of the cardiovascular system and cfVAD models that are integrated in the control structure to allow the prediction of the control function.

All control strategies mentioned above improve the responsiveness of VADs, however, they do not address the diminished blood pulsatility induced by cfVADs support. Whether or not the diminished pulsatility is among the major contributors of adverse events of cfVADs is still a controversial issue (24). Nonetheless, recent studies have reported strong evidence that the lack of pulsatility can negatively affect the endothelial and peripheral vascular function (25–27) and, hence, increase the risk of non-surgical bleeding (28). Additionally, various studies highlight the better control of ventricular unloading and patient's hemodynamics when VADs that effectively resemble the pulsatile flow conditions are deployed (29–32).

In an attempt to imitate the pulsatile blood pressure and flow waveforms, while exploiting the reliability and implantability of cfVADs, various approaches of cfVAD speed modulation have been proposed in literature (33–38). A recent review shows that predefined speed profiles implemented in synchrony with the native heart can systematically manipulate the ventricular load and the pulsatility in the arterial tree, confirming the positive effect of speed modulation (39). These approaches focus on the modulation of the speed-profile which is readily available in the clinical setting. However, cfVAD speed-profiles are greatly influenced by the VAD design, hindering the deduction of a direct relation to hemodynamics, as well as, their transferability to different VADs. A more intuitive approach is the modulation of cfVAD speed based on predefined pump flow-profiles. By utilizing an iterative learning control (ILC) scheme, Rüschen et al. (40) provided evidence that accurate tracking of optimized pump flow-profiles can be achieved, resulting in a significant reduction of the left ventricular stroke work (LVSW). For the latter study, a detailed model of the VAD is necessary to enable the accurate flow-profile tracking.

In this study, we introduce a physiologic data-driven iterative learning controller (PDD-ILC) for left ventricular cfVADs. The proposed PDD-ILC enables the generation of preload-adaptive reference pump-flow trajectories based on the Frank-Starling mechanism and treatment objectives, such as pulsatility maximization or LVSW minimization, selected by the clinicians. The tracking of the reference flow trajectories is achieved by measuring left ventricular pressure (LVP) and pump flow (PF), and then implementing the data-driven ILC (DD-ILC). The DD-ILC exploits the recurrent nature of the heart cycle to incorporate the errors identified in previous cycles to the control input of the new cycle and, hence, enhance the tracking performance without requiring a system model. Finally, to enable feedback in the time-domain, a proportional-derivative controller is coupled with the PDD-ILC. The performance of the proposed PDD-ILC was assessed with respect to physiologic responsiveness and trajectory tracking with *in-silico* experiments that emulated various physiologic conditions, and compared with a constant speed (CS) controller and a newly developed physiological pump flow proportional-integral-derivative controller (PF-PIDC).

METHODS AND MATERIALS

Cardiovascular System Model

In this work, the performance of the PDD-ILC was assessed solely with *in-silico* experiments, wherein the deployed human cardiovascular system (CVS) was modeled based on the lumped-parameter representation proposed by Colacino et al. (41). In this representation, the systemic and pulmonary circulations were divided into the arterial and venous systems. The arterial and venous systems were modeled with five-element and classic Windkessel models, respectively. The CVS model incorporated autoregulatory mechanisms for the adaptation of the flow resistance in the systemic and pulmonary arterial systems, as well as the adaptation of the unstressed volume in the systemic veins. All four chambers of the heart were included as actively contracting elements and they were defined by a non-linear time-varying elastance model and an energy dissipation term. A detailed description of the model and its validation in physiological and pathological states can be found in the work of Colacino et al. (41). In all simulations, the pathologic conditions defined by Ochsner et al. (42) were used.

Numerical Models of Blood Pumps

The conditions of a cfVAD supported patient were imitated by coupling the CVS model described above with a numerical model of a non-implantable mixed-flow turbodynamic blood pump (Deltastream DP2, Medos Medizintechnik AG, Stolberg, Germany). The later model was based on the work of Amacher

et al. (37). In detail, the mathematical description includes two differential Equations that define the acceleration of fluid (1) and the acceleration of the rotor (2):

$$\frac{dQ}{dt} = \frac{1}{L}\left(H\left(Q(t), \omega(t)\right) - \left(p_{ds}(t) - p_{us}(t)\right)\right) \quad (1)$$

$$\frac{d\omega}{dt} = \frac{1}{\Theta}\left(-\left(Q\left(t\right), \omega\left(t\right)\right) + k \cdot I(t)\right) \quad (2)$$

where Q, ω, and I are the flow-rate, the rotational speed and the current of the pump, respectively. p_{ds} and p_{us} are the pressures downstream and upstream of the pump, which correspond to the aortic and left ventricular pressures, respectively. L and Θ are the fluid inertance and the rotor inertia, while k is the torque-constant of the pump motor. H and T are matrices containing two-dimensional maps of the pressure across the pump and the hydraulic torque applied on the shaft. The values of the these parameters were retrieved from Amacher et al. (37).

Overview of PDD-ILC

The proposed PDD-ILC scheme for LVADs aims to provide an accurate reference tracking of predefined, therapy-oriented, PF profiles while it achieves physiological VAD response when preload changes are encountered. A schematic overview of the PDD-ILC structure is depicted in **Figure 1** and it can be divided into four main subsystems, namely, signal processing and feature extraction, reference PF trajectory generator, DD-ILC, and time-domain PD-controller.

Signal Processing and Feature Extraction

The function of the PDD-ILC is based on the LVP, specifically the end-diastolic (LV-EDP) value, and the PF. The acquisition of these variables is envisaged by integrating two pressure sensors into a tapered inflow cannula and exploiting the difference in the dynamic pressure component between the measuring ports to estimate the PF, as proposed by von Petersdorff-Campen et al. (43). However, in this *in-silico* study, the simulated signals were used instead and white noise was added in specified experiments to emulate a realistic sensor signal and challenge the PDD-ILC, as described in the section "Experiments for Performance evaluation." Both LVP and PF signals were low-pass filtered with a first-order filter with cut-off frequency of 25 Hz.

The extraction of the LV-EDP and left ventricular systolic pressure (LV-SP) from the entire time sequence of the LVP was based on the work of Petrou et al. (34). In detail, the LVP was further low-pass filtered with a second-order filter with a cut-off frequency of 8 Hz. From the timeseries data, the indices of the local maxima corresponding to the LV-SP were extracted and the heartbeat was defined as the interval between two consecutive LV-SP indices (**Figure 2A**). As it is shown in **Figure 2A**, for each heartbeat, the local minima of the LVP as well as the points of inflection, where the curvature changed from concave to convex, were identified as possible LV-EDP candidates. From the inflection points, only the points where the first derivative of the LVP was below a certain threshold (here 40 mmHg/s) were qualified as possible LV-EDP candidates. From all candidates, the one closest to the LV-SP index was identified as LV-EDP.

Although this approach is accurate, the changes in the LVP waveform due to the in-cycle speed modulation of the cfVAD can increase the LV-EDP misdetections. To address this, an extension for the LV-EDP extraction process was developed in this work. Specifically, as it can be seen in **Figure 2**, the LV-EDP values identified in the last three heartbeats are used to estimate through linear regression the LV-EDP value of the new heartbeat. The LV-EDP identified for the new heartbeat is compared with the estimate and if it lies within predefined boundaries (here $\pm$ 1 mmHg) it is extracted as the LV-EDP. When the identified LV-EDP lies outside the boundaries (**Figure 2C**), it is considered an outlier and the mean LV-EDP value of the last three heartbeats is extracted as LV-EDP of the new cycle. The latter value is used along with the LV-EDP of the previous two heartbeats for the estimation of the LV-EDP of the next heartbeat. The outlier is saved in memory and if three consecutive outliers have been identified, a flag is created that the LV-EDP has indeed changed significantly and the new LV-EDP estimate is projected from these three outliers (**Figure 2C**). The latter step is incorporated to ensure that rapid changes in the LV-EDP are not obscured.

Reference Pump Flow Trajectory Generator

In this work, reference PF trajectories were used to modulate the pump speed since they provide more intuitive control of the hemodynamics and the interactions between the cfVAD and the CVS, (40, 44) while at the same time, they are highly transferable to different cfVAD designs when a sufficiently accurate tracking performance is guaranteed. The generation of these trajectories followed a two-step approach. As a first step, the Frank-Starling mechanism was imitated to obtain a physiological preload response of the cfVAD. More precisely, the LV-EDP extracted at each heartbeat was used as a surrogate of the preload (EDP_{LV}) and, by assuming that the flow from the aortic valve is negligible and the PF approximates the cardiac output (CO), the linear part of the starling-relationship between the LV-EDP and the CO was used to provide the necessary average PF ($\bar{q}^*_{bp}$) as follows:

$$\bar{q}^*_{bp} = q_{bp,\,ref} + k_{Fs}(EDP_{LV} - EDP_{LV,ref}) \quad (3)$$

Here $q_{bp,\,ref}$ and $EDP_{LV,ref}$ are reference values for the PF and LV-EDP, respectively, identified from the healthy heart at rest conditions and a CO of 5 L/min during calibration. The parameter k_{Fs} denotes the preload sensitivity which can be selected by the clinician. This ability to directly select the preload sensitivity is paramount to achieve a patient-specific response of the controller and constitutes a major advantage compared to speed-based controllers, where the control gain needs to be tuned to reach a satisfying preload sensitivity.

The second step to obtain the reference PF trajectories was to incorporate an in-cycle pulsatile profile that enables the accomplishment of treatment-based objectives selected by the clinician. These pulsatile trajectories were based on trapezoidal profiles, wherein the minimum PF was selected to be $q^*_{bp,min} = 20\ mL/s$ to provide a safety margin against backflow, and the

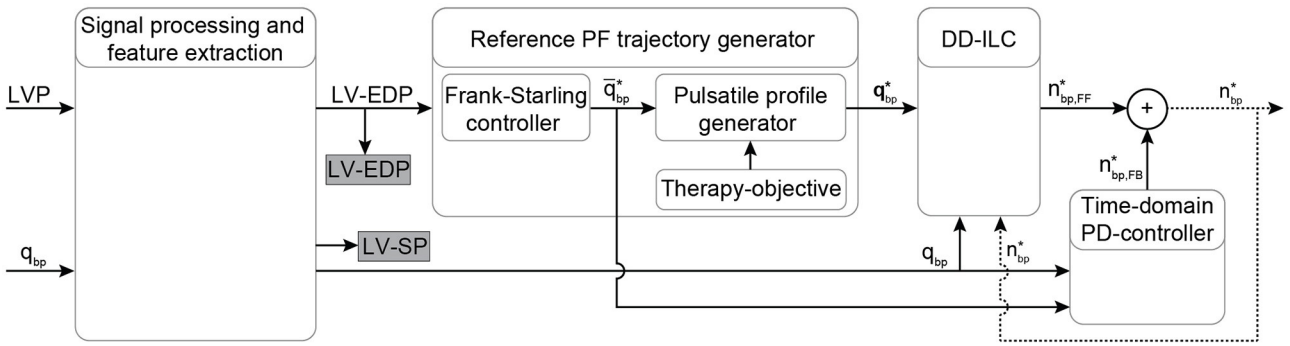

FIGURE 1 | Schematic overview of the physiological data-driven iterative learning controller. The input signals LVP and PF are filtered and the EDP and SP indices are extracted from the LVP. Based on the Frank-starling mechanism, the desired average PF is calculated based on the LV-EDP that is used as a preload surrogate, and the reference pulsatile PF trajectory is obtained based on the objectives of the therapy. A data-driven iterative learning controller is implemented to achieve accurate tracking of the reference PF without requiring modeling of the CVS or the pump. Finally, a proportional-derivative (PD) controller is coupled coupled to enable feedback in the time-domain. The desired pump speed is the output of the controller. Bold letters define vectors. LVP, left ventricular pressure; EDP, end-diastolic pressure; SP, systolic pressure; PF, pump flow; q_{bp}, measured pump flow; $\bar{q}^*_{bp}$, heart cycle average pump flow; $\boldsymbol{q}^*_{\boldsymbol{bp}}$, time vector of the desired pump flow trajectory; $n^*_{bp,FF}$, feed forward desired pump speed; $n^*_{bp,FB}$, feedback desired pump speed; n^*_{bp}, desired pump speed output.

maximum PF was calculated based on the $q^*_{bp,min}$ and the necessary average PF provided by the starling-relation ($\bar{q}^*_{bp}$). For each trajectory, the minimum flow was applied for 30% of the cardiac cycle, the maximum flow for 50% of the cardiac cycle, while each transition phase had a duration of 10% of the cardiac cycle. This proportion was chosen to prevent short spikes of desired maximum flow, since such trajectories could not be tracked using cfVADs and would be susceptible to high blood damage. For the pulsatile trajectories, various phase shifts (45) with respect to the onset of cardiac cycle can be applied to achieve different concurrent objectives; however, in this work, only copulsation and counterpulsation trajectories were investigated to achieve maximization of the aortic pulse pressure and minimization of LVSW, respectively, as proposed by Ising et al. (44). The maximum PF was applied during the entire systole for the copulsation trajectory, whereas for the counterpulsation trajectory the maximum PF was applied during diastole. In **Figure 3** the reference PF trajectories for an average PF of 85 mL/s are depicted.

Data-Driven Iterative Learning Controller

To achieve the desired response of the PDD-ILC, accurate reference tracking of the PF trajectory is required. Considering the repeating disturbances applied on the cfVAD in each cardiac cycle by the changes in the head pressure (difference between pressure at the outlet and pressure at the inlet of the cfVAD) from the remaining heart function, as well as the periodic changes in the preload, ILC schemes are suitable for reference trajectory tracking. More precisely, in repetitive process, ILC strategies can exploit the knowledge obtained in previous iterations to produce a feed-forward control input that progressively enhances the tracking performance. In this study, the DD-ILC was developed based on the approach proposed by Chi et al. (46) wherein a pseudo partial derivative (PPD) computed from the input and output signals serves as system model in the iteration domain, where one iteration stands for one heartbeat. The model is then used in a quadratic optimization procedure to minimize a cost function subject to input and output constraints.

The implementation of the DD-ILC is illustrated in **Figure 4**. Initially, a memory block is incorporated to store the per-cycle vectors of the pump speed setpoint $\boldsymbol{n}^*_{bp}$ and the PF $\boldsymbol{q}_{bp}$, with varying number of samples N:

$$\boldsymbol{n}^*_{bp,j} = [n^*_{bp,j}(0), n^*_{bp,j}(1), \ldots, n^*_{bp,j}(N-1), n^*_{bp,j}(N)] \quad (4)$$

$$\boldsymbol{q}_{bp,j} = [q_{bp,j}(0), q_{bp,j}(1), \ldots, q_{bp,j}(N-1), q_{bp,j}(N)] \quad (5)$$

These vectors contain the information of the entire time sequences of the previous cycles (iterations). They are used to obtain a representation of the CVS and the cfVAD system in the iteration domain through dynamic linearization. Specifically, the dynamic linearization model is based on the identification of the PPD Φ_j by relating the difference in the output signal $\boldsymbol{q}_{bp}$ and the input signal $\boldsymbol{n}^*_{bp}$ between consecutive iterations:

$$\Delta \boldsymbol{q}_{bp,j} = \Phi_j \Delta \boldsymbol{n}^*_{bp,j}$$
$$\textit{with} \qquad \Delta \boldsymbol{q}_{bp,j} = \boldsymbol{q}_{bp,j} - \boldsymbol{q}_{bp,j-1}, \quad \Delta \boldsymbol{n}^*_{bp,j} = \boldsymbol{n}^*_{bp,j} - \boldsymbol{n}^*_{bp,j-1} \quad (6)$$

where j denotes the iteration index. Since the system is causal, Φ_j is a lower triangular matrix. To compute an estimate of the PPD, denoted as $\hat{\Phi}_j$, the update formula described by Chi et al. (46) was used:

$$\hat{\varphi}^t_{j+1} = \hat{\varphi}^t_j + \frac{\eta(\Delta \boldsymbol{q}_{bp,j}(k+1) - \hat{\varphi}^t_j \Delta \boldsymbol{n}^*_{bp,j}(k)) \Delta \boldsymbol{n}^{*T}_{bp,j}(k)}{\mu + \left\| \Delta \boldsymbol{n}^*_{bp,j}(k) \right\|^2} \quad (7)$$

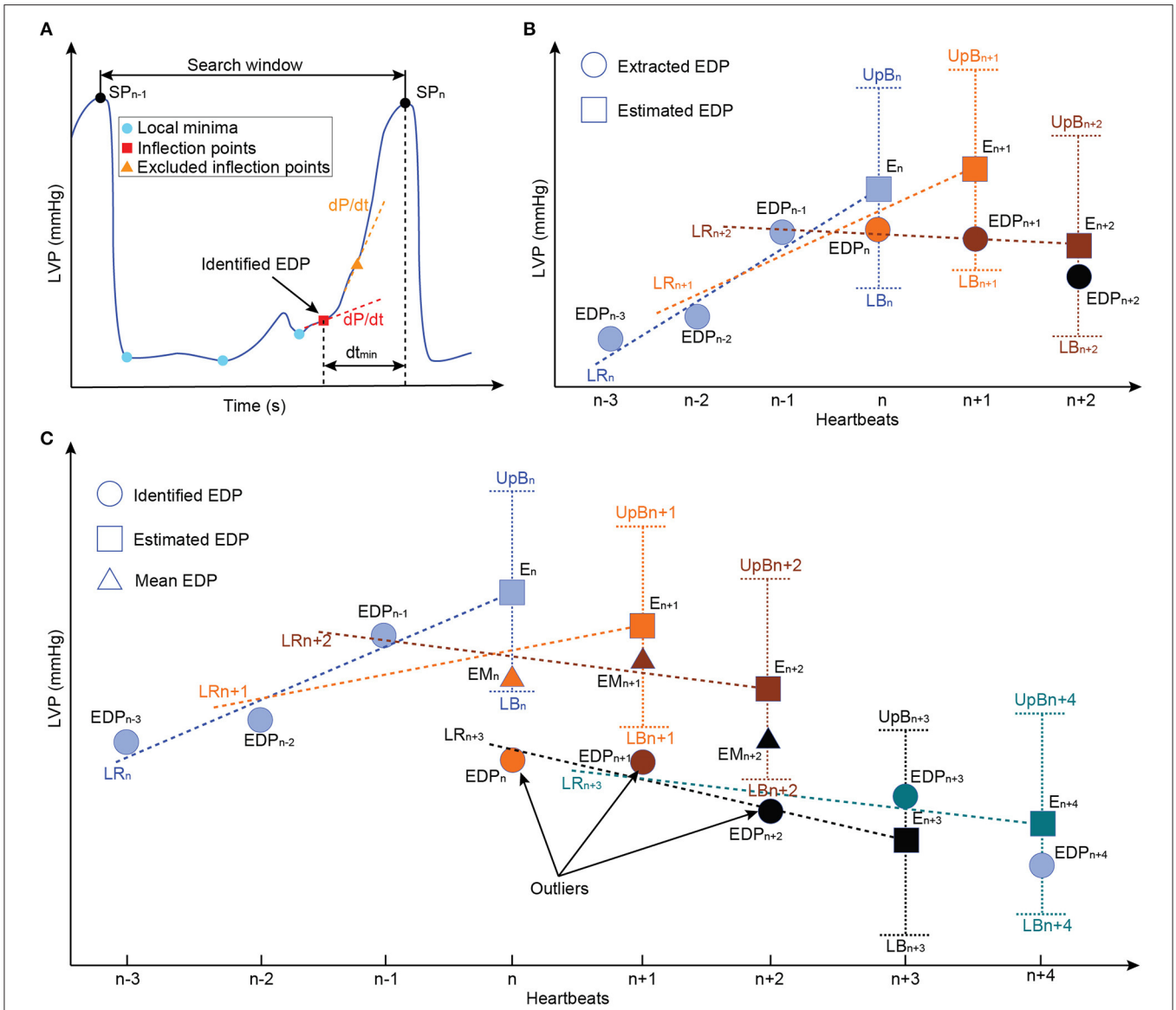

FIGURE 2 | Schematic representation of the LV-EDP extraction process and the extension for the minimization of misdetections. **(A)** Identification of all local minima (cyan circles) and inflection points (red rectangles) as LV-EDP candidates. The inflection points with large first LVP derivative (dLVP/dt > 40 mmHg/s) are excluded and the candidate with the smaller distance from the SP index (dt_{min}) is identified as the LV-EDP. **(B)** Comparison of the identified LV-EDP (filled circles) with the LV-EDP estimated (filled rectangles) based on linear regression of the LV-EDP extracted on the previous three heartbeats. If the identified LV-EDP is within the boundaries, it is extracted as LV-EDP value. **(C)** Based on the comparison described in b, if the identified LV-EDP is outside the boundaries it is considered an outlier and the mean value of the last three LV-EDPs is extracted as LV-EDP (filled triangles) of the investigated heartbeat. The outliers are stored in memory and if three consecutive identified LV-EDPs constitute outliners a flag is raised and the new LV-EDP estimate is based on the outliers (LR_{n+3}) instead of the extracted LV-EDPs. In this way, physiological rapid changes in preload are not obscured. LVP, left ventricular pressure; EDP, end-diastolic pressure; LR, linear regression; EM, extracted mean value; E, extracted; UpB, upper boundary; LB, lower boundary.

where $\hat{\varphi}_{j+1}^{t}$ denotes the nonzero vector of the $(t+1)^{th}$ row of $\hat{\Phi}_{j+1}$. Accordingly, $\boldsymbol{n}_{bp,j}^{*}(k)$ contains the PF setpoints at iteration j up to time index k and based on Equation (4) is a varying dimension vector with k elements. The learning process can be tuned by selecting the normalization value μ and the learning gain η. The values of the later parameters were identified through the controller gain optimization described in section "Optimization of Controller Parameters".

For the first iteration, the initial values for the pump speed setpoint, the PF and the PPD required from the algorithm were selected as:

$$\hat{\Phi}_0 = 10^{-4}\begin{pmatrix} 1\,0\ldots 0 \\ 1\,1\ldots 0 \\ \vdots\ \ddots\ \ddots\ 0 \\ 1\,1\ \ldots\ 1 \end{pmatrix},\ \mathbf{n}^*_{bp,0} = \begin{pmatrix} 0 \\ 0 \\ \vdots \\ 0 \end{pmatrix},\ q^*_{bp,0} = \begin{pmatrix} 0 \\ 0 \\ \vdots \\ 0 \end{pmatrix} \quad (8)$$

Hence, no model knowledge is required to initialize the controller. None of the previously converged solutions were used in the initialization procedure, and no model knowledge was included.

As a next step, the estimated PPD is used in a quadratic optimization problem to minimize the predicted PF tracking error under actuator constraints. The cost function in this optimization problem comprises two terms, namely the predicted PF tracking error (J_q) and the change in the input vector (J_u). The J_u cost component provides robustness against undesirably high changes in the pump speed setpoint during the transient behavior of the learning algorithm. The predicted PF tracking error to be minimized is described as:

$$\boldsymbol{e}_j = \boldsymbol{q}^*_{bp,j+1} - \hat{\boldsymbol{q}}^*_{bp,j+1} \quad (9)$$

where $\hat{\boldsymbol{q}}^*_{bp,j+1}$ denotes the predicted PF at cycle $j+1$ using the updated PPD given by:

$$\hat{\boldsymbol{q}}^*_{bp,j+1} = \hat{\boldsymbol{q}}^*_{bp,j} + \hat{\Phi}_{j+1}\,\Delta\boldsymbol{n}^*_{bp,j} \quad (10)$$

Hence, by combining the two cost components, the cost function can be written as:

$$J_{j+1} = J_{q,j+1} + J_{u,j+1} = \boldsymbol{e}_j^T\boldsymbol{Q}\,\boldsymbol{e}_j + \Delta\boldsymbol{n}^{*T}_{bp,j+1}\boldsymbol{R}\Delta\boldsymbol{n}^*_{bp,j+1} \quad (11)$$

where $\boldsymbol{Q}$ and $\boldsymbol{R}$ are positive definite weighting matrices that, in this work, are identified during the controller gain optimization described in section "Optimization of Controller Parameters".

Additionally, to avoid unrealistic pump speed setpoints, the pump speed is constrained between a minimum and maximum value defined based on the pump design. Hence, the final optimization problem can be written as:

$$min_{\Delta\boldsymbol{n}^*_{bp,j+1}}\ (J_{j+1}) \quad (12)$$

$$s.t.\quad \Delta\boldsymbol{n}^*_{bp,j+1} \geq \boldsymbol{n}_{bp,min} - \boldsymbol{n}^*_{bp,j} \quad (13)$$

$$\Delta\boldsymbol{n}^*_{bp,j+1} \leq \boldsymbol{n}_{bp,max} - \boldsymbol{n}^*_{bp,j} \quad (14)$$

The optimization problem is solved using the quadprog function provided by MATLAB R2020b (The MathWorks Inc., Natick, MA, USA). The optimized change in the pump speed setpoint vector is added to the speed setpoint vector of the previous iteration to provide the new control input vector as:

$$\boldsymbol{n}_{bp,j+1} = \boldsymbol{n}_{bp,j} + \Delta\boldsymbol{n}^*_{bp,j+1} \quad (15)$$

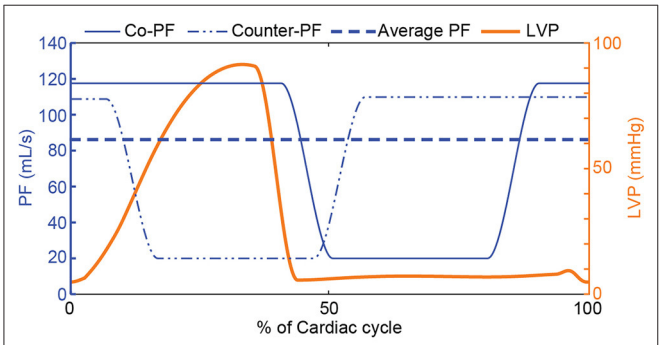

FIGURE 3 | Reference PF trajectories that incorporate a physiological response to preload changes based on the Frank-Starling mechanism and therapy-oriented pulsatile PF profiles. A copulsation and a counterpulsation PF trajectory along with the LVP for one cardiac cycle are depicted. For both PF trajectories, the minimum PF is $q^*_{bp,min} = 20\ mL/s$ and the maximum PF is calculated based on the $q^*_{bp,min}$ and the necessary average PF provided by the starling-relation ($\bar{q}^*_{bp}$). PF, pump flow; LVP, left ventricular pressure; Co-PF, copulsation pump flow; Counter-PF, counterpulsation pump flow.

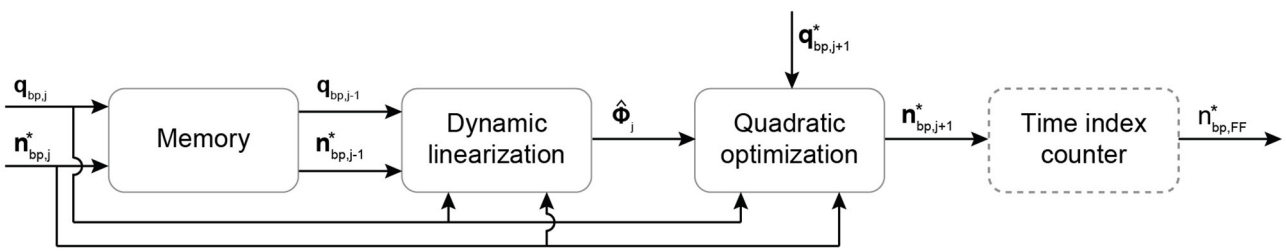

FIGURE 4 | Schematic overview of the DD-ILC algorithm. The pump speed setpoint and the PF are stored in a memory block. Then, they are used at the beginning of each cycle to update the system model through dynamic linearization. The model is used in a quadratic optimization problem to minimize the PF tracking error under pump speed constraints. The time index counter operates continuously to extract and output the feedforward pump speed setpoint at every time step within an iteration. Bold letters define vectors. $\boldsymbol{n}^*_{bp,j}$, pump speed setpoint vector of the j^{th} cycle; $\boldsymbol{q}_{bp,j}$, measured PF vector of the j^{th} *cycle;* $\hat{\boldsymbol{\Phi}}_j$, pseudo partial derivative denoting the linearized system model; $\boldsymbol{q}^*_{bp,j+1}$, PF reference trajectory; $n^*_{bp,FF}$, feedforward pump speed setpoint in the time domain.

Finally, since the dynamic linearization and the quadratic optimization are executed only at the beginning of each cycle, an additional module that operates at the full control frequency extracts the feedforward pump speed setpoint $n^*_{bp,FF}$ at every time index.

Time-Domain Proportional-Derivative Controller

The DD-ILC incorporates feedback in the iteration domain; however, it is a feedforward controller in the time domain. Therefore, an additional PD controller that operates in parallel to the DD-ILC is introduced (**Figure 1**). The PD controller showed to deteriorate the convergence speed of the DD-ILC during transient phases. However, it restricts the tracking error to become unbounded when the desired average PF changes rapidly due to changes in LV EDP. Hence, to exploit the latter characteristic without compromising convergence, the time domain PD controller is only activated if the desired average PF changes by at least 1 mL/s and, therefore, it is described as:

$$n^*_{bp,FB}(k) = \begin{cases} k_p\left(q^*_{bp}(k) - q_{bp}(k)\right) + k_d\frac{d\left(q^*_{bp}(k) - q_{bp}(k)\right)}{dk} & if \ \left|\bar{q}^*_{bp,j+1} - \bar{q}^*_{bp,j}\right| \geq 1 \\ 0 & Otherwise \end{cases} \tag{16}$$

Finally, by incorporating the feedback in the iteration domain provided by the DD-ILC and the feedback in the time domain provided by the PD controller, the pump speed setpoint at time index k is given by:

$$n^*_{bp}(k) = n^*_{bp,FF}(k) + n^*_{bp,FB}(k) \tag{17}$$

Physiological Flow PID Controller

A PID controller was also developed to achieve PF tracking and it was used to further evaluate the performance of the PDD-ILC. This controller uses the LVP and the PF to regulate the pump speed and achieve a physiological response to preload changes while it tracks specific PF profiles. The signal processing and feature extraction blocks, as well as the flow trajectory generator are the same as described for the PDD-ILC. As it can been seen in **Figure 5**, a time index counter is used after the flow trajectory generator to extract the feedforward PF setpoint at every time step. The measured PF is compared with the PF setpoint and the error is used as feedback to the PID controller. The output of the PID controller corresponds to the desired change in the pump speed. This change is added to a pump speed constant and the desired pump speed is defined. The pump speed is not constrained between a minimum and maximum value as in the PDD-ILC, however, the step-change in pump speed is constraint to 2,500 rotations per minute.

Experiments for Performance Evaluation

The assessment of the PDD-ILC was based on *in-silico* experiments that simulate a pathologic CVS supported by a cfVAD, using the numerical models described in sections "Cardiovascular System Model" and "Numerical Models of Blood Pumps". Additionally, to allow a detailed evaluation, several clinical conditions and everyday scenarios emulating resting (Exp0), preload variations (Exp1), afterload variations (Exp2), sleep-to-wake (Exp3), contractility variations (Exp4) as well as rest-to-exercise (Exp5), were tested with the PDD-ILC regulating the cfVAD speed. The parameters of the CVS, as well as the specific values used to simulate the aforementioned conditions are based on the experimental procedure described by Petrou et al. (19) and they are given in **Supplementary Tables S1–S3** of the supplementary material. To test the robustness of the PDD-ILC when real measured signals are used instead of the simulated ones, all experiments were repeated with white noise with a variance of 0.86 $mmHg^2$ (Exp0n−5n) and 1.72 $mmHg^2$ (Exp0nn−5nn) on the LVP or/and a variance of 0.86 $(mL/s)^2$ (Exp0n−5n) and 1.72 $(mL/s)^2$ (Exp0nn−5nn) PF signals.

To benchmark the performance of the proposed PDD-ILC in comparison to the state of the art, the same experiments have been conducted with a simulated healthy heart (HH), wherein the contractility parameter was set to 1, a constant speed controller (CS), and the developed PF-PIDC. All experiments were executed on MATLAB/Simulink R2020b (The MathWorks Inc., Natick, MA, USA) for 200 s.

Optimization of Controller Parameters

The performance of the PDD-ILC, as well as the PF-PIDC, is highly dependent on the selection of the control parameters. Although for PID controllers the Ziegler-Nichols approach (47) is most commonly used to fine-tune their parameters (K_P, K_I, K_D), its applicability to non-linear, time-variant systems, such as the CVS system, is prohibited. For the developed PDD-ILC, which includes six control parameters (μ, η, Q, R, k_p, k_d), there is no intuitive method to fine-tune these parameters.

In this work, the genetic algorithm-based optimization framework (GAOF) described by Magkoutas et al. (48) was used to obtain a set of optimal parameters for each controller. In this framework, the user defines the VAD control structure, the numerical model of the CVS coupled with the numerical model of the selected VAD, the objective function (OF) to be evaluated, the experiments for the evaluation of the OF, and the genetic algorithm (GA) parameters. During the execution, each individual, defined as a set of control parameters, is fed to the controller and the numerical model of the VAD-supported heart is simulated. The simulation results are used for the evaluation of the OF and the obtained value is assigned to the respective individual as "score." As long as the convergence criterion of the optimization problem is not met and the maximum number of generations (each generation includes multiple individuals) is not achieved, the scores of the individuals are fed to the genetic algorithm. Based on those scores, the GA uses genetic operations, namely elitism, crossover, and mutation, to create new individuals for the next generation. The process continues for each individual and each generation until an optimum (or multiple) set of control parameters has been identified.

To enable the execution of the GAOF for the PDD-ILC and the PF-PIDC, the numerical model of the CVS and the cfVAD described in sections "Cardiovascular System Model" and

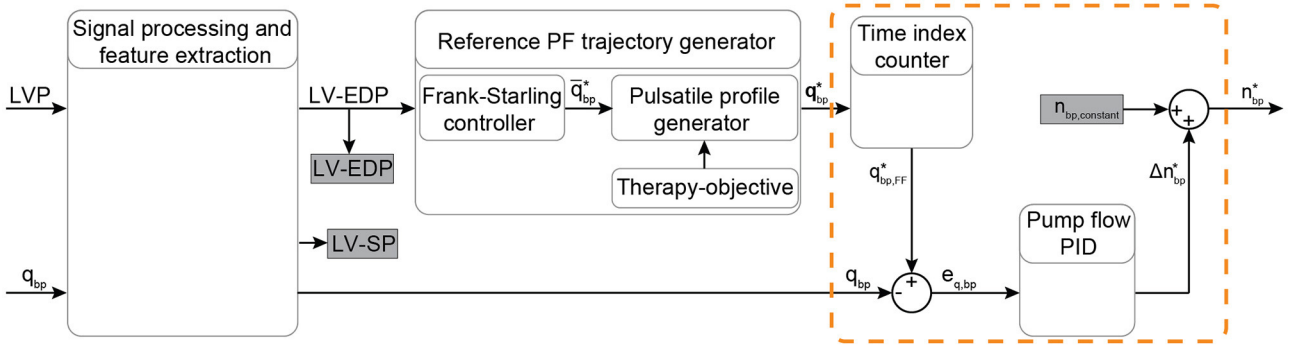

FIGURE 5 | Schematic overview of the physiological flow PID controller. The input signals LVP and PF are filtered and the EDP and SP indices are extracted from the LVP. Based on the Frank-Starling mechanism, the average PF is calculated based on the LV-EDP that is used as a preload surrogate, and the reference pulsatile PF trajectory is obtained based on the objectives of the therapy. A time index counter operates continuously to extract and output the feedforward PF setpoint at every time step. A PID flow controller (included in the orange dashed-line box) provides the necessary change in the pump speed setpoint based on the error between the measured and the desired PF. The desired pump speed is the output of the controller. Bold letters define vectors. LVP, left ventricular pressure; EDP, end-diastolic pressure; SP, systolic pressure; PF, pump flow; PID, proportional-integral-derivative; q_{bp}, measured pump flow; $\bar{q}^*_{bp}$, heart cycle average pump flow; $\boldsymbol{q}^*_{\boldsymbol{bp}}$, time vector of the desired pump flow trajectory; $q^*_{bp,FF}$, feed forward desired pump flow; $e_{q,bp}$, feedback error between the measured and the desired PF; Δn^*_{bp}, desired pump speed change; $n_{bp,constant}$, pump speed constant; n^*_{bp}, desired pump speed output.

"Numerical Models of Blood Pumps" were used. The contractility parameter of the CVS was set to 34% of the value described for the healthy heart, emulating a pathological circulation. The experiments Exp1–Exp5 described in section "Experiments for Performance Evaluation" were used for the evaluation of the OF.

For each controller, a two-objective optimization problem was defined, aiming to minimize the overall error in tracking the reference PF trajectory. For the first objective, the root-mean-square-error (RMSE) of the tracking error was initially calculated for each cardiac cycle by:

$$RMSE_j = \sqrt{\frac{\sum_{k=1}^{N}\left(q_{bp,j}(k) - q^*_{bp,j}(k)\right)^2}{N}} \tag{18}$$

where j denotes the index of the cardiac cycle, k denotes the time index and N the total number of time indices within the cardiac cycle j. As a next step, to ensure that only converged cycles are considered, the last 80 cycles of each experiment (m) were obtained and the mean value of *RMSE* was calculated as:

$$\overline{RMSE}_m = \sqrt{\frac{\sum_{j=0}^{80} RMSE_j}{80}} \tag{19}$$

Hence, the first objective function including the mean value of the *RMSE* for the six experiments was defined as:

$$J_1 = a_1\overline{RMSE}_1 + a_2\overline{RMSE}_2 + a_3\overline{RMSE}_3 + a_4\overline{RMSE}_4 + a_5\overline{RMSE}_5 + a_6\overline{RMSE}_6 \tag{20}$$

where $a_1 = 0.2$, $a_2 = 0.2, a_3 = 0.15, a_4 = 0.15, a_5 = 0.15$, and $a_6 = 0.15$ are weighting factors corresponding to experiments Exp1–6. The latter factors allow the experiments that account for a major fraction of the everyday life of a patient to have a greater influence on the value of the OF.

The second objective of the optimization problem was developed to evaluate the individuals regarding the convergence of the tracking error. Hence, the standard deviation of the *RMSE* in the last 80 cycles of each experiment (m) was calculated as:

$$\overline{std}_m = \sqrt{\frac{\sum_{j=1}^{80}\left(RMSE_j - \overline{RMSE}_m\right)^2}{80}} \tag{21}$$

Accounting the terms of all experiments and using the weighting factors described for J_1, the second objective function is defined as:

$$J_2 = a_1\overline{std}_1 + a_2\overline{std}_2 + a_3\overline{std}_3 + a_4\overline{std}_4 + a_5\overline{std}_5 + a_6\overline{std}_6 \tag{22}$$

To avoid unrealistic control parameters, their values were constrained between a minimum and a maximum value given in **Supplementary Table S4** in the **Supplementary Material**. Hence, the final optimization problem for the PDD-ILC was described as:

$$min_x(J_1(\boldsymbol{x}), J_2(\boldsymbol{x})) \tag{23}$$

$$s.t. \quad \mu_{min} \leq \mu \geq \mu_{max} \tag{24}$$

$$\eta_{min} \leq \eta \geq \eta_{max} \tag{25}$$

$$Q_{min} \leq Q \geq Q_{max} \tag{26}$$

$$R_{min} \leq R \geq R_{max} \quad (27)$$

$$k_{p,min} \leq k_p \geq k_{p,max} \quad (28)$$

$$k_{d,min} \leq k_d \geq k_{d,max} \quad (29)$$

where $\boldsymbol{x}$ denotes the set of control parameters (μ, η, Q, R, k_p, k_d). The optimization problem for the PF-PIDC, wherein the set of control parameters was $\mathbf{x} = (K_P, K_I, K_D)$, was described as:

$$min_x(\, J_1(\boldsymbol{x}), J_2(\boldsymbol{x})) \quad (30)$$

$$s.\,t. \quad K_{P,min} \leq K_P \geq K_{P,max} \quad (31)$$

$$K_{I,min} \leq K_I \geq K_{I,max} \quad (32)$$

$$K_{D,min} \leq K_D \geq K_{D,max} \quad (33)$$

where the minimum and maximum constraint values are given in **Supplementary Table S4** in the **Supplementary Material**.

The solution of the described two-objective optimization problem did not provide a single optimum solution, but a set of non-dominated solutions (pareto front) that were chosen as optimal if any of the objectives could not be improved without sacrificing the other objective. Hence, from the several individuals included in the pareto front of each controller, the final control parameters (**Table 1**) were selected after evaluating the overall performance of several sets of optimum parameters under the dynamic tests described in section "Experiments for Performance Evaluation".

For both controllers, the optimization problem was solved by using the multi-objective genetic algorithm provided in the global optimization toolbox of MATLAB. The default parameters of the genetic algorithm were applied for the genetic operations, while the initial population and the size of each generation was 500 individuals. The convergence criteria were met when for 15 consecutive generations any new individual was included in the pareto front, or when a maximum number of 50 generations was reached.

TABLE 1 | Optimized control parameters for PDD-ILC and flow PID controllers.

PDD-ILC		Flow PID	
μ	0.7315	K_P	401.23
η	0.7859	K_I	67.51
Q	120.7388	K_D	19.15
R	0.1365		
k_p	3.2155		
k_d	3.1926		

RESULTS

Trajectory Tracking and Convergence

The performance of the PDD-ILC and the PF-PIDC in tracking the PF reference trajectories was evaluated under all physiological conditions simulated with the experiments described in section "Experiments for Performance Evaluation" for copulsation and counterpulsation modes (**Figures 6–8**). In **Figure 6**, the tracking performance during rest conditions (Exp0, **Supplementary Table S1**, **Supplementary Material**) is shown for one cardiac cycle with both controllers being converged. When the copulsation mode is selected (**Figure 6A**), both controllers show excellent performance with the minimum and maximum PF values being achieved without overshoot and time delay. During the counterpulsation mode the tracking is accurate and without time delays in the transition phases (**Figure 6B**). However, the highly changing pressure conditions applied on the cfVAD during the contraction of the LV deteriorate the tracking performance in the region of low PF of both controllers.

In **Figure 7**, the RMSE calculated based on Equation (18) as well as the maximum instantaneous tracking error computed for each cardiac cycle are depicted for all physiological experiments (Ex0–5, **Supplementary Table S1**, **Supplementary Material**) under copulsation mode. During the rest-conditions experiment

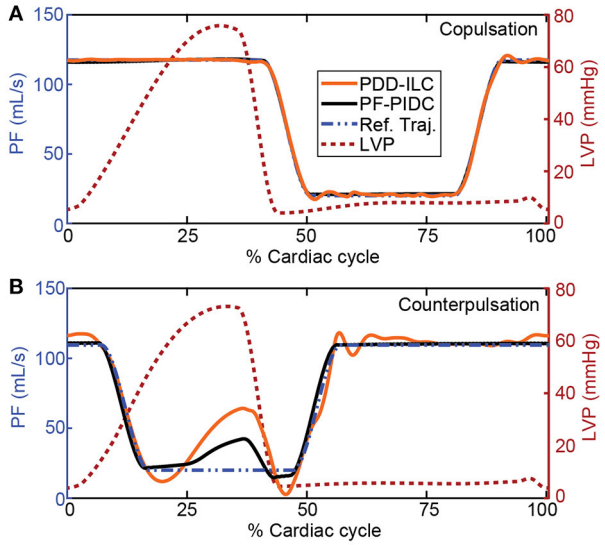

FIGURE 6 | Reference trajectory tracking performance of the PDD-ILC and the PF-PIDC during one cardiac cycle of the rest-conditions experiment (Exp0, **Supplementary Table S1**, **Supplementary Material**) under **(A)** copulsation and **(B)** counterpulsation. The reference trajectories, along with the left ventricular pressure profile that corresponds to the main source of disturbance are given for both modes. Both controllers are able to track accurately the reference trajectory during copulsation, reaching the maximum and minimum PF values without time lag. During the counterpulsation, the high disturbance of the fast change in LVP cannot be compensated completely from any of the controllers, however, the overall tracking is adequate. PDD-ILC, physiologic data-driven iterative learning controller; PF-PIDC, pump flow proportional-integral-derivative controller; Ref. Traj., reference trajectory; LVP, left ventricular pressure.

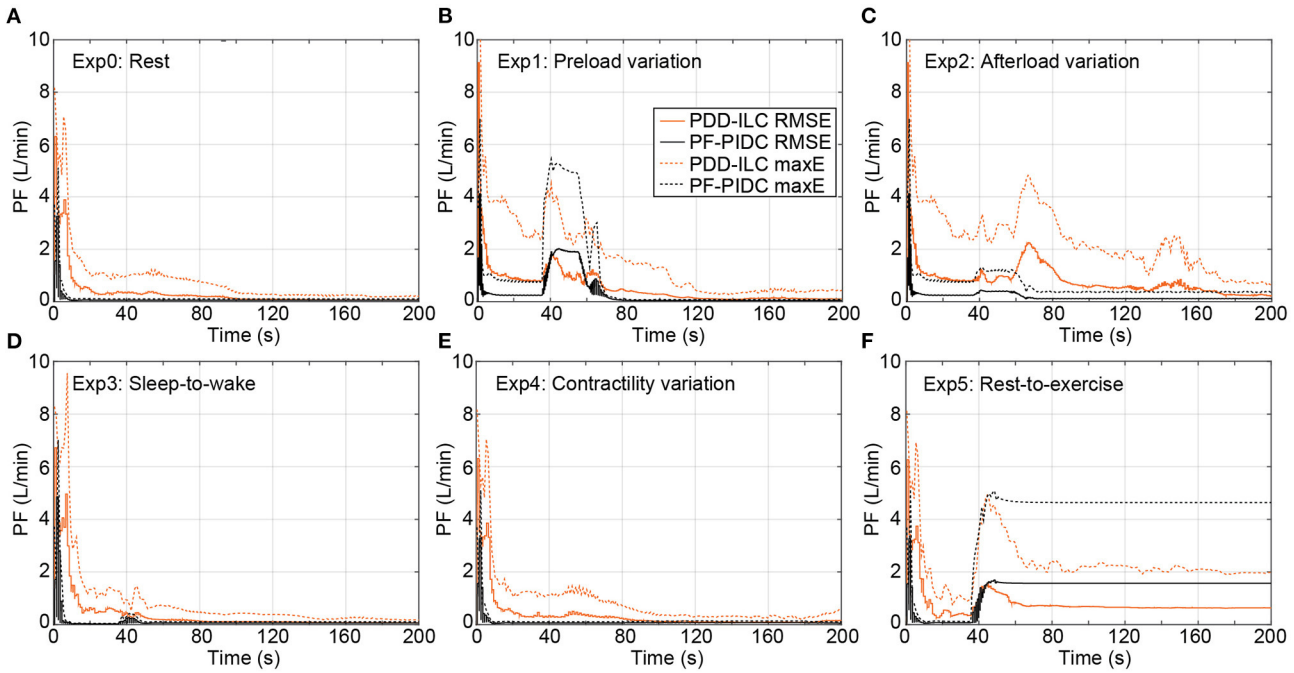

FIGURE 7 | Transient performance of the PDD-ILC and the PF-PIDC in terms of RMSE and maximum instantaneous error in tracking the reference trajectory under all physiological conditions and scenarios executed with the copulsation mode. **(A)** Rest-conditions (Exp0): The PDD-ILC converged after 100 iterations, obtaining an RMSE of 0.07 L min^{-1} and maximum error of 0.19 L min^{-1}. The PF-PIDC obtained an RMSE of 0.06 L min^{-1} and maximum error of 0.11 L min^{-1}. **(B)** Preload variation (Exp1): Last variation at 85 seconds. The converged RMSE and maximum error for the PDD-ILC was 0.07 L min^{-1} and 0.23 L min^{-1}, respectively. The RMSE and maximum error for the PF-PIDC was 0.05 L min^{-1} and 0.08 L min^{-1}, respectively. **(C)** Afterload variation (Exp2): Last variation at 85 seconds. The converged RMSE and maximum error for the PDD-ILC was 0.20 L min^{-1} and 0.73 L min^{-1}, respectively. The RMSE and maximum error for the PF-PIDC was 0.11 L min^{-1} and 0.38 L min^{-1}, respectively. **(D)** Sleep-to-wake (Exp3): Last variation at 85 seconds. The converged RMSE and maximum error for the PDD-ILC was 0.05 L min^{-1} and 0.21 L min^{-1}, respectively. The RMSE and maximum error for the PF-PIDC was 0.06 L min^{-1} and 0.11 L min^{-1}, respectively. **(E)** Contractility variation (Exp4): Last variation at 85 seconds. The converged RMSE and maximum error for the PDD-ILC was 0.05 L min^{-1} and 0.18 L min^{-1}, respectively. The RMSE and maximum error for the PF-PIDC was 0.06 L min^{-1} and 0.10 L min^{-1}, respectively. **(F)** Rest-to-exercise (Exp5): Last variation at 85 seconds. The converged RMSE and maximum error for the PDD-ILC was 0.68 L min^{-1} and 2.46 L min^{-1}, respectively. The RMSE and maximum error for the PF-PIDC was 1.56 L min^{-1} and 4.63 L min^{-1}, respectively. RMSE, root mean square error; maxE, maximum error; PDD-ILC, physiologic data-driven iterative learning controller; PF-PIDC, pump flow proportional-integral-derivative controller.

(Exp0), the PDD-ILC obtained an RMSE below 0.33 $L\ min^{-1}$ after 30 iterations and converged to 0.07 $L\ min^{-1}$ after 100 iterations (**Figure 7A**). Except for the initial 10 iterations, wherein the system was not settled, the maximum tracking error remained below 1.21 $L\ min^{-1}$ and reduced continuously to achieve 0.19 $L\ min^{-1}$ after convergence. During the same experimental conditions, the PF-PIDC obtained an RMSE of 0.06 $L\ min^{-1}$ and a maximum error of 0.11 $L\ min^{-1}$. During the preload variations (Exp1), the controllers showed an increase in both the RMSE and the maximum error during the transition phases of the experiment, however after the last transition (at about 75 s) both reached the error values achieved in Exp0, with the PDD-ILC converging in <60 iterations. As depicted in **Figure 7C**, the PF-PIDC showed a slightly increased RMSE of 0.24 $L\ min^{-1}$ during the afterload experiment (Exp2). In this setting, the PDD-ILC also presented higher RMSE and maximum error throughout the entire experiment, achieving an RMSE of 0.87 $L\ min^{-1}$at the end of the experiment. During the sleep-to-wake (Exp3) and contractility variation (Exp4) settings both controllers showed excellent tracking performance, resulting in RMSE and maximum error values similar to the rest-conditions experiment (**Figures 7D,E**). In **Figure 7F**, the tracking performance during the rest-to-exercise experiment is illustrated for both controllers. During this experiment, wherein the pump has to provide the major fraction of the CO, the RMSE obtained with the PF-PIDC remained at a level of 1.56 $L\ min^{-1}$, while the maximum error converged to 4.63 $L\ min^{-1}$. The PDD-ILC although showed a reduction in the tracking accuracy, it considerably outperformed the PF-PIDC. More precisely, the RMSE and the maximum error obtained by the PDD-ILC after convergence was 0.68 $L\ min^{-1}$ and 2.46 $L\ min^{-1}$, respectively.

The tracking performance of the controllers under counterpulsation mode is illustrated in **Figure 8** for the conducted simulations. During Exp0 (**Figure 8A**), the PF-PIDC reached an RMSE and maximum error of 0.42 $L\ min^{-1}$ and 1.32 $L\ min^{-1}$, respectively. In this setting, the PDD-ILC required 50 iterations to converge at an RMSE and maximum error of 0.88 $L\ min^{-1}$ and 2.64 $L\ min^{-1}$, although it obtained similar error values already after the thirtieth iteration. During Exp1 (**Figure 8B**), Exp3 (**Figure 8D**), and Exp4 (**Figure 8E**) both

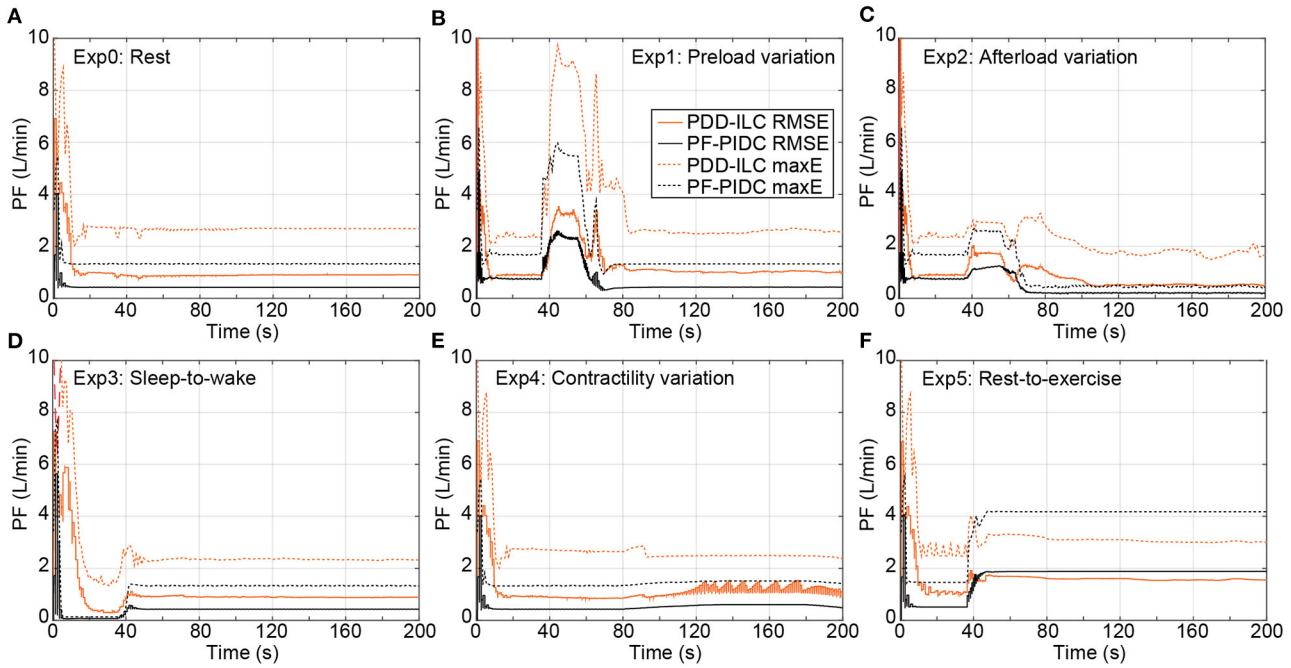

FIGURE 8 | Transient performance of the PDD-ILC and the PF-PIDC in terms of RMSE and maximum instantaneous error in tracking the reference trajectory under all physiological conditions and scenarios executed with the counterpulsation mode selected. **(A)** Rest-conditions (Exp0): The PDD-ILC converged after 50 iterations, obtaining an RMSE of 0.88 $L\ min^{-1}$ and maximum error of 2.64 $L\ min^{-1}$. The PF-PIDC obtained an RMSE of 0.42 $L\ min^{-1}$ and maximum error of 1.32 $L\ min^{-1}$. **(B)** Preload variation (Exp1): Last variation at 85 seconds. The converged RMSE and maximum error for the PDD-ILC was 0.94 $L\ min^{-1}$ and 2.60 $L\ min^{-1}$, respectively. The RMSE and maximum error for the PF-PIDC was 0.43 $L\ min^{-1}$ and 1.32 $L\ min^{-1}$, respectively. **(C)** Afterload variation (Exp2): Last variation at 85 seconds. The converged RMSE and maximum error for the PDD-ILC was 0.50 $L\ min^{-1}$ and 1.67 $L\ min^{-1}$, respectively. The RMSE and maximum error for the PF-PIDC was 0.19 $L\ min^{-1}$ and 0.50 $L\ min^{-1}$, respectively. **(D)** Sleep-to-wake (Exp3): Last variation at 85 seconds. The converged RMSE and maximum error for the PDD-ILC was 0.90 $L\ min^{-1}$ and 2.30 $L\ min^{-1}$, respectively. The RMSE and maximum error for the PF-PIDC was 0.43 $L\ min^{-1}$ and 1.34 $L\ min^{-1}$, respectively. **(E)** Contractility variation (Exp4): Last variation at 85 seconds. The converged RMSE and maximum error for the PDD-ILC was 1.08 $L\ min^{-1}$ and 2.36 $L\ min^{-1}$, respectively. The RMSE and maximum error for the PF-PIDC was 0.48 $L\ min^{-1}$ and 1.41 $L\ min^{-1}$, respectively. **(F)** Rest-to-exercise (Exp5): Last variation at 85 seconds. The converged RMSE and maximum error for the PDD-ILC was 1.61 $L\ min^{-1}$ and 3.06 $L\ min^{-1}$, respectively. The RMSE and maximum error for the PF-PIDC was 1.88 $L\ min^{-1}$ and 4.18 $L\ min^{-1}$, respectively. RMSE, root mean square error; maxE, maximum error; PDD-ILC, physiologic data-driven iterative learning controller; PF-PIDC, pump flow proportional-integral-derivative controller.

controllers obtained tracking errors similar to those in Exp0 after convergence, however, the tracking error was increased during the transition phases of the experiments. During Exp2 both controllers converged to error values lower than Exp0 (**Figure 8C**). More precisely, the PDD-ILC converged to an RMSE and maximum error of 0.50 $L\ min^{-1}$ and 1.67 $L\ min^{-1}$ and the PF-PIDC to 0.19 $L\ min^{-1}$ and 0.50 $L\ min^{-1}$, respectively. Similar to the copulsation mode, during the rest-to-exercise experiment (Exp5), the tracking error was increased for both controllers. As it can be seen in **Figure 8F**, the PDD-ILC obtained an RMSE and maximum error of 1.61 $L\ min^{-1}$ and 3.06 $L\ min^{-1}$, outperforming the PF-PIDC that converged to 1.88 $L\ min^{-1}$ and 4.18 $L\ min^{-1}$, respectively.

The addition of noise in the simulated LVP and PF signals had infinitesimal effect on the reference trajectory tracking. In the **Supplementary Material**, the detailed results for white noise of 0.86 variance can be found in **Supplementary Figure S1** for all experiments under copulsation and **Supplementary Figure S2** under counterpulsation, while for white noise of 1.72 variance can be found in **Supplementary Figure S3** for all experiments under copulsation and **Supplementary Figure S4** under counterpulsation.

Ventricular Unloading, Pulsatility and Hemodynamic Response

In this study, the reference PF trajectories were obtained by using copulsation and counterpulsation as support modes, aiming to increase the pulsatility or reduce the LVSW, respectively. The influence of both modes on the LVSW is illustrated in **Figure 9** for the executed experiments and is compared with the LVSW produced by the simulated diseased heart (DH) and the DH supported with a cfVAD with a constant speed controller (CS). During the experiments Exp0 (**Figure 9A**), Exp3 (**Figure 9D**), Exp4 (**Figure 9E**), and Exp5 (**Figure 9F**), using copulsation mode, both the PDD-ILC and the PF-PIDC controller followed the LVSW values obtained with the CS controller. In the same experiments, under counterpulsation, both the PDD-ILC and the PF-PIDC controller reduced the LVSW by 54.3, 55.9, 69.8, and 24% compared to the CS support. During the preload variation

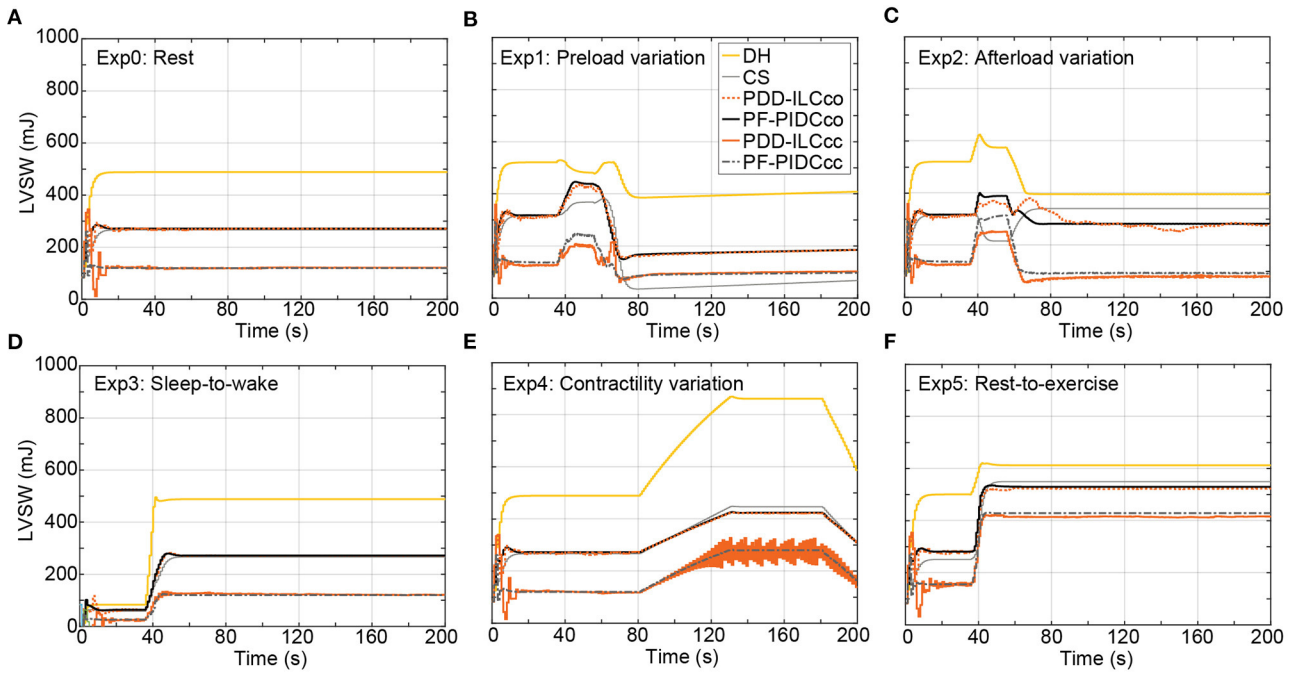

FIGURE 9 | Influence of the copulsation and counterpulsation modes on the left ventricular stroke work (LVSW) of the diseased heart (DH) during: **(A)** Rest-conditions (Exp0), **(B)** Preload variation (Exp1 **(C)** Afterload variation (Exp2) **(D)** Sleep-to-wake (Exp3) **(E)** Contractility variation (Exp4) **(F)** Rest-to-exercise (Exp5). DH, diseased heart; CS, constant speed control; PDD-ILCco, physiologic data-driven iterative learning controller copulsation; PF-PIDCco, pump flow proportional-integral-derivative controller copulsation; PDD-ILCcc, physiologic data-driven iterative learning controller counterpulsation; PF-PIDCcc, pump flow proportional-integral-derivative controller counterpulsation.

(**Figure 9B**), the PDD-ILC and the PF-PIDC controller showed similar responses, reducing the LVSW by 56% compared to the CS and by 57.2% compared to the copulsation modes. However, during the low preload conditions, applied after the last transition point of Exp1, the CS reduced the LVSW by 26.3% compared to the PDD-ILC and PF-PIDC controller under counterpulsation. As it can be seen in **Figure 9C**, during low afterload conditions (between 40 and 80 seconds), the PDD-ILC and the PF-PIDC controller under counterpulsation, as well as the CS controller, obtained similar LVSW values, while the copulsation modes resulted in 31.2% higher LVSW values. However, during the high afterload conditions in Exp 2 (after 80s in **Figure 9C**), the PDD-ILC and the PF-PIDC controller under counterpulsation resulted in 75.7 and 72.7%, respectively, compared to CS support. Overall, both the PDD-ILC and the PF-PIDC achieved the intended LVSW reduction during counterpulsation modes.

The influence of the copulsation and the counterpulsation modes on the pulsatility is evaluated based on the aortic pulse pressure (PP = systolic aortic pressure – diastolic aortic pressure) and is illustrated in **Figure 10** for all experiments. During Exp0 (**Figure 10A**) and Exp3 (**Figure 10D**) the CS diminishes significantly the pulsatility, obtaining a PP of only 10.1 mmHg. Both the PDD-ILC and the PF-PIDC under the counterpulsation mode increased the PP to 16.2 and 17.9 mmHg for Exp0 and Exp3, respectively, while under copulsation, the PDD-ILC and the PF-PIDC further increased the PP to 21.1 and 20.9 mmHg for Exp0 and Exp3, respectively. During the preload experiment (**Figure 10B**) and after the convergence of all controllers, the CS resulted in the lowest PP of 4.0 mmHg, the PDD-ILC resulted in 14.6 and 15.2 mmHg for counterpulsation and copulsation, respectively, while the PF-PIDC resulted in 9.4 and 11.6 mmHg for counterpulsation and copulsation. During the transition phases of the afterload experiment (**Figure 10C**), the CS reduced the PP to only 4.1 mmHg, however, the PDD-ILC resulted in significantly increased PP values of 8.4 and 18.7 mmHg with counterpulsation and copulsation, respectively. During the same settings, the PF-PIDC increased further the PP with respect to CS and PDD-ILC, achieving a PP of 13.8 and 29.9 mmHg under counterpulsation and copulsation, respectively. At high afterload conditions in Exp2 (after 110 s in **Figure 10C**), all controllers resulted in similar PP value of approximately 14.9 mmHg. During the Exp4 (**Figure 10E**) both the PDD-ILC and the PF-PIDC with copulsating mode resulted in PP of 19.8 mmHg, while the CS, as well as the PDD-ILC and the PF-PIDC under counterpulsation showed reduced pulsatility, obtaining a PP of 10.5, 20.0 and 18.9 mmHg, respectively. The PDD-ILC presented an oscillating PP when the contractility reached 17% of that of the HH. During the rest-to-exercise experiment (**Figure 10F**), the PDD-ILC with counterpulsation resulted in the lowest PP of 17.5 mmHg, while the CS and the PF-PIDC resulted in 19.5 and 19.1 mmHg. Under the same settings, the PID-controller and the PDD-ILC under

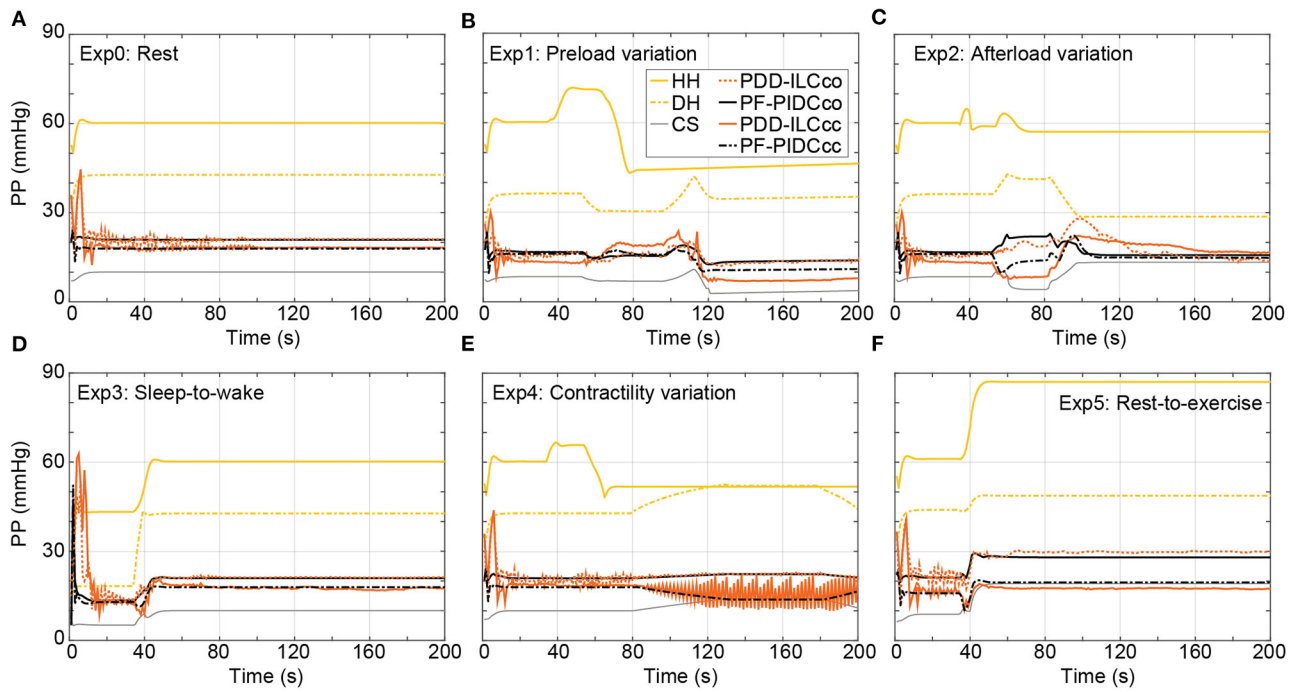

FIGURE 10 | Influence of the copulsation and counterpulsation modes on the aortic pulse pressure (PP) of the diseased heart (DH) during: **(A)** Rest-conditions (Exp0), **(B)** Preload variation (Exp1) **(C)** Afterload variation (Exp2) **(D)** Sleep-to-wake (Exp3) **(E)** Contractility variation (Exp4) **(F)** Rest-to-exercise (Exp5). HH, healthy heart; DH, diseased heart; CS, constant speed control; PF-PIDCco, pump flow proportional-integral-derivative controller copulsation; PDD-ILCcc, physiologic data-driven iterative learning controller counterpulsation; PF-PIDCcc, pump flow proportional-integral-derivative controller counterpulsation.

TABLE 2 | Preload and afterload sensitivity of the healthy heart (HH), the constant speed (CS) controller, the PDD-ILC, and the PF-PIDC calculated in experiments Exp1 and Exp2.

System	Preload (increase) ($L\ min^{-1}/mmHg$)	Preload (decrease) ($L\ min^{-1}/mmHg$)	Afterload (increase) ($L\ min^{-1}/mmHg$)	Afterload (decrease) ($L\ min^{-1}/mmHg$)
Healthy heart	0.502	0.481	−0.015	−0.016
CS controller	0.039	0.040	−0.046	−0.057
PDD-ILCco	0.496	0.466	−0.019	−0.024
PDD-ILCcc	0.177	0.386	−0.030	−0.030
PF-PIDCco	0.488	0.377	−0.018	−0.011
PF-PIDCcc	0.470	0.411	−0.026	−0.019

copulsation increased significantly the PP achieving 28.0 and 30.0 mmHg, respectively.

Preload and Afterload Sensitivity

The sensitivity of the developed controllers in preload and afterload changes was evaluated in Exp1 and Exp2, respectively, and it was compared with the sensitivities of the CS controller and the HH. Based on the equations given in **Supplementary Text T1** in the **Supplementary Material**, the end-diastolic LV pressure and the mean aortic pressure (MAP) were used as surrogates of the preload and the afterload, respectively, and a summary of all sensitivities is provided in **Table 2**. As it can be seen in **Table 2**, both the PDD-ILC and the PF-PIDC showed physiological sensitivities compared to the HH, while the CS support resulted in highly non-physiological sensitivities in all cases. More precisely, during preload increase the HH showed a sensitivity of 0.502 $L\ min^{-1}/mmHg$. The PDD-ILC in copulsation mode followed closely this value, resulting in 0.496 $L\ min^{-1}/mmHg$, while the PF-PIDC showed 0.488 $L\ min^{-1}/mmHg$ and 0.470 $L\ min^{-1}/mmHg$ under copulsation and counterpulsation, respectively. The PDD-ILC in counterpulsation mode had a lower preload sensitivity of 0.177 $L\ min^{-1}/mmHg$ and the CS showed a highly non-physiologic sensitivity of 0.039 $L\ min^{-1}/mmHg$. Similar to preload increase, during preload decrease the developed controllers followed closely the sensitivity of the HH, while the CS showed again a sensitivity of 0.040 $L\ min^{-1}/mmHg$. The sensitivity of the HH was −0.015 $L\ min^{-1}/mmHg$ and −0.016 $L\ min^{-1}/mmHg$

during afterload increase and decrease, respectively. The PDD-ILC in copulsation mode showed a sensitivity of -0.019 $L\ min^{-1}/mmHg$ and -0.024 $L\ min^{-1}/mmHg$ during afterload increase and decrease, while in counterpulsation showed high sensitivity values of $L\ min^{-1}/mmHg$ in all afterload changes. The PF-PIDC in copulsation and counterpulsation modes responded with a sensitivity of -0.018 $L\ min^{-1}/mmHg$ and -0.011 $L\ min^{-1}/mmHg$ to afterload increase, and with a sensitivity of -0.026 $Lmin^{-1}/mmHg$ and -0.019 $L\ min^{-1}/mmHg$ to afterload decrease. The CS controller showed more than three times higher afterload response that the HH, resulting in sensitivities of -0.046 $L\ min^{-1}/mmHg$ and -0.057 $L\ min^{-1}/mmHg$ to afterload increase and decrease, respectively.

DISCUSSION

In the current work, we presented a data-driven iterative learning physiological controller and a pump flow PID-controller that accurately track predefined pump flow trajectories, aiming to achieve physiological, pulsatile and treatment-driven response of cfVADs. A trajectory generator, which can be incorporated as a standalone block in other cfVAD control approaches, was also developed and by exploiting the LV-EDP it provided preload adaptive reference trajectories. In the case of the PDD-ILC, the reference PF trajectories were tracked by a model-free, data-driven ILC that used the time-sequences of LVP and PF to obtain a model. To the best of our knowledge, this is the first application of such a DD-ILC for cfVAD control. Both control approaches have been extensively tested in an *in-silico* environment under various physiological conditions, including rest, pre- and afterload variations, contractility variations, as well as everyday scenarios like sleep-to-wake and rest-to-exercise. Additionally, two treatment objectives were investigated, termed minimization of LVSW (counterpulsation) and maximization of pulsatility (copulsation). Under all experimental conditions, the PDD-ILC and the PF-PIDC demonstrated highly accurate tracking of the reference PF trajectories, outperforming existing model-based iterative ILC approaches, (40) while they also achieved the predefined treatment objectives and resulted in improved hemodynamics and preload sensitivities compared to a CS controller that is the current state-of-the-art in the clinical practice (**Table 2**) (49).

The reference trajectories constituted a critical component of the DD-IILPC and the PF-PIDC since they were responsible to provide preload adaptivity and incorporate the treatment objectives. To obtain preload adaptivity, the Frank-Starling mechanism was imitated by selecting the preload sensitivity of the controller in Equation (3). To our knowledge, this is the first time that the preload sensitivity can be directly selected based on clinical input, constituting a great improvement compared to CS controllers and speed-based controllers, where fine-tuning of the control gains is necessary to achieve adequate sensitivity (19, 34, 50). Based on the results in section "Preload and Afterload Sensitivity", the PDD-ILC and the PF-PIDC were able to follow the set value and provide preload sensitivities similar to the healthy heart, while the CS controller showed infinitesimal sensitivity. Hence, based on our approach, a patient-specific preload sensitivity is feasible for both controllers, offering new opportunities in cfVAD treatment management.

The treatment objectives incorporated in the reference trajectories were the minimization of LVSW and the maximization of pulsatility. To minimize the LVSW, a counterpulsating pump modulation with respect to the native heart has been applied as proposed in the literature (35, 37, 44). By accurately tracking the counterpulsation PF trajectories developed in section "Reference Pump Flow Trajectory Generator", the PDD-ILC and the PF-PIDC were able to substantially reduce the LVSW by more than 50% compared to the CS support in the majority of the investigated physiological conditions. This is important when treatment approaches for LV training are considered. To maximize the pulsatility, a copulsation trajectory was developed and tracked by the PDD-ILC and the PF-PIDC controller. During all physiological conditions studied, both controllers increased drastically the PP compared to the CS support. These results agree with the literature (35, 37, 44) and, consequently, they can be implemented to enhance the pulsatility and investigate its effects and its necessity on cfVAD supported patients. It is important to mention that the effectiveness of our pipeline in reducing the LVSW and increasing the PP is mainly dependent on the developed PF reference trajectories. The difference in LVSW reduction and PP increase between the PDD-ILC and the PFPIDC are a result of their slightly different tracking performance. By exploiting the accurate trajectory tracking achieved from both the PDD-ILC and the PF-PIDC, various phase shifts can be investigated to deduce a better understanding of the interactions between the cfVAD and the native heart to improve the treatment of heart failure patients.

The tracking performance of the DD-ILC and the PF-PIDC was excellent for the copulsation mode, regardless of the physiological conditions applied and the rapid changes in the hemodynamics and the heartbeat. During the counterpulsation, both controllers demonstrated lower tracking accuracy in all experiments compared to the copulsation. However, they significantly outperformed existing ILC approaches (40). The inferior tracking performance of the controllers under counterpulsation can be attributed to two reasons. Firstly, during the counterpulsation, a rapid change of head pressure is applied on the pump from the heart contraction, which cannot be counteracted by the slower dynamic response of the pump. Secondly, the controller parameters were optimized for the copulsation mode, hence better tracking performance during counterpulsation could be achieved with the further optimization of the control parameters.

The control parameters have a strong influence on the stability and the tracking performance of both the PDD-ILC and the PF-PIDC; hence, their selection is of high importance. In this work, we implemented the genetic-algorithm-based optimization framework proposed by Magkoutas et al. (48) to obtain the optimum parameter sets for our control approaches. By using the latter optimization framework, intuitive tuning of the control parameters can be achieved based on the selection of the objective

functions to be minimized. Hence, by exploiting the GAOF, the gains of the PDD-ILC and the PF-PIDC controller can be further optimized to facilitate patient-specific treatment goals and, consequently, enhance the prognosis of cfVAD supported patients. However, it has to be mentioned that, depending on the selected objective functions and the experiments in the optimization process, the development phase of the controller can be prolonged since the completion of the optimization might take up to 20 days.

Although the superiority of the PDD-ILC and the PF-PIDC over the CS controller with respect to hemodynamics and pre- and afterload sensitivities has been demonstrated, the proposed control approaches have also limitations. The development of the reference trajectories assumes negligible flow through the aortic valve, however, when a phase shift between the pump pulsation and the native heart has to be incorporated in the reference trajectory (e.g., counterpulsation) the assumption of negligible flow through the aortic valve is violated. This affects the development of a feasible PF trajectory. Additionally, the assumption of negligible aortic valve flow results in reference trajectories that aim to achieve the necessary CO only through the cfVAD operation. Consequently, the flow through the aortic valve is minimized and the risk of aortic valve insufficiency increases. Although such pathological consequences were not within the scope of this study, to ameliorate the risk of aortic valve insufficiency we envisage the addition of a support level parameter to manipulate the percentage of the CO delivered by the pump and the CO expected from the remaining contraction of the native heart.

The excellent tracking performance of both the PDD-ILC and the PF-PIDC necessitates the accurate measurement of LVP and PF signals. We are aware that no reliable, long-term blood pressure and flow sensors are currently available for cfVADs; however, the approach developed by von Petersdorff-Campen et al. (43) is promising and could pave the way toward the realization of LVP and PF measurements. In this study, we have accounted for the inherent noise of real measurement and its effect on the tracking performance by assessing the PDD-ILC and the PF-PIDC tracking ability when white noise was added on the LVP and the PF signals. Additionally, the overall performance of the proposed control approaches has been evaluated only in an *in-silico* environment with a numerical model of a non-implantable mixed-flow turbodynamic blood pump. *In-silico*, studies with the numerical model of the current state of the art blood pump HeartMate 3 have to be also performed. Furthermore, to prove the performance of the controllers in the real-time setting and allow the translation of the controllers into the clinical practice, *in-vitro* and *in-vivo* studies have to be conducted.

Finally, considering the high complexity of the presented control schemes, suction prevention features were not included in the main control structures. Although no suction events were identified in the executed experiments, safety controllers similar to those proposed by Petrou et al. (34) could be incorporated.

DATA AVAILABILITY STATEMENT

The raw data supporting the conclusions of this article will be made available by the authors, without undue reservation.

AUTHOR CONTRIBUTIONS

The study was performed at the Product Development Group Zurich, ETH Zurich, Zurich. The control schemes and the evaluation experiments were conceived and designed by KM and PA. Data collection and analysis was performed by KM and PA. Literature search and study discussions conducted by KM, AP, and MS. The manuscript was prepared by KM and reviewed by PA, MS, and MM. All authors contributed to the article and approved the submitted version.

FUNDING

This work was supported by Stavros Niarchos Foundation (SNF). Open access funding provided by ETH Zurich.

ACKNOWLEDGMENTS

The authors thankfully acknowledge N. Steffen, M. Heim, and L. Gloor for their assistance in the development and evaluation of the feature extraction algorithm and the genetic-algorithm based optimization framework. This work is part of the Zurich Heart project under the umbrella of Hochschuldmedizin Zurich and it is supported by the Stavros Niarchos Foundation (SNF).

SUPPLEMENTARY MATERIAL

The Supplementary Material for this article can be found online at: https://www.frontiersin.org/articles/10.3389/fcvm.2022.922387/full#supplementary-material

REFERENCES

1. Virani SS, Alonso A, Benjamin EJ, Bittencourt MS, Callaway CW, Carson AP, et al. *Heart Disease and Stroke Statistics—2020 Update*. American Heart Association (2020).
2. Roger VL. Epidemiology of heart failure. *Circ Res.* (2021) 128:1421–34. doi: 10.1161/CIRCRESAHA.121.318172
3. Groenewegen A, Rutten FH, Mosterd A, Hoes AW. Epidemiology of heart failure. *Eur J Heart Fail.* (2020) 22:1342–56. doi: 10.1002/ejhf.1858
4. Khush KK, Cherikh WS, Chambers DC, Harhay MO, Hayes D, Hsich E, et al. The international thoracic organ transplant registry of the international society for heart and lung transplantation: thirty-sixth adult heart transplantation report — 2019; focus theme: donor and recipient size match. *J Hear Lung Transplant.* (2019) 38:1056–66. doi: 10.1016/j.healun.2019.08.004
5. Cain MT, Firstenberg MS, Cleveland JC. Heart transplant and ventricular assist: cardiac surgery and heart failure perspective. *US Cardiol Rev.* (2021) 24:15. doi: 10.15420/usc.2021.11
6. Theochari CA, Michalopoulos G, Oikonomou EK, Giannopoulos S, Doulamis IP, Villela MA, et al. Heart transplantation vs. left ventricular assist devices as destination therapy or bridge to transplantation for 1-year mortality: a systematic review and meta-analysis. *Ann Cardiothorac Surg.* (2018) 7:3–11. doi: 10.21037/acs.2017.09.18

7. Murali S. Long-term circulatory support – the left ventricular assist system for advanced heart failure. *US Cardiol Rev.* (2004) 1:145–7. doi: 10.15420/usc.2004.1.1.145
8. Kormos RL, Cowger J, Pagani FD, Teuteberg JJ, Goldstein DJ, Jacobs JP, et al. The society of thoracic surgeons intermacs database annual report: evolving indications, outcomes, and scientific partnerships. *Ann Thorac Surg.* (2019) 107:341–53. doi: 10.1016/j.athoracsur.2018.11.011
9. Molina EJ, Shah P, Kiernan MS, Cornwell WK, Copeland H, Takeda K, et al. The society of thoracic surgeons intermacs 2020 annual report. *Ann Thorac Surg.* (2021) 111:778–92. doi: 10.1016/j.athoracsur.2020.12.038
10. Schmid Daners M, Kaufmann F, Amacher R, Ochsner G, Wilhelm MJ, Ferrari A, et al. Left ventricular assist devices: challenges toward sustaining long-term patient care. *Ann Biomed Eng.* (2017) 45:1836–51. doi: 10.1007/s10439-017-1858-9
11. Loor G, Gonzalez-Stawinski G. Pulsatile vs. continuous flow in ventricular assist device therapy. *Best Pract Res Clin Anaesthesiol.* (2012) 26:105–15. doi: 10.1016/j.bpa.2012.03.004
12. Shah P, Tantry US, Bliden KP, Gurbel PA. Bleeding and thrombosis associated with ventricular assist device therapy. *J Hear Lung Transplant.* (2017) 36:1164–73. doi: 10.1016/j.healun.2017.05.008
13. Pak SW, Uriel N, Takayama H, Cappleman S, Song R, Colombo PC, et al. Prevalence of de novo aortic insufficiency during long-term support with left ventricular assist devices. *J Hear Lung Transplant.* (2010) 29:1172–6. doi: 10.1016/j.healun.2010.05.018
14. van der Merwe J, Paul E, Rosenfeldt FL. Early gastrointestinal complications from ventricular assist devices is increased by non-pulsatile flow. *Hear Lung Circ.* (2020) 29:295–300. doi: 10.1016/j.hlc.2019.01.009
15. AlOmari A-HH, Savkin AV, Stevens M, Mason DG, Timms DL, Salamonsen RF, et al. Developments in control systems for rotary left ventricular assist devices for heart failure patients: a review. *Physiol Meas.* (2013) 34:R1–27. doi: 10.1088/0967-3334/34/1/R1
16. Bozkurt S. Physiologic outcome of varying speed rotary blood pump support algorithms: a review study. *Australas Phys Eng Sci Med.* (2016) 39:13–28. doi: 10.1007/s13246-015-0405-y
17. Hall JE, Guyon AC. *Guyton and HAll Textbook of Madical Physiology 12th ed*. Philadelphia, PA: W B Saunders/Elsevier (2011).
18. Ochsner G, Amacher R, Wilhelm MJ, Vandenberghe S, Tevaearai H, Plass A, et al. A physiological controller for turbodynamic ventricular assist devices based on a measurement of the left ventricular volume. *Artif Organs.* (2014) 38:527–38. doi: 10.1111/aor.12225
19. Petrou A, Lee J, Dual S, Ochsner G, Meboldt M, Schmid Daners M. Standardized comparison of selected physiological controllers for rotary blood pumps: *in vitro* study. *Artif Organs.* (2018) 42:E29–42. doi: 10.1111/aor.12999
20. Mansouri M, Gregory SD, Salamonsen RF, Lovell NH, Stevens MC, Pauls JP, et al. Preload-based Starling-like control of rotary blood pumps: an *in-vitro* evaluation. *PLoS ONE.* (2017) 12:1–15. doi: 10.1371/journal.pone.0172393
21. Li T, Cui W, Xie N, Li H, Liu H, Li X, et al. Intelligent and strong robust CVS-LVAD control based on soft-actor-critic algorithm. *Artif Intell Med.* (2022) 128:102308. doi: 10.1016/j.artmed.2022.102308
22. Ketelhut M, Schrödel F, Stemmler S, Roseveare J, Hein M, Gesenhues J, et al. Iterative learning control of a left ventricular assist device. *IFAC-PapersOnLine.* (2017) 50:6684–90. doi: 10.1016/j.ifacol.2017.08.1161
23. Ketelhut M, Stemmler S, Gesenhues J, Hein M, Abel D. Iterative learning control of ventricular assist devices with variable cycle durations. *Control Eng Pract.* (2019) 83:33–44. doi: 10.1016/j.conengprac.2018.10.012
24. Soucy KG, Koenig SC, Giridharan GA, Sobieski MA, Slaughter MS. Rotary pumps and diminished pulsatility. *ASAIO J.* (2013) 59:355–66. doi: 10.1097/MAT.0b013e31829f9bb3
25. Witman MAH, Garten RS, Gifford JR, Groot HJ, Trinity JD, Stehlik J, et al. Further Peripheral Vascular Dysfunction in Heart Failure Patients With a Continuous-Flow Left Ventricular Assist Device: The Role of Pulsatility. *JACC Hear Fail.* (2015) 3:703–11. doi: 10.1016/j.jchf.2015.04.012
26. Sathianathan S, Bhat G, Dowling R. Vasoplegia from continuous flow left ventricular assist devices. *Curr Cardiol Rep.* (2021) 23:101. doi: 10.1007/s11886-021-01534-y
27. Ivak P, Netuka I, Kralova-Lesna I, Wohlfahrt P, Pitha J. Changes in circulating stem cells and endothelial progenitor cells over a 12-month period after implantation of a continuous-flow left ventricular assist device. *Arch Med Sci.* (2020) 16:1440–3. doi: 10.5114/aoms.2020.100306
28. Wever-Pinzon O, Selzman CH, Drakos SG, Saidi A, Stoddard GJ, Gilbert EM, et al. Pulsatility and the risk of nonsurgical bleeding in patients supported with the continuous-flow left ventricular assist device heartmate II. *Circ Hear Fail.* (2013) 6:517–26. doi: 10.1161/CIRCHEARTFAILURE.112.000206
29. Kato TS, Chokshi A, Singh P, Khawaja T, Cheema F, Akashi H, et al. Effects of continuous-flow vs. pulsatile-flow left ventricular assist devices on myocardial unloading and remodeling. *Circ Hear Fail.* (2011) 4:546–53. doi: 10.1161/CIRCHEARTFAILURE.111.962142
30. Letsou G V, Pate TD, Gohean JR, Kurusz M, Longoria RG, Kaiser L, et al. Improved left ventricular unloading and circulatory support with synchronized pulsatile left ventricular assistance compared with continuous-flow left ventricular assistance in an acute porcine left ventricular failure model. *J Thorac Cardiovasc Surg.* (2010) 140:1181–8. doi: 10.1016/j.jtcvs.2010.03.043
31. Magkoutas K, Rebholz M, Sündermann S, Alogna A, Faragli A, Falk V, et al. Control of ventricular unloading using an electrocardiogram-synchronized pulsatile ventricular assist device under high stroke ratios. *Artif Organs.* (2020) 44:E394–405. doi: 10.1111/aor.13711
32. Naito N, Nishimura T, Iizuka K, Takewa Y, Umeki A, Ando M, et al. Rotational speed modulation used with continuous-flow left ventricular assist device provides good pulsatility†. *Interact Cardiovasc Thorac Surg.* (2018) 26:119–23. doi: 10.1093/icvts/ivx236
33. Ando M, Nishimura T, Takewa Y, Yamazaki K, Kyo S, Ono M, et al. Electrocardiogram-synchronized rotational speed change mode in rotary pumps could improve pulsatility. *Artif Organs.* (2011) 35:941–7. doi: 10.1111/j.1525-1594.2011.01205.x
34. Petrou A, Monn M, Meboldt M, Schmid Daners M. A novel multi-objective physiological control system for rotary left ventricular assist devices. *Ann Biomed Eng.* (2017) 45:2899–910. doi: 10.1007/s10439-017-1919-0
35. Ising MS, Sobieski MA, Slaughter MS, Koenig SC, Giridharan GA. Feasibility of pump speed modulation for restoring vascular pulsatility with rotary blood pumps. *ASAIO J.* (2015) 61:526–32. doi: 10.1097/MAT.0000000000000262
36. Soucy KG, Giridharan GA, Choi Y, Sobieski MA, Monreal G, Cheng A, et al. Rotary pump speed modulation for generating pulsatile flow and phasic left ventricular volume unloading in a bovine model of chronic ischemic heart failure. *J Hear Lung Transplant.* (2015) 34:122–31. doi: 10.1016/j.healun.2014.09.017
37. Amacher R, Asprion J, Ochsner G, Tevaearai H, Wilhelm M, Plass A, et al. Numerical optimal control of turbo dynamic ventricular assist devices. *Bioengineering.* (2013) 1:22–46. doi: 10.3390/bioengineering1010022
38. Zeile C, Rauwolf T, Schmeisser A, Mizerski JK, Braun-Dullaeus RC, Sager S. An intra-cycle optimal control framework for ventricular assist devices based on atrioventricular plane displacement modeling. *Ann Biomed Eng.* (2021) 49:3508–23. doi: 10.1007/s10439-021-02848-2
39. Amacher R, Ochsner G, Schmid Daners M. Synchronized pulsatile speed control of turbodynamic left ventricular assist devices: review and prospects. *Artif Organs.* (2014) 38:867–75. doi: 10.1111/aor.12253
40. Rüschen D, Prochazka F, Amacher R, Bergmann L, Leonhardt S, Walter M. Minimizing left ventricular stroke work with iterative learning flow profile control of rotary blood pumps. *Biomed Signal Process Control.* (2017) 31:444–51. doi: 10.1016/j.bspc.2016.09.001
41. Colacino FM, Moscato F, Piedimonte F, Arabia M, Danieli GA. Left ventricle load impedance control by apical VAD can help heart recovery and patient perfusion: a numerical study. *ASAIO J.* (2007) 53:263–77. doi: 10.1097/MAT.0b013e31805b7e39
42. Ochsner G, Amacher R, Amstutz A, Plass A, Schmid Daners M, Tevaearai H, et al. A novel interface for hybrid mock circulations to evaluate ventricular assist devices. *IEEE Trans Biomed Eng.* (2013) 60:507–16. doi: 10.1109/TBME.2012.2230000
43. Von Petersdorff-Campen K, Dupuch MA, Magkoutas K, Hierold C, Schmid Daners M. Pressure and bernoulli-based flow measurement *via* a tapered inflow VAD cannula. *IEEE Trans Biomed Eng.* (2021) 69:1620–9. doi: 10.1109/TBME.2021.3123983
44. Ising M, Warren S, Sobieski MA, Slaughter MS, Koenig SC, Giridharan GA. Flow modulation algorithms for continuous flow left ventricular assist devices to increase vascular pulsatility: a computer simulation study. *Cardiovasc Eng Technol.* (2011) 2:90–100. doi: 10.1007/s13239-011-0042-x

45. Rebholz M, Amacher R, Petrou A, Meboldt M, Schmid Daners M. High-frequency operation of a pulsatile VAD – a simulation study. *Biomed Eng / Biomed Tech*. (2017) 62:1–10. doi: 10.1515/bmt-2016-0052
46. Chi R, Liu X, Zhang R, Hou Z, Huang B. Constrained data-driven optimal iterative learning control. *J Process Control*. (2017) 55:10–29. doi: 10.1016/j.jprocont.2017.03.003
47. Ziegler JG, Nichols NB. Optimum settings for automatic controllers. *J Dyn Syst Meas Control*. (1993) 115:220–2. doi: 10.1115/1.2899060
48. Konstantinos M, Leonardo NR, Marco H, Mirko M, Schmid Daners M. Genetic algorithm-based optimization framework for control parameters of ventricular assist devices introduction (under preparation). *Front Cardiovasc Med*. (2022) 2020:7686724. doi: 10.1155/2020/7686724
49. Fukamachi K, Shiose A, Massiello A, Horvath DJ, Golding LAR, Lee S, et al. Preload sensitivity in cardiac assist devices. *Ann Thorac Surg*. (2013) 95:373–80. doi: 10.1016/j.athoracsur.2012.07.077
50. Mansouri M, Salamonsen RF, Lim E, Akmeliawati R, Lovell NH. Preload-based starling-like control for rotary blood pumps:Numerical comparison with pulsatility control and constant speed operation. *PLoS ONE*. (2015) 10:1–16. doi: 10.1371/journal.pone.0121413

Conflict of Interest: The authors declare that the research was conducted in the absence of any commercial or financial relationships that could be construed as a potential conflict of interest.

frontiers | Frontiers in Cardiovascular Medicine

ORIGINAL RESEARCH
published: 13 July 2022
doi: 10.3389/fcvm.2022.871967

Monte Carlo Simulation and Reconstruction: Assessment of Myocardial Perfusion Imaging of Tracer Dynamics With Cardiac Motion Due to Deformation and Respiration Using Gamma Camera With Continuous Acquisition

*Yoonsuk Huh[1], Uttam M. Shrestha[1], Grant T. Gullberg[1,2] and Youngho Seo[1,2,3]**

[1] Department of Radiology and Biomedical Imaging, University of California, San Francisco, San Francisco, CA, United States, [2] Molecular Biophysics and Integrated Bioimaging Division, Lawrence Berkeley National Laboratory, Berkeley, CA, United States, [3] Department of Nuclear Engineering, University of California, Berkeley, Berkeley, CA, United States

OPEN ACCESS

Edited by:
Caglar Ozturk,
Massachusetts Institute of Technology, United States

Reviewed by:
Benjamin Tsui,
Johns Hopkins University, United States
Christopher T. Nguyen,
Cleveland Clinic, United States

***Correspondence:**
Youngho Seo
youngho.seo@ucsf.edu

Specialty section:
This article was submitted to General Cardiovascular Medicine, a section of the journal Frontiers in Cardiovascular Medicine

Received: 08 February 2022
Accepted: 16 June 2022
Published: 13 July 2022

Citation:
Huh Y, Shrestha UM, Gullberg GT and Seo Y (2022) Monte Carlo Simulation and Reconstruction: Assessment of Myocardial Perfusion Imaging of Tracer Dynamics With Cardiac Motion Due to Deformation and Respiration Using Gamma Camera With Continuous Acquisition. Front. Cardiovasc. Med. 9:871967. doi: 10.3389/fcvm.2022.871967

Purpose: Myocardial perfusion imaging (MPI) with single photon emission computed tomography (SPECT) is routinely used for stress testing in nuclear medicine. Recently, our group extended its potential going from 3D visual qualitative image analysis to 4D spatiotemporal reconstruction of dynamically acquired data to capture the time variation of the radiotracer concentration and the estimated myocardial blood flow (MBF) and coronary flow reserve (CFR). However, the quality of reconstructed image is compromised due to cardiac deformation and respiration. The work presented here develops an algorithm that reconstructs the dynamic sequence of separate respiratory and cardiac phases and evaluates the algorithm with data simulated with a Monte Carlo simulation for the continuous image acquisition and processing with a slowly rotating SPECT camera.

Methods: A clinically realistic Monte Carlo (MC) simulation is developed using the 4D Extended Cardiac Torso (XCAT) digital phantom with respiratory and cardiac motion to model continuous data acquisition of dynamic cardiac SPECT with slowly rotating gamma cameras by incorporating deformation and displacement of the myocardium due to cardiac and respiratory motion. We extended our previously developed 4D maximum-likelihood expectation-maximization (MLEM) reconstruction algorithm for a data set binned from a continuous list mode (LM) simulation with cardiac and respiratory information. Our spatiotemporal image reconstruction uses splines to explicitly model the temporal change of the tracer for each cardiac and respiratory gate that delineates the myocardial spatial position as the tracer washes in and out. Unlike in a fully list-mode data acquisition and reconstruction the accumulated photons are binned over a specific but very short time interval corresponding to each cardiac and respiratory

gate. Reconstruction results are presented showing the dynamics of the tracer in the myocardium as it continuously deforms. These results are then compared with the conventional 4D spatiotemporal reconstruction method that models only the temporal changes of the tracer activity. Mean Stabilized Activity (MSA), signal to noise ratio (SNR) and Bias for the myocardium activities for three different target-to-background ratios (TBRs) are evaluated. Dynamic quantitative indices such as wash-in (K_1) and wash-out (k_2) rates at each gate were also estimated.

Results: The MSA and SNR are higher with higher TBRs while biases were improved with higher TBRs to less than 10%. The correlation between exhalation-inhalation sequence with the ground truth during respiratory cycle was excellent. Our reconstruction method showed better resolved myocardial walls during diastole to systole as compared to the ungated 4D image. Estimated values of K_1 and k_2 were also consistent with the ground truth.

Conclusion: The continuous image acquisition for dynamic scan using conventional two-head gamma cameras can provide valuable information for MPI. Our study demonstrated the viability of using a continuous image acquisition method on a widely used clinical two-head SPECT system. Our reconstruction method showed better resolved myocardial walls during diastole to systole as compared to the ungated 4D image. Precise implementation of reconstruction algorithms, better segmentation techniques by generating images of different tissue types and background activity would improve the feasibility of the method in real clinical environment.

Keywords: myocardial perfusion imaging, dynamic SPECT, cardiac motion, motion correction, continuous acquisition

INTRODUCTION

Non-invasive myocardial perfusion imaging (MPI) using single photon emission computed tomography (SPECT) and positron emission tomography (PET) have been used for diagnosis and prognosis of ischemic myocardial infarction and several coronary artery diseases (1). In conventional SPECT and PET MPI, usually a combined rest and stress study is performed after the radiotracer is fully stabilized in the myocardium. Comparisons of the rest and stress scans thus provide information about ischemic heart disease and myocardial reversibility while the electrocardiogram (ECG)-gated images provide information about the wall motion for the diagnosis of myocardial akinesis and viability. Conventional SPECT MPI has been used as a workhorse to identify patients with coronary artery diseases (CAD) and referrals to a catherization laboratory for possible coronary artery revascularization (2, 3). However, it does not provide information on radiotracer kinetics and hemodynamically significant quantitative information such as uptake rate (K_1), myocardial blood flow (MBF) and coronary flow reserve (CFR). The quantification of MBF and CFR can detect significant stenotic lesion and microvascular dysfunction. The current state-of-the-art solid-state SPECT MPI technology (4) can provide improved photon sensitivity that has facilitated fast MPI and the feasibility to quantify MBF. Dynamic imaging has been used with PET to quantify MBF (5, 6), and recently some studies have shown that dynamic SPECT imaging can also quantify MBF and CFR (7–12).

This work is inspired by recent activities involving continuous image acquisition and processing with a SPECT camera for myocardial perfusion imaging (13). Basically, the importance of "continuous image acquisition" is to eliminate the dead time between the angles at consecutive detector positions by not acquiring the data which results in loss of significant number of photons. In fact a tomographic step-and-shoot continuous mode acquisition, so-called SwiftScan, has been investigated to determine whether this can be used in clinical practice as a part of time reduction strategy, while preserving image quality and accuracy (14–16). The continuous image acquisition for dynamic scan using conventional two-head gamma cameras provides an additional attribute to MPI, which to our knowledge, has not been initiated yet. The main bottleneck of the dynamic reconstruction with the continuous image acquisition is the inconsistency of the data. For a slowly rotating gamma camera it is difficult to obtain consistent tomographic data to solve dynamic inverse problems frame-by-frame. However, by estimating coefficients of spatiotemporal basis functions directly from projection measurements one can fairly accurately reconstruct the dynamic images and thus estimate the wash-in and wash-out rate parameters of a myocardial perfusion SPECT tracer (7).

The conventional MPI usually results in spatial blurring and motion artifacts due to cardiac and respiratory motion and

leads to inconsistency in the tomographic reconstruction that undermines the diagnostic accuracy. Respiratory motion artifacts can be minimized with proper breath holding and shortened scan time or can be partially reduced by ECG gating (17). This method, however, cannot be utilized for dynamic imaging. The cardiac and respiratory motion can be modeled by binning the list-mode (LM) data into projections of different cardiac-respiratory gates. This allows to reconstruct each gate separately (18). This is a powerful reconstruction approach in PET where all projection views can be acquired simultaneously in a LM format and can be used to reconstruct each cardiac or respiratory gate (19). However, this method has not been implemented for SPECT due to limited number of projections and very low camera sensitivity. The incorporation of motion in dynamic imaging with commonly available SPECT system has immense clinical significance. Several methods, mostly applicable for PET system, have been proposed to reduce the motion artifacts (18, 20–26), but cardiac motion is difficult to handle especially when tracer kinetics (wash-in and wash-out) is involved.

In dynamic cardiac SPECT imaging using a slowly rotating gamma camera, photons can be detected and recorded continuously as camera rotates around the subject. Acquiring data in LM format with angle and bin location, in addition to the tags for cardiac and respiratory phases of each photon, allows for more accurate estimation of quantitative measurements and flexibility in modeling the physiological processes of the time varying activity changes with cardiac and respiratory motion. The LM data also allows for retrospective gating and reconstruction to a specific portion of the scan, and thus help to eliminate unwanted artifacts.

A LM maximum-likelihood expectation-maximization (LM-MLEM) iterative reconstruction algorithm can, in principle, provide more accurate image reconstruction than reconstructing the data frame-by-frame. However, reconstruction of LM dynamic data with several tags requires reconstruction of each event and is computationally very challenging. This is particularly difficult to implement in the dynamic reconstruction with the cardiac and respiratory motion for the kinetic parameter estimation when the blood pool is involved.

Recent advent of new dedicated cardiac SPECT cameras has provided a promising avenue for the quantification of MPI and opportunities for the measurement of kinetic parameters, MBF, and CFR non-invasively using either a directly reconstructing parametric images from the projection data (27) or an indirect method of reconstructing the dynamic data frame by frame and then fitting parameters with appropriate compartment model. Both the direct and indirect methods for MPI have been extensively utilized in PET imaging. However, only recently attention has been shifted to SPECT due to improved noise level. Particularly, direct LM parametric reconstruction from the projection data could significantly reduce the noise level. The proposed method emphasizes the importance of "continuous image acquisition" in dynamic cardiac SPECT which eliminates the dead time between the angles of consecutive detector head positions by not acquiring the data which results in loss of a significant number of photons as is done in conventional 3D clinical SPECT.

The stationary dedicated cardiac SPECT camera can acquire data in multiple views without rotating the camera head for dynamic imaging. The main purpose of the proposed method is to extend the static imaging capabilities of the conventional and commonly available dual head SPECT geometry (GE Infinia Hawkeye) to dynamic imaging capabilities with cardiac and respiratory motion correction by acquiring the data in a continuous fashion for quantitative MPI and the method, in principle, can also be applicable to stationary dedicated cardiac SPECT cameras.

In our earlier work, we have demonstrated that it is possible to model all 6 dimensions of space, time, cardiac deformation, and cardiac-respiratory motion from a synthetic data acquired by forward projection using system matrix for a slowly rotating SPECT camera with only a few views per respiratory and cardiac gates (28). Because of the small number of detector heads and the rotation speed of the SPECT camera, it is necessary to obtain the sufficient tomographic views in each cardiac and respiratory state. This can be achieved by increasing the number of views per rotation.

Here, we implemented the 4D maximum-likelihood expectation-maximization (MLEM) reconstruction algorithm (7, 28) for the realistic data generated by MC simulation with the 4D XCAT phantom (29). We extended our earlier work with the data that simulates the clinical continuous acquisition scenario rather than a synthetic data generated by the forward projection of the cardiac torso phantom with the system matrix for the SPECT camera geometry. Unlike in our previously reported 6D spatiotemporal image reconstruction where we have incorporated fully 6D image reconstruction with Gaussian basis functions to model cardiac and respiratory motion (28), here we used the 4D reconstruction for each cardiac and respiratory-gated binned data. Our spatiotemporal image reconstruction uses splines to explicitly model the temporal change of the tracer activity. This method partly follows the development by Verhaeghe et al. for the PET application with spatiotemporal basis functions (30), and for SPECT application (31). Reconstruction results are presented showing the dynamics of the tracer in the myocardium as it moves due to cardiac beating and respiratory motion. These results are then compared with the conventional 4D-spatiotemporal reconstruction method that models only the temporal changes of the tracer activity.

MATERIALS AND METHODS

The SPECT System

In this study, a dual head SPECT camera (GE Infinia Hawkeye) was used to model the activity projection. Monte Carlo (MC) simulations were performed using the GATE (Geant4 Application for Tomographic Emission, version 7.2) (32) for all data acquisitions. Two gamma cameras having 563.2 mm × 563.2 mm × 9.5 mm NaI (Tl) crystals acquired projection data with a radius of rotation of 320 mm. A low-energy high-resolution (LEHR) collimator was coupled with the cameras. Lead shielding on all four sides of each detector was included to avoid scatter events at the side and

back compartments representing photomultipliers. Associated electronics were also added to account for potential interactions between emitted photons and photomultipliers. An overall intrinsic spatial blurring of 2.5 mm FWHM was considered at the level of the electronics. A 10% energy resolution at the energy reference of 140 keV for Tc-99m was incorporated (33). Photoelectric effect, Compton scattering, Rayleigh scattering, bremsstrahlung and ionization were also included in the GATE simulation. In order to apply dual-energy window (DEW) scatter correction, scatter and main energy windows were set up in the range of 100 ∼ 125 keV and 126 ∼ 154 keV, respectively, with the scatter multiplication factor of 0.5 (34, 35). **Table 1** shows the details of the MC simulation parameters for the SPECT system.

The Phantom

4D XCAT phantom was used to model the torso part of the human body that included cardiac beating and respiratory motion (36). The original phantom model was established from CT data using Non-uniform Rational B-Splines (NURBS). This simplified torso model has up to 20 materials consisting of myocardium and pericardium, blood pool, ventricles, arteries, veins, muscle, gallbladder, lungs, spleen, stomach, rib bone, cortical bone, spine bone, and liver. These materials were categorized into 4 groups: myocardium, blood, liver, and the rest as background. The matrix size of the original phantom was also modified to reduce the simulation time with particular focus on the cardiac and diaphragm motion. The simplified torso phantom was a matrix of 180 × 120 × 110 elements each corresponding to voxels of 2.2 mm × 2.2 mm × 2.2 mm (**Figure 1**). Attenuation maps for the same phantom were also generated assuming a Tc-99m isotope at an energy of 140 keV.

The beating of the heart and respiratory motions were incorporated in the 4D XCAT phantom. The periods of the cardiac and respiratory cycles were set to be 1 s and 5 s, respectively. The duration between the end-diastolic to the end-systolic phase was fixed at 0.325 s. The extent of anterior-posterior (AP) expansion was 1.2 cm and the displacement due to diaphragm (up and down) motion was initially set to 2.0 cm. The respiratory and cardiac motion were discretized from end-inhalation to exhalation in a series of 40 phantoms each with a duration of 0.125 s corresponding to 8 cardiac gates per heartbeat and 5 heartbeats in each respiratory cycle (**Figure 2**).

TABLE 1 | MC simulation parameters for SPECT system modeling.

Parameter	SPECT System
Detector head	2
Detector type	NaI (Tl)-PMT
Detector size (mm^3)	563.2 × 563.2 × 9.5
Pixel (binning) size (mm^2)	4.4
Hole shape	Hexagonal
Material	Lead
Hole length (mm)	35
Septal thickness (mm)	0.2
Hole diameter (mm)	1.5
Radius of Rotation (mm)	320

Time Activity Curves and Data Acquisition

Once the phantom was specified, the activities of different organ tissues such as myocardium, blood, liver and background were simulated using typical time-activity-curves (TACs) of patients in our previously completed dynamic cardiac SPECT studies with Tc-99m tetrofosmin (12). The activity in each tissue in the series of 40 phantoms was changed as a function of time according to the activities in the TACs (**Figure 3**). Once the activity in the phantom was assigned with a given TAC, the camera was rotated continuously around the phantom acquiring the data at each 0.125 s interval. The rotation speed of the detector heads was adjusted in such a way that the gamma camera acquired the projection data per 0.5^0 angle increment as the activity in the phantom changes continuously. Therefore, the time per rotation (period) of each camera head was 90 s, which is a typical rotation speed of the GE Infinia Hawkeye SPECT camera. In our simulation, there was a total of 4 rotations per detector head corresponding to the total acquisition time of 6 min.

To test and validate the reconstruction algorithm, we simulated 5 different cases by modeling the TACs with different target (myocardium) to background activity ratios (TBRs) (**Table 2**). In all cases, we kept the total activity fixed with approximately 25 mCi at the maximum activity point in the injected dose and varied the ratios of activity of the TBR at 5, 8 and 10 at the end of the acquisition time (Case 1–3). In our simulation we considered Case 1 (TBR = 8) as the reference case for this study. Case 2 with TBR = 5 and Case 3 with TBR = 10 were considered as upper and lower bound of TBR around this reference. We have not explicitly incorporated additional noise in the simulation. However, the lower TBR corresponded to higher background activities which involved higher noise levels. **Figure 4** shows the myocardial activities as a function of time for these 3 cases and **Figure 5** shows the coronal views of the phantom at the end of the acquisition time (t = 360 s) corresponding to these cases.

We have also simulated the effect of LV wall non-uniformity (Case 4) as well as the variation in the diaphragm motion (Case 5) for a fixed TBR = 8 (**Figure 6**). These cases are summarized in **Table 2**. All simulations were performed in parallel on the high-performance computing clusters in our lab with Xeon (Intel) series CPUs. The output format from the MC simulation can be configured in the fully LM format with information of each photon with the temporal, cardiac-respiratory tag or binned data at a given angle position and the tag of cardiac-respiratory phase. We used binned data with a temporal resolution of 0.125 s in the output of the projection with a detector pixel bin size of 4.4 mm for the reconstruction.

Spatiotemporal Reconstruction

We modeled the activity distribution of the radionuclide as a function $A(x, t, \tau(t), \zeta(t))$, where x is the spatial coordinate, t is the temporal coordinate, $\tau(t)$ is the cardiac phase coordinate due to beating of the heart, and $\zeta(t)$ is the cardiac

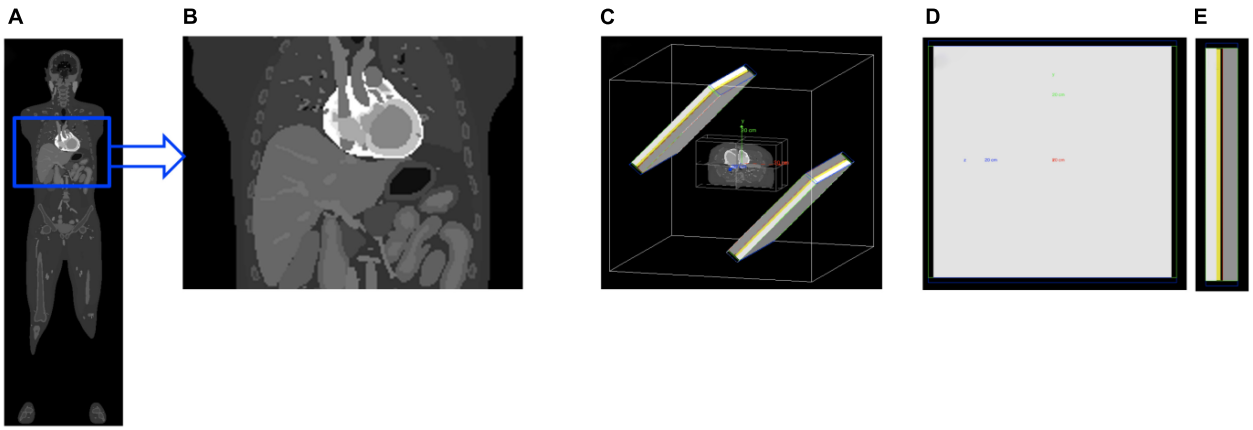

FIGURE 1 | The 4D XCAT whole-body phantom **(A)** was cropped and simplified to model a cardiac torso **(B)**. The torso was then imported to a SPECT system geometry **(C)** with collimator (gray), detector crystal (yellow), back-compartment (white) and lead-shields (blue and green). Also shown are the rear **(D)** and side **(E)** view of the detector.

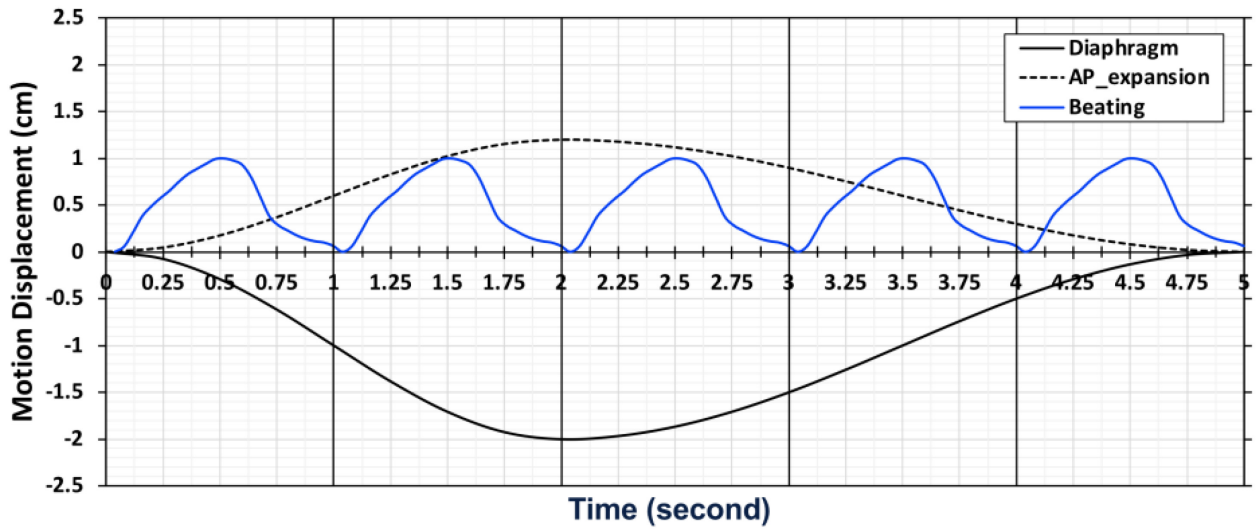

FIGURE 2 | A chart depicting the motion of cardiac and respiratory series for 40 phantoms with 5 cardiac and 1 respiratory cycle from end-inhalation to exhalation.

displacement coordinate due to the respiratory motion. The activity distribution can be written as a tensor product of the basis functions:

$$A\left(x, t, \tau\left(t\right), \zeta\left(t\right)\right) = \sum_{m,n,q,r} a_{mnqr} S^m\left(x\right) V^n\left(t\right) W^q\left(t\right) R^r\left(t\right), \quad (1)$$

where $S^m(x)$, $m = 1, 2, \ldots M$, are the spatial and $V^n(t)$, $n = 1, 2, \ldots N$, are the temporal basis functions, while $W^q(t)$, $q = 1, 2, \ldots Q$, and $R^r(t)$, $r = 1, 2, \ldots R$, are basis functions corresponding to the cardiac and respiratory phases, respectively. The reconstruction problem thus involves the estimation of the expansion coefficients a_{mnqr}.

For the geometry of our acquisition scheme using continuous rotation shown in **Figure 1**, the projection of the activity at any particular instant depends on the angular position of the detector. The detector is also pixelated so that for an arbitrary i^{th} pixel, the projection of the activity at time point t is given by

$$p_i\left(t, \tau\left(t\right), \zeta\left(t\right)\right) = \int_{\chi} F\left[x, d_i\left(t\right)\right] A\left(x, t, \tau\left(t\right), \zeta\left(t\right)\right) dx, \quad (2)$$

where the spatiotemporal distribution of the activity is integrated along the line of projection in the image space χ. The function $F[x, d_i(t)]$ maps the activity from a position x in the image space into the projection at the detector position $d_i(t)$, cardiac phase coordinate $\tau(t)$ due to beating of the heart, and respiratory phase coordinate $\zeta(t)$.

Details of the reconstruction algorithm and its derivation are given in the Ref. (28). The time-varying activity distribution of the radiotracer concentration for each respiratory and cardiac cycle was simulated as described in the previous section. There were 720 projections per rotation per detector head in each simulation and 8 cardiac and 5 respiratory gates corresponding

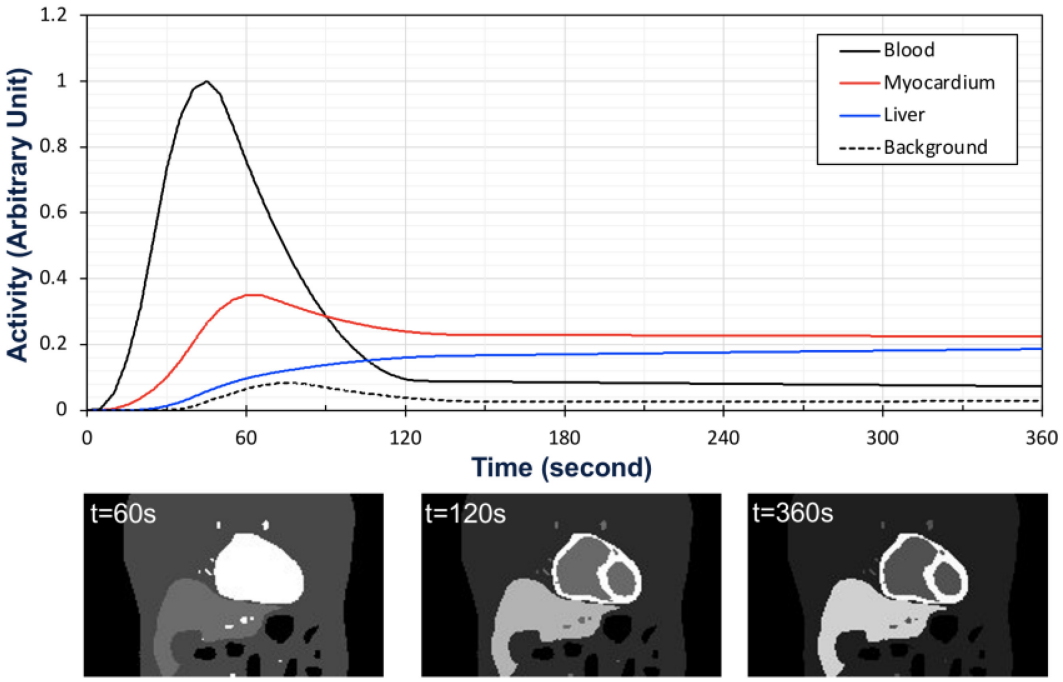

FIGURE 3 | Time activity curves used for the activity map (top) and the corresponding coronal views of the activity distribution in the phantom at time t = 60 s, t = 120 s, and t = 360 s (bottom).

to 40 gates for each 4D XCAT phantom configuration (**Figure 7**). The rotation of the detector head was adjusted in such a way that the projection time frames were discretized at an interval of 0.125 s per a 0.5^0 angle increment in a continuous fashion so that the accumulated photons at a given angle position and time were binned corresponding to each cardiac-respiratory phase of the heart as shown in **Figure 7**. In order to avoid any confusion and preserve the symmetry of the matrix, we have used both the detector bin size in the projection and reconstruction voxel size equal to 4.4 mm.

In our previous study we used an average attenuation map of all 40 phantoms (28). Incorporating the time dependent attenuation map into the system matrix for an "on-the-fly" fully 6D reconstruction would be computationally very costly due to the massive data size. Here, we have generated 40 system matrices corresponding to each gate with a given attenuation map since there were 40 attenuation maps corresponding to each phantom. The attenuation map is the cyclic function of cardiac and respiratory phase. Therefore, there are 18 projections per gate per 360° rotation. The system matrix models the attenuation as well as the geometric point response using the line integral approach developed for the 3D geometry (37, 38), and can be adapted for the 4D model (39). Even though the activity distribution differs greatly with cardiac deformation and respiration, a different system matrix for each cardiac-respiratory phase eliminates the motion artifact in the reconstruction.

The activity distribution was reconstructed for five sets of data with different TBRs to see how the noise in the reconstructed images affects the signal-to-noise-ratio (SNR). There is a trade-off between the number of gates and the number of projections per gate that affects the quality of the reconstructed image (**28**). However, in the current study we kept the number of cardiac-respiratory gates fixed. In addition to the number of gates all detector parameters were also kept unchanged. The activity distribution in each voxel in the volume changes with time due to not only the temporal changes of the radiotracer distribution but as well as due to the cardiac-respiratory motion. For the gated cardiac-respiratory reconstruction, we modeled the temporal dynamics of the tracer by optimized cubic B-spline basis functions to reconstruct the dynamic time activity of each gate separately. **Figure 8** shows a typical set of B-spline basis functions used in the reconstruction.

The scattered correction was implemented in the projections with double energy window. In our reconstruction, we have not incorporated regularization explicitly. However, the use of basis functions in the reconstruction provided some regularization in time (40).

The continuously acquired data was binned for cardiac and respiratory gate and the reconstruction was performed for the binned data set, not for each photon event. It should be pointed out that our reconstruction method, unlike 3D reconstruction, does not directly estimate the activity distribution in the image volume, but solves the coefficients of the basis functions, which are then transformed into a continuous function of activity (Equation 1). The gated reconstructed image provides the information on tracer dynamics for each cardiac respiratory gate thus effectively eliminates the motion artifact.

TABLE 2 | Simulation cases in this study.

Case	Max. Activity (mCi)	*Myocardium: Background	*Myocardium: Blood	*Myocardium: Liver	LV Thickness	Diaphragm displacement (cm)
1	25.01	8.05:1	3.08:1	1.20:1	Uniform	2.0
2	25.11	5.11:1	3.08:1	1.20:1	Uniform	2.0
3	25.01	10.2:1	3.08:1	1.20:1	Uniform	2.0
4	24.98	8.05:1	3.08:1	1.20:1	Non-uniform	2.0
5	24.99	8.05:1	3.08:1	1.20:1	Uniform	1.5

**Activity ratios at 6 min after injection.*

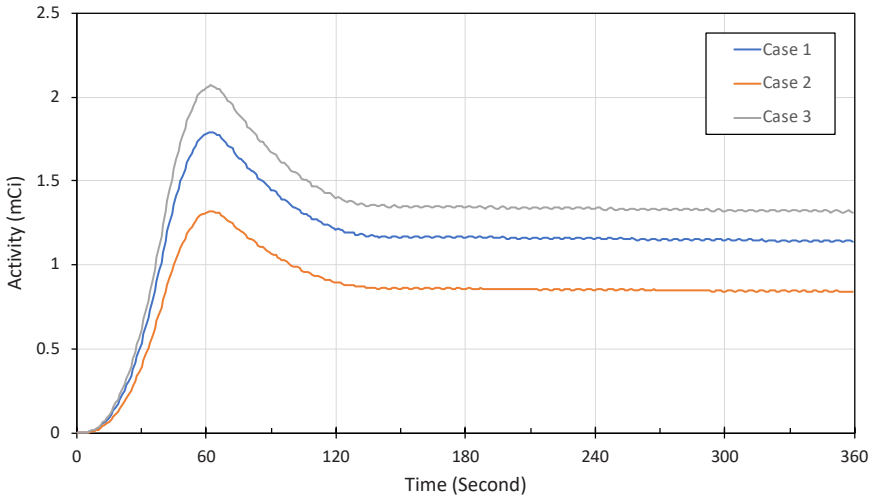

FIGURE 4 | Approximate activity distribution in the myocardium for three different TBRs: 8 (Case 1), 5 (Case 2), and 10 (Case 3).

FIGURE 5 | (Top) Coronal view of the activity maps for different TBRs at time t = 360 s after the tracer injection (Case 1, 2, 3). All images were normalized by the maximum pixel value of the image with TBR = 10 (Bottom).

The reconstructed images were then filtered with 4D Gaussian filter (FWHM = 4.5 mm and kernel size = 9).

Performance Evaluation

To evaluate the performance of our algorithm we compared the SNR and Bias for three different TBRs at 5, 8 and 10. For this purpose, we considered data for only the last minute after the tracer injection with 720 projections per rotation, corresponding to total counts of 2.1×10^6, 1.8×10^6 and 2.4×10^6 for three different TBRs of 8, 5 and 10, respectively. Each view in the detector plane was pixelized with 128×128 bins, and the mean photon counts per pixel was 1.2 ensuring the count rate was within the tolerance of the SPECT camera (41). For a given TBR, Mean Stabilized Activity (MSA), SNR and Bias were calculated over the region of interest (ROI). Left Ventricular myocardium was the ROI considered for all performance evaluations. We have also tested the level of significance of the difference between MSA using two-tailed t- test for different TBRs.

Utility of Dynamic Gated Myocardial Perfusion Imaging

The method described in this study is capable of estimating dynamic quantitative indices such as wash-in (K_1) and wash-out (k_2) rates for each gate. These parameters can be estimated

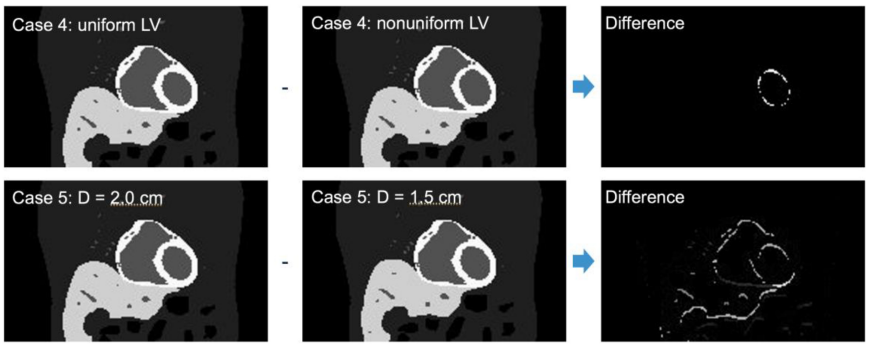

FIGURE 6 | Similar activity map as in **Figure 5** for non-uniform LV thickness (Case 4) and uniform LV thickness but with diaphragm displacement of D = 1.5 cm (Case 5) and their corresponding differences.

by fitting the TAC of the myocardial tissue activity using a compartment model. The myocardial TACs were fitted using a 1-tissue compartment model (1TCM) with LV blood pool as an input function (12) for Cases 1, 2 and 3. The spillover from LV into the myocardium was also corrected by incorporating the blood fraction (V_L) in the model.

RESULTS

Figure 9 shows an example of the reconstructed image at systolic and diastolic phases for three different TBRs at 6 min after tracer injection. The mean myocardial activity is lower for an initial lower myocardial dose in the phantom, for instance the mean activities at diastole and systole were 0.077, 0.063, 0.10 and 0.089, 0.071, 0.11 for the ratios 8:1, 5:1 and 10:1, respectively, consistent with the ground truth activities. Since the cardiac motion is coined with respiratory phases the systolic and diastolic phases do not represent the same respiratory phase. That means the results presented in **Figure 9** do not represent the same image slices.

The sharpness of the image is clearly manifested with no motion blurring. The streak artifact as seen previously in the transverse view in our previous work (28) due to the inconsistency in the projections, with only 12 views per gate, have been eliminated despite the reconstruction was still underdetermined with only 18 views per gate per rotation.

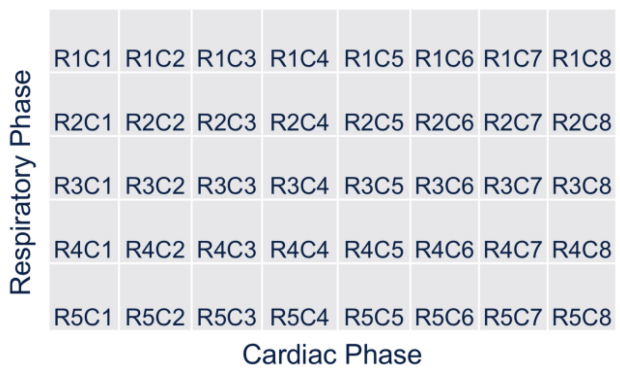

FIGURE 7 | Gating scheme for the reconstruction: There are 8 cardiac and 5 respiratory gates corresponding to 40 gates for each 4D XCAT phantom configuration.

Like in the case of 6D image reconstruction of the tensor product of basis functions (28) the gated cardiac reconstruction was able to delineate the deformation as well as the upward displacement of the heart due to respiration. In **Figure 10** we show the cardiac displacement in an exhalation-inhalation sequence during one respiratory cycle. The crosshair marks indicate the center of the left ventricle while the fiduciary horizontal line is the reference drawn at the end-exhalation phase. The vertical arrow is the cardiac displacement from the reference line. Only 7 respiratory phases at time points 300.0, 301.0, 302.0, 302.5, 303.0, 304.0, and 305.0 s are shown. The first frame represents the end-exhalation.

In order to compare the magnitude of the displacement of the heart due to respiratory motion we plotted the center of the left ventricle as a function of the respiratory gates (the length of the vertical arrows in **Figure 10**) and is shown in **Figure 11**. The displacement is consistent with the displacement of the original phantom as shown in **Figure 2**.

Figure 12 shows the detailed results of the statistical analysis of the reconstructed image for 3 different TBRs, namely Mean Stabilized Activity (MSA), SNR and Bias (%) at systolic and diastolic phases of the heart. The MSA and SNR were higher for a higher TBR while biases were improved for a higher TBR. There is no statistical difference between SNR at the TBRs = 8 and 10 (P = NS) while the SNR is decreased significantly for TBR = 5 compared to TBR = 8 ($P < 0.001$) with better bias-noise characteristics. This indicates that the TBR = 8 is sufficient to test the algorithm. Also, the variances were higher at TBR = 5 compared to 8 and 10.

Comparison of 4D Reconstruction With Conventional Spatiotemporal Reconstruction

The spatiotemporal 4D reconstruction provides information of the temporal changes of the radiotracer at each spatial point without specifics of the cardiac or respiratory motion.

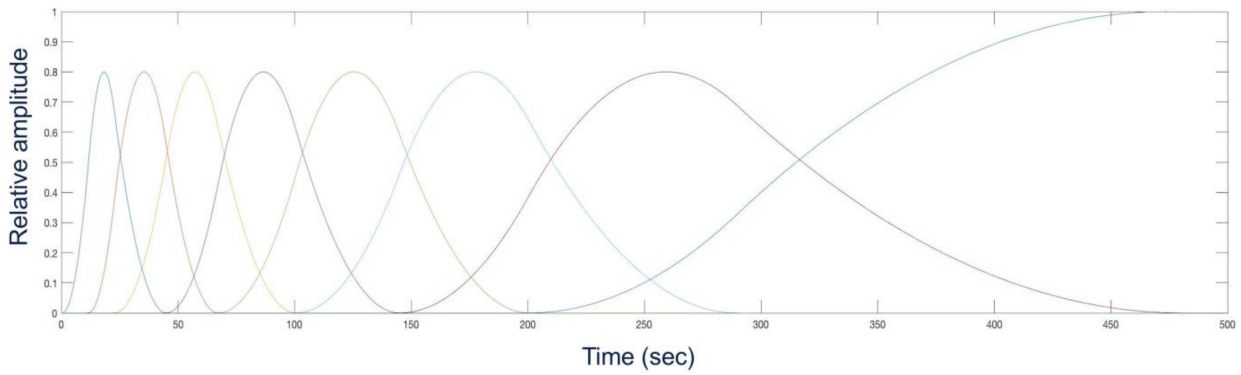

FIGURE 8 | A representative set of temporal cubic B-spline basis functions that were optimized for a specific input time activity curve (TAC) in **Figure 3**.

The reconstructed images with MC simulation were compared with the data obtained from the conventional spatiotemporal 4D reconstruction that has been implemented in our earlier publications in patient studies (12, 42). In these studies, for a TBR = 8 we binned data over each 3-degree view for a total of 120 views per rotation per detector head. Despite the under sampled data set with only 18 views per rotation, the image quality has significantly improved with the proposed method. In **Figure 13** we show the comparison of the gated reconstruction (B) proposed in this work with conventional 4D spatiotemporal reconstruction without gating (C). The 4D conventional reconstruction showed image blurs due to respiratory motion while the gated reconstruction provided the information of cardiac and respiratory motion. Our reconstruction method also showed better resolved myocardial walls during diastole to systole as compared to the conventional ungated 4D spatiotemporal reconstructed image.

LV Wall Non-uniformity and Diaphragm Displacement

Our MC simulation with 4D XCAT phantom is capable of simulating the heterogeneous myocardial wall thickness (Case 4) as well as variable diaphragm displacement (Case 5). We also simulated variable myocardial wall thickness to test our reconstruction method. In **Figure 14** we show the difference between the reconstructed images with and without LV wall non-uniformity and compared with the ground truth derived from the original phantom (**Figure 6**). Despite of highly under-sampled data, the thinner myocardial wall regions are clearly delineated with higher intensity.

Figure 15 shows an example of diaphragm displacement with D = 1.5 cm (Case 5). As in **Figure 10**, the amplitude of the displacement approximately matched with the true displacement derived from phantom data. The images are shown after the end-inhalation to full exhalation of the respiratory phase.

Estimation of Dynamical Quantitative Indices

In **Figure 16** we show an example of TACs of the LV blood pool and total myocardium at systole and diastole for the Case 1 study (TBR = 8) and the corresponding fits using the 1TCM. **Table 3** provides the results of the quantitative dynamic rate constants (K_1 and k_2) and V_L for Tc-99m tetrofosmin derived from the fits for different TBRs along with the corresponding ground truth values.

DISCUSSION

This study was designed to simultaneously model the changes in activity in the myocardium by incorporating cardiac and respiratory motion using a commonly available two-head SPECT system. This was accomplished by a continuous acquisition of the data during wash-in and wash-out of the radiotracer. Although the rotation was relatively slow (90 s per rotation per head), the projection views were tuned to capture the respiratory and cardiac gate along with the changes in radiotracer activity. By acquiring the data in a LM format that has the information of cardiac and respiratory phases while camera rotates continuously, the emitted photons were binned for a very short time duration (0.125 s) in each detector pixel. With no photon loss between

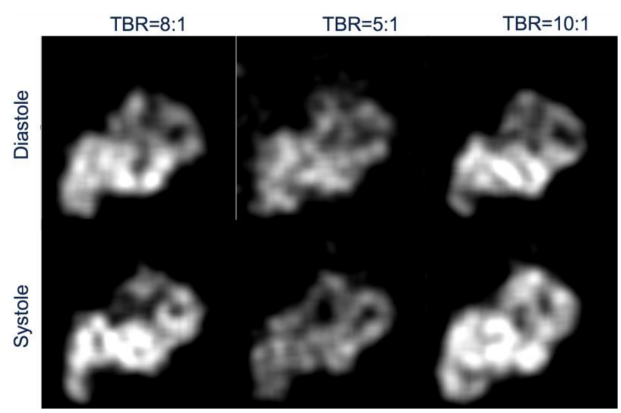

FIGURE 9 | Reconstructed image of myocardial activity distribution during diastole and systole phases of the heart for three different TBRs at full exhalation.

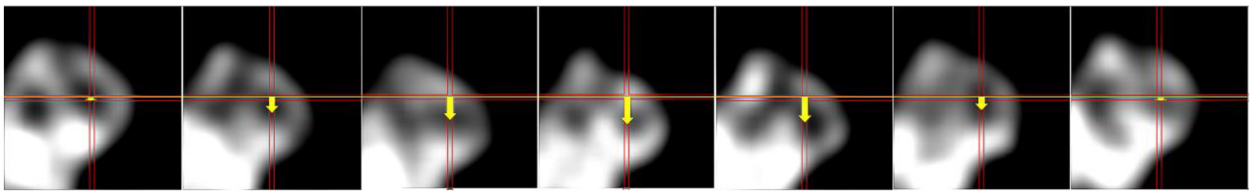

FIGURE 10 | Coronal views of heart in an exhalation-inhalation sequence during one respiratory cycle. The respiratory period was 5 s while the heart beating period was 1 s. The cross hair marks the center of the left ventricle and the first frame represents the end-exhalation. The vertical shift of the myocardium is represented by an arrow.

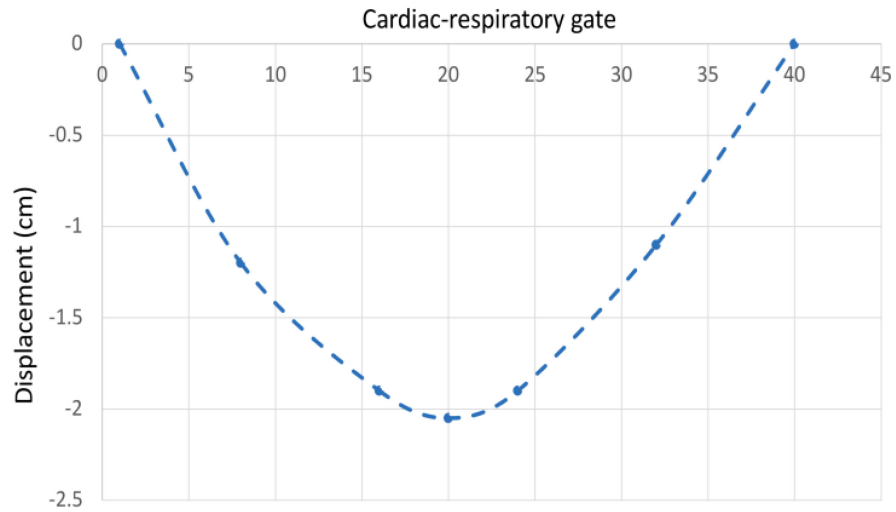

FIGURE 11 | Liver displacement over a respiratory cycle.

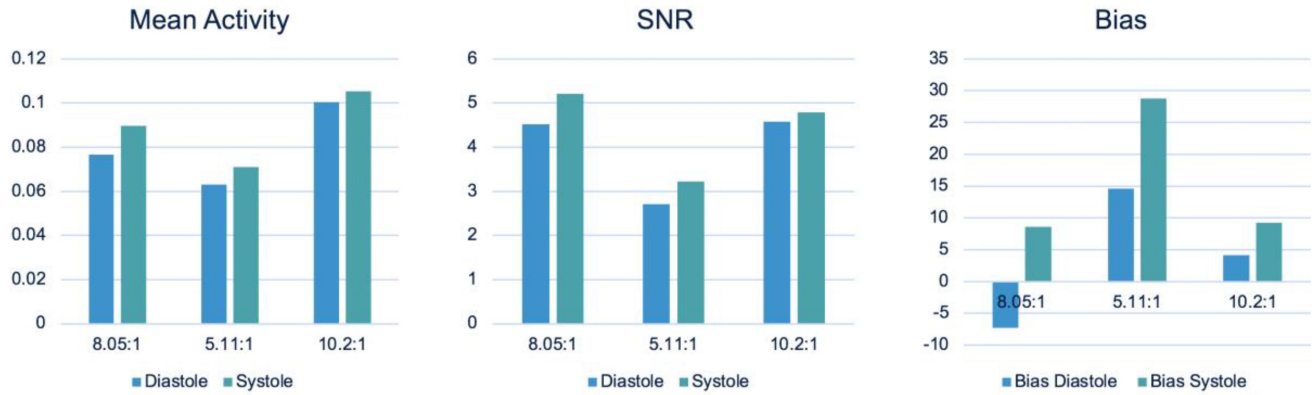

FIGURE 12 | Performance evaluation: Mean Stabilized Activity (MSA), SNR and Bias for three different TBRs for myocardium and systole and diastole phases.

detector consecutive positions, we were able to capture essentials of regional myocardial perfusion dynamics in a deformed tissue due to cardiac-respiratory motion. The method described in this work, though technically feasible, requires a very large number of views per rotation and thus a very small number of photons per pixel per view with significantly higher noise in the system and requires a more accurate reconstruction algorithm.

A general approach for cardiac motion compensation assumes the 3D configuration and relies on the fact that the activity in a given voxel is fixed. This is true in conventional (static SPECT) clinical acquisition where the data is acquired only after the tracer is fully stabilized in the myocardium. However, for dynamic acquisition the tracer activity changes significantly during wash-in and wash-out phase. Therefore, to calculate more accurate

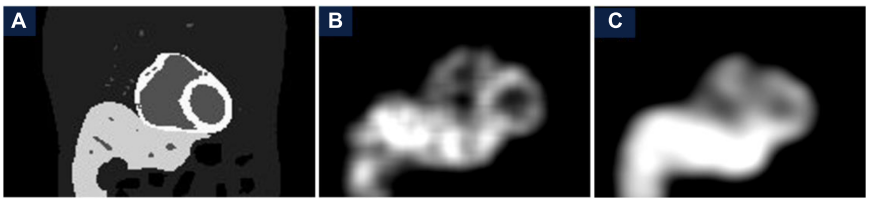

FIGURE 13 | Comparison of gated reconstruction proposed in this work with conventional 4D spatiotemporal reconstruction without gating. Ground truth image **(A)** and the corresponding reconstructed images with the method proposed in this work with only 18 views per rotation **(B)** and with the conventional method with 120 views per rotation for the same data set **(C)** without gating.

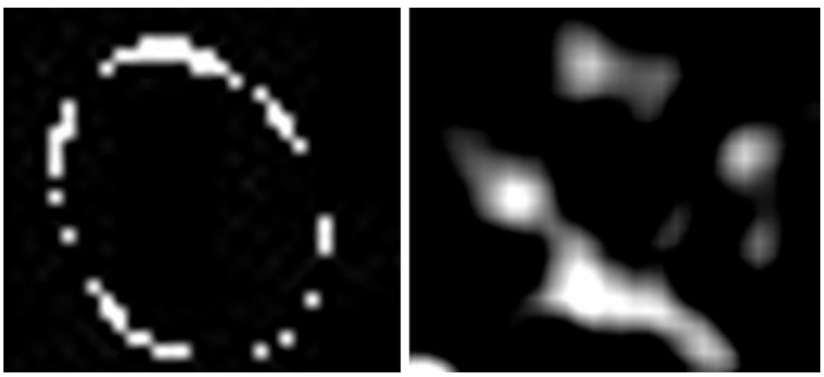

FIGURE 14 | Effect of LV wall non-uniformity (Case 4): Comparison of the difference in LV wall thickness between the ground truth (left) and the reconstructed image.

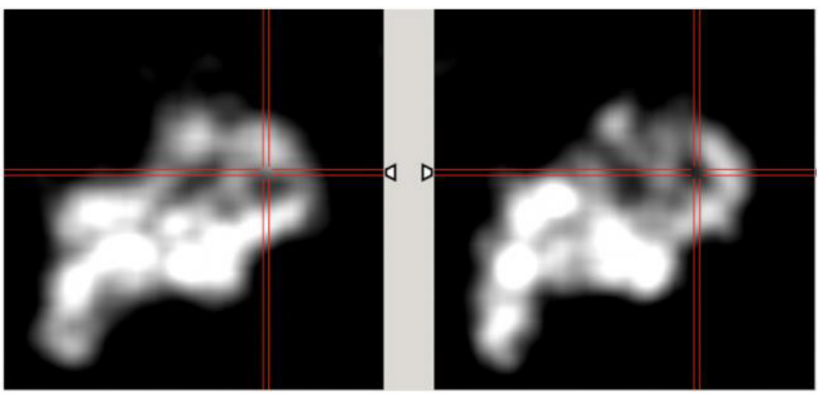

FIGURE 15 | Effect of diaphragm displacement (Case 5). The images are shown at the interval of 0.5 s after full inhalation to show the myocardial displacement due to respiration for diaphragm displacement $D = 1.5$.

kinetic modeling parameters the temporal changes of the activity along with the cardiac-respiratory motion must be incorporated.

In this work, we extended our previous work and applied our 6D reconstruction algorithm to reconstruct the dynamic cardiac SPECT data with realistic Monte Carlo simulation acquired by a slowly rotating gamma camera. The term "slowly rotating camera" here refers to the rate of rotation that is comparable or smaller than the tracer kinetics i.e., the wash-in and wash-out rates of the given radiotracer.

A major issue of the dynamic acquisition with rotating SPECT system is the inconsistency of the data, as there are only two views at a given time. Inconsistency would not be a problem during the late phase of the tracer dynamics once the activity distribution stabilizes in the myocardium. Myocardial radiotracers such as Tc-99m sestamibi or Tc-99m tetrofosmin, which are usually utilized in clinical SPECT, generally stabilizes 20 min after the injection. But for the dynamic acquisition, this is particularly challenging during the early phase of the blood-myocardial wash-in and wash-out exchanges. This problem is much more difficult in SPECT than for ring detector systems such as dynamic cardiac PET (43). To address this issue, we have developed a 4D reconstruction algorithm (7, 39) to

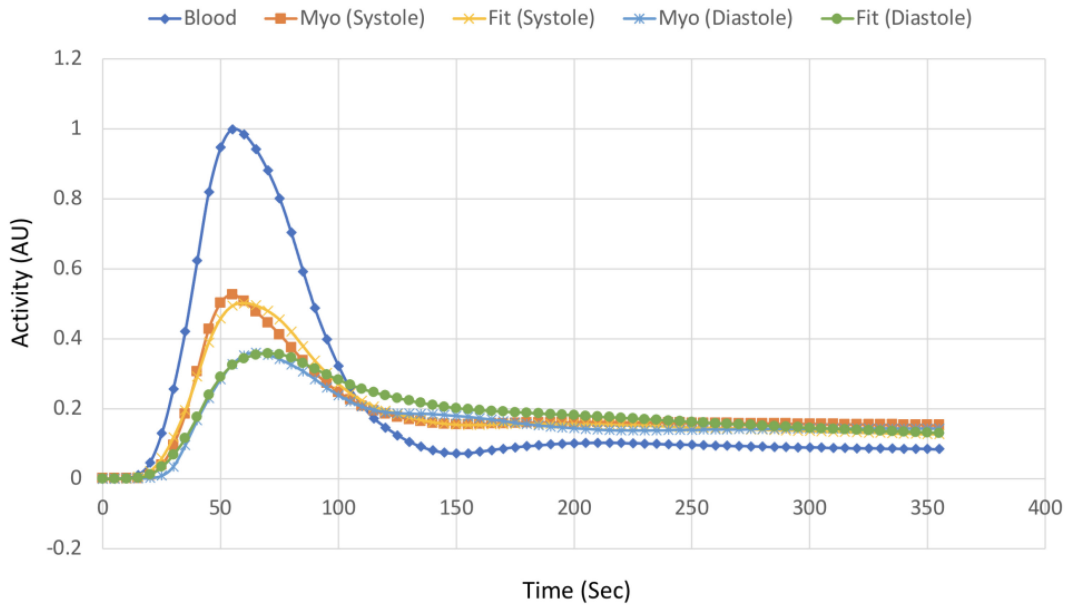

FIGURE 16 | TACs of the myocardium at systole and diastole phase and corresponding fits along with the input function (LV blood pool) for Case 1 study. The data was fitted with the 1TCM for the simulation using LV blood pool as an input function.

simultaneously solve a smooth time varying distribution of the tracer activity concentration in the myocardium using B-spline basis functions in both phantom and clinical patient studies (12), and extended the method to 6D by incorporating cardiac and respiratory motions (28).

In our previous algorithm (28), we used the tensor product of spatiotemporal basis functions (B-splines) and basis functions of the subspace of cardiac and respiratory phases (Gaussians) with synthetic data from the mathematical cardiac torso (MCAT) phantom generated by the forward projection of the cardiac torso using the same system matrix for a given detector configuration. This method had two major problems, mainly the computational complexity, as it requires the tensor products of 6 basis functions and the size of the system matrix which was assumed to be time independent. It should be noted that the system matrix for a cardiac-respiratory system is inherently time-dependent due to continuous motion of the heart and lungs. In order to simplify the problem, we decouple the cardiac and respiratory gates by translating the 6D problem into 4D while still capturing the cardiac and respiratory motions as well as tracer dynamics by acquiring the data in a continuous fashion. We used the more advanced 4D XCAT phantom (29) and Monte Carlo simulation to delineate a realistic clinical scenario of the myocardial perfusion imaging dynamics by incorporating cardiac and respiratory motion information.

We used the standard maximum likelihood expectation maximization (ML-EM) algorithm (44) for estimating the activity distribution. The ML-EM algorithm was successfully implemented in the past for modeling four-dimensional (4D) SPECT acquisition as well as for five-dimensional (5D) PET and SPECT acquisitions (45). The change of the radiotracer concentration in the myocardium is modeled using spatiotemporal cubic B-spline basis functions corresponding to each cardiac and respiratory gate. Spatiotemporal basis functions have been the basic building blocks to model the smooth variation of radiotracer distribution in space and time (39). Generally, the number of basis functions and their temporal extents (knots) can be optimized for an arterial input function. In all simulations we have used 9 basis functions optimized with the blood pool peak and wash-out rate in a patient's TAC.

Our group has also investigated in some detail the L-mode acquisition without cardiac respiratory gating for dynamic cardiac SPECT (46). In our previous work with the Philips Precedence SPECT/CT dual-headed scanner we demonstrated that a 1 min infusion with a two-headed SPECT system with L-mode acquisition rotating 180° every 54 s can produce reliable measurements of blood pool and myocardial TACs. The present work was to investigate a dynamic cardiac acquisition with our current GE Infinia Hawkeye clinical scanner with H-mode acquisition. Both H-mode and L-mode acquisitions present challenges in acquiring dynamic data. The L-mode acquisition provides more consistent views in a shorter time interval, whereas

TABLE 3 | Quantitative indices estimated using 1TCM at systole and diastole.

		K_1 (ml/g/min)	k_2 (1/min)	V_L (%)
Case 1	Systole	0.32	0.25	42
	Diastole	0.39	0.27	33
Case 2	Systole	0.28	0.23	45
	Diastole	0.31	0.26	34
Case 3	Systole	0.38	0.3	40
	Diastole	0.42	0.35	33
Ground truth		0.33	0.21	40

H-mode provides less consistent views in a time interval but more opposing views in a shorter time interval with additional attenuation information. In both cases it is necessary to correct for the attenuation in the projections. The purpose of the dynamic acquisition with continuous camera rotation is to develop a model for tracer kinetics that can capture as many views as possible for a given tracer concentration to avoid tomographic inconsistencies. We utilize a continuous camera rotation scheme with B-splines that smooth out the irregularities coming from under-sampled data (inconsistency). We have not simulated L-mode acquisition in this work, but it is interesting to see how these two acquisition methods compare.

Counterintuitively, in **Figure 12**, the SNR for TBR = 8 in the systolic phase is higher than for TBR = 10 but they are not statistically significant. There are many confounding factors including selection of ROI that may have caused this discrepancy. For MC simulation, we already know the segmented organ information from the 4D XCAT phantom. We therefore did not need the additional segmentation information during simulation and reconstruction. However, for the reconstructed image analysis a better segmentation will delineate a clear myocardium boundary. In this work we used a manual segmentation that may have caused this error.

Despite the limited angle reconstruction and non-homogeneity in the myocardium due to inconsistency, our gated reconstruction method faithfully reproduces the K_1 and k_2 values as derived from the conventional method without gate and the results are very close to the ground truth. This method also enables us to differentiate these dynamic parameters during different phases of the heart, though we do not know the clinical significance of these differences at this time. The higher k_2 value in the gated reconstruction compared to conventional ungated method seems to arise from the fact that we have simulated and fitted only up to 6 min of dynamic data out of a total of 20 min of acquisition in the patient study.

As described in our earlier publication (28), our method has some limitations on future clinical implementation. Our method requires a very large number of views and a sufficient number of cardiac-respiratory phases per rotation, with a small number of photons per pixel per view. This could significantly increase the noise in the system if the injected dose is small. For a sufficient number of photons per pixel, one has to increase the injection dose. Although this study was performed with realistic data generated by Monte Carlo simulation, it is still considered as a simulation. For example, even as we set different activities in different organs, only a few organs were considered in the simulations. There were significant liver scattering and background activities that were ignored in the simulation. Therefore, our results might be oversimplified. We did not test our method with real patient data because the current camera system does not provide gating information during a dynamic acquisition. A modification in clinical SPECT systems should be able to acquire dynamic cardiac and respiratory-gated data and this will be a future plan. We therefore believe that this method can be within the reach of clinical testing with real patient data.

CONCLUSION

Our study demonstrated the viability of using continuous image acquisition method on a widely used clinical two-head SPECT system by eliminating the dead time between the angles at consecutive detector positions. The continuous image acquisition for dynamic scan using conventional gamma cameras can provide valuable information to myocardial perfusion imaging. Precise implementation of reconstruction algorithms, better segmentation techniques by generating images of different tissue types and background activity would improve the feasibility of the method in real clinical environment.

DATA AVAILABILITY STATEMENT

The raw data supporting the conclusions of this article will be made available by the authors, without undue reservation.

AUTHOR CONTRIBUTIONS

YH: MC simulation and manuscript writing. US: reconstruction and manuscript writing. GG and YS: conceptualize the problem, design simulation, manuscript writing, and review. All authors contributed to the article and approved the submitted version.

FUNDING

This work was supported in part by the National Institutes of Health under grant nos. R01 EB026331, and R01 HL135490.

REFERENCES

1. Beller GA, Heede RC. SPECT imaging for detecting coronary artery disease and determining prognosis by noninvasive assessment of myocardial perfusion and myocardial viability. *J Cardiovasc Transl Res.* (2011) 4:416–24. doi: 10.1007/s12265-011-9290-2
2. Ueshima K, Yamashina A, Usami S, Yasuno S, Nishiyama O, Yamazaki T, et al. Prognostic value of myocardial perfusion SPECT images in combination with the maximal heart rate at exercise testing in Japanese patients with suspected ischemic heart disease: a sub-analysis of J-ACCESS. *Ann Nucl Med.* (2009) 23:849–54. doi: 10.1007/s12149-009-0315-8
3. Hachamovitch R, Berman DS, Kiat H, Cohen I, Cabico JA, Friedman J, et al. Exercise myocardial perfusion SPECT in patients without known coronary artery disease: incremental prognostic value and use in risk stratification. *Circulation.* (1996) 93:905–14. doi: 10.1161/01.cir.93.5.905
4. Slomka PJ, Miller RJH, Hu LH, Germano G, Berman DS. Solid-state detector SPECT myocardial perfusion imaging. *J Nucl Med.* (2019) 60:1194–204. doi: 10.2967/jnumed.118.220657
5. Kuhle WG, Porenta G, Huang SC, Buxton D, Gambhir SS, Hansen H, et al. Quantification of regional myocardial blood flow using 13N-ammonia and reoriented dynamic positron emission tomographic imaging. *Circulation.* (1992) 86:1004–17. doi: 10.1161/01.cir.86.3.1004

6. Di Carli M, Czernin J, Hoh CK, Gerbaudo VH, Brunken RC, Huang SC, et al. Relation among stenosis severity, myocardial blood flow, and flow reserve in patients with coronary artery disease. *Circulation.* (1995) 91:1944–51.
7. Gullberg GT, Reutter BW, Sitek A, Maltz JS, Budinger TF. Dynamic single photon emission computed tomography–basic principles and cardiac applications. *Phys Med Biol.* (2010) 55:R111–91. doi: 10.1088/0031-9155/55/20/R01
8. Alhassen F, Nguyen N, Bains S, Gould RG, Seo Y, Bacharach SL, et al. Myocardial blood flow measurement with a conventional dual-head SPECT/CT with spatiotemporal iterative reconstructions - a clinical feasibility study. *Am J Nucl Med Mol Imaging.* (2013) 4:53–9. Epub 2014/01/01.,
9. Wells RG, Timmins R, Klein R, Lockwood J, Marvin B, deKemp RA, et al. Dynamic SPECT measurement of absolute myocardial blood flow in a porcine model. *J Nucl Med.* (2014) 55:1685–91. doi: 10.2967/jnumed.114.139782
10. Ben-Haim S, Murthy VL, Breault C, Allie R, Sitek A, Roth N, et al. Quantification of myocardial perfusion reserve using dynamic SPECT imaging in humans: a feasibility study. *J Nucl Med.* (2013) 54:873–9. doi: 10.2967/jnumed.112.109652
11. Garcia EV, Faber TL, Esteves FP. Cardiac dedicated ultrafast SPECT cameras: new designs and clinical implications. *J Nucl Med.* (2011) 52:210–7. doi: 10.2967/jnumed.110.081323
12. Shrestha U, Sciammarella M, Alhassen F, Yeghiazarians Y, Ellin J, Verdin E, et al. Measurement of absolute myocardial blood flow in humans using dynamic cardiac SPECT and (99m)Tc-tetrofosmin: method and validation. *J Nucl Cardiol.* (2017) 24:268–77. doi: 10.1007/s12350-015-0320-3
13. Dorbala S, Ananthasubramaniam K, Armstrong IS, Chareonthaitawee P, DePuey EG, Einstein AJ, et al. Single photon emission computed tomography (SPECT) myocardial perfusion imaging guidelines: instrumentation, acquisition, processing, and interpretation. *J Nucl Cardiol.* (2018) 25:1784–846. doi: 10.1007/s12350-018-1283-y
14. Picone V, Makris N, Boutevin F, Roy S, Playe M, Soussan M. Clinical validation of time reduction strategy in continuous step-and-shoot mode during SPECT acquisition. *EJNMMI Phys.* (2021) 8:10. doi: 10.1186/s40658-021-00354-x
15. Bailly M, Le Rouzic G, Metrard G, Ribeiro MJ. Faster acquisition for dopamine transporter imaging using swiftscan step and shoot continuous SPECT without impairing visual and semiquantitative analysis. *Front Med.* (2020) 7:235. doi: 10.3389/fmed.2020.00235
16. Thibault F, Bailly M, Le Rouzic G, Metrard G. Clinical evaluation of general electric new Swiftscan solution in bone scintigraphy on NaI-camera: a head to head comparison with Siemens Symbia. *PLoS One.* (2019) 14:e0222490. doi: 10.1371/journal.pone.0222490
17. Kalisz K, Buethe J, Saboo SS, Abbara S, Halliburton S, Rajiah P. Artifacts at Cardiac CT: physics and Solutions. *Radiographics.* (2016) 36:2064–83. doi: 10.1148/rg.2016160079
18. Kovalski G, Israel O, Keidar Z, Frenkel A, Sachs J, Azhari H. Correction of heart motion due to respiration in clinical myocardial perfusion SPECT scans using respiratory gating. *J Nucl Med.* (2007) 48:630–6. Epub 2007/04/03.,
19. Nichols TE, Qi J, Asma E, Leahy RM. Spatiotemporal reconstruction of list-mode PET data. *IEEE Trans Med Imaging.* (2002) 21:396–404. doi: 10.1109/TMI.2002.1000263
20. Parker JG, Mair BA, Gilland DR. Respiratory motion correction in gated cardiac SPECT using quaternion-based, rigid-body registration. *Med Phys.* (2009) 36:4742–54. Epub 2009/11/26., doi: 10.1118/1.3215531
21. Livieratos L, Stegger L, Bloomfield PM, Schafers K, Bailey DL, Camici PG. Rigid-body transformation of list-mode projection data for respiratory motion correction in cardiac PET. *Phys Med Biol.* (2005) 50:3313–22. doi: 10.1088/0031-9155/50/14/008
22. Rahmim A, Tang J, Zaidi H. Four-dimensional (4D) image reconstruction strategies in dynamic PET: beyond conventional independent frame reconstruction. *Med Phys.* (2009) 36:3654–70. doi: 10.1118/1.3160108
23. Nam WH, Ahn IJ, Kim KM, Kim BI, Ra JB. Motion-compensated PET image reconstruction with respiratory-matched attenuation correction using two low-dose inhale and exhale CT images. *Phys Med Biol.* (2013) 58:7355–74. doi: 10.1088/0031-9155/58/20/7355
24. Bai W, Brady M. Regularized B-spline deformable registration for respiratory motion correction in PET images. *Phys Med Biol.* (2009) 54:2719–36. doi: 10.1088/0031-9155/54/9/008
25. Picard Y, Thompson CJ. Motion correction of PET images using multiple acquisition frames. *IEEE Trans Med Imaging.* (1997) 16:137–44. doi: 10.1109/42.563659
26. Mukherjee JM, McNamara JE, Johnson KL, Dey J, King MA. Estimation of rigid-body and respiratory motion of the heart from marker-tracking data for SPECT motion correction. *IEEE Trans Nucl Sci.* (2009) 56:147–55. doi: 10.1109/TNS.2008.2010319
27. Shi L, Lu Y, Wu J, Gallezot JD, Boutagy N, Thorn S, et al. Direct list mode parametric reconstruction for dynamic cardiac SPECT. *IEEE Trans Med Imaging.* (2020) 39:119–28. doi: 10.1109/TMI.2019.2921969
28. Shrestha UM, Seo Y, Botvinick EH, Gullberg GT. Image reconstruction in higher dimensions: myocardial perfusion imaging of tracer dynamics with cardiac motion due to deformation and respiration. *Phys Med Biol.* (2015) 60:8275–301. doi: 10.1088/0031-9155/60/21/8275
29. Segars WP, Veress AI, Sturgeon GM, Samei E. Incorporation of the living heart model into the 4D XCAT phantom for cardiac imaging research. *IEEE Trans Radiat Plasma Med Sci.* (2019) 3:54–60. doi: 10.1109/TRPMS.2018.2823060
30. Reader AJ, Verhaeghe J. 4D image reconstruction for emission tomography. *Phys Med Biol.* (2014) 59:R371–418. doi: 10.1088/0031-9155/59/22/R371
31. Rahmim A, Tang J, Zaidi H. Four-dimensional image reconstruction strategies in cardiac-gated and respiratory-gated PET imaging. *PET Clin.* (2013) 8:51–67. doi: 10.1016/j.cpet.2012.10.005
32. Jan S, Benoit D, Becheva E, Carlier T, Cassol F, Descourt P, et al. V6: a major enhancement of the GATE simulation platform enabling modelling of CT and radiotherapy. *Phys Med Biol.* (2011) 56:881–901. doi: 10.1088/0031-9155/56/4/001
33. Garcia M-P, Bert J, Benoit D, Bardiès M, Visvikis D. Accelerated GPU based SPECT monte carlo simulations. *Phys Med Biol.* (2016) 61:4001.
34. Koral KF, Swailem FM, Buchbinder S, Clinthorne NH, Rogers WL, Tsui BM. SPECT dual-energy-window Compton correction: scatter multiplier required for quantification. *J Nucl Med.* (1990) 31:90–8.
35. Luo J-Q, Koral KF, Ljungberg M, Floyd CE Jr., Jaszczak R. A monte carlo investigation of dual-energy-window scatter correction for volume-of-interest quantification in 99Tcm SPECT. *Phys Med Biol.* (1995) 40:181. doi: 10.1088/0031-9155/40/1/015
36. Segars WP, Sturgeon G, Mendonca S, Grimes J, Tsui BM. 4D XCAT phantom for multimodality imaging research. *Med Phys.* (2010) 37:4902–15.
37. Siddon RL. Fast calculation of the exact radiological path for a three-dimensional CT array. *Med Phys.* (1985) 12:252–5. doi: 10.1118/1.595715
38. Zeng GL, Gullberg GT. Iterative and analytical reconstruction algorithms for varying-focal-length cone-beam projections. *Phys Med Biol.* (1998) 43:811–21. doi: 10.1088/0031-9155/43/4/010
39. Reutter BW, Gullberg GT, Huesman RH. Direct least-squares estimation of spatiotemporal distributions from dynamic SPECT projections using a spatial segmentation and temporal B-splines. *IEEE Trans Med Imaging.* (2000) 19:434–50. doi: 10.1109/42.870254
40. Cabello J, Rafecas M. Comparison of basis functions for 3D PET reconstruction using a Monte Carlo system matrix. *Phys Med Biol.* (2012) 57:1759–77. doi: 10.1088/0031-9155/57/7/1759
41. Seo Y, Mari C, Hasegawa BH. Technological development and advances in single-photon emission computed tomography/computed tomography. *Semin Nucl Med.* (2008) 38:177–98. doi: 10.1053/j.semnuclmed.2008.01.001
42. Sciammarella M, Shrestha UM, Seo Y, Gullberg GT, Botvinick EH. A combined static-dynamic single-dose imaging protocol to compare quantitative dynamic SPECT with static conventional SPECT. *J Nucl Cardiol.* (2017) 26:763–71. doi: 10.1007/s12350-017-1016-7
43. Verhaeghe J, D'Asseler Y, Staelens S, Vandenberghe S, Lemahieu I. Reconstruction for gated dynamic cardiac PET imaging using a tensor product spline basis. *IEEE T Nucl Sci.* (2007) 54:80–91. doi: 10.1109/Tns.2006.888814
44. Shepp LA, Vardi Y. Maximum likelihood reconstruction for emission tomography. *IEEE Trans Med Imaging.* (1982) 1:113–22. doi: 10.1109/TMI.1982.4307558

45. Niu X, Yang Y, Jin M, Wernick MN, King MA. Regularized fully 5D reconstruction of cardiac gated dynamic SPECT images. *IEEE Trans Nucl Sci.* (2010) 57:1085–95. doi: 10.1109/TNS.2010.2047731
46. Winant CD, Aparici CM, Zelnik YR, Reutter BW, Sitek A, Bacharach SL, et al. Investigation of dynamic SPECT measurements of the arterial input function in human subjects using simulation, phantom and human studies. *Phys Med Biol.* (2012) 57:375–93. doi: 10.1088/0031-9155/57/2/375

Conflict of Interest: The authors declare that the research was conducted in the absence of any commercial or financial relationships that could be construed as a potential conflict of interest.

Publisher's Note: All claims expressed in this article are solely those of the authors and do not necessarily represent those of their affiliated organizations, or those of the publisher, the editors and the reviewers. Any product that may be evaluated in this article, or claim that may be made by its manufacturer, is not guaranteed or endorsed by the publisher.

frontiers | Frontiers in Cardiovascular Medicine

TYPE Methods
PUBLISHED 22 July 2022
DOI 10.3389/fcvm.2022.910120

OPEN ACCESS

EDITED BY
Marianne Schmid Daners,
ETH Zürich, Switzerland

REVIEWED BY
Manisha Singh,
Massachusetts Institute of Technology, United States
Seraina A. Dual,
KTH Royal Institute of Technology, Sweden

*CORRESPONDENCE
Aamir Hameed
aamirhameed@rcsi.ie

SPECIALTY SECTION
This article was submitted to General Cardiovascular Medicine, a section of the journal Frontiers in Cardiovascular Medicine

RECEIVED 31 March 2022
ACCEPTED 30 June 2022
PUBLISHED 22 July 2022

CITATION
Malone A, Gallagher S, Saidi J, Rizq G, O'Dowd E, Vallence D and Hameed A (2022) *In vitro* benchtop mock circulatory loop for heart failure with preserved ejection fraction emulation. *Front. Cardiovasc. Med.* 9:910120. doi: 10.3389/fcvm.2022.910120

In vitro benchtop mock circulatory loop for heart failure with preserved ejection fraction emulation

Andrew Malone[1], Sean Gallagher[2], Jemil Saidi[1], Gina Rizq[1,3], Enda O'Dowd[2], Derek Vallence[2] and Aamir Hameed [1,4]*

[1]Tissue Engineering Research Group, Department of Anatomy and Regenerative Medicine, The Royal College of Surgeons in Ireland (RCSI), University of Medicine and Health Sciences, Dublin, Ireland, [2]Medical Device Design, National College of Art and Design, Dublin, Ireland, [3]School of Medicine, The Royal College of Surgeons in Ireland (RCSI), University of Medicine and Health Sciences, Dublin, Ireland, [4]Trinity Centre for Biomedical Engineering, Trinity College Dublin, Dublin, Ireland

In this work, a novel mock circulatory loop (MCL) is presented that is capable of simulating both healthy cardiac function and Heart Failure with preserved Ejection Fraction (HFpEF). This MCL differs from others presented in the literature as it features two independently actuated heart chambers, representing the left atrium and the left ventricle. This is an important improvement over other designs as it allows for potential HFpEF treatments to be examined, not just in relation to their effect on the left ventricle but also on the left atrium. The aim of this work was to show that novel MCL designs could be developed to allow for testing of new mechanical circulatory support devices for the treatment of HFpEF. Two loop configurations are presented, one featuring hard PVC cylindrical chambers and one that features soft silicone chambers which are anatomically analogous to the native heart. We show that both MCLs are capable of simulating the onset of HFpEF with a sustained increase in diastolic pressure of 62.03% and a sustained decrease in end diastolic volume (EDV) of 14.24%.

KEYWORDS

Heart Failure with preserved Ejection Fraction (HFpEF), left atrium (LA), left ventricle (LV), mock circulation loop, electro-pneumatic regulator

Introduction

Heart Failure with Preserved Ejection Fraction (HFpEF) is one of two main phenotypes of Heart Failure (HF), the other being Heart Failure with Reduced Ejection Fraction (HFrEF). They are characterized by Left Ventricular ejection fraction (LVEF) $\geq$ 50% and LVEF $\leq$ 40%, respectively (1). HFpEF makes up approximately 50% of the HF population (2), a number that is expected to rise in the coming decades due to a combination of rising life expectancy, increased prevalence of metabolic disorders associated with this disease, and a lack of adequate therapies (2–6). This is despite the estimated economic burden associated with HFpEF predicted to $53.1 Billion in the United States by 2030 (7).

There is a clinical need for a robust *in vitro* testbed to develop technologies for the treatment of HFpEF. This is challenging as HFpEF is a multifactorial disease, typified by four phenotypes (8) which makes the simulation of the condition challenging. Previous attempts at developing a mock circulatory loop (MCL) have utilized single pneumatic chambers (9, 10), piston actuated *ex-vivo* hearts (11, 12), and external drive motors (13). The problems with *ex-vivo* heart models have been well documented; namely the rapid deterioration of electrophysiological and hemodynamic functions. One prominent *ex-vivo* model, the PhysioHeart^{TM} (Life-Tec Group, The Netherlands) has been shown to be able to maintain homeostasis for just 171.4 ± 54 min (14). In addition, the use of *ex-vivo* and *in-vivo* models is becoming the subject of a growing ethical debate on animal rights, further complicating their use (15). This has led to the growing adoption of *in vitro* MCLs as alternatives to *in-vivo* and *ex-vivo* heart models (16).

Swier et al. developed one of the earliest *in vitro* cardiac models in 1989 (17). This model consisted of a 50-cc polyurethane right ventricle connected to a horse-shoe shaped blood reservoir which drove blood pneumatically. Ideally, an *in vitro* cardiac model should accurately mimic the physiological or pathological conditions of the human heart, including the tissue structure, extracellular matrix network, orientation, and circulation (18). We can further stipulate that a given model should capture the physiological markers and processes of disease where the model is designed for testing treatment options for said disease.

No *in vitro* testbed has been developed that can both mimic the cardiac cycle and features two independently controlled cardiac chambers to fully simulate the hemodynamics of the left atrium and left ventricle during diastole. A fully simulated left atrium is superior to a simple compliance chamber or preload reservoir as it can be used to monitor and actively control the left atrial pressure, an important physiological parameter in HFpEF. This is also important as the dynamics of HFpEF are complex and crucially, any treatment for HFpEF would necessarily be required to operate in tandem with both left heart chambers to function successfully (19). The requirement for a robust *in vitro* testbed necessitates a dynamic two-chambered MCL which can be altered to limit diastolic filling of the left ventricle while maintaining a functional cardiac cycle.

This work aims to present a new bench top MCL which can mimic both healthy cardiac function and HFpEF conditions through the limiting of diastolic relaxation.

Materials and methods

For both designs the MCL was divided into two main sections. The "blood" loop, consisting of the left atrium, the left ventricle, and the vasculature (here meaning a simplified analog of the cardiovascular system outside of the left heart modeled using tubing and a tap to simulate peripheral resistance); and the air loop consisting of the pneumatic components to control the cardiac cycle. A schematic diagram of this apparatus is included in **Figure 1**.

The air loop for both MCLs consisted of a EMD400-41 pneumatic pressure supply (GCE Group Ltd., Sweden) connected *via* flexible PVC tubing (12 mm OD, Radionics Ltd., Ireland) to a filter, regulator, lubricator (FRL) unit consisting of an AMG350C-F04D water separator (SMC Pneumatics Corporation, Japan), an AF40-F04-A air filter (SMC Pneumatics Corporation, Japan), and an AR40-F04-1-B regulator (SMC Pneumatics Corporation, Japan). The FRL unit was then connected to an ITV1010-212BL5-X88 electro-pneumatic regulator (SMC Pneumatics Corporation, Japan) which delivered the final pressure into the system.

The electro-pneumatic regulator was set to deliver a pressure of 120 mm Hg through a T-junction to both cardiac chambers simultaneously. The chambers were also connected to two solenoid valves which were independently controlled using a transistor circuit and Arduino microprocessor (Arduino, Italy). By sending a signal *via* Arduino at a specific time interval, the two solenoids could be independently activated to vent their respective chamber, lowering the pressure, and cause blood to enter the chamber. When the solenoids deactivated the chamber repressurised and the blood was forced out, moving in a forward direction due to the presence of the PVC-U non-return valves.

Mock circulatory loop mark I (Mk 1) production

The heart chambers of the Mk I were constructed of two vertical sections of acrylic pipe (38 mm OD × 32 m ID, Radionics Ltd., Ireland) while the vasculature was formed with a loop of the same piping while peripheral resistance was simulated using a PVC-U two-way ball valve (Georg Fischer Ltd., Switzerland). Three PVC-U ball non-return valves (Georg Fischer Ltd., Switzerland) were added to the blood loop to maintain forward blood flow. One was positioned before the left atrium to prevent backflow into the vasculature during atrial systole; the other two valves were positioned analogously to the mitral and aortic valves.

Mock circulatory loop mark II (Mk II) production

Following initial testing with the MCL Mk I, work began on an updated MCL design which would incorporate anatomically realistic cardiac chambers, acquired from casting a porcine heart sourced in a local butcher. The MCL Mk I, while

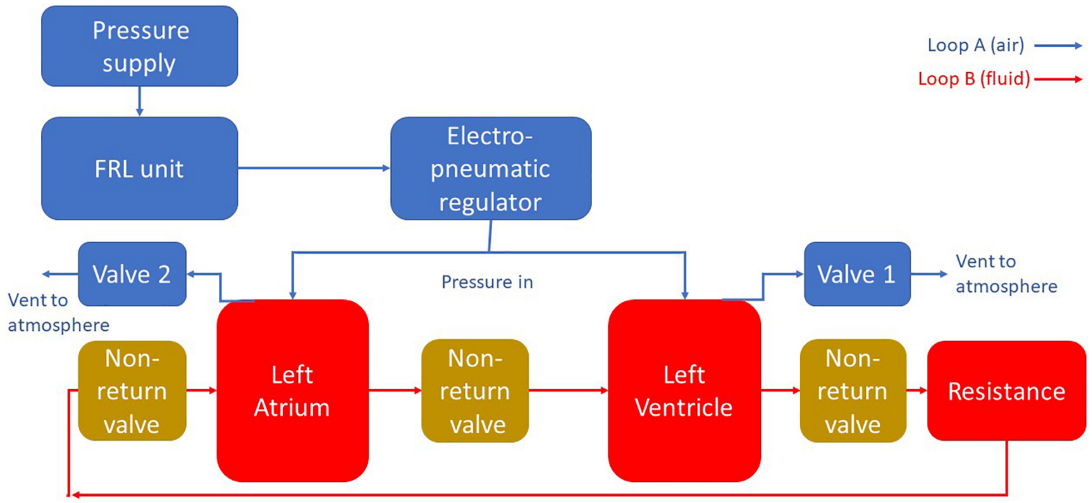

FIGURE 1
A schematic diagram of the MCL apparatus. Pressure is delivered to the chambers using pneumatic regulation. The flow in the blood loop is achieved by selectively pressurizing and depressurizing the heart chambers using solenoid valves. Backflow is prevented through the use of non-return valves.

FIGURE 2
The internal volume of the left ventricle was cast using room-temperature vulcanizing silicone. Chavant clay was used with attached tubing to form the core for the reverse molding of the RTV silicone. The silicone outer mold was then used to rapidly produce multiple cores made of paraffin wax. Finally, the final chamber model was produced by pouring Platsil Gel 10 silicone into the interstitial space between the larger mold and the wax core.

cheaper and easier to assemble, did not fully capture the anatomical geometry and structure of the heart, the updated Mk II design was developed to move closer to mimicking the situation *in vivo*. The internal space of the left ventricle was cast using room-temperature-vulcanizing (RTV) silicone. The silicone cast was used to model the geometry for a secondary cast made of Chavant modeling clay with a volume of 135 ml.

The negative space of the aorta was modeled using the outer diameter of the acrylic tubing used in the MCL Mk I, and a secondary piece of tubing was added to model the negative space of a connecting tube between the ventricle and the atrium. This secondary tube was used because this design of the MCL necessitated that the atrium and the left ventricle be physically separated. Using the Chavant clay and tubing as a core, a two-part reverse mold was produced using RTV silicone which was used to produce multiple ventricle cores from paraffin wax, approximately 10 mm of water-based clay was added to the Chavant core in layers to represent the myocardium of the left ventricle. A large two-part silicone reverse mold was produced using this core to provide an outer surface for the finished chamber (**Figure 2**).

Each wax core was painted with a thin layer of Platsil Gel 10 silicone and left to cure. This thin layer of silicone ensured that the final piece was fully watertight as well as ensuring that the core was not in direct contact with the wall of the outer mold. The painted wax core was placed into the outer mold and Platsil Gel 10 silicone was poured into the interstitial space between the core and the mold. Once set, the silicone cast was removed and placed upside-down in an oven at 180°C. The

wax core melted away after approximately 2 h, leaving only a hollow silicone ventricle model with two vessels representing the aorta and atrium attachment. The final dimensions of the silicone model were internal diameter = 5.9 ± 0.02 cm, internal length = 8.6 ± 0.02 cm, wall thickness = 1.0 ± 0.02 cm. To allow for two chambers to be operated, a second chamber was produced with a reduced internal volume to function as the left atrium. This was achieved in the same manner as the production of the ventricle but with a 15 mm layer of clay to create a smaller internal volume. The left atrium had dimensions of internal diameter = 4.8 ± 0.02 cm, internal length = 7.7 ± 0.02 cm, wall thickness = 1.6 ± 0.02 cm. The use of a second chamber provides a further advantage in that it can be modeled to represent the enlargement of the left atrium which is typically seen in HFpEF.

To allow for compression of the silicone heart chamber, the model was placed in a modified plastic container. A render of this design can be seen in **Figure 3**. The plastic container was chosen because it was a readily available, airtight vessel with a removable lid that was large enough to house the silicone ventricle. It was important that the testing assembly included a lid so that the device could be adjusted during testing. Using forstner drill bits, two holes were drilled into the side of the container and PVC tubing that was positioned in the holes. The tubing was then secured in place using hot glue. The silicone blood vessels were then pushed over the PVC tubing and secured in place using cable ties. Two additional holes were drilled into the side of the box so that compressed air could be pumped into the box using the pneumatic system and vented through the solenoid valve, respectively. The container was pressurized to a pressure of 20 kPa (~150 mm Hg) to overcome the stiffness of the silicone and deliver physiological pressure to the internal blood mimic.

Fluid enters the silicone left ventricle *via* the smaller diameter PVC inlet tube (15 mm). Compressed air is then injected into the box. This increased pressure causes the silicone ventricle to contract, forcing fluid out of the larger tube that represents the aorta. Backflow is prevented through the use of PVC-U non return valves as in the MCL Mk I design. During operation, air is vented out of the container, lowering the pressure, and allowing the silicone chamber to relax and refill with fluid.

Measurement of cardiac parameters

The two cardiac parameters of interest modeled by the MCL were volume and pressure. Pressure was measured using two 24PCBFA6G gauge pressure sensors (Honeywell International Inc., United States) connected to two INA125 instrumentation amplifiers (Texas Instruments Inc., United States). The output from the pressure sensors was read using an Arduino and instantaneous pressure values could be recorded from both cardiac chambers simultaneously. The baud rate of the Arduino was set at 115,200 bits/s.

Graduation marks were placed on the side of the chambers to allow for qualitative estimates of maximum and minimum volumes to be made by eye but the measurement of volume in the cardiac chambers was not possible quantitatively. Instead, volume was determined indirectly using Doppler ultrasound. An acoustic blood mimicking fluid (BMF) was produced using Orgasol© particles (2001UDNAT1, 5 μm diameter) based on work carried out by Ramnarine et al. (20). Three measurement sites were selected in the circulatory loop where blood velocities would be measured: immediately prior to the atrium (A), between the atrium and the ventricle (B), and immediately after the ventricle (C). Prior to measurement, the BMF was degassed, and the system allowed to run continuously for 1 h to ensure that no bubbles remained in the fluid.

A Logiq P6 ultrasound scanner (GE Healthcare, United States) with a broadband linear transducer (GE 11L) was used for determining the velocity of the BMF in pulsed wave spectral Doppler mode. A scanning well containing degassed water-glycerol (10% glycerol and 90% water) solution was used as an acoustic window between the transducer and the tubing. A beam-to-vessel angle of 60 was produced and the transducer face was positioned with a 20 mm layer of the water-glycerol solution separating it from the tubing. The B-mode image was adjusted to position the tubing in the center of the field of view, and the focal zone was set to the depth of the tubing in the middle of the image. The pulsed wave spectral Doppler mode was optimized by setting the Doppler gain to 65%, the Doppler range gate was set to 1 mm and positioned in the center of the tubing, the pulse repetition frequency was adjusted so that the Doppler spectrum encompassed 75% of the available spectrum window, and the wall filter was turned off. For each measurement site, five spectra were recorded of 4 s in duration each. These spectra were saved as JPEG files and exported to USB.

Custom code was developed in MATLAB (Mathworks, United States) to analyze the recorded Doppler spectra. First, the image was opened, and the user was asked to specify where the 0 and 100 cm/s graduations are in the image. This step had two purposes: the first was to calculate a pixel to velocity conversion factor and the second was to generate a scale bar in terms of pixels which the velocity spectrum will be compared against. A high pass filter was applied to the image to remove low level noise and isolate the pixel intensities of the spectrum. An edge detection algorithm was run on the image to trace the top of the velocity spectrum, which gave the maximum velocity with respect to time. The velocity information was then converted to volumetric flow rate by multiplying by the cross-sectional area of the tubing. Finally, the cumulative volume was determined using numerical trapezoidal integration on the volumetric flow rate. By comparing the cumulative volumes at

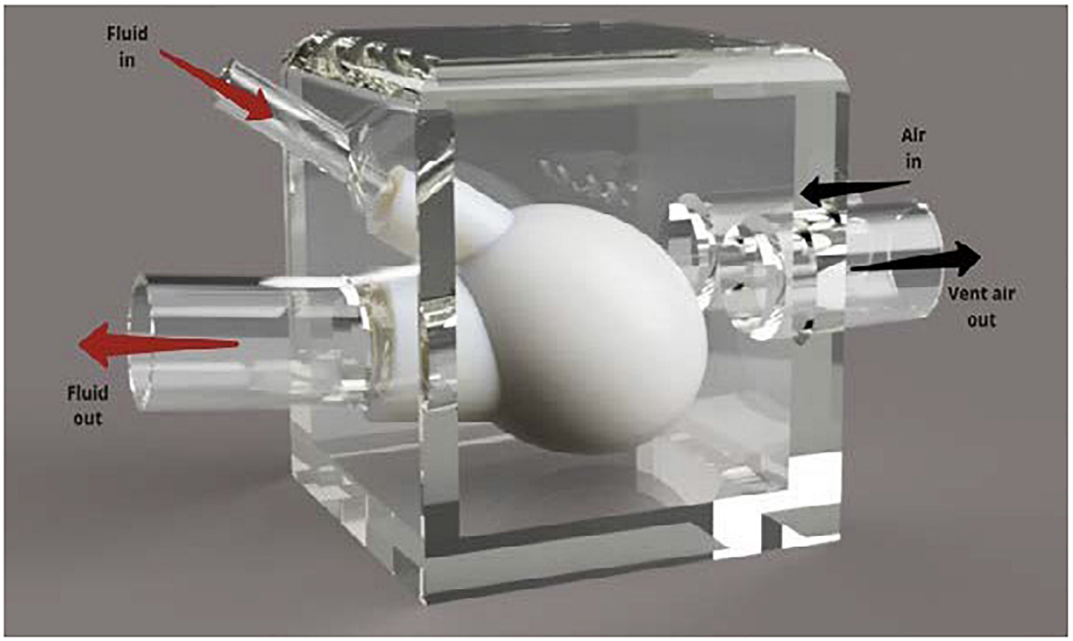

FIGURE 3
Annotated render of the silicone heart chamber inside a Tupperware container. The rigid plastic container was used to redirect the pressurized air to compress the heart chamber during systole.

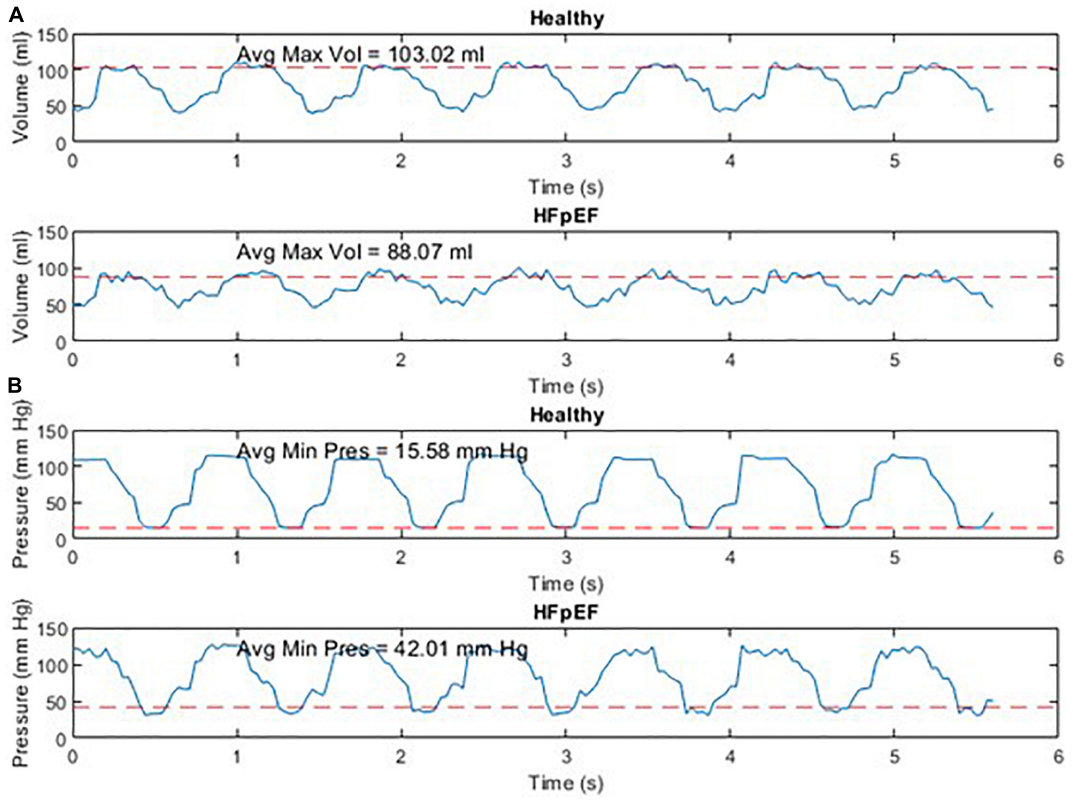

FIGURE 4
Instantaneous volume and instantaneous pressure for healthy cardiac function and for HFpEF for the Mk I MCL **(A)** and the Mk II MCL **(B)**.

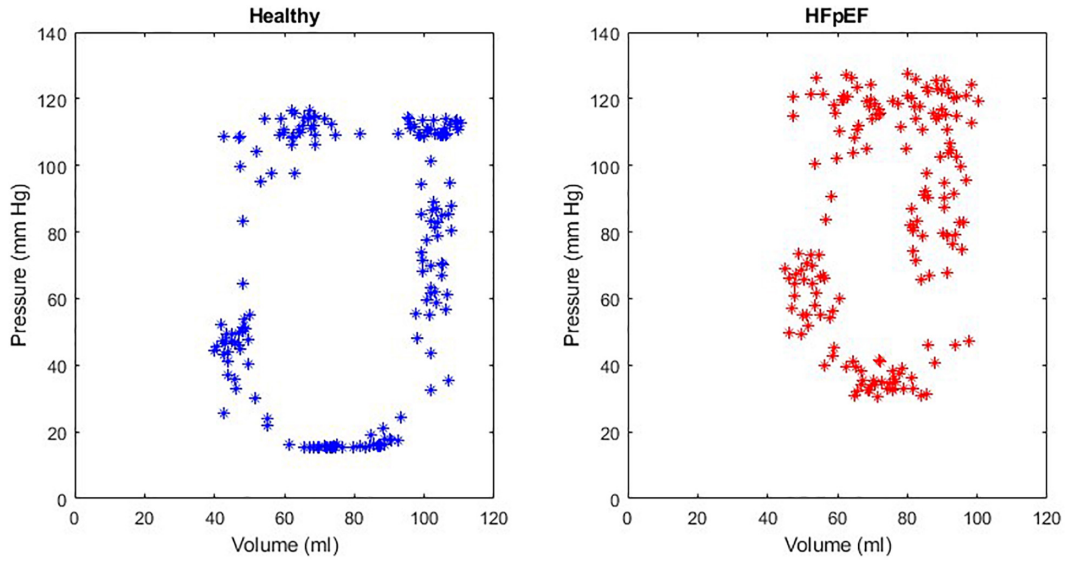

FIGURE 5
An example of a healthy PV loop and HFpEF PV loop generated from data recorded on the MCL Mk I.

the different measurement sites, cardiac chamber volumes could be determined as follows:

$$Vol_{LA} = CumVol_A - CumVol_B \quad (1)$$

$$Vol_{LV} = CumVol_B - CumVol_C \quad (2)$$

Where Vol_{LA} and Vol_{LV} are the volumes of the atrium and ventricle, respectively, and $CumVol_A$, $CumVol_B$, and $CumVol_C$ are the cumulative volumes at measurement sites A, B, and C, respectively.

Simulating heart failure with preserved ejection fraction

In both MCLs, it was possible to simulate heart failure with preserved ejection fraction (HFpEF) through the adjustment of the solenoid controls. HFpEF can be simulated through the following mechanism: As the diastolic phase of the cardiac cycle was initiated by venting pressure from the ventricle chamber itself (MCL Mk I) or the container housing the ventricle (MCL Mk II), reducing the amount of time that the solenoid valve was open for would result in an incomplete depressurization and insufficient ventricular filling.

This method of simulating HFpEF had the side effect of shortening the cardiac cycle as the length of diastole is decreased. In order to account for this when testing cardiac-gated medical devices, the response of the device must be adapted to match the change in heart rate. This was not seen as a problem for the testing of these devices as variable heart rate is to be expected *in vivo* and any device that is designed to operate at only certain points in the cardiac cycle should be capable of varying its duty cycle to match the current heart rate.

For both HFpEF and healthy cardiac function, the performance of each MCL was compared to each other using a paired *t*-test. The null hypothesis for this test was that the MCLs did not have any difference in performance at simulating both cardiac conditions and the alternative hypothesis was that the MCLs did perform differently. The significance level was set at $p < 0.05$.

Results

An example of the instantaneous volume and instantaneous pressure curves for healthy heart function and for HFpEF for the Mk I and Mk II MCLs is included in **Figure 4**. An example of a pressure volume (PV) loop produced from the MCL Mk I for both health cardiac function and for HFpEF is included in **Figure 5** and an example of a PV loop produced from the MCL Mk II for both health cardiac function and for HFpEF is included in **Figure 6**. The loops were produced by plotting the instantaneous pressure and volume against each other.

The performance of the MCL Mk I and Mk II was found to not be significantly different using a paired *t*-test ($p = 0.60$). The overall performance of both MCLs is presented in **Figure 7** which shows the difference in End Diastolic Volume (EDV) and diastolic pressure averaged over ten cardiac cycles between healthy function and HFpEF in the MCLs. It can be seen in **Figure 7** that when the reduction in diastolic duration is implemented, the average maximum volume decreases by 14.24% and the average minimum pressure increases by 62.03%.

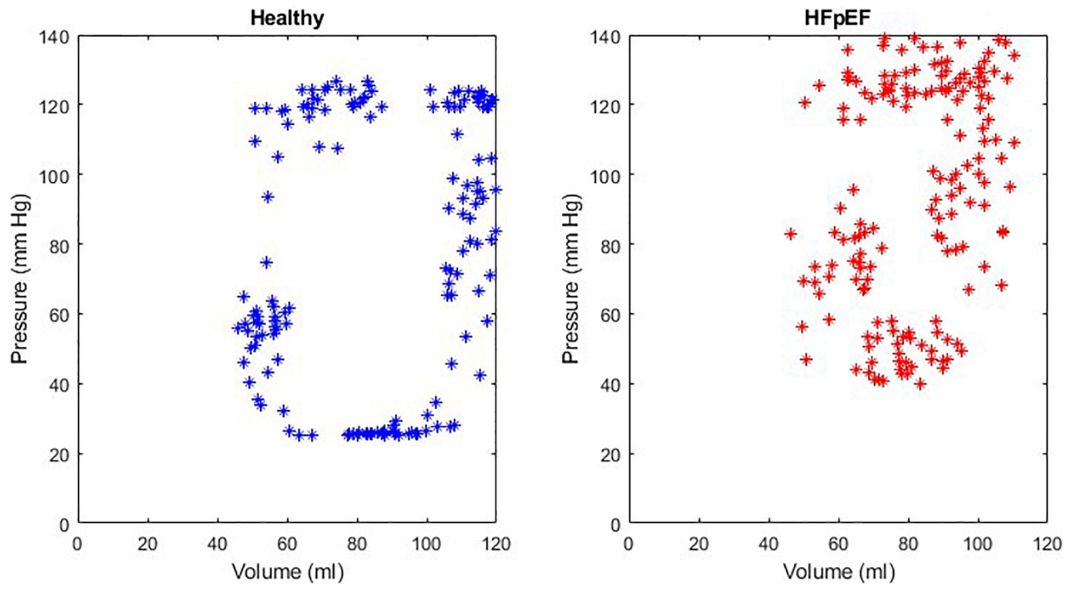

FIGURE 6
An example of a healthy PV loop and HFpEF PV loop generated from data recorded on the MCL Mk II.

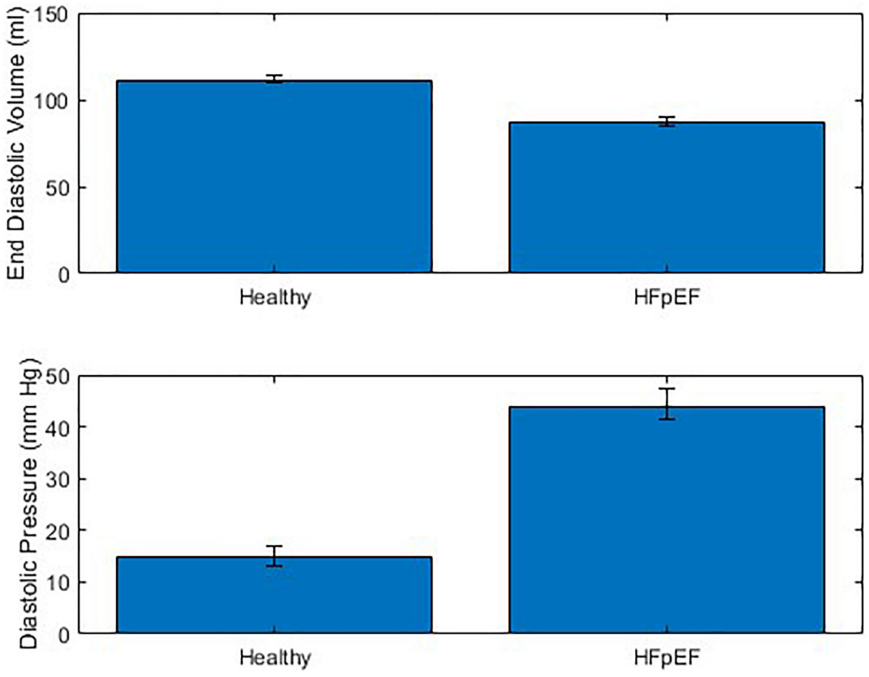

FIGURE 7
Combined performance of MCL Mk I and Mk II at simulating healthy cardiac function and HFpEF across 10 cardiac cycles ($N = 30$).

These values can be compared to values for end diastolic pressure and volume in the literature: The expected EDV decrease with HFpEF is from 121 (101–132) to 101 (86–105) as measured using echocardiography and the expected end diastolic pressure increase with HFpEF is from 8.0 (7.0–10.9) to 14.1 (10.6–18.0) (21). This is a volume decrease of 16.5% and a pressure increase of 43.26%.

While the MCL Mk II showed comparable results to the MCL Mk I but required additional pressure applied to the heart chambers to result in the same internal pressure

being applied to the blood. This was hypothesized to be due to the silicones inherent elasticity resisting the compression from the external pressure. For physiological pressure ranges, the required additional pressure was found to be a linear relationship and for all pressure values, a flat additional 10 mm Hg was sufficient to overcome the elasticity of the silicone.

An additional issue was noted with the MCL Mk II caused by the geometry of the silicone; because the chamber was modeled on cardiac anatomy but did not contain any cardiomyocytes, the thickness of the silicone was not proportional to the local cardiac contraction and was instead inversely proportional. This is due to the fact that *in vivo*, the thickest part of the myocardium is usually the strongest, whereas when using inert silicone, the thickness adds to the chambers overall elasticity and reduces overall compression. This meant that higher external pressures were required to compress the thickest parts of the cardiac chamber.

Discussion

A new MCL was presented for the purpose of early testing and validation of novel technologies for the treatment of HFpEF that interact only with the left side of the heart, such as circulatory support devices providing cannulation between the left atrium and left ventricle. Examples of devices which could be tested in this way are the mechanical circulatory support devices outlined by Rosalia et al. (1). Two models of the MCL were developed and assessed for their abilities to simulate HFpEF. The first MCL used vertical PVC columns as heart chambers and demonstrated the ability to adequately model both healthy cardiac function and HFpEF, while the second MCL used silicone heart chambers encased in plastic container to direct the applied pneumatic pressure. The MCLs were shown to not be significantly different in terms of performance and demonstrated a sustained increase in diastolic pressure of 62.03% and a sustained decrease in EDV of 14.24%. These results can be compared to literature values for end diastolic pressure and volume of 43.26 and 16.5%, respectively.

Miyagi et al. developed a similar MCL to that presented in this work for testing of the Left Atrial Assist Device (LAAD) for the treatment of HFpEF (9). In this study, Miyagi et al. used a mock ventricle (AB5000, ABIOMED Inc., Danvers, MA) in conjunction with a static blood reservoir representing the left atrium, and adjustable afterload and compliance simulators. Despite describing the AB5000 as a mock ventricle, the system is intended for use as a ventricular assist device, designed to provide temporary support to one or both sides of a patient's heart. While we could expect that output of this device to be broadly equivalent to that of an *in vivo* heart, it cannot be considered analogous to the human heart. Furthermore, the lack of an independently operating left atrium limits the testbed's ability to discern any treatments effect on the left atrium during its own cardiac cycle. Fukamachi et al. developed a similar MCL to Miyagi et al. using the same AB 5000 mock ventricle and static blood reservoir to represent the left ventricle and left atrium, respectively [Fukamachi et al., (10)]. Again, the issue with this design is the lack of any independent control over the left atrial pressure and the inability to examine any HFpEF treatments effect on the atrial cardiac parameters throughout diastole.

Leopaldi et al. developed a MCL using an *ex vivo* porcine heart model (11). The advantages of using an *ex vivo* model are clear, it allows for the most accurate representation of anatomical structures possible while still not having the same complexities associated with a full animal model. The primary disadvantage of using an *ex vivo* model is the limited lifespan of the model and requirement of replacing the model as the tissue degrade. This can lead to an inconsistent model geometry as models are replaced or inaccurate results due to altered mechanical properties in situations when *ex vivo* tissue is preserved to increase its lifespan. Furthermore, the model developed by Leopaldi et al. has a similar issue as discussed previously with Miyagi et al. and Fukamachi et al. namely the lack of an independently operated left atrium. In this study, the *ex vivo* heart is connected hydraulically to a piston pump *via* an apical connector and a preload reservoir representing the left atrium *via* an atrial connector. The atrial preload in this model is a constant, determined by the height of fluid in the reservoir. This makes it impossible to examine the performance of any HFpEF treatment in conjunction with atrial systole, which forms a key part of the left atrial hypertension seen alongside HFpEF (1).

Leopaldi et al. updated the MCL developed in a later work (12). This model again features an *ex vivo* porcine heart, which has been encased in a fluid filled chamber with a hydraulically connected piston pump. This model used a vacuum seal to ensure that the left ventricle could be isolated for independent actuation by the piston but again used a preload reservoir in place of the left atrium.

Liu et al. developed a MCL using a soft silicone model of the left ventricle based on CT images of a patient heart and thoracic aorta (13). The silicone model was placed inside an acrylic chamber and driven using an electric motor, although details on how this is achieved (be it direct actuation, pneumatic compression, or another method) are not given in the paper. This model is the similar to the MCL Mk II developed in this work and features a high degree of anatomical realism, although the study authors do note that they could not match the geometry of the native heart while it is pulsing. The MCL Liu et al. developed still lacks a left atrium and simply uses a preload reservoir as others have done. This again, limits the MCLs ability to examine any HFpEF treatment option in relation to the left atrium during diastole.

The literature on the development of MCLs shows a variety of approaches to mimic the anatomical structure of the heart for testing of HFpEF treatment options, however, most work

in this space is subject to the same issue, a lack of an independently controlled left atrium and left ventricle. This limits any MCLs ability to assess the effectiveness of proposed treatment options with regard to the left atrium and its pressure-volume relationship through the cardiac cycle but specifically during ventricular diastole and atrial systole.

A major limitation of this work was a lack of raw hemodynamic data to directly compare the performance of the MCLs to the conditions *in-vivo*. Although the authors could not acquire raw pressure and volume data to provide a direct comparison across the cardiac cycle, it was possible to compare values at the key time point of end-diastole. At this time point, the percentage decrease in volume and percentage increase in pressure were broadly in agreement, however, the magnitude of the pressure change was larger for the MCLs. This discrepancy is likely due to the peripheral resistance being too high, resulting in a higher pressure needed to achieve the required blood volume. A solution to this would be the use of larger diameter tubing as well as a reduction in the LV afterload applied in the experiment.

Another limitation was the requirement that HFpEF be implemented by shortening the diastolic filling duration during the cardiac cycle. This resulted in an elevated heart rate and prevented a direct comparison of the HFpEF and healthy systems with an equal heart rate without also varying the durations of other periods in the cardiac cycle for the healthy system. This problem could be solved in several ways: (1) by lengthening the other periods of the cardiac cycle proportionally, losing a temporally analogous heart rate but maintaining the relative intervals, (2) using pulse wave modulation (PWM) functionality and a compatible solenoid, the valve to the left ventricle could be only partially opened, reducing the pressure reduction achieved in the same time interval, (3) in the case of the Mk II rig, the compliance of the chamber could be reduced while keeping the cardiac cycle timings unchanged.

A further limitation is the inability to adequately model the heterogenous population of HFpEF patients. Future work in this space would need to more accurately model the peripheral impedance of patients and perhaps more extensively model the cardiovascular system.

Another limitation of this work was the requirement for a specially formulated BMF to allow ultrasonic measurement of flow and determine chamber volume from the flow differences. A simpler, albeit more expensive method would be the use of flow probes which use time of flight measurements to determine velocity (and can be calibrated for tube size to output flow rate) and do not require specific BMF.

Conclusion

The MCLs presented in this work are both are capable of simulating health heart function and can provide a method of mimicking HFpEF. Future iterations of this design have the potential to allow for full simulation of the spectrum of HFpEF severity. They both feature two chambers which can be independently controlled using a single pneumatic pressure source. They represent a key step forward in the development of a robust *in vitro* testbed for HFpEF treatments as well having potential for the simulation of other cardiac conditions which affect both the atria and the ventricles.

Data availability statement

The original contributions presented in this study are included in the article/supplementary material, further inquiries can be directed to the corresponding author.

Author contributions

AH, EO'D, and DV supervised and critically reviewed the manuscript. AM designed the *in vitro* rig and took a lead in writing the manuscript. SG developed the silicone heart model. JS and AM performed the experiments. JS and GR did the literature search and contributed toward writing the manuscript. All authors contributed to the article and approved the submitted version.

Funding

AH received funding from the Enterprise Ireland through their Commercialization Fund (grant no. CF-2019-1136-P), to develop a novel device based solution for HFpEF.

Conflict of interest

The authors declare that the research was conducted in the absence of any commercial or financial relationships that could be construed as a potential conflict of interest.

Publisher's note

References

1. Rosalia L, Ozturk C, Shoar S, Fan Y, Malone G, Cheema FH, et al. Device-based solutions to improve cardiac physiology and hemodynamics in heart failure with preserved ejection fraction. *JACC Basic to Transl Sci.* (2021) 6:772–95. doi: 10.1016/j.jacbts.2021.06.002

2. Oktay AA, Rich JD, Shah SJ. The emerging epidemic of heart failure with preserved ejection fraction. *Curr Hear Fail Rep.* (2013) 10:401–10. doi: 10.1007/s11897-013-0155-7

3. Borlaug BA. The pathophysiology of heart failure with preserved ejection fraction. *Nat Rev Cardiol.* (2014) 11:507–15. doi: 10.1038/nrcardio.2014.83

4. Borlaug BA, Paulus WJ. Heart failure with preserved ejection fraction: pathophysiology, diagnosis, and treatment. *Eur Heart J.* (2011) 32:670–9. doi: 10.1093/eurheartj/ehq426

5. Borlaug BA. Evaluation and management of heart failure with preserved ejection fraction. *Nat Rev Cardiol.* (2020) 17:559–73. doi: 10.1038/s41569-020-0363-2

6. Owan TE, Hodge DO, Herges RM, Jacobsen SJ, Roger VL, Redfield MM. Trends in prevalence and outcome of heart failure with preserved ejection fraction. *N Engl J Med.* (2009) 355:251–9. doi: 10.1056/NEJMoa052256

7. Heidenreich PA, Albert NM, Allen LA, Bluemke DA, Butler J, Fonarow GC, et al. Forecasting the impact of heart failure in the united states a policy statement from the American heart association. *Circ Hear Fail.* (2013) 6:606–19. doi: 10.1161/HHF.0b013e318291329a

8. Granegger M, Dave H, Knirsch W, Thamsen B, Schweiger M, Hübler M. A valveless pulsatile pump for the treatment of heart failure with preserved ejection fraction: a simulation study". *Cardiovasc Eng Technol.* (2018) 10:69–79. doi: 10.1007/s13239-018-00398-8

9. Miyagi C, Kuban BD, Flick CR, Polakowski AR, Miyamoto T, Karimov JH, et al. Left atrial assist device for heart failure with preserved ejection fraction: initial results with torque control mode in diastolic heart failure model. *Heart Fail Rev.* (2021) 1:1–10. doi: 10.1007/s10741-021-10117-6

10. Fukamachi K, Horvath DJ, Karimov JH, Kado Y, Miyamoto T, Kuban BD, et al. Left atrial assist device to treat patients with heart failure with preserved ejection fraction: initial in vitro study. *J Thorac Cardiovasc Surg.* (2021) 162:120–6. doi: 10.1016/j.jtcvs.2019.12.110

11. Leopaldi AM, Vismara R, Lemma M, Valerio L, Cervo M, Mangini A, et al. In vitro hemodynamics and valve imaging in passive beating hearts. *J Biomech.* (2012) 45:1133–9. doi: 10.1016/j.jbiomech.2012.02.007

12. Leopaldi AM, Vismara R, van Tuijl S, Redaelli A, van de Vosse FN, Fiore GB, et al. A novel passive left heart platform for device testing and research. *Med Eng Phys.* (2015) 37:361–6. doi: 10.1016/j.medengphy.2015.01.013

13. Liu G-M, Hou J-F, Wei R-J, Hu S-S. A 3-dimensional-printed left ventricle model incorporated into a mock circulatory loop to investigate hemodynamics inside a severely failing ventricle supported by a blood pump. *Artif Organs.* (2021) 45:143–50. doi: 10.1111/aor.13802

14. Kappler B, Ledezma CA, van Tuijl S, Meijborg V, Boukens BJ, Ergin B, et al. Investigating the physiology of normothermic ex vivo heart perfusion in an isolated slaughterhouse porcine model used for device testing and training. *BMC Cardiovasc Disord.* (2019) 19:254. doi: 10.1186/s12872-019-1242-9

15. Walker RL, Eggel M. From mice to monkeys? Beyond orthodox approaches to the ethics of animal model choice. *Animals.* (2020) 10:77. doi: 10.3390/ani10010077

16. Festing S, Wilkinson R. The ethics of animal research. Talking point on the use of animals in scientific research. *EMBO Rep.* (2007) 8:526–30. doi: 10.1038/sj.embor.7400993

17. Swier P, Bos WJ, Mohammad SF, Olsen DB, Kolff WJ. An in vitro test model to study the performance and thrombogenecity of cardiovascular devices. *ASAIO Trans.* (1989) 35:683–6. doi: 10.1097/00002480-198907000-00167

18. Mathur A, Ma Z, Loskill P, Jeeawoody S, Healy KE. In vitro cardiac tissue models: current status and future prospects. *Adv Drug Deliv Rev.* (2016) 96:203–13. doi: 10.1016/j.addr.2015.09.011

19. Burkhoff D, Maurer MS, Joseph SM, Rogers JG, Birati EY, Rame JE, et al. Left atrial decompression pump for severe heart failure with preserved ejection fraction: theoretical and clinical considerations. *JACC Heart Fail.* (2015) 3:275–82. doi: 10.1016/j.jchf.2014.10.011

20. Ramnarine KV, Nassiri DK, Hoskins PR, Lubbers J. Validation of a new blood-mimicking fluid for use in doppler flow test objects. *Ultrasound Med Biol.* (1998) 24:451–9. doi: 10.1016/s0301-5629(97)00277-9

21. Kasner M, Sinning D, Burkhoff D, Tschöpe C. Diastolic pressure-volume quotient (DPVQ) as a novel echocardiographic index for estimation of LV stiffness in HFpEF. *Clin Res Cardiol.* (2015) 104:955–63. doi: 10.1007/s00392-015-0863-y

frontiers | Frontiers in Cardiovascular Medicine

TYPE Original Research
PUBLISHED 01 August 2022
DOI 10.3389/fcvm.2022.895291

OPEN ACCESS

EDITED BY
Ellen T. Roche,
Massachusetts Institute of Technology,
United States

REVIEWED BY
Luca Rosalia,
Massachusetts Institute of Technology,
United States
Daniel Bautista-Salinas,
Imperial College London,
United Kingdom
Simon Dunham,
Cornell University, United States

*CORRESPONDENCE
Seraina A. Dual
seraina.dual@alumni.ethz.ch

SPECIALTY SECTION
This article was submitted to
General Cardiovascular Medicine,
a section of the journal
Frontiers in Cardiovascular Medicine

RECEIVED 13 March 2022
ACCEPTED 13 July 2022
PUBLISHED 01 August 2022

CITATION
Arduini M, Pham J, Marsden AL,
Chen IY, Ennis DB and Dual SA (2022)
Framework for patient-specific
simulation of hemodynamics in heart
failure with counterpulsation support.
Front. Cardiovasc. Med. 9:895291.
doi: 10.3389/fcvm.2022.895291

Framework for patient-specific simulation of hemodynamics in heart failure with counterpulsation support

Mattia Arduini[1], Jonathan Pham[2], Alison L. Marsden[3,4], Ian Y. Chen[5,6], Daniel B. Ennis[1,5,7] and Seraina A. Dual[1,5]*

[1]Department of Radiology, Stanford University, Palo Alto, CA, United States, [2]Mechanical Engineering, Stanford University, Palo Alto, CA, United States, [3]Department of Bioengineering, Stanford University, Palo Alto, CA, United States, [4]Department of Pediatrics, Stanford University, Palo Alto, CA, United States, [5]Cardiovascular Institute, Stanford University, Palo Alto, CA, United States, [6]Division of Medicine (Cardiology), Veterans Affairs Health Care System, Palo Alto, CA, United States, [7]Division of Radiology, Veterans Affairs Health Care System, Palo Alto, CA, United States

Despite being responsible for half of heart failure-related hospitalizations, heart failure with preserved ejection fraction (HFpEF) has limited evidence-based treatment options. Currently, a substantial clinical issue is that the disease etiology is very heterogenous with no patient-specific treatment options. Modeling can provide a framework for evaluating alternative treatment strategies. Counterpulsation strategies have the capacity to improve left ventricular diastolic filling by reducing systolic blood pressure and augmenting the diastolic pressure that drives coronary perfusion. Here, we propose a framework for testing the effectiveness of a soft robotic extra-aortic counterpulsation strategy using a patient-specific closed-loop hemodynamic lumped parameter model of a patient with HFpEF. The soft robotic device prototype was characterized experimentally in a physiologically pressurized (50–150 mmHg) soft silicone vessel and modeled as a combination of a pressure source and a capacitance. The patient-specific model was created using open-source software and validated against hemodynamics obtained by imaging of a patient (male, 87 years, HR = 60 bpm) with HFpEF. The impact of actuation timing on the flows and pressures as well as systolic function was analyzed. Good agreement between the patient-specific model and patient data was achieved with relative errors below 5% in all categories except for the diastolic aortic root pressure and the end systolic volume. The most effective reduction in systolic pressure compared to baseline (147 vs. 141 mmHg) was achieved when actuating 350 ms before systole. In this case, flow splits were preserved, and cardiac output was increased (5.17 vs. 5.34 L/min), resulting in increased blood flow to the coronaries (0.15 vs. 0.16 L/min). Both arterial elastance (0.77 vs. 0.74 mmHg/mL) and stroke work (11.8 vs. 10.6 kJ) were decreased compared to baseline, however left atrial pressure increased (11.2 vs. 11.5 mmHg). A higher actuation pressure is associated with higher systolic pressure reduction and slightly higher coronary flow. The soft robotic device prototype achieves reduced systolic pressure, reduced stroke work, slightly

increased coronary perfusion, but increased left atrial pressures in HFpEF patients. In future work, the framework could include additional physiological mechanisms, a larger patient cohort with HFpEF, and testing against clinically used devices.

KEYWORDS

HF, patient-specific, hemodynamics, lumped parameter, counterpulsation, McKibben, soft robot

1. Introduction

In heart failure (HF) the heart is unable to appropriately supply the receiving organs with blood, leading to over five million hospitalizations yearly (1–4). To date, we have limited evidence-based treatment options for patients with heart failure with preserved ejection fraction (HFpEF) even though they represent nearly half of the HF population (5). HFpEF is characterized by suboptimal filling of the LV during diastole due to lower compliance of the ventricular walls (6). The syndrome leads to higher LV pressure levels to obtain a certain LV volume than in healthy subjects (7). Consequently, patients experience dyspnea on exertion, reduced quality of life, and reduced life expectancy (6, 8).

Recent efforts have proposed multiple device-based treatment options such as the intra-atrial shunt device (9, 10), use of conventional left ventricular assist devices (11, 12) for atrial decompression, a valveless pulsatile left ventricular assist device (13), and a left atrial assist device (14). However, the development of treatment strategies for HFpEF is complicated by the heterogeneity in pathophysiologies and associated comorbidities (3, 15, 16). A recent study compared the above therapies for multiple cohorts of patients with HFpEF (17) and found that each treatment may be effective only in a sub-cohort of HFpEF. As an alternative to grouping patients, we aimed to present a framework for patient-specific testing of treatment strategies and use it to test the usefulness of aortic counterpulsation in HFpEF.

Counterpulsation is a treatment strategy often applied in HF with reduced ejection fraction (HFrEF), but understudied for its usefulness in HFpEF. Counterpulsation reduces afterload and systolic pressure, and increases coronary perfusion (18). Intra-aortic balloon pumps (IABPs) are the most commonly used form of counterpulsation; the device is placed in the descending aorta and directs diastolic blood flow toward the periphery (18). The risk factors of IABPs include vascular injury, embolic complications during deployment or removal, and bacterial infections (19), motivating a need for non-blood contacting extra-aortic actuation. The C-Pulse System (Nuwellis Inc., Eden Prairie, Mn) is an extra-aortic counterpulsation device for HF which has shown to reduce systolic pressure and afterload in clinical trials (20, 21). The hemodynamic benefits of counterpulsation, such as decreased systolic pressures and increased coronary filling, have previously been suggested in small cohorts to improve diastolic filling (22, 23). Potential benefits of counterpulsation in patients with HFpEF have not been previously assessed.

Patient-specific lumped parameter computational models provide a low-cost option for proof-of concept testing of innovative treatment options in interaction with the cardiovascular system. Lumped parameter computational models are efficient (24) and are particularly suitable for testing in heterogeneous patient populations as each component can be tuned to match anatomical and hemodynamic data in a patient-specific manner (25, 26). Given the heterogeneity of the HFpEF population, a patient-specific approach is particularly important to allow an extension to a patient cohort in the future.

We demonstrated and evaluated a framework (Figure 1) for prototyping a soft robotic device prototype and modeling its interaction with patient-specific HFpEF hemodynamics. An extra-aortic soft-robotic counterpulsation device prototype was characterized experimentally, as a part of this work. We assess the impact of this device prototype on lowering peak systolic pressures and increasing coronary filling using a closed-loop patient-specific lumped parameter model at different timings and actuation levels.

2. Materials and methods

2.1. Patient-specific lumped parameter model of HFpEF

We created a patient-specific lumped parameter model of the cardiovascular system tuned to the hemodynamics of a patient with HFpEF. The study was approved by the local IRB board. Aortic blood flows measurements were obtained by 2D phase contrast cardiac magnetic resonance imaging and blood pressures as upper arm cuff pressures within 1 h of acquisition (male, 87 years, HR = 60 bpm). The patient was selected based on high diastolic filling pressures assessed by echocardiography (Lat E/e' = 14.5, Med E/e' = 18.4 at/above 15), a criteria defined by the American Society of Echocardiography

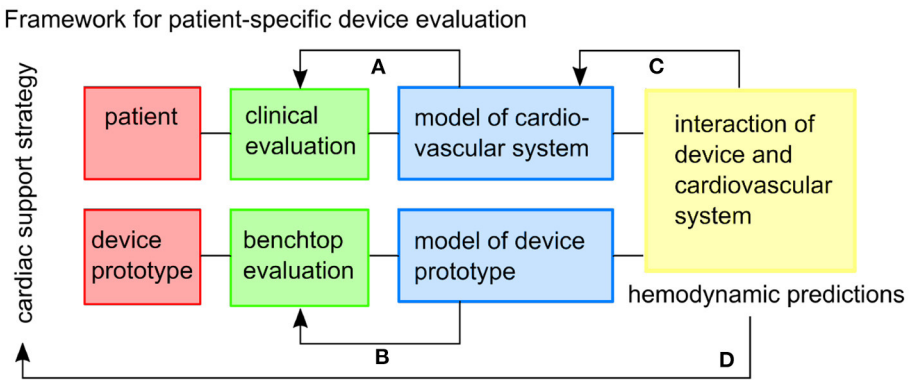

FIGURE 1
The framework envisioned for patient-specific testing of cardiac support strategies. Feedback within the framework includes: **(A)** the patient-specific cardiovascular model is tuned to the clinical data, **(B)** the model of the device prototype is informed by benchtop experiments, **(C)** the combined model might inform additional physiological mechanisms to be included in the cardiovascular model, **(D)** and hemodynamic predictions can inform the usefulness of the cardiac support strategy in the specific patient cohort.

and the European Association of Cardiovascular Imaging in (27). We utilized an estimate of end-diastolic pressure of 16 mmHg based on Lat E/e' = 14.5, Med E/e' = 18.4, a conversion proposed by Ommen et al. (28), as no invasive pressure data was available.

The computational model consisted of the vessels of the upper and lower bodies, the left heart and the valves (Figure 2) connected as a closed-loop. Each component was represented as a combination of resistors R representing the pressure drop caused by viscous losses, capacitors C capturing the elastance of the vessels, and inductances L modeling the inertial component of blood.

Initial conditions of pressure, flow, and volume for the first cardiac cycle were estimated using a minimum squared error function. The function starts solving for the initial conditions based on values found in literature. A time-periodic state is reached after five cardiac cycles.

2.1.1. The vessels

The lumped parameter model of the main arterial vessels (aortic arch) was created with the following steps. We first constructed an anatomic model using SimVascular (http://simvascular.github.io) (Point 1 in Figure 2) based on a computational tomography (CT) scan of the HFpEF patient. First, we drew pathlines along the centerlines of the arterial vessels of interest. We then segmented the CT scan by outlining each vessel lumen manually to produce 10 to 20 evenly spaced cross sections normal to the vessel centerlines (29). We then ran an automated script in SimVascular to calculate the resistances of each aortic branch vessel based on the average of its varying cross sectional area assuming Poiseuille flow (30). Each vessel element was reduced to three resistor sub-elements placed in series. At the end of each branch a resistor capacitor resistor (RCR) element tuned to achieve the patient's

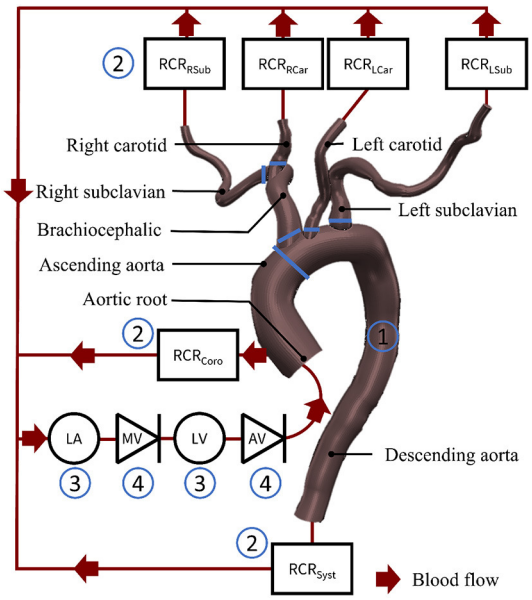

FIGURE 2
The lumped parameter model of the cardiovascular system, **(1)** is the aorta, **(2)** are the peripheral circulation elements, **(3)** are the chamber elements, **(4)** are the valve elements. LA, left atrium; MV, mitral valve; LV, left ventricle; AV, aortic valve; RCRRSub, resistance capacitance resistance element at the right subclavian artery; RCRRCar, resistance capacitance resistance element at the right carotid artery; RCRLCar, resistance capacitance resistance element at the left carotid artery; RCRLSub, resistance capacitance resistance element at the left subclavian artery; RCRCoro, resistance capacitance resistance element at the coronary arteries; RCRSyst, resistance capacitance resistance element of the systemic circulation.

flow splits represented the distal vasculature (including the microvasculature) (Point 2 in Figure 2). We assumed rigid vessel walls (29, 31).

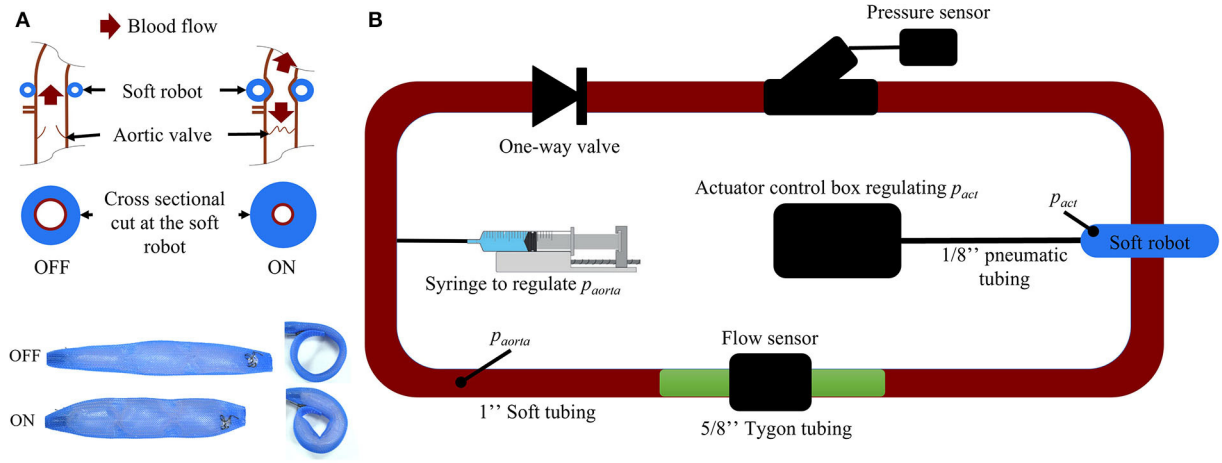

FIGURE 3
(A) Working mechanism of the soft robotic McKibben actuator on the ascending aorta. **(B)** Passive flow loop for the soft robot characterization [p_{aorta}, pressure inside the passive loop (mmHg); p_{act}, pressure inside the soft robot (psi)].

2.1.2. The left heart

A time-dependent elastance model relating pressure to volume (Point 3 in Figure 2) represented the left ventricle and atrium of the heart and was presented by Colacino et al. (32). Diastole and systole were modeled through a passive and an active pressure component.

2.1.3. The valves

The mitral valve (MV) and the aortic valve (AV) (Point 4 in Figure 2) were modeled as pressure-actuated valves (33). The modeled heart valves only allow the flow to go through when the pressure on the inlet side is higher than the pressure on the outlet side. The state $s(t)$ of the valve changes between 0 and 1 with 0 being a fully closed valve.

2.2. Lumped parameter model of the soft robot

The prototype of the soft robot is based on the McKibben actuator principle and consists of a single non-elastic pneumatically actuated bladder in a mesh which is wrapped around the ascending aorta (Figure 3A). When injecting a user-determined pressure p_{act}, the McKibben actuator will shorten circumferentially while thickening circumferentially and thus contract the aorta. The maximum width of the device prototype upon inflation is 12 mm. The inflation of the actuator induces a pressure on the ascending aorta, which in turn induces a change in volume inside the vessel. We used the capacitance-based approach proposed by Schampaert et al. to model the soft robot (34). The capacitor element receives an input by an experimentally defined pressure source p_{sr} composed of a contraction part followed by a relaxation part (Equation 1) mimicking the soft robot's effect on a vessel (Section 2.2.2).

2.2.1. Analytical definition

The parameters defining the soft robot actuation were the duration of the contraction t_{act}, the delay with respect to the beginning of the cardiac cycle δt_{act} (measured as R-wave of the electrocardiogram), the pressure inside the actuator p_{act}, and the pressure inside the aorta p_{aorta}. The duration of the actuator contraction was always 300 ms, such that for delays above 700 ms the actuator only deflated at the beginning of the next cycle. The duration of the contraction of the soft robot was t_{on} while t_{off} was the duration of a full actuation cycle including the relaxation. The times t_{on} and t_{off} varied for different p_{act} and were determined experimentally (Supplementary material). Our experimental results confirmed that a higher p_{act} leads to higher peak pressures while the peak pressure is reduced for higher p_{aorta}.

$$p_{sr}(t) = \begin{cases} \frac{p_{aorta}(t_{norm})}{1-g_{act}(p_{aorta},p_{act})} * (1 - g_{act} & \text{for } 0 \leq t_{norm} \leq t_{on} \\ (p_{aorta},p_{act}) * e^{-k_1 * t_{norm}}) & \\ c_2 * e^{-k_2 * (t_{norm} - t_{on})} + c_2 & \text{for } t_{on} < t_{norm} \leq t_{off} \\ 0 & \text{else} \end{cases} \quad (1)$$

here $t_{norm} = t - \lfloor \frac{t - \delta t_{act} * HR}{60} \rfloor * \frac{60}{HR} - \delta t_{act}$ is the time t normalized with respect to the cycle and actuation delay. $g_{act}(p_{aorta}, p_{act})$ is an experimental coefficient. Time coefficients k_1 and k_2 were determined experimentally and are equal to 13.04 and 34.66 respectively. δt_{act} is the delay of the soft robot

actuation. Coefficients c and d ensure continuity between the contraction and relaxations functions at moments t_{on} and t_{off}.

$$g_{act}(p_{act}, p_{aorta}) = a_1 * p_{aorta}^2 + a_2 * p_{aorta} + a_3 * p_{act} + a_4 + a_5 * p_{aorta} * p_{act} \quad (2)$$

where the coefficients a_1, a_2, a_3, a_4 and a_5 were obtained by minimizing the root mean square error (RMSE = $\sqrt{(g_{act} - g_{exp})^2}$) with respect to experimental data (g_{exp}) using the Curve Fitting Tool from MATLAB (Version R2020b, MathWorks, Natick, MA, USA).

2.2.2. Experimental characterization

To determine the coefficients of p_{sr}, a closed-, non-actuated loop filled with a glycerine-water (40–60%) mix mimicking the viscosity of blood (Figure 3A) was subjected to the contraction of the soft robot at 60 bpm with p_{act} at 6, 7, 8, 9, 10, 11, and 12 psi. The duration of actuation t_{act} was set to 300 ms which was previously found to be most effective in generating pressure between different parts of the cardiac cycle (35). We used 2.5 cm diameter silicone tubing (high-temperature silicone rubber, durometer 35A) with 1 mm wall thickness and total length of 2 m. A one-directional flow valve was used to inhibit back flow in the loop. The pressure p_{aorta} was tuned to 50, 60, 70, 80, 90, 100, 125, and 150 mmHg by changing the glycerine-water mixture volume in the loop *via* a syringe (Figure 3). No significant kinking of the silicone vessel wall was observed during actuation of the soft robot at $p_{aorta} = 75 mmHg$ as measured my magnetic resonance imaging (Supplementary material). Pressure and flow were measured using a pressure transducer (Mikro-Tip Catheter Transducer SPR-350s, Millar Inc., Houston, Texas, USA) and flow probe (ME14PXL294, Transonic Systems Inc., Ithaca, New York, USA). The measured data was recorded using the LabChart software (ADInstruments, Dunedin, New Zealand) and the PowerLab 8/35 combined with the Power Bridge Amp hardware (ADInstruments, Dunedin, New Zealand).

2.3. Coupling the patient-specific and soft robot lumped parameter models

The formulation of p_{sr} was validated through RMSE analysis (Supplementary material). After validating the patient-specific lumped parameter model through comparison with hemodynamic data, the soft robot lumped parameter element was added between the first two ascending aorta vessel elements of the patient-specific cardiovascular model. A difference in capacitance and resistance between the experimental set-up and the patient leading to a different peak p_{sr}. We solved this by multiplying p_{sr} by a correcting factor. The factor was determined for p_{aorta} = 100 mmHg. The resulting coupled system was solved numerically with a time step of 0.1 ms over 10 cardiac cycles.

TABLE 1 Patient data compared with the patient-specific closed-loop computational model (abs, absolute; press., pressure).

	Patient	Model	Δ (abs)	Δ (%)
Heart rate (bpm)	60	60	0	0
Diastolic aortic root press. (mmHg)	68	73	+5	+7
Systolic aortic root press. (mmHg)	150	147	−3	−2
Peak flow (mL/s)	266	267	+1	+1
Cardiac output (L/min)	5.17	5.17	0	0
Flow split (upper/lower body) (%)	29/71	30/70	1	1
End diastolic LV volume (mL)	116	119	+3	+3
End systolic LV volume (mL)	36	34	−2	−8
End diastolic LV press. (est.) (mmHG)	16	16	0	0

3. Results

3.1. Patient-specific model

The patient-specific lumped parameter model was validated through a comparison with key hemodynamic parameters of the *in vivo* patient data acquired through magnetic resonance imaging and echocardiogarphy (Table 1). Good agreement between the patient-specific model and patient data was achieved (relative error) for all important hemodynamic parameters such as diastolic aortic pressure (+7%), systolic aortic root pressures (+1%), peak flow (+1%), cardiac output (+0%), flow split (1%), end-diastolic volume (+3%) (Table 1).

The waveform as well as the peak flow rate of the model, presented in Figure 4A, match well with the flow measured in the HFpEF patient. The RMSE between the *in vivo* flow data and the patient-specific model calculated over a full cardiac cycle is 36.1 mL/s. The RMSE can be partly explained through the small time shift between both flow peaks. The modeled PV loop of the LV (Figure 4B) is composed of an isovolumetric pressure increase and decrease phases during LV contraction and relaxation as well as a small pressure increase during diastole. The flow splits into the main branches of the cardiovascular system are in line with the *in vivo* flow splits presented in literature (36). Moreover, the PV loop is closed, proving that the computational model has stabilized and is running identical cycles as it has reached a time periodic state.

3.2. The impact of the soft robotic device prototype on the patient

We present the influence of the actuator delay δt_{act} between 50 and 950 ms with a step of 50 ms and the different p_{sr} between 6 and 12 psi with a step of 2 psi on the patient where peak systolic pressure reduction, lower stroke work, and higher

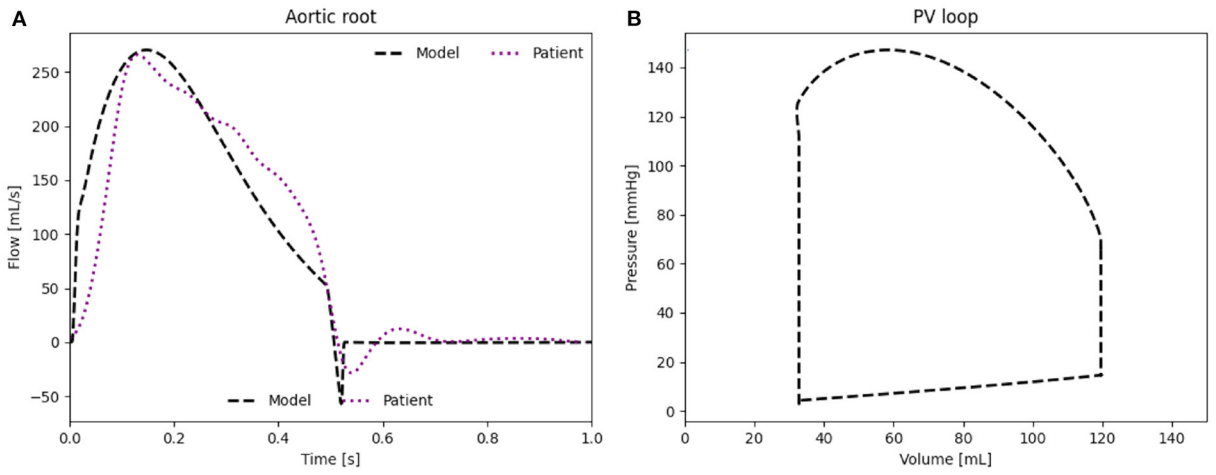

FIGURE 4
(A) Flow rate through the aortic root induced by the LV. **(B)** PV loop of the LV of the patient-specific model.

cardiac output are the key indicators for beneficial actuation of the soft robot.

An actuation delay of 650 ms results in maximal peak systolic pressure reductions (141 vs. 147 mmHg), allows for the highest cardiac output (5.34 vs. 5.17 L/min) and the lowest stroke work (10.6 kJ compared to 11.8 kJ) compared to baseline (Figure 5). In this optimal case, the arterial elastance EA ($EA = ESP/CO$, where ESP is the end systolic pressure) is also reduced compared to baseline. The delay of 650 ms together with 300 ms actuation time mean that the soft robot relaxes shortly after the start of the ventricular contraction. However, the left atrial pressure increases upon actuation (11.5 mmHg compared to 11.2 mmHg). On the contrary, the worst case actuation was found to be at a delay of 0 ms and thus occurring simultaneous to the ventricular contraction creating higher peak systolic pressure (164 vs. 147 mmHg) and stroke work (11.8 vs. 11.1 kJ).

When comparing the PV loops of the optimal and baseline settings we see that the diastolic filling volume is increased while the end systolic volume is decreased resulting in a larger stroke volume. Moreover, the peak systolic pressure is decreased (Figure 6). A second pressure and flow peak during diastole can be seen in all branches of the aorta in the optimal case (Figure 7). The pressure peak decays slowly over 0.3 s while the flow peak reaches its maximum after 0.1 s before disappearing after 0.2 s. The highest device-induced diastolic pressure increase at $p_{act} =$ 12 psi is seen in the coronary arteries (25 mmHg), followed by the carotid arteries (23 mmHg) and the descending aorta (11 mmHg). While, the overall cardiac output increased, this diastolic support did only lead to a small increase in coronary flow. In the worst case, the pressure and flow created by the soft robot adds up on top of the systolic activity of the heart, further increasing the afterload.

The flow splits toward the separate parts of the upper body are not known for the patient but their modeled values are presented in Table 2. The flow splits to the peripheral vessels remain similar to baseline in the optimal case. The soft robot increased absolute flows into each branch compared to baseline. The largest increase in flow is directed toward the descending aorta increasing the percentage of received flow. The absolute flow to the coronaries increased by six percent when the patient is supported by the extra-aortic support device.

3.3. The effect of actuator pressure

We note a higher diastolic pressure increase during diastole with a higher p_{sr} (Figure 8). In turn, this also leads to stronger reduction of peak systolic pressures. Similarly, the cardiac output increases with the higher p_{sr} (5.22 L/min at 6 psi, 5.26 L/min at 8 psi, 5.29 L/min at 10 psi, and 5.34 L/min at 12 psi).

4. Discussion

We created a patient-specific lumped parameter model of a HFpEF patient and a soft robotic extra-aortic counterpulsation device prototype to study the physiological implications of varying operating conditions. Full tuning to the patient-specific flow dynamics was achieved. We found that if operated in the optimal setting, we could achieve lower systolic pressure, a lower stroke work, and slightly improved perfusion of the coronaries at the cost of higher left atrial pressures.

This study evaluated a treatment strategy for HFpEF in a patient-specific model tuned to an individual subject. Previous work on modeling device-based treatment strategies in HFpEF

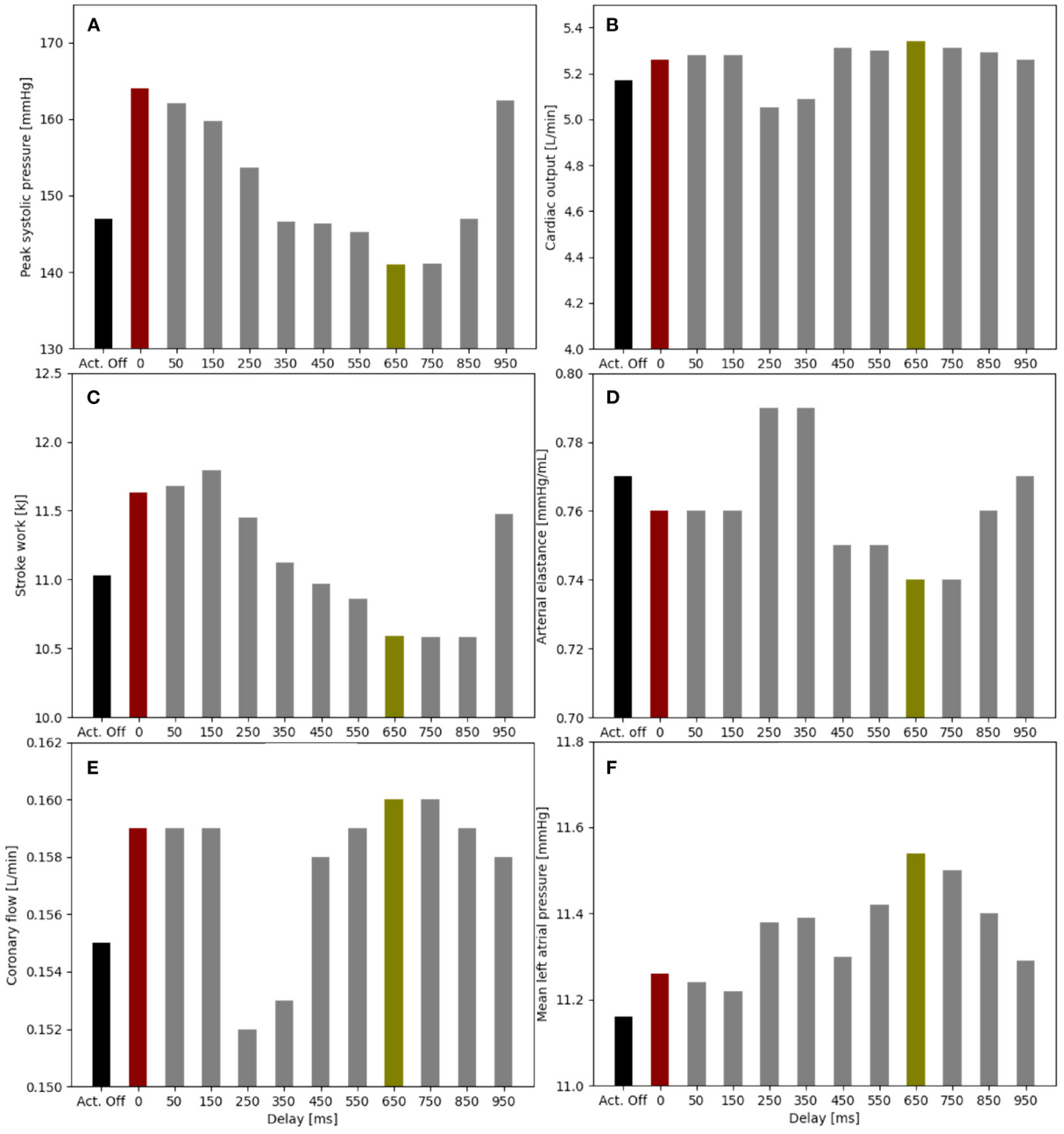

FIGURE 5
Impact of the soft robot delay on peak systolic pressure **(A)**, cardiac output **(B)**, stroke work **(C)**, arterial elastance **(D)**, coronary flow **(E)**, and mean left atrial pressure **(F)** ($p_{act} = 12$ psi). Optimal case for delay at 650 ms (green), baseline for actuator off (Act. Off) (black) and worst case for delay at 0 ms (red).

have focused on the use of averaged population characteristics and grouping based on hemodynamic phenotypes (11–14, 37). Burkhoff et al. extensively modeled four distinct phenotypes of HFpEF. The paper acknowledges that the group of patients with HFpEF induced by hypertension is highly variable in its hemodynamic characterization (11). We extended the prior population based approaches using an open-source computational framework to re-create a patient-specific hemodynamic model using the open-source framework Simvascular.

The device modeling was inspired by previous work on modeling counterpulsation devices in lumped parameter and 1D models (38, 39). Our approach informed the device model directly from an experimental analysis of the studied

counterpulsation device prototype. Combining the model of the device prototype and patient-specific model allowed for patient-specific simulations of their interaction, which is critical given the number of different pathophysiologies found in HFpEF. Our simulation allows one to tune the settings of any potential device to the needs of a specific patient. In the future, the computational model could also allow to predict treatment effects prior to implantation.

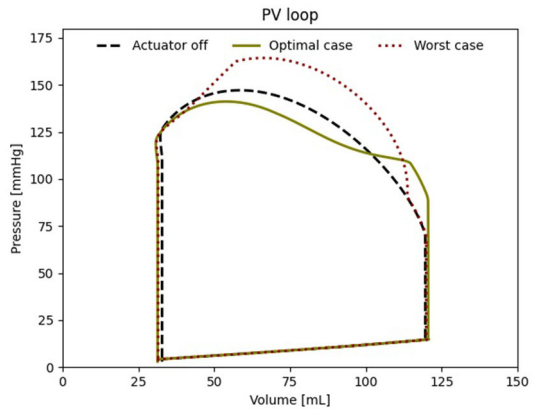

FIGURE 6
Left ventricular PV loop for the best case (650 ms delay), the worst case (000 ms delay) and baseline (p_{act} = 0 psi).

Using our simulation, we evaluated the effect of counterpulsation on the hemodynamics in HFpEF at different timings. When actuated during optimal setting actuation (p_{act} = 12 psi, delay = 650 ms), an additional diastolic pressure and flow waveform is observed in all cardiovascular branches, which is inline with previous studies (34). The effect on systolic aortic pressure is similar to previous *in vivo* studies about IABPs and the C-Pulse System, however the cardiac output is increased to a much lesser extent (18, 21, 39, 40). While the effect on decreasing aortic pressure is similar, the soft robotic device prototype covers a significantly smaller aortic arch length then

TABLE 2 Flow splits into the different parts of the cardiovascular system in the patient-specific model without and with support (delay = 650 ms) at 60 bpm, (CO, cardiac output; Abs., absolute).

	Actuator off		Optimal case	
CO (L/min)	5.17		5.34	
Vessel	**Abs. flow (L/min)**	**%**	**Abs. flow (L/min)**	**%**
Descending aorta	3.63	70.27	3.74	70.37
Coronaries	0.16	3.00	0.16	3.00
Right subclavian	0.38	7.45	0.39	7.42
Right carotid	0.47	9.18	0.49	9.15
Left subclavian	0.25	5.25	0.28	5.23
Left carotid	0.25	4.86	0.26	4.84

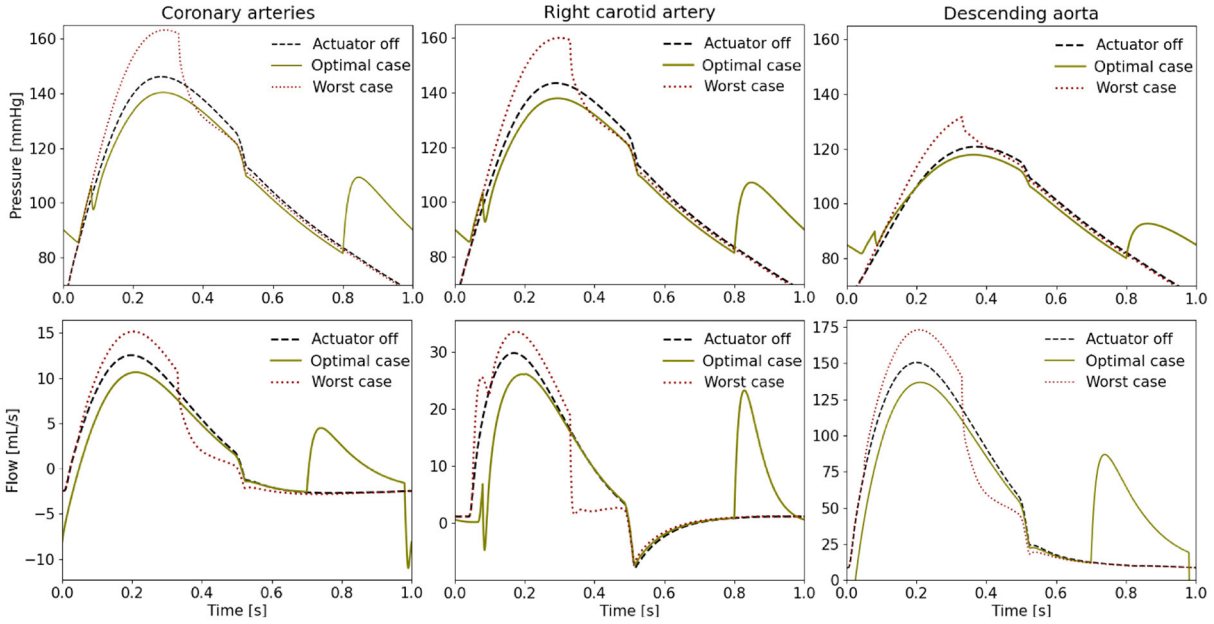

FIGURE 7
Pressure and flow waveforms in the coronary and carotid arteries and the descending aorta (p_{act} = 12 psi). All the measurements presented in this figure are made at the interaction of the last vessel element of the branch of interest and its proximal RCR element.

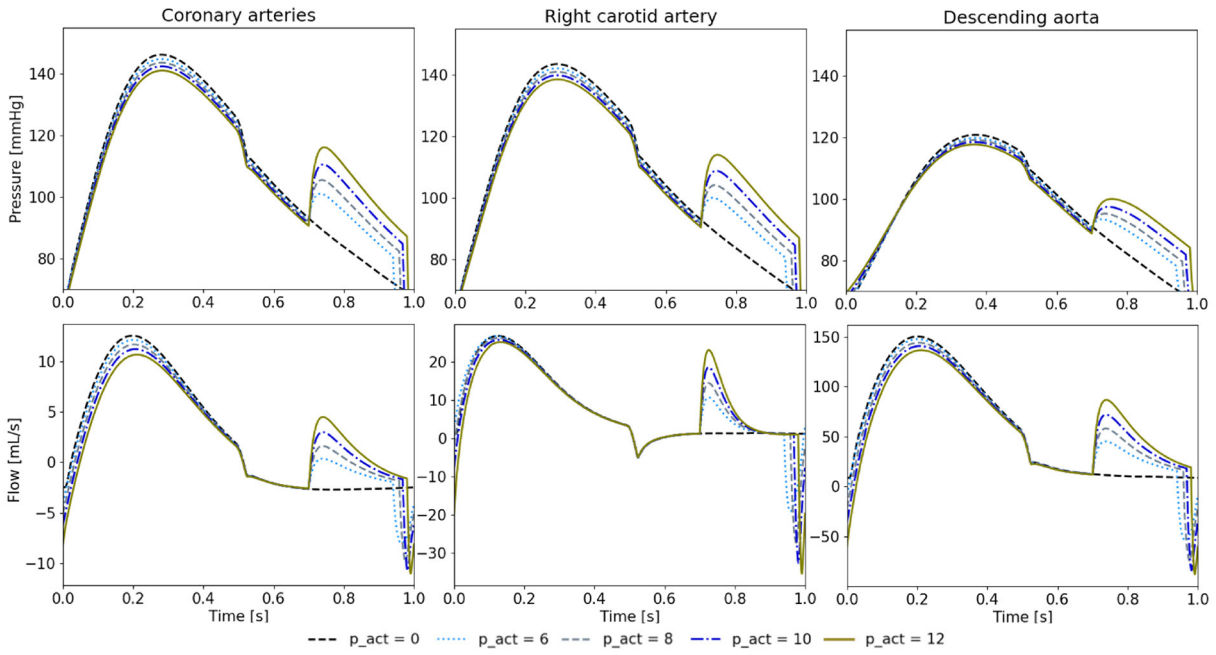

FIGURE 8
Pressure and flow waveforms in the coronary and carotid arteries and the descending aorta for 650 ms of delay and different p_{sr} in psi. All the measurements presented in this figure are made at the interaction of the last vessel element of the branch of interest and its proximal RCR element.

the C-pulse system. The small width of the actuator could allow for serial integration of multiple actuators in the future. Finally, we observed increased diastolic filling volume allowing for a larger stroke volume, however this comes at the cost of a higher left atrial pressure. In our simulation, the device is able to reduce the load on the heart, evidenced by the reduced stroke work.

The worst case actuation points toward the risks of the counterpulsation device with increased peak systolic pressure. A systolic actuation of the device can lead to an increase of peak systolic pressure by 17 mmHg, while the stroke work of the native heart increases by 0.7 kJ compared to baseline. The soft robotic actuator relies on accurate real-time sensing of the ventricular contraction to avoid harming the cardiovascular system, as has been shown in other pulsating soft robotic devices. While, the existing approaches to trigger IABPs might be useful for triggering of a soft robot, our results point toward the risks of pulsating technologies. In contrast to IABPs, the extra-aortic approach mitigates risks associated with infection and thromboembolic considerations, while several other risk factors will need to be addressed such as long-term functioning of the device as well as implications for the aortic valve.

We were also able to show the importance of the chosen p_{act} in tuning the effect of the soft robotic device prototype on the patient's physiology. A higher p_{act} led to lower systolic peak pressures as well as higher cardiac output. The ability to tune the impact allows for scenario-specific adaptation such as rest and exercise but also for gradual increase in support to the heart. Furthermore, a bridge to recovery application can be envisioned through support modulation. Based on the similarity of the flow waveforms between the soft robot and IABPs, no impact on cerebral function is expected (41).

Clinical considerations: The usefulness of counterpulsation strategies is highly debated (35). While IABP are used to bridge patients with HFrEF effectively, the underlying physiological mechanism remain unclear. The current recommendation made by the American College of Cardiology, the American Heart Association, and the Heart Failure Society of America is to lower the systolic blood pressure (SBP) under 130 mmHg for HFpEF patients with hypertension (42). However, Zouein et al. have shown antihypertensive medication to be ineffective in diminishing mortality in patients with HFpEF (4). If lowering systolic pressure (afterload) is beneficial in HFpEF, our study suggest that extra-aortic counterpulsation could be beneficial. However, the design of the current device prototype requires further optimization in order to displace sufficient volume.

Limitations: The study constitutes a framework for patient-specific hemodynamic modeling of device based treatment. The cohort of patients will need to be increased to cover a larger variety of patients as well as the heterogeneity in pathophysiology found in HFpEF. Moreover, the simulation currently lacks integration of the autoregulatory control mechanisms such as the baroreflex as well as coronary blood

flow regulations. Furthermore, the effect of the silicon vessel on the evaluation of the soft robots was not specifically addressed in this work. Ongoing experimental work and *in-vivo* trials with the soft robotic actuator will enable further validation of the findings of the lumped parameter model presented.

Data availability statement

The original contributions presented in the study are included in the article/Supplementary material, further inquiries can be directed to the corresponding author/s.

Ethics statement

The studies involving human participants were reviewed and approved by IRB Veteran Association Palo Alto. The patients/participants provided their written informed consent to participate in this study.

Author contributions

MA, DE, SD, and IC contributed to conception and design of the study. IC organized the data acquisition and provided clinical context. MA and SD performed the experiments and wrote the first draft of the manuscript. JP and AM provided access to the original code. All authors contributed to manuscript revision, read, and approved the submitted version.

Funding

SD received funding from the Swiss National Research Foundation P2EZP2_188964. SD, IC, and DE received funding from the NIH grant RO1 HL131823. AM and JP received funding from NIH grants R01EB029362 and R01EB018302.

Conflict of interest

The authors declare that the research was conducted in the absence of any commercial or financial relationships that could be construed as a potential conflict of interest.

Publisher's note

All claims expressed in this article are solely those of the authors and do not necessarily represent those of their affiliated organizations, or those of the publisher, the editors and the reviewers. Any product that may be evaluated in this article, or claim that may be made by its manufacturer, is not guaranteed or endorsed by the publisher.

Supplementary material

The Supplementary Material for this article can be found online at: https://www.frontiersin.org/articles/10.3389/fcvm.2022.895291/full#supplementary-material

References

1. Savarese G, Lund LH. Global public health burden of heart failure. *Cardiac Fail Rev*. (2017) 3:7. doi: 10.15420/cfr.2016:25:2

2. Lekavich CL, Barksdale DJ, Neelon V, Wu JR. Heart failure preserved ejection fraction (HFpEF): an integrated and strategic review. *Heart Fail Rev*. (2015) 20:643–53. doi: 10.1007/s10741-015-9506-7

3. Shah KS, Xu H, Matsouaka RA, Bhatt DL, Heidenreich PA, Hernandez AF, et al. Heart failure with preserved, borderline, and reduced ejection fraction: 5-year outcomes. *J Am Coll Cardiol*. (2017) 70:2476–86. doi: 10.1016/j.jacc.2017.08.074

4. Zouein FA, de Castro Brás LE, da Costa DV. Heart failure with preserved ejection fraction: emerging drug strategies. *J Cardiovasc Pharmacol*. (2013) 62:s13–21. doi: 10.1097/FJC.0b013e31829a4e61

5. Roh J, Houstis N, Rosenzweig A. Why don't we have proven treatments for HFpEF? *Circ Res*. (2018) 120:1243–5. doi: 10.1161/CIRCRESAHA.116.310119

6. Borlaug BA. The pathophysiology of heart failure with preserved ejection fraction. *Nat Rev Cardiol*. (2014) 11:507–15. doi: 10.1038/nrcardio.2014.83

7. Yancy CW, Jessup M, Bozkurt B, Butler J, Casey DE, Drazner MH, et al. 2013 ACCF/AHA guideline for the management of heart failure: A report of the American College of Cardiology Foundation/American Heart Association Task Force on practice guidelines. *J Am Coll Cardiol*. (2013) 61:e147–e239. doi: 10.1161/CIR.0b013e31829e8776

8. Oktay AA, Rich JD, Shah SJ. The emerging epidemic of heart failure with preserved ejection fraction. *Curr Heart Fail Rep*. (2013) 10:401–10. doi: 10.1007/s11897-013-0155-7

9. Feldman T, Mauri L, Kahwash R, Litwin S, Ricciardi MJ, Van Der Harst P, et al. Transcatheter interatrial shunt device for the treatment of heart failure with preserved ejection fraction (REDUCE LAP-HF i [reduce elevated left atrial pressure in patients with heart failure]): a phase 2, randomized, sham-controlled trial. *Circulation*. (2018) 137:364–75. doi: 10.1161/CIRCULATIONAHA.117.032094

10. Shah SJ, Feldman T, Ricciardi MJ, Kahwash R, Lilly S, Litwin S, et al. One-year safety and clinical outcomes of a transcatheter interatrial shunt device for the treatment of heart failure with preserved ejection fraction in the reduce elevated left atrial pressure in patients with heart failure (REDUCE LAP-HF I) trial: a randomized clinical trial. *JAMA Cardiol*. (2018) 3:968–77. doi: 10.1001/jamacardio.2018.2936

11. Burkhoff D, Maurer MS, Joseph SM, Rogers JG, Birati EY, Rame JE, et al. Left atrial decompression pump for severe heart failure with preserved ejection fraction: theoretical and clinical considerations. *JACC Heart Fail*. (2015) 3:275–82. doi: 10.1016/j.jchf.2014.10.011

12. Moscato F, Wirrmann C, Granegger M, Eskandary F, Zimpfer D, Schima H. Use of continuous flow ventricular assist devices in patients with heart failure and a normal ejection fraction: a computer-simulation study. *J Thorac Cardiovasc Surg*. (2013) 145:1352–8. doi: 10.1016/j.jtcvs.2012.06.057

13. Escher A, Choi Y, Callaghan F, Thamsen B, Kertzscher U, Schweiger M, et al. A valveless pulsatile pump for heart failure with preserved ejection fraction: hemo- and fluid dynamic feasibility. *Ann Biomed Eng*. (2020) 48:1821–36. doi: 10.1007/s10439-020-02492-2

14. Fukamachi K, Horvath DJ, Karimov JH, Kado Y, Miyamoto T, Kuban BD, et al. Left atrial assist device to treat patients with heart failure with preserved ejection fraction: initial *in vitro* study. *J Thorac Cardiovasc Surg*. (2021) 162:120–6. doi: 10.1016/j.jtcvs.2019.12.110

15. Gevaert AB, Boen JRA, Segers VF, Van Craenenbroeck EM. Heart failure with preserved ejection fraction: a review of cardiac and noncardiac pathophysiology. *Front Physiol*. (2019) 10:638. doi: 10.3389/fphys.2019.00638

16. Maurer MS, King DL, Rumbarger LEK, Packer M, Burkhoff D. Left heart failure with a normal ejection fraction: identification of different pathophysiologic mechanisms. *J Cardiac Fail*. (2005) 11 3:177–87. doi: 10.1016/j.cardfail.2004.10.006

17. Granegger M, Gross C, Siemer D, Escher A, Sandner S, Schweiger M, et al. Comparison of device-based therapy options for heart failure with preserved ejection fraction: a simulation study. *Sci Rep*. (2022) 12:1–10. doi: 10.1038/s41598-022-09637-4

18. Bajan K. Intra-aortic balloon pump. In: Chawla R, Todi S, editors. *ICU Protocols: A Step-wise Approach*. vol 2. Singapore: Springer (2020). p. 509–17. doi: 10.1007/978-981-15-0902-5_50

19. Parissis H, Soo A, Al-Alao B. Intra aortic balloon pump: literature review of risk factors related to complications of the intraaortic balloon pump. *J Cardiothorac Surg*. (2011) 6:147. doi: 10.1186/1749-8090-6-147

20. Cheng A, Monreal G, William ML, Sobieski M, Slaughter MS. Extended extra-aortic counterpulsation with the c-pulse device does not alter aortic wall structure. *ASAIO J*. (2014) 60:e5–7. doi: 10.1097/MAT.0000000000000131

21. Abraham WT, Aggarwal S, Prabhu SD, Cecere R, Pamboukian SV, Bank AJ, et al. Ambulatory extra-aortic counterpulsation in patients with moderate to severe chronic heart failure. *JACC Heart Fail*. (2014) 2:526–33. doi: 10.1016/j.jchf.2014.04.014

22. Malliaras K, Charitos E, Diakos N, Pozios I, Papalois A, Terrovitis J, et al. Effects of intra-aortic balloon pump counterpulsation on left ventricular mechanoenergetics in a porcine model of acute ischemic heart failure. *J Cardiovasc Transl Res*. (2014) 7:810–20. doi: 10.1007/s12265-014-9600-6

23. Khir AW, Price S, Henein MY, Parker KH, Pepper JR. Intra-aortic balloon pumping: Effects on left ventricular diastolic function. *Eur J Cardio Thorac Surg*. (2003) 24:277–82. doi: 10.1016/S1010-7940(03)00268-9

24. Marsden AL, Bazilevs Y, Long CC, Behr M. Recent advances in computational methodology for simulation of mechanical circulatory assist devices. *Wiley Interdiscipl Rev Syst Biol Med*. (2014) 6:169–88. doi: 10.1002/wsbm.1260

25. Harrod KK, Rogers JL, Feinstein JA, Marsden AL, Schiavazzi DE. Predictive modeling of secondary pulmonary hypertension in left ventricular diastolic dysfunction. *Front Physiol*. (2021) 12:666915. doi: 10.3389/fphys.2021.666915

26. Marsden AL, Esmaily-Moghadam M. Multiscale modeling of cardiovascular flows for clinical decision support. *Appl Mech Rev*. (2015) 67:1–11. doi: 10.1115/1.4029909

27. Nagueh SF, Smiseth OA, Appleton CP, Byrd I Benjamin F, Dokainish H, Edvardsen T, et al. Recommendations for the evaluation of left ventricular diastolic function by echocardiography: an update from the American Society of Echocardiography and the European Association of Cardiovascular Imaging. *Eur Heart J Cardiovasc Imaging*. (2016) 17:1321–60. doi: 10.1016/j.echo.2016.01.011

28. Ommen SR, Nishimura RA, Appleton CP, Miller FA, Oh JK, Redfield MM, et al. Clinical utility of Doppler echocardiography and tissue Doppler imaging in the estimation of left ventricular filling pressures: a comparative simultaneous Doppler-catheterization study. *Circulation*. (2000) 102:1788–94. doi: 10.1161/01.CIR.102.15.1788

29. Updegrove A, Wilson NM, Merkow J, Lan H, Marsden AL, Shadden SC. SimVascular: an open source pipeline for cardiovascular simulation. *Ann Biomed Eng*. (2017) 45:525–41. doi: 10.1007/s10439-016-1762-8

30. Formaggia L, Quarteroni A, Veneziani A. *Cardiovascular Mathematics: Modeling and Simulation of the Circulatory System* (Milano: Springer), vol. 1. (2009). doi: 10.1007/978-88-470-1152-6

31. Mirramezani M, Shadden SC. A distributed lumped parameter model of blood flow. *Ann Biomed Eng*. (2020) 48:2870–86. doi: 10.1007/s10439-020-02545-6

32. Colacino FM, Moscato F, Piedimonte F, Arabia M, Danieli GA. Left ventricle load impedance control by apical VAD can help heart recovery and patient perfusion: a numerical study. *ASAIO J*. (2007) 53:263–77. doi: 10.1097/MAT.0b013e31805b7e39

33. Mynard JP, Davidson MR, Penny DJ, Smolich JJ. A simple, versatile valve model for use in lumped parameter and one-dimensional cardiovascular models. *Int J Num Methods Biomed Eng*. (2012) 28:626–41. doi: 10.1002/cnm.1466

34. Schampaert S, Rutten MCM, Van T Veer M, Van Nunen LX, Tonino PAL, Pijls NHJ, et al. Modeling the interaction between the intra-aortic balloon pump and the cardiovascular system: the effect of timing. *ASAIO J*. (2013) 59:30–6. doi: 10.1097/MAT.0b013e3182768ba9

35. Fresiello L, Khir AW, Di Molfetta A, Kozarski M, Ferrari G. Effects of intra-aortic balloon pump timing on baroreflex activities in a closed-loop cardiovascular hybrid model. *Artif Organs*. (2013) 37:237–47. doi: 10.1111/j.1525-1594.2012.01540.x

36. Zimmermann J, Bäumler K, Loecher M, Cork TE, Kolawole FO, Gifford K, et al. Quantitative hemodynamics in aortic dissection: comparing *in vitro* MRI with FSI simulation in a compliant model. In: Ennis DB, Perotti LE, Wang VY, editors. *Functional Imaging and Modeling of the Heart*. Cham: Springer International Publishing (2021). p. 575–86. doi: 10.1007/978-3-030-78710-3_55

37. Ozturk C, Rosalia L, Roche ET. A multi-domain simulation study of a pulsatile-flow pump device for heart failure with preserved ejection fraction. *Front Physiol*. (2022) 13:815787. doi: 10.3389/fphys.2022.815787

38. Rosalia L, Ozturk C, Roche ET. Lumped-parameter and finite element modeling of heart failure with preserved ejection fraction. *J Visual Exp*. (2021) 2021:1–19. doi: 10.3791/62167

39. Campos Arias D, Londono F, Rodríguez Moliner T, Georgakopoulos D, Stergiopulos N, Segers P. Hemodynamic impact of the C-pulse cardiac support device: a one-dimensional arterial model study. *Artif Organs*. (2017) 41:E141–54. doi: 10.1111/aor.12922

40. Annamalai SK, Buiten L, Esposito ML, Paruchuri V, Mullin A, Breton C, et al. Acute hemodynamic effects of intra-aortic balloon counterpulsation pumps in advanced heart failure. *J Cardiac Fail*. (2017) 23:606–14. doi: 10.1016/j.cardfail.2017.05.015

41. Caldas JR, Panerai RB, Bor-Seng-Shu E, Ferreira GSR, Camara L, Passos RH, et al. Intra-aortic balloon pump does not influence cerebral hemodynamics and neurological outcomes in high-risk cardiac patients undergoing cardiac surgery: an analysis of the IABCS trial. *Ann Intensive Care*. (2019) 9:1–11. doi: 10.1186/s13613-019-0602-z

42. Tsimploulis A, Lam PH, Arundel C, Singh SN, Morgan CJ, Faselis C, et al. Systolic blood pressure and outcomes in patients with heart failure with preserved ejection fraction. *JAMA Cardiol*. (2018) 3:288–97. doi: 10.1001/jamacardio.2017.5365

frontiers | Frontiers in Cardiovascular Medicine

ORIGINAL RESEARCH
published: 04 August 2022
doi: 10.3389/fcvm.2022.886874

Development of the Centrifugal Blood Pump for a Hybrid Continuous Flow Pediatric Total Artificial Heart: Model, Make, Measure

*Carson S. Fox[1], Thomas Palazzolo[1], Matthew Hirschhorn[1], Randy M. Stevens[2], Joseph Rossano[3], Steven W. Day[4], Vakhtang Tchantchaleishvili[5] and Amy L. Throckmorton[1]**

[1] School of Biomedical Engineering, Science and Health Systems, Drexel University, Philadelphia, PA, United States, [2] St. Christopher's Hospital for Children, Philadelphia, PA, United States, [3] Division of Cardiology, Children's Hospital of Philadelphia, Philadelphia, PA, United States, [4] Department of Biomedical Engineering, Kate Gleason College of Engineering, Rochester Institute of Technology, Rochester, NY, United States, [5] Cardiac Surgery, Thomas Jefferson University, Philadelphia, PA, United States

OPEN ACCESS

Edited by:
Christopher T. Nguyen,
Cleveland Clinic, United States

Reviewed by:
Richard Figliola,
Clemson University, United States
Hoda Hatoum,
Michigan Technological University, United States

***Correspondence:**
Amy L. Throckmorton
alt82@drexel.edu

Specialty section:
This article was submitted to General Cardiovascular Medicine, a section of the journal Frontiers in Cardiovascular Medicine

Received: 01 March 2022
Accepted: 16 June 2022
Published: 04 August 2022

Citation:
Fox CS, Palazzolo T, Hirschhorn M, Stevens RM, Rossano J, Day SW, Tchantchaleishvili V and Throckmorton AL (2022) Development of the Centrifugal Blood Pump for a Hybrid Continuous Flow Pediatric Total Artificial Heart: Model, Make, Measure. Front. Cardiovasc. Med. 9:886874. doi: 10.3389/fcvm.2022.886874

Clinically-available blood pumps and total artificial hearts for pediatric patients continue to lag well behind those developed for adults. We are developing a hybrid, continuous-flow, magnetically levitated, pediatric total artificial heart (TAH). The hybrid TAH design integrates both an axial and centrifugal blood pump within a single, compact housing. The centrifugal pump rotates around the separate axial pump domain, and both impellers rotate around a common central axis. Here, we concentrate our development effort on the centrifugal blood pump by performing computational fluid dynamics (CFD) analysis of the blood flow through the pump. We also conducted transient CFD analyses (quasi-steady and transient rotational sliding interfaces) to assess the pump's dynamic performance conditions. Through modeling, we estimated the pressure generation, scalar stress levels, and fluid forces exerted on the magnetically levitated impellers. To further the development of the centrifugal pump, we also built magnetically-supported prototypes and tested these in an *in vitro* hydraulic flow loop and *via* 4-h blood bag hemolytic studies ($n = 6$) using bovine blood. The magnetically levitated centrifugal prototype delivered 0–6.75 L/min at 0–182 mmHg for 2,750–4,250 RPM. Computations predicted lower pressure-flow performance results than measured by testing; axial and radial fluid forces were found to be <3 N, and mechanical power usage was predicted to be <5 Watts. Blood damage indices (power law weighted exposure time and scalar stress) were <2%. All data trends followed expectations for the centrifugal pump design. Six peaks in the pressure rise were observed in the quasi-steady and transient simulations, correlating to the blade passage frequency of the 6-bladed impeller. The average N.I.H value ($n = 6$) was determined to be 0.09 ± 0.02 g/100 L, which is higher than desired and must be addressed through design improvement. These data serve as a strong foundation to build upon in the next development phase, whereby we will integrate the axial flow pump component.

Keywords: pediatric mechanical circulatory support, pediatric total artificial heart, rotary blood pump, rotary blood pump modeling, pediatric ventricle assist device, pediatric ventricular support

CLINICAL SIGNIFICANCE AND MOTIVATION

Globally, more than 17.5 million patients die of cardiovascular disease, the leading cause of death worldwide (1). Congestive heart failure (CHF), which is a result of end-stage cardiovascular disease, affects more than 60 million patients around the world (2). The clinical need is expected to increase, and the necessity for effective therapeutic strategies is of critical importance, especially for infants and children. Millions of pediatric patients around the world die each year from heart failure due to congenital or acquired cardiac diseases (3). Complex congenital heart defects and exposure to viruses and bacteria that attack the cardiac muscle lead to severely depressed ventricular function and usually require surgical and therapeutic intervention (4, 5). Annually, more than 10,000 children in the United States are hospitalized with CHF-related symptoms, with a mortality rate of 7–15% (6–8). These pediatric patients often require a heart transplantation, the current standard of care. Transplantation in pediatric patients is complicated by challenges in donor-recipient size matching and anticipated growth potential (9). Despite ∼74% of children being matched and transplanted within 90 days of listing, the mortality rate range for patients awaiting a donor organ remains high (5–39%) (7, 10, 11). Thus, this necessitates the use of alternative therapies, such as mechanical circulatory support (MCS) devices, including blood pumps.

MCS devices, such as ventricular assist devices (VADs) and total artificial hearts (TAHs) have been employed to support pediatric patients with some success (12). The Berlin Heart EXCOR (Berlin Heart, Berlin Germany) has been employed for thousands of pediatric patients, and Abbott Laboratories received U.S. FDA labeling for use of the HeartMate III in older pediatric patients with advanced refractory left ventricular HF in December 2020. On a case-by-case basis, blood pumps, such as the Jarvik Heart (Jarvik Heart Inc., New York, NY) and HeartMate II axial flow pump, may be employed for pediatric compassionate use. The SynCardia TAH has 2 sizes (50 and 70 cc) that both have limitations of use in smaller pediatric patients. Researchers at the Cleveland Clinic have multiple TAHs under development, including a standard sized device for adults and adolescents, and a pediatric device, which is 1/3 the total volume of the adult device.

Development and translation of pediatric MCS devices continue to lag well behind those developed for adults. To address the ongoing limitations of existing MCS devices for pediatric patients, we are developing a hybrid, continuous-flow, implantable or extracorporeal, magnetically levitated, TAH for pediatric patients (13, 14). This new device has the capability to be employed as a right-sided or left-sided VAD, or TAH for partial or full pediatric cardiovascular support. The hybrid TAH design integrates both an axial and centrifugal blood pump within a single, compact housing. **Figure 1** displays an illustration of the clinical implantation of the devices during pediatric MCS of both the left ventricle (centrifugal blood pump) and the right ventricle (axial blood pump). The centrifugal pump rotates around the separate axial pump domain, and both impellers rotate around a common central axis. In this configuration, the axial flow blood pump serves to provide MCS to the pulmonary circulation, and the centrifugal flow blood pump supports blood flow in the systemic circulation. The internal axial flow pump is designed to generate 1–6 *L/min* of flow with a pressure rise range of 10–30 *mmHg* for the pulmonary circulation, and the outer centrifugal blood pump is designed to produce 60–140 *mmHg* for the systemic circulation at rotational speeds to 10,000 RPM. This range of pressure generation and flow capacity is required to support a pediatric cardiovascular load. This constitutes the first-ever technology to integrate an axial and centrifugal blood pump as a TAH. **Figure 2** illustrates this design concept, also referred to as the *Drexel Dragon Heart*. Since the blood pump domains are separate, we have to-date concentrated on development of the centrifugal blood pump, which will contribute most substantially to the overall size of the device. The centrifugal flow pump has an inlet volute, exit volute, and magnetically levitated impeller. The inlet volute supports flow entering the pump and distributes the flow evenly into the impeller region. The exit volute directs blood flow out of the pump by slowly increasing the cross-sectional area to convert fluid velocity to pressure. The development results presented in this manuscript reflect the latest design work for the centrifugal blood pump, after 4 design phases.

Here, we performed computational fluid dynamics (CFD) analysis of the blood flow through the centrifugal pump during steady and transient conditions. To initiate design of the motor and magnetic suspension system, we conducted a transient CFD analysis on the magnetically suspended centrifugal blood

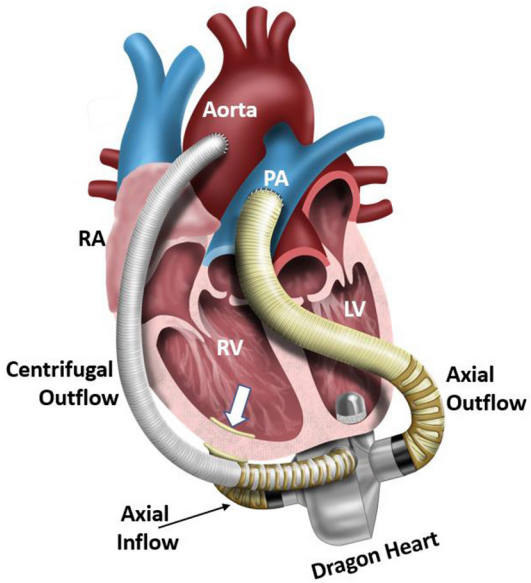

FIGURE 1 | Illustration of an implanted Dragon Heart hybrid continuous-flow blood pump technology. The centrifugal blood pump is designed to support the systemic circulation and left ventricle, and the axial flow blood pump is designed to support the pulmonary circulation and right ventricle. In this study, we focus on the design-build-test of the centrifugal blood pump component of this device. RA, right atrium; RV, right ventricle; LV, left ventricle; PA, pulmonary artery.

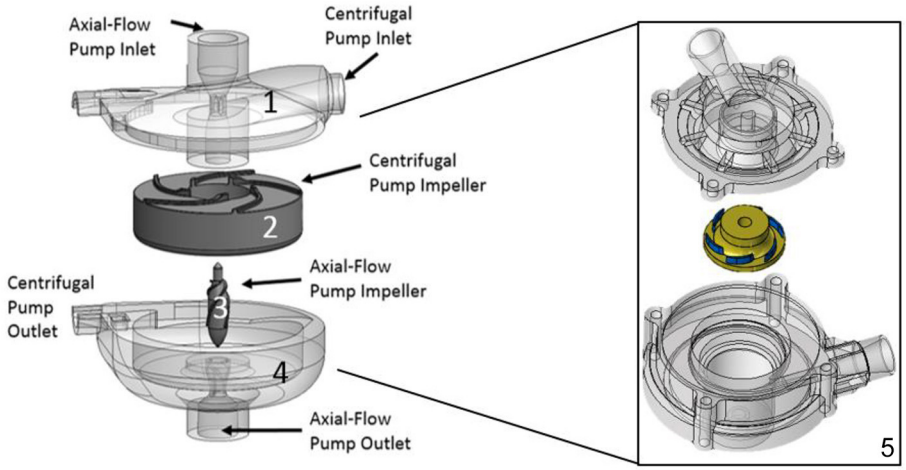

FIGURE 2 | Hybrid continuous-flow TAH. (1) Upper housing, (2) Centrifugal pump impeller, (3) Axial pump impeller, (4) Lower housing. This configuration consists of two separate pump domains combined into one pump housing, (5) Concentrated design focus on the centrifugal pump design only: Reduced overall size with an improved and compact centrifugal impeller and pump design, overall 60 mm in diameter by 50 mm in height, having a radial inlet volute and 37 mm impeller diameter (6 bladed design).

pump design to assess its dynamic performance conditions. The suspension system must compensate for both fluid disturbances and force perturbations on the levitated rotor-impeller to consistently maintain its optimally centered position during operation. Transient simulations are utilized to investigate more dynamic estimations of fluid disturbances and to quantify the fluid forces that are required to the design and development the robust magnetic suspension and motor (15–17). Three types of simulations were investigated: (1) steady flow simulations using a frozen-rotor interface specification; (2) quasi-steady simulations whereby the impeller is rotated manually and a steady state simulation is performed; (3) transient rotational sliding interfaces (TRSI), where the rotor-stator domains of the impeller move in relative motion to each other, simulating blade rotation. Through computational modeling, we estimated the pressure generation, scalar stress levels, and fluid forces exerted on the magnetically levitated impeller. To further the development of the centrifugal pump, we also built prototypes of the designs and tested those in an *in vitro* hydraulic flow loop and by blood bag hemolytic studies. The findings of these analyses are described in subsequent sections.

MATERIALS AND METHODS

Computational Studies

We employed ANSYS-CFX (ANSYS Inc., Canonsburg, PA) to simulate both steady and transient blood flow through the centrifugal pump, and the approach is shown in **Figure 3**. The centrifugal pump model (**Figure 4A**) consisted of several fluid domains: (1) inlet volute; (2) impeller; (3) outlet volute; and (4) the secondary flow path. Each of these domains were connected *via* fluid-fluid interfaces. We determined the global Reynolds number using the standard formula for pumps: $\rho\omega D^2/\mu$, where ω is the angular speed, D signifies impeller diameter, and μ is fluid viscosity. Global and local Reynolds numbers were calculated to above 4,000, leading us to implement a turbulence model. Both the k-epsilon turbulence and shear stress transport (SST) model were employed. The shear stress transport (SST) turbulence model was selected because it combines the robustness of the k-ε in the bulk flow regime and the k-ω model along the surfaces or boundaries. A grid independence study was performed to determine when the grid resolution was no longer affecting the physics being modeled; we examined parameter values of velocity (radial and axial) and pressures at more than 10 locations in the centrifugal pump. Mesh quality was confirmed using standard mesh metrics, including aspect ratio, Jacobian ratio, skewness and an ANSYS metric called element quality. All surfaces were set to a no-slip condition and the simulations were executed using a high resolution advection scheme. The convergence criterion was set to a maximum residual threshold below 1×10^{-3}.

Fluid Physics

Blood is well-known to be a Non-Newtonian fluid (18); it has been established, however, that a Newtonian fluid assumption is valid above a threshold strain rate whereby the stress-strain relationship of blood is primarily linear, indicating Newtonian behavior (18, 19). For k-epsilon turbulence modeling, we employed a Newtonian behavior model with a constant viscosity of 0.0035 Pa*s, corresponding to patient hematocrit of ∼33% (20). In contrast, for the SST turbulence studies, we implemented a Non-Newtonian model based on a Generalized Oldroyd-B (GOB) model using relevant coefficients found in literature (18, 19). This approach utilizes a form of the Naiver-Stokes where the stress tensor is separated in terms of blood plasma components ($\boldsymbol{\tau}_s$) and red blood cell components ($\boldsymbol{\tau}_p$), as shown

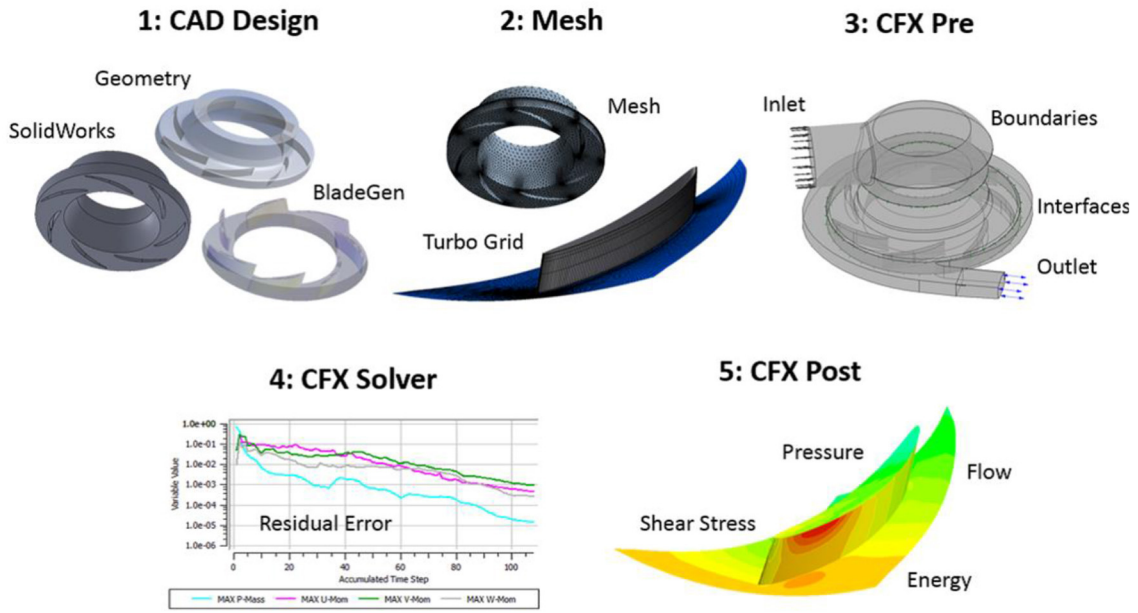

FIGURE 3 | Computational modeling approach using ANSYS CFX. (1) SolidWorks CAD design of the pump, (2) ANSYS meshing of pump regions, (3) ANSYS CFX-Pre to define physics and boundary conditions, (4) ANSYS CFX solver to complete the simulation, and (5) ANSYS CFX-post to quantify and visualize the pump performance metrics (pressure generation, fluid stress levels, velocity profiles). For CFX-post, nodal properties are exported to a Matlab code in order to estimate the blood damage index for a given operating condition. As an exemplar of the approach, a contour plot of a single bladed centrifugal impeller is illustrated.

in Equation (1):

$$\rho\frac{\partial\vec{u}}{\partial t}+\rho\vec{u}\cdot\nabla\vec{u}=-\nabla p+\nabla\cdot\left(\tau_s+\tau_p\right) \quad (1)$$

where **ρ** signifies the fluid density, **p** represents the pressure, and $\vec{u}$ is the fluid velocity vector.

The red blood cell stress tensor component includes a dissipative term using the Oldroyd derivative (τ'_p), which relates the red blood cells stresses to the rate of change of the stress. In the model developed by *Good* et al. (18), a parameter limited term with constant $\alpha = 0.5$ was included to mathematically bound the predicted stress. The coefficients of this model were experimentally derived using pediatric blood, including two coefficients (η, η_1) bounding the viscosities as the shear rates approach zero and infinity. The elastic shear modulus (μ) was determined by finding a least squares fit of experimental data. In this study, we utilized this model and selected the closest hematocrit option of 40% and therefore the η, η_1, and μ were defined as 31.1, 8.9, and 53, respectively (19). We specified a fluid density of 1,050 kg/m^3 for these simulations.

Modeling Reference Frames

Two reference frames (rotating and stationary domains) were established in these simulations. The impeller domain was specified to be in the rotating reference frame. The inlet volute, outlet volute and secondary flow path were assigned to the stationary reference frame. ANSYS CFX provides two main options to define the interfaces between two differing frames of reference: frozen rotor and rotor/stator interfaces. In the frozen rotor mode, the two frames of reference link with a fixed relative position, but have the correct frame transformation occurring across the interface. This frame transformation occurs *via* a patch mapping technique to interpolate mass flux across interfaces of varying reference frames (i.e., Frozen Rotor Interface). A transient rotor/stator simulation, however, involves two or more domains in relative motion to each other, which more accurately reflects the physics of a rotating impeller. The transient rotor/stator interface solution is updated with each time step as the relative position of the two-grid regions change with time. The frozen rotor (steady flow) simulation results were applied as the initial guess for the transient rotor/stator simulations. The transient interface treatment accounts for all interaction effects between components in relative motion to each other, but requires more calculation resources and time (15–17).

Boundary Conditions

Non-uniform Inflow Velocity

To simulate fully developed inlet flow, a non-uniform inflow velocity profile was implemented as the inlet boundary condition to the centrifugal blood pump. Equation (2) details the expression that was defined for the inlet velocity profile with a power variable (β) equal to 1/7 for turbulent inflow conditions. The radius of inflow boundary of the inlet volute is specified as R_{max} (4 mm), and a maximum fluid velocity (u_{max}) is defined to achieve the

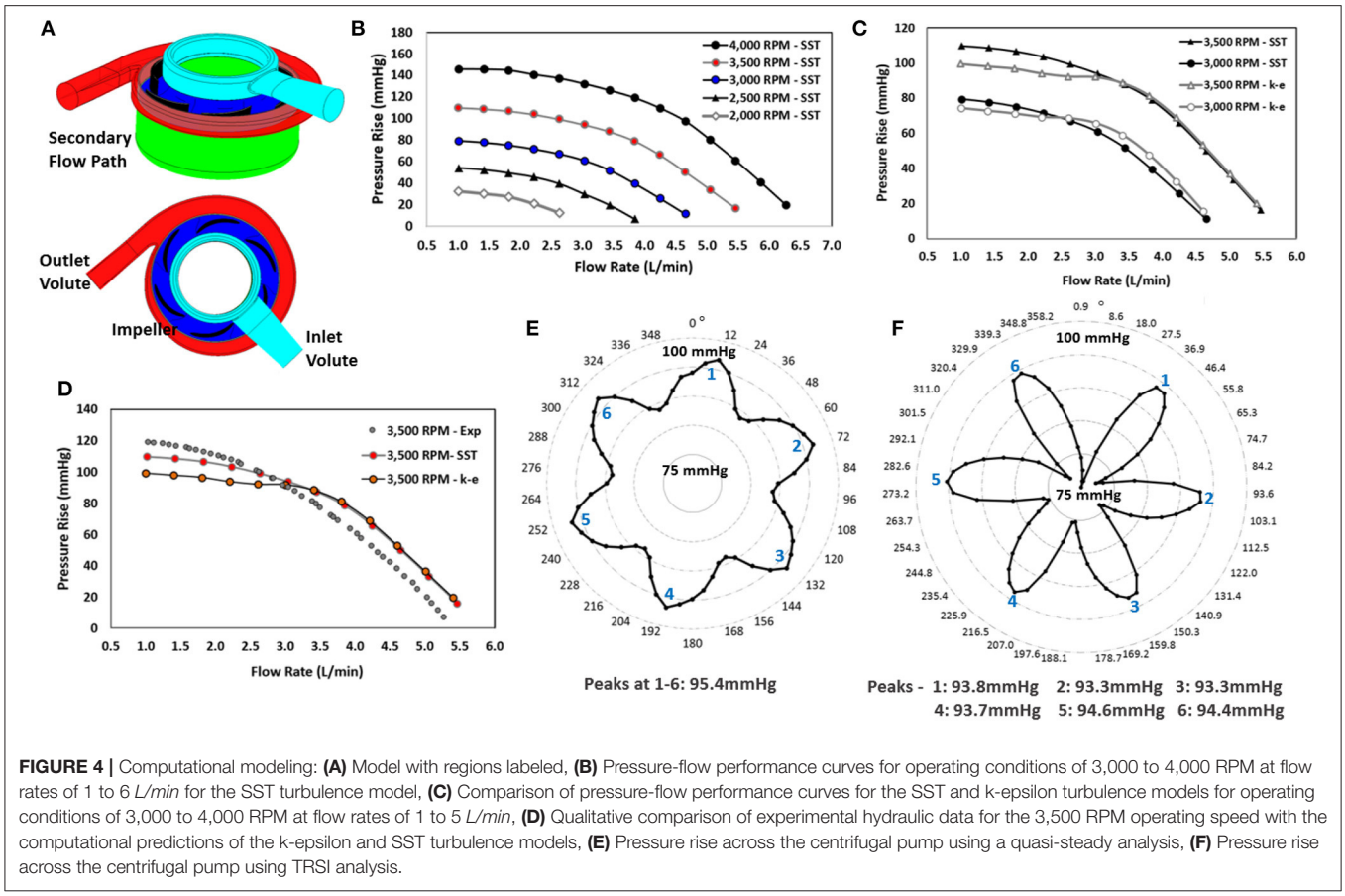

FIGURE 4 | Computational modeling: **(A)** Model with regions labeled, **(B)** Pressure-flow performance curves for operating conditions of 3,000 to 4,000 RPM at flow rates of 1 to 6 *L/min* for the SST turbulence model, **(C)** Comparison of pressure-flow performance curves for the SST and k-epsilon turbulence models for operating conditions of 3,000 to 4,000 RPM at flow rates of 1 to 5 *L/min*, **(D)** Qualitative comparison of experimental hydraulic data for the 3,500 RPM operating speed with the computational predictions of the k-epsilon and SST turbulence models, **(E)** Pressure rise across the centrifugal pump using a quasi-steady analysis, **(F)** Pressure rise across the centrifugal pump using TRSI analysis.

target flow rates of ∼1–5 L/min (0.25–1.55 m/s).

$$u(r) = u_{\max}\left(1 - \frac{r}{R_{\max}}\right)^{\beta} \quad (2)$$

Frozen Rotor Steady Flow Simulations

Flow through the centrifugal pump was initially modeled as steady state. The impeller rotor was specified as rotating in the counterclockwise direction in accordance with the blade orientation, and the impeller hub, in the secondary flow path domain, was specified as a rotating surface. The frozen rotor interface linked regions of differing reference frames. The non-uniform mass inflow rate and operational rotational speed were specified for each steady-flow simulation. The outflow pressure was set to be a constant, static pressure afterload (200 mmHg). Both the k-epsilon turbulence and the shear stress transport (SST) model were specified, and rotational speeds of 3,000, 3,500, and 4,000 RPM were modeled for flow rates of 1-6 L/min, set by establishing the maximum velocity value, u_{max} (0.25–1.55 m/s), in Equation (2).

Quasi-Steady Flow Simulations

The purpose of the quasi-steady study was to assess the impact of centrifugal impeller blade rotational position on pump performance and fluid dynamics. We incrementally rotated the impeller blades by 6° and created a new, separate model for each rotational position (i.e., 60 models at 6° impeller rotations to achieve a 360° full rotation). The inlet boundary condition was specified as a non-uniform velocity profile (u_{max} of 0.75 m/s; β of 1/7), and the outlet boundary condition was defined as a constant, static pressure afterload (200 mmHg). We ran 60 simulations to derive the full 360° time-averaged performance profile for the centrifugal pump at 3,500 RPM (15–17).

Transient Rotational Sliding Interfaces (TRSI) Simulations

The TRSI simulations involved the application of a non-uniform inflow velocity profile (u_{max} of 0.75 m/s; β of 1/7) and a rotational speed of 3,500 RPM according to the pump design point. The outflow boundary condition or aortic mean pressure (AOP) was set to a constant physiologic value. We employed the rotor-stator interface, rather than the frozen-rotor, for the regions of differing reference frames. The rotor-stator interface more accurately models the motion of the rotating impeller relative to the stationary pump internal housing. Since the rotational speed is relatively high in each case, this simulation requires a small time step to resolve the transient fluid dynamics and capture the impact of the blade passage frequency (BPF). Rotational increments of 4.725°, corresponding to a time step of 2.225×10^{-4} s, were implemented for 3,500 RPM. This set of simulations included two full revolutions of the impeller (720°) (15–17).

Scalar Fluid Stress Analysis

High operating rotational speeds and narrow (blade tip) clearances between the rotating and stationary regions of the centrifugal pump may produce unacceptable shear stresses and result in damage to red blood cells. This blood trauma may, in turn, activate platelets and trigger clot initiation downstream, contributing to potential thromboemboli. Irregular flow patterns also contribute to the risk of hemolysis and thrombosis by increasing levels of fluid stresses. Thus, scalar stress values were numerically estimated during these simulations along with corresponding blood damage indices. An estimation of the scalar fluid stress levels in blood pumps was proposed by Bludszweit et al. (21, 22). This approach leverages comparative stress theory to produce a mathematical expression for fluid stresses based on the von Mises yield criterion of solid mechanics theory. Equation (3) was used in this study to calculate the scalar stress (σ), which includes the components of the stress tensor and represents the level of stress experienced by the blood:

$$\sigma = \left(\frac{1}{6} \sum \left(\sigma_{ii} - \sigma_{jj} \right)^2 + \sum \sigma_{ij}^2 \right)^{1/2} \quad (3)$$

We also examined fluid streamlines as indicators of numerically predicted fluid residence times. A power law relationship according to Equation (4) was utilized to relate the scalar stresses and residence time in the estimation of a blood damage index:

$$D = \sum_{Inlet}^{Outlet} 1.8x10^{-6} * \sigma^{1.991} * \Delta t^{0.765} \quad (4)$$

where "Inlet" and "Outlet" represent the inflow and outflow faces of the pump domain and the fluid inlet region to the bundle, D is the damage index, σ signifies the scalar stress and t is the exposure time (23). This provides a statistical estimation of the probability for blood damage to occur from the inlet to the outlet of the centrifugal pump. Using this power law relationship between the scalar stress level and the exposure time, a blood damage index was estimated (23). We assess a maximum scalar stress value of 425 Pa and a maximum residence time of 600 ms as our design threshold (24, 25). In this analysis, we track the stress history of the fluid *via* particle streamlines. The accumulation of stress and exposure time was discretely summed along the streamlines to evaluate the potential for blood damage. This approach provides a statistical estimate of damage to blood cells traveling through this blood pump using a power law equation, as described in (13, 14).

Prototype Manufacturing

After modeling, the centrifugal impeller and volutes were prototyped from watershed resin material using stereolithographic techniques (**Figure 5**). The centrifugal impeller, made by rapid prototyping, was attached to a set of diametrically polarized magnets, designed and manufactured by our team. The lower housing of the centrifugal pump, containing both the outlet and outlet volute, was adapted to encapsulate the magnets inside of the pump housing. The prototypes were then fitted with fluid seals and tested in existing hydraulic and hemolytic test loops to characterize the pressure-flow pump performance and hemolytic potential.

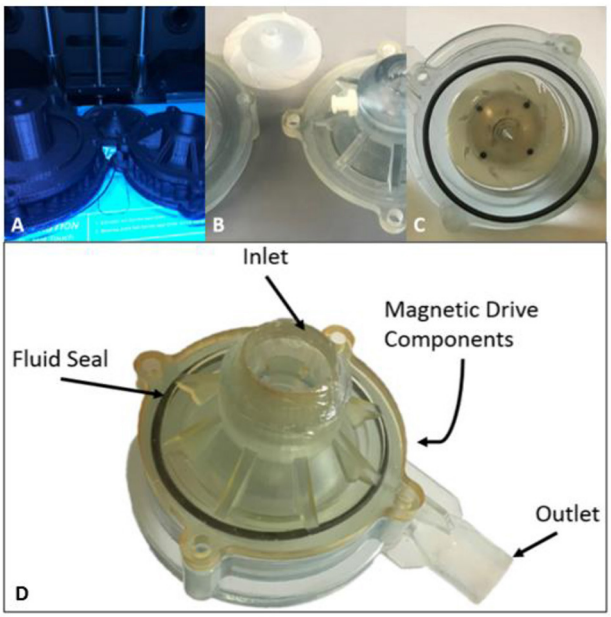

FIGURE 5 | Design Progression of Magnetically Levitated Centrifugal Pump Prototypes. **(A)** Initial polylactic acid (PLA) extruded pro-totypes, **(B)** Stereolithographic 3D printing prototypes machined for testing, **(C)** Final pump prototype with point and support stabilization, **(D)** Top inlet volute with fluid seal in place and magnetic drive components to support impeller.

Hydraulic Testing

The centrifugal prototype was hydraulically evaluated utilizing a blood analog solution composed of water and glycerol (standard 60/40% v/v). **Figures 6A–K** illustrates the test rig configuration and pump prototype. This analog fluid was calibrated to have a measured viscosity and density of ∼0.00353 Pa*s and 1,054 kg/m^3, respectively. After filling the hydraulic test-rig, we removed entrained air bubbles. The test loop consisted of two reservoir tanks (inlet and outlet tank) with the pump located between them and a tubing clamp to adjust resistance and therefore flow in the circuit. Each tank was connected to a differential pressure transducer (Validyne, Northridge, CA, USA) to measure the pressure rise across the pump prototypes. Flow was measured using an external flow sensor (Transonic, Ithaca, NY, USA). A BLDC motor and controller (Faulhaber GmbH, Schonaich, Germany) was used in conjunction with the integrated magnets to induce impeller rotation (13). We collected flow rates and pressure measurements at rotational speeds from 2,750 to 4,250 RPM in 250 RPM intervals. Data were collected using a data acquisition (DAQ) board (LabJack Corp., Lakewood, CO, USA).

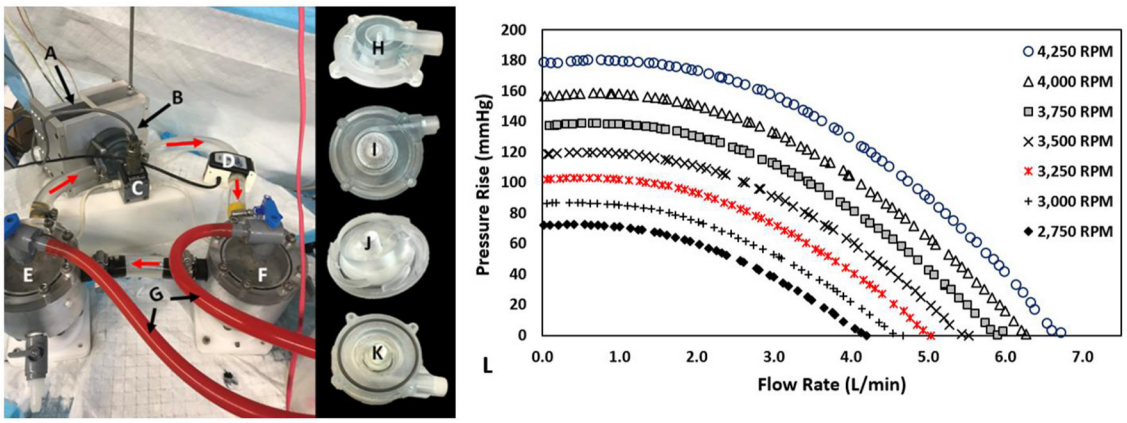

FIGURE 6 | Hydraulic Test Rig, Centrifugal Prototype, and Performance Results: **(A)** Magnetically Levitated Drive System, **(B)** centrifugal blood pump, **(C)** Validyne differential pressure transducer, **(D)** Transonic Ultrasonic flow probe, **(E)** Inlet tank, **(F)** Outlet tank, **(G)** Air bleed hoses, **(H)** Inlet volute, **(I)** Outlet volute, **(J)** Impeller, **(K)** Partially assembled prototype, **(L)** Prototype Performance Results: 0-6.7 L/min at 0.5-180.3 mmHg for 2,750-4,250 RPM.

Hemolytic Experiments

Figure 7 illustrates the experimental configuration for the *in vitro* hemolysis testing. The experiments were completed using bovine blood, selected in accordance with ASTM 1830-97 (Standard Practice for Selection of Blood for *in vitro* Evaluation of Blood Pumps). The accumulated levels of plasma free hemoglobin (pfHb) were measured hourly for 4-h using the optical Cripps method (26) to characterize the degree of hemolysis for the centrifugal prototype. Experiments ($n = 6$) were performed according to our lab protocol, which follows ASTM 1841-97 (Standard Practice for Assessment of Hemolysis in Continuous Flow Blood Pumps). The flow loop was partially submerged in a 37°C water bath, controlled with a thermocouple and heating element, to maintain the temperature of the blood at or near 37°C for the duration of the experiment. Prior to filling, the flow loop was filled with phosphate buffered saline (PBS) solution to wet the internal surfaces of the loop. The bovine blood (Lampire Laboratories, Pipersville, PA, USA) was collected *via* venipuncture and shipped in a standard 1,000 *mL* bags containing citrate phosphate dextrose adenine (CDPA) anticoagulant. The blood bags were slowly warmed to 37°C in a water bath prior to the experiment.

After quickly draining the PBS solution, blood was introduced into the loop through a 150-micron filter. Once full, a blood sample was collected for the baseline measurement (initial condition, time = 0). The pump was started and slowly brought to operational rotational speed over 15 min, yielding a flow of about 2 L/min. At each 30-min interval, ∼2–4 *mL* of blood aliquot was collected from the inlet tank. Two capillary tubes were filled using this sample and then placed into a centrifuge (Hettich Haematokrit 210 centrifuge, Oxford, CT). After rotation (8 min at 8,000 RPM), visual inspection using the 210 centrifuge tool itself enabled us to measure the hematocrit. Measurements were taken twice in parallel and averaged.

The remaining blood was then transferred to Covidien EDTA blood collection tubes and centrifuged for 8 min at 4,000 RPM to separate the plasma layer from the packed red cells. Using a transfer pipette, the plasma layer was collected for spectrophotometric analysis. The optical density or absorbance was measured at 576.5 *nm*, 560 *nm*, and 593 *nm,* using a Genesys

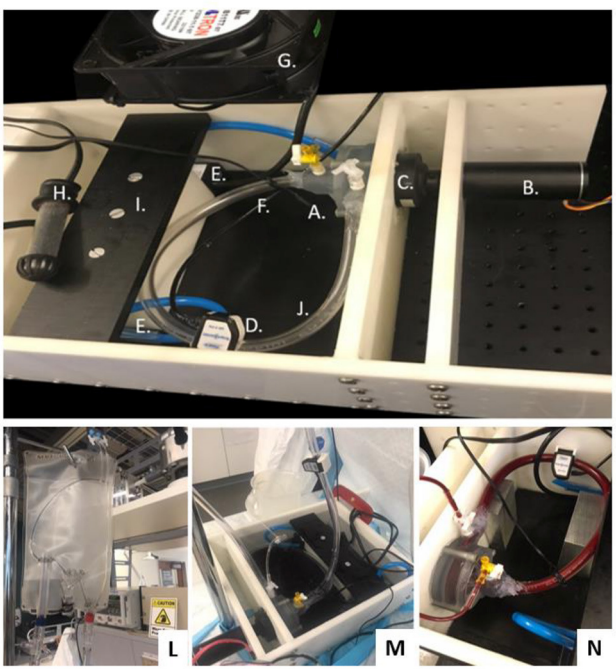

FIGURE 7 | Magnetically Levitated Centrifugal Pump for Hemolysis Testing: **(A)** Centrifugal Pump (Inlet Volute, Outlet Volute, Fluid Seal, Magnetic Drive Impeller and Ceramic Thrust Bearings), **(B)** Brushless DC Motor, **(C)** No Contact Diametrically Magnetized Cup Magnet, **(D)** Flow Sensor, **(E)** Heat Bath Circulation Pumps, **(F)** Waterproof Thermocouple, **(G)** Cooling Fan, **(H)** Heater, **(I)** Heath Bath Partition, **(J)** Heparin Coated Tubing, **(K)** Leur-Lok Fill and Draw Ports, **(L)** Commercial blood bag as supply reservoir, **(M)** Connected set-up, **(N)** Pump placement and filled test rig.

10Vis spectrophotometer (ThermoFisher Scientific, Waltham, MA). We determined the pfHb based on the weighted difference in absorbance measurements, according to the Cripps method in Equation (4) (26):

$$pfHb(mg/dL) = 177.6 \times \left[A_1 - (A_2 + A_3)/2\right] \quad (5)$$

where A_1 corresponds to the absorbance at wavelength (λ_1) of 576.5 *nm*, A_2 reflects the absorbance at wavelength (λ_2) of 560.0 *nm*, and A_3 is the absorbance wavelength (λ_3) of 593.0 *nm*. The normalized index of hemolysis (N.I.H) was calculated using the following standard relationship in Equation (5):

$$N.I.H(g/100L) = V * \Delta pfHb * \frac{(100 - Hct)}{100} * \frac{100}{\Delta t * Q} \quad (6)$$

where $V * \Delta pfHb$ signifies the increase in plasma free hemoglobin (g/L) over the sampling time interval, Hct is the blood hematocrit (%), Δt corresponds to the sampling time in minutes, Q represents the flow rate in liters per minute, and V is the circulating volume of the hydraulic loop in liters.

Data Analysis

Simulation results were assessed qualitatively and quantitively. We estimated the pressure generation, scalar stress levels, and fluid forces exerted on the magnetically levitated impeller. For the transient runs, data analysis was performed on the second revolution results for each case. To quantitatively compare the pressure-flow performance of the models with the prototype performance, we used a regression analysis that is detailed in (27). This approach involves the calculation of non-dimensional pressure and flow coefficients for the data sets. The regression model includes characteristic constants (β_0, β_1, β_2), as described in this equation:

$$\psi_{TYPE} = \beta_2 \left(\varphi_{TYPE}{}^2\right) + \beta_1 \left(\varphi_{TYPE}\right) + \beta_0 \quad (7)$$

The subscript "Type" is generic since comparisons were made across data sets of computational predictions and experiments. The F-test for the regression analysis was used to assess the significance of the coefficients and polynomial models based on the data normality. We then determined an average and maximum deviation between data sets.

The hemolytic data were analyzed according to standard ANOVA principles using SPSS. A Shapiro-Wilk normality test was completed in conjunction with a Tukey-Hoaglin outlier test. A test of homogeneity of variance was conducted to analyze the variance between the six different experimental results for N.I.H. values, and heteroskedasticity test was utilized to assess significance of time point values across experiments. All statistical analyses were based on a preset α value of 0.05.

COMPUTATIONAL RESULTS

Mesh Quality

The mesh for all fluid domains was created using the mesh generator within ANSYS, and the required mesh density was determined using a grid independence study to determine when the grid resolution was no longer affected the physics being modeled (<3% variable variance). All mesh elements were required to have an aspect ratio <100, Jacobian ratio <40, a skewness <0.25 and an element quality measure >0.75; these were achieved for all model constructs. The k-epsilon model satisfied the y+ mesh requirement of being >11 along all walls and surfaces. Inflation layers were also used to achieve the SST turbulence model requirement (y+ <2). This mesh-build analysis indicated that ∼3 million elements was sufficient to achieve grid independence.

Steady Flow Simulation Findings

Over 400 simulations were performed on the centrifugal pump using the model in **Figure 4A**. **Figures 4B,C** illustrate the pressure-flow performance for this pump design over a range of flow rates and rotational speeds for both the SST and k-epsilon turbulence models. Each data point corresponds to a steady state simulation for a specific flow rate and rotational speed. The pressure rise across the centrifugal pump design was determined for flow rates of 0.5 to 6 L/min for 2,750 to 4,250 RPM. A pressure rise of 10 to 145 *mmHg* was achieved over these operating conditions (**Figure 4B**). The design point of 3 L/min at 3,500 RPM demonstrated a pressure rise of ∼95 mmHg. Pressure rise was found to decrease with increasing flow rate and was higher at faster rotational speeds. This trend, as expected, was observed for both turbulence models. The pressure performance curves demonstrate the pump's ability to deliver an adequate flow range with target pressure rises at reasonable rotational speeds. For flow rates <3 L/min, the calculated expected pressure rises for the two turbulence models were observed to be 12–23% *mmHg* different in magnitude. At flow rates >3 L/min, the pressure rises were within 4–8% of each other, as seen in **Figure 4C**.

Axial fluid forces exerted on the magnetically levitated impeller rotor surface ranged from 0.4 to 2.5 N, and the radial fluid forces were found to be much lower in magnitude, ranging from 0.17 N to 0.84 N. As expected, higher axial fluid forces were observed for operating conditions yielding higher pressure generations. Hydraulic efficiencies (10–28%) were determined using the computational torque, enabling an estimation of the mechanical power usage, which ranged from 0.79 Watts to 4.58 Watts.

Fluid velocities were inspected in all models and at all operating conditions. **Figure 8** displays the fluid velocity vectors for the centrifugal pump model at the design point. Highlighted regions include the cutwater at the outlet of the pump, impeller tip clearance, and secondary flow path. These regions demonstrated irregular, vortical flow conditions, per the computational predictions. Outside of these regions, blood flow transitioned well from region to region across the centrifugal blood pump.

Tables 1, **2** indicate the scalar stress estimations and blood damage index calculations. All operating conditions resulted in blood damage indices of <2%, the threshold level for our designs. Approximately 99% of the computational walls and surfaces had scalar stresses below 425 Pascals. The fluid residence times, measured *via* streamlines, were all <600 ms, meeting the target

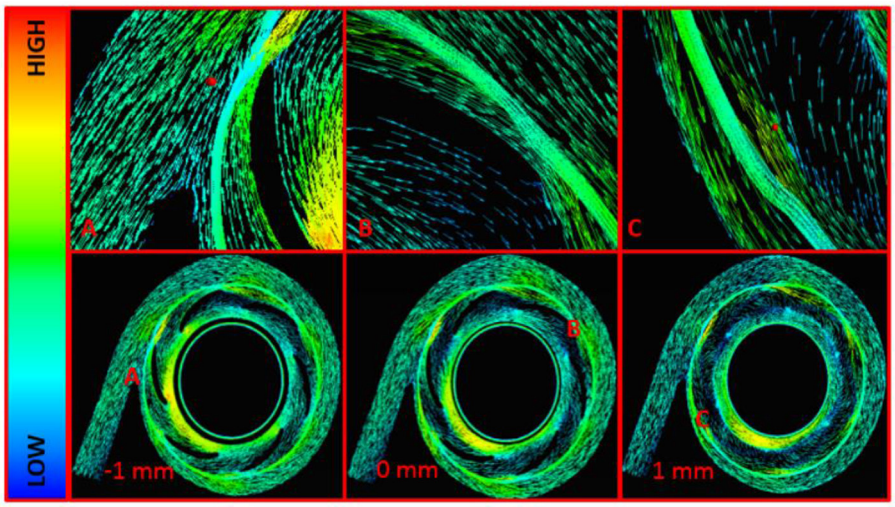

FIGURE 8 | Velocity Vectors for the Centrifugal Pump Model at 3,500 RPM and 3 L/min. **(A)** Cutwater Region, **(B)** Impeller Blade Tip, **(C)** Secondary Flow Path and Impeller Cutwater Region at the Outlet Volute. These are midspan views across the centrifugal blood pump. The central midspan is indicated at 0 mm, and two additional midspan views are shown 1 mm above and -1 mm below the central midspan.

TABLE 1 | Fluid stress level and blood damage index estimations for the centrifugal pump model.

Flow rate	Scalar stress (Pa)		Damage index (%)	
(L/min)	Avg	% > 425	Mean	Max
Operating rotational speed of 4,250 RPM				
3	59.9	0.7	0.170	1.12
4	66.6	1.0	0.193	1.06
5	66.5	1.0	0.178	0.80
Flow rate	**Scalar stress (Pa)**		**Damage index (%)**	
(L/min)	**Avg**	**% > 425**	**Mean**	**Max**
Operating rotational speed of 3,500 RPM				
3	42.0	0.08	0.083	0.66
4	50.2	0.27	0.099	0.53
5	54.0	0.55	0.098	0.58

Flow rates of 3–5 L/min at Rotational Speeds of 3,500 RPM and 4,250 RPM.

TABLE 2 | Fluid stress level and blood damage index estimations for the centrifugal pump model.

	Scalar stress (Pa)		Damage index (%)	
RPM	Avg	% > 425	Mean	Max
Operating flow rate of 3 L/min				
4,250	59.9	0.7	0.170	1.12
4,000	53.6	0.4	0.141	0.81
3,750	47.7	0.2	0.129	0.15
3,500	42.0	0.1	0.083	0.66

Rotational Speeds of 3,500–4,250 RPM at 3 L/min.

requirement. As expected, higher rotational speeds yielded higher scalar stress levels. Higher scalar stresses were found in the blade tip clearances, at the leading edge of the blades, near the cutwater region in the outlet volute, and on the suction side (i.e., backside) of the impeller blades.

Transient Flow Simulation Findings

Quasi-Steady Study on the Centrifugal Impeller

Figure 4E illustrates the computational predictions for the quasi-steady analysis of the centrifugal blood pump and the impact on pressure generation as a function of rotational position of the impeller blades. Sixty simulations were completed for rotational increments of 6°. This study was performed at 3,500 RPM and 3 *L/min*. Six peak pressure generations were observed, and these peak pressure generations occurred at every 60°. The peaks correlate with blade number, and a shift in the pressure rise was observed from 86 to 95 *mmHg*, indicating a blade passage influence in the pressure rise across the pump.

TRSI Results

Figure 4F demonstrates the TRSI simulations for a rotational speed of 3,500 RPM at 3 *L/min*. The average pressure generation was found to range from 74 to 96 *mmHg*, which is a much wider range than indicated by the quasi-steady study. Pressure fluctuations due to the blade passage frequency are more significant and can be observed with the expected 6 peaks in a full rotation. The axial and radial fluid forces ranged from 1.71 to 1.93 N, and 0.16 to 0.79 N, respectively.

TABLE 3 | Normalized Index of Hemolysis (N.I.H) for bovine blood studies.

Experiment	N.I.H (g/100 L)
$N = 1$	0.10
$N = 2$	0.10
$N = 3$	0.12
$N = 4$	0.11
$N = 5$	0.07
$N = 6$	0.06
Ave	0.09 ± 0.02*

*Repeated (n = 6) hemolytic studies at ∼2 L/min using magnetically levitated centrifugal pump prototype. *p < 0.05.*

Hydraulic Results

Figure 6L displays the pressure-flow hydraulic performance results for the testing speeds of 2,750–4,250 RPM in 250 RPM intervals. The magnetically levitated centrifugal prototype delivered 0–6.75 L/min at 0–182 mmHg over those rotational speeds. Higher rotational speeds led to more substantial pressure rises at a given rotational speed. Moreover, higher flow rates produced lower pressure rises at a given rotational speed. These trends met expectations for centrifugal pumps. The full flow range of testing for 2 rotational speeds were re-measured, and the pressure-flow performance data demonstrated repeatability.

Hemolytic Results

Over each 4-h hemolytic test period, the rotational speed, temperature and flow rate were held constant, and we drew test samples every 30 min. The bovine blood in the circuit was maintained at a temperature of $36.31 \pm 1.94^{\circ}$C, a flow rate of 2.06 ± 0.06 L/min and rotational speed of $1{,}080 \pm 228$ RPM. The initial bovine blood hematocrit values ranged between 30 and 38% and slightly decrease over the duration of the study; an average hematocrit drop of $1.8\% \pm 0.7\%$ ($p < 0.5$) was measured for all experiments. The pfHb levels increased linearly over the experiment 4-hr duration, as expected. The Shapiro–Wilk test supported a normality assumption ($p > 0.05$), and the pfHb concentration linearity was verified *via* regression statistics using F-test and coefficient *t*-test ($p < 0.5$). The significance and independence of each hourly average pfHb level was also assessed. No outliers were determined per the Tukey-Hoaglin outlier test. A test of homogeneity of variance was showed that there was equal variance between experimental data sets ($p > 0.5$). An F-test for heteroskedasticity demonstrated that the variance of the errors does not depend on time, thus further supporting the significance and independence of each hourly average pfHb measurement. **Table 3** shows the N.I.H determinations for each experiment, which ranged from 0.06 g/100 L to 0.12 g/100L. The average N.I.H value ($n = 6$) for all of the experiments was determined to be 0.09 ± 0.02 g/100 L ($p < 0.05$).

DISCUSSION

To provide a new therapeutic solution for pediatric patients with heart failure, we are developing a new blood pump technology in the form of a continuous-flow, magnetically levitated TAH (13, 14). The overall target size of this TAH is 50 mm in diameter by 50 mm in height and has only 2 moving parts, an axial and centrifugal impeller, each levitated by magnetic suspension. Thus, this blood pump technology is expected to be able to provide extracorporeal MCS to patients <0.65 m^2 (i.e., <12 kg or younger than ∼2 years old) and intracorporeal MCS to patients >0.65 m^2 (i.e., >15 kg or older than ∼2 years old). The axial pump mechanically supports the pulmonary circulation, and the centrifugal impeller supports the systemic circulation. The device utilizes the latest generation of magnetic bearing technology to levitate the impellers, enabling a longer operational lifespan and wider clearances between the rotating impeller surfaces and pump housing (about 5× wider than mechanical bearings). These wider clearances reduce fluid shear stresses and lower the risk of thrombosis and hemolysis. This design also avoids the use of the mechanical or biologic valves that can fail prematurely.

Initial designs have been developed for both the axial and centrifugal pumps (13, 14). Since the axial region and centrifugal fluid domains are separate and independent from each other, the pumps can initially be developed separately. The data presented in this paper, consisting of both computational and experimental studies, has concentrated on the design and development of the centrifugal pump and presents the latest developmental progress.

In the computational studies, two turbulence models were employed: k-epsilon and SST models. A quantitative comparison of the computational predictions, using both turbulence models, and the experimental measurements of the centrifugal pump prototype was performed. **Figure 4D** illustrates this comparison. For flow rates <3 *L/min*, the SST model correlated to within 10% of the experimental measurements, and the k-epsilon model correlated to within 19% of the experimental measurements. The SST and k-epsilon models correlated to within 5–8% of the experimental measurements for flow rates >3 *L/min*. The SST turbulence model utilizes a blending function to transition between near-wall modeling equations and bulk k-epsilon modeling equations. It is expected that as the flow rate increases, yielding higher Reynolds numbers, the SST and k-epsilon models would predict more similar results. This was observed computationally. Deviations between CFD and experiments are expected. While the choice of turbulence model is important to the accuracy of the simulations, there is no definitive approach to determine which turbulence model is optimally suited for miniature blood pumps; where the blood flow conditions are highly dynamic and likely fluctuate among laminar, unsteady transitional, and truly turbulent flow conditions.

The only rotating component in the centrifugal pump is the impeller and its 6-bladed impeller that causes the observed blade passage frequency in the fluid physics. This effect was observed using both quasi-steady analysis and the transient TRSI approach. Six peak pressure rises, corresponding to the six blades, were observed in the computational data sets. Pressure fluctuations due to the blade passage frequency were more

pronounced for the TRSI simulations, and axial and radial fluid force ranges were wider for the TRSI study. Nevertheless, significant pressure and fluid force deviations between the quasi-steady and TRSI simulations were not found, in accordance with prior studies (16).

Per the hydraulic studies, the centrifugal pump prototype delivered target pressure rises and capacities to support pediatric patients. We chose the tightest tolerancing for prototype manufacturing (Applied Rapid Technologies, Fredericksburg, Virginia, USA) in support of the impeller geometry, blade tip clearance and secondary flow path dimensions. Trends among performance of the computational models and prototypes were similar for the centrifugal model and prototype testing; both data sets followed expected trends according to pump design theory (28). Computations predicted the axial fluid forces to be <3 N and radial forces of <1 N for the centrifugal pumps; these forces correlate well with levels of other magnetically-levitated centrifugal blood pumps. The higher scalar stress along the blade tips, leading edge of the impeller blades, and at the cutwater region is also to be expected due to the presence of transitional velocity gradients and proximity of rotating-stationary surfaces. After completing this study, we explored improving the mesh element in these regions and found that the scalar stress is highly sensitive to the volume skew of the elements in these regions. A recent publication also indicates shear stresses being sensitive to mesh characteristics (29). The majority of scalar stress values were below 425 Pascals, and blood damage indices were below the design criteria of 2% for all operating conditions.

The magnetically levitated centrifugal prototype incorporated touchdown surfaces on the center spindle region and a constraining secondary flow path. Thus, the N.I.H. values for the repeated 4 h studies were found to be higher than desired. Clinically approved blood pumps have demonstrated N.I.H values of <0.04 g/100 L, and our results average N.I.H was 0.09 ± 0.02 g/100 L. The hemolytic potential of our current centrifugal prototype design is problematic, and the hemolytic potential must be reduced with further design improvement. Next phase development will integrate the axial flow blood pump, and thus the spindle region and secondary flow path will be modified to address the complex fluid dynamics in these regions.

Study Limitations and Future Work

This study has limitations that must be addressed in future work. The focus of this work has been on the centrifugal pump design, and we must improve the axial pump in future development phases. The axial blood pump is currently under redesign to reduce size, lower fluid forces on the levitated impeller, and improve energy transfer. We are in the process of combining the centrifugal prototype with the axial pump to conduct an integrated configuration for hydraulic and hemolytic testing. We must evaluate the integrated, full pediatric TAH design both computationally and experimentally to evaluate the hydraulic performance, hemolytic levels, and magnetic flux directions to assess and address any interference between suspension systems. Next phase hemolytic studies must include more flow rates and rotational speeds and be conducted for a minimum of 6 h study durations. Inflow and outflow cannulae are currently being designed using 3-D MRI images of human thoracic cavities. Moreover, we have constructed a lumped parameter model of the cardiovascular system such that we can include downstream and upstream boundary conditions in a multi-scale computational platform. The balance of blood flow and preload distribution between the pulmonary and systemic circulations is also an ongoing challenge for continuous flow TAHs, especially for those that utilize a single-rotor configuration. In this configuration, the axial and centrifugal pumps are separate and thus can be controlled independently; nevertheless, we must determine optimal control algorithms during the next development phase. Fit and placement will also be virtually examined, and control algorithms will be devised to ensure either RPM for pulsatility in the outflow for long-term mechanical circulatory assistance or to maintain continuous flow during acute support scenarios. A focus is also currently on the motor and magnetic suspension system integration and a size reduction in preparation for acute animal experiments during next steps.

CONCLUSIONS

Clinically-available blood pumps and total artificial hearts for pediatric patients continue to lag behind those developed for adults. To address this unmet clinical need, we are developing a hybrid-design, continuous-flow, magnetically levitated, pediatric total artificial heart (TAH). The hybrid TAH design integrates both an axial and centrifugal blood pump within a single, compact housing. The centrifugal pump rotates around the separate axial pump domain, and both impellers rotate around a common central axis. Here, we performed computational studies and prototyping testing for the centrifugal pump component. The computational studies and the prototype testing demonstrated that the centrifugal design is effective; design requirements for the centrifugal pump were achieved. The pressure-flow performance, axial and radial fluid forces, scalar stresses, blood damage indices and mechanical power consumption estimates fell within target design requirements, except that the hemolytic potential must be reduced with further design improvement. These data support the next phase of development for the motor and magnetic suspension of the centrifugal pump and integration of the axial flow blood pump component.

DATA AVAILABILITY STATEMENT

The raw data supporting the conclusions of this article will be made available by the authors, without undue reservation.

AUTHOR CONTRIBUTIONS

AT and CF: concept and design, data collection, data analysis and interpretation, critical revision of article, and approval of article. TP: data collection, data analysis and interpretation, drafting article, critical revision of article, and approval of article. MH: data collection, data analysis and interpretation, drafting article,

critical revision of article, and approval of article. RS, JR, SD, and VT: data analysis and interpretation, critical revision of article, and approval of article. All authors contributed to the article and approved the submitted version.

ACKNOWLEDGMENTS

The authors wish to acknowledge the financial support as provided by partial support from a 2016 Individual Biomedical Research Award from The Hartwell Foundation, from 2019 U.S. Department of Education GAANN Fellowship (MH) and from a 2022 U.S. Department of Education GAANN Fellowship (TP). A portion of this research reported in this publication was also supported by the National Heart, Lung, And Blood Institute of the National Institutes of Health, under Award Number: R01HL153536. The content is solely the responsibility of the authors and does not necessarily represent the official views of the National Institutes of Health.

REFERENCES

1. World Health Organization. *Cardiovascular Diseases*. Geneva: World Health Organization (2021).
2. Lippi G, Sanchis-Gomar F. Global epidemiology and future trends of heart failure. *AME Med J.* (2020) 5:15. doi: 10.21037/amj.2020.03.03
3. Das B. Current state of pediatric heart failure. *Children.* (2018) 5:88. doi: 10.3390/children5070088
4. Benjamin EJ, Blaha MJ, Chiuve SE, Cushman M, Das SR, Deo R, et al. Heart Disease and stroke statistics'2017 update: a report from the American Heart Association. *Circulation*. (2017) 135:e146–603. doi: 10.1161/CIR.0000000000000491
5. Adachi I, Jaquiss RDB. Mechanical circulatory support in children. *Curr Cardiol Rev*. (2016) 12:132–40. doi: 10.2174/1573403X12666151119165841
6. Rossano JW, Kim JJ, Decker JA, Price JF, Zafar F, Graves DE, et al. Prevalence, morbidity, and mortality of heart failure-related hospitalizations in children in the United States: a population-based study. *J Card Fail.* (2012) 18:459–70. doi: 10.1016/j.cardfail.2012.03.001
7. Bryant R, Wisotzkey B, Velez DA. The use of mechanical assist devices in the pediatric population. *Sem Pediatr Surg.* (2021) 30:151041. doi: 10.1016/j.sempedsurg.2021.151041
8. Hope KD, Bhat PN, Dreyer WJ, Elias BA, Jump JL, Santucci G, et al. Pediatric palliative care in the heart failure, ventricular assist device and transplant populations: supporting patients, families and their clinical teams. *Children*. (2021) 8:468. doi: 10.3390/children8060468
9. Dipchand AI. Current state of pediatric cardiac transplantation. *Ann Cardiothor Surg.* (2018) 7:31–55. doi: 10.21037/acs.2018.01.07
10. Almond CSD, Thiagarajan RR, Piercey GE, Gauvreau K, Blume ED, Bastardi HJ, et al. Waiting list mortality among children listed for heart transplantation in the United States. *Circulation.* (2009) 119:717–27. doi: 10.1161/CIRCULATIONAHA.108.815712
11. Lichtenstein KM, Tunuguntla HP, Peng DM, Buchholz H, Conway J. Pediatric ventricular assist device registries: update and perspectives in the era of miniaturized continuous-flow pumps. *Ann Cardiothor Surg.* (2021) 10:329–38. doi: 10.21037/acs-2020-cfmcs-18
12. Palazzolo T, Hirschhorn M, Garven E, Day S, Stevens RM, Rossano J, et al. Technology landscape of pediatric mechanical circulatory support devices: a systematic review 2010–2021. *Artif Organs*. (2022). doi: 10.1111/aor.14242. [Epub ahead of print].
13. Fox C, Sarkisyan H, Stevens R, et al. New versatile dual-support pediatric heart pump. *Artif Organs*. (2019) 43:1055–64. doi: 10.1111/aor.13507
14. Fox C, Chopski S, Murad N, Allaire P, Mentzer R Jr, Rossano J, et al. Hybrid continuous-flow total artificial heart. *Artif Organs*. (2018). 42:500–9. doi: 10.1111/aor.13080
15. Fraser KH, Taskin ME, Griffith BP, Wu ZJ. The use of computational fluid dynamics in the development of ventricular assist devices. *Med Eng Phys*. (2011) 33:263–80. doi: 10.1016/j.medengphy.2010.10.014
16. Song X, Throckmorton AL, Wood HG, Allaire PE, Olsen DB. Transient and quasi-steady computational fluid dynamics study of a left ventricular assist device. *ASAIO J.* (2004) 50:410–7. doi: 10.1097/01.MAT.0000136507.57707.0F
17. Bhavsar SS, Kapadia JY, Chopski SG, Throckmorton AL. intravascular mechanical cavopulmonary assistance for patients with failing fontan physiology. *Artif Organs.* (2009) 33:977–87. doi: 10.1111/j.1525-1594.2009.00940.x
18. Pekkan K, Dur O, Sundareswaran K, Kanter K, Fogel M, Yoganathan A. Neonatal aortic arch hemodynamics and perfusion during cardiopulmonary bypass. *J Biomech Eng.* (2008) 130:10–3. doi: 10.1115/1.2978988
19. Good B, Deutsch S, Manning KB. Hemodynamics in a pediatric ascending aorta using a viscoelastic pediatric blood model. *Ann Biomed Eng.* (2016) 44:1019–35. doi: 10.1007/s10439-015-1370-z
20. Wells, Roe E Jr, Merrill EW. Influence of flow properties of blood upon viscosity – hematocrit relationships. *J Clin Invest*. (1962) 41:1592–8. doi: 10.1172/JCI104617
21. Bludszuweit C. Three-dimensional numerical prediction of stress loading of blood particles in a centrifugal pump. *Artif Organs.* (1995) 19:590–6. doi: 10.1111/j.1525-1594.1995.tb02386.x
22. Paul R, Apel J, Klaus S, Schugner F, Schwindke P, Reul H. Shear stress related blood damage in laminar couette flow. *Artif Organs.* (2003) 27:517–29. doi: 10.1046/j.1525-1594.2003.07103.x
23. Giersiepen, M., Wurzinger, LJ, Opitz, R, Reul H. Estimation of shear stress-related blood damage in heart valve prostheses-*in vitro* comparison of 25 aortic valves. *Int J Artif Organs*. (1990) 13:300–6. doi: 10.1177/039139889001300507
24. Chopski SG, Fox CS, McKenna KL, Riddle ML, Kafagy DH, Stevens RM, et al. Physics-driven impeller designs for a novel intravascular blood pump for patients with congenital heart disease. *Med Eng Phys*. (2016) 38:622–32. doi: 10.1016/j.medengphy.2016.03.010
25. Song X, Throckmorton AL, Wood HG, Antaki JF, Olsen DB. Quantitative evaluation of blood damage in a centrifugal VAD by computational fluid dynamics. *J Fluids Eng.* (2004) 126:410–8. doi: 10.1115/1.1758259
26. Cripps CM. Rapid method for the estimation of plasma haemoglobin levels. *J Clin Pathol*. (1968) 21:110–2. doi: 10.1136/jcp.21.1.110
27. Throckmorton AL, Untaroiu A, Allaire PE, Wood HG, Lim DS, McCulloch MA, et al. Numerical design and experimental hydraulic testing of an axial flow ventricular assist device for infants and children. *ASAIO J*. (2007) 53:754–61. doi: 10.1097/MAT.0b013e31815581ea
28. Pumps, S. *Centrifugal Pump Handbook*. 3rd Edn. Oxford, UK: Butterworth-Heinemann (2010).
29. Gross-Hardt, S, Boehning F, Steinseifer U, Schmitz-Rode T, Kaufmann T. Mesh sensitivity analysis for quantitative shear stress

assessment in blood pumps using computational fluid dynamics. *J Biomechan Eng.* (2019) 141. doi: 10.1115/1.4042043. [Epub ahead of print].

Conflict of Interest: The authors declare to disclose that the lead and corresponding authors (CF and AT) from the BioCirc Research Laboratory are inventors on patents for the Drexel Dragon Heart blood pumps (two awarded USPTO patents and patent applications that are currently under consideration by the USPTO). JR discloses that he has served as a consultant for Abiomed, MyoKardia, Merck, Bayer, and Novartis.

The remaining authors declare that the research was conducted in the absence of any commercial or financial relationships that could be construed as a potential conflict of interest.

Publisher's Note: All claims expressed in this article are solely those of the authors and do not necessarily represent those of their affiliated organizations, or those of the publisher, the editors and the reviewers. Any product that may be evaluated in this article, or claim that may be made by its manufacturer, is not guaranteed or endorsed by the publisher.

frontiers | Frontiers in Cardiovascular Medicine

TYPE Review
PUBLISHED 14 September 2022
DOI 10.3389/fcvm.2022.971028

OPEN ACCESS

EDITED BY
Caglar Ozturk,
Massachusetts Institute of Technology, United States

REVIEWED BY
Manfred F. Maitz,
Leibniz Institute of Polymer Research (LG), Germany
Bowen Wang,
University of Virginia, United States

*CORRESPONDENCE
Timo Z. Nazari-Shafti
nazari@dhzb.de

SPECIALTY SECTION
This article was submitted to General Cardiovascular Medicine, a section of the journal Frontiers in Cardiovascular Medicine

RECEIVED 16 June 2022
ACCEPTED 01 August 2022
PUBLISHED 14 September 2022

CITATION
Exarchos V, Zacharova E, Neuber S, Giampietro C, Motta SE, Hinkov H, Emmert MY and Nazari-Shafti TZ (2022) The path to a hemocompatible cardiovascular implant: Advances and challenges of current endothelialization strategies. *Front. Cardiovasc. Med.* 9:971028. doi: 10.3389/fcvm.2022.971028

The path to a hemocompatible cardiovascular implant: Advances and challenges of current endothelialization strategies

Vasileios Exarchos[1,2], Ema Zacharova[1,2,3], Sebastian Neuber[1,2], Costanza Giampietro[4,5], Sarah E. Motta[6], Hristian Hinkov[1,2], Maximilian Y. Emmert[1,2,6,7,8] and Timo Z. Nazari-Shafti[1,2,9]*

[1]Cardiosurgical Research Group, Department of Cardiothoracic and Vascular Surgery, German Heart Center Berlin, Berlin, Germany, [2]Translational Cardiovascular Regenerative Technologies Group, Berlin Institute of Health at Charité – Universitätsmedizin Berlin, BIH Center for Regenerative Therapies, Berlin, Germany, [3]Department of Life Sciences, IMC University of Applied Sciences Krems, Krems an der Donau, Austria, [4]Experimental Continuum Mechanics, Empa Swiss Federal Laboratories for Materials Science and Technology, Dübendorf, Switzerland, [5]Department of Mechanical and Process Engineering, Institute for Mechanical Systems, ETH Zürich, Zurich, Switzerland, [6]Institute for Regenerative Medicine, University of Zurich, Zurich, Switzerland, [7]Clinic for Cardiovascular Surgery, Charité – Universitätsmedizin Berlin, Berlin, Germany, [8]Department of Health Sciences and Technology, ETH Zürich, Zurich, Switzerland, [9]Berlin Institute of Health at Charité – Universitätsmedizin Berlin, BIH Biomedical Innovation Academy, BIH Charité (Junior) (Digital) Clinician Scientist Program, Berlin, Germany

Cardiovascular (CV) implants are still associated with thrombogenicity due to insufficient hemocompatibility. Endothelialization of their luminal surface is a promising strategy to increase their hemocompatibility. In this review, we provide a collection of research studies and review articles aiming to summarize the recent efforts on surface modifications of CV implants, including stents, grafts, valves, and ventricular assist devises. We focus in particular on the implementation of micrometer or nanoscale surface modifications, physical characteristics of known biomaterials (such as wetness and stiffness), and surface morphological features (such as gratings, fibers, pores, and pits). We also review how biomechanical signals originating from the endothelial cell for surface interaction can be directed by topography engineering approaches toward the survival of the endothelium and its long-term adaptation. Finally, we summarize the regulatory and economic challenges that may prevent clinical implementation of endothelialized CV implants.

KEYWORDS

cardiovascular implants, hemocompatibility, endothelialization, valves, topography

Introduction

Coronary artery disease, heart valve dysfunction and heart failure are the leading causes of death worldwide (1, 2). Today, cardiovascular (CV) implants such as coronary stents, vascular grafts, bioprosthetic heart valves, and ventricular assist devices (VADs) are cornerstones in the treatment of CV disease. However, they are still associated with considerable adverse events such as thromboembolic events and infection (3).

In most cases, obstructive coronary artery disease is treated with percutaneous stent implantation or balloon angioplasty. However, both approaches increase the peri-interventional risk for endothelial damage and local inflammation, leading to restenosis due to intimal hyperplasia. To date, these adverse effect are counteracted by coating the stents with biodegradable polymers loaded with anti-proliferative drugs (e.g., sirolimus, everolimus, or paclitaxel) (4). However, local pharmacological therapy also disrupts endothelialization across the stent surface, which in turn increases the risk of late in-stent thrombosis and thus the need for a long-term inhibition of platelet aggregation (5). In patients with progressive multi-vessel coronary disease, coronary revascularization with autologous arterial grafts is the gold standard. However, in an increasingly aging and multi-morbid population, appropriate autologous arterial and venous grafts are often difficult to obtain. In addition, co-morbidities such as diabetes negatively impact graft remodeling and a significant number of patients suffer from a high rate of long-term graft failure (6). Therefore, there is an increasing clinical demand for small-diameter tissue engineered vascular grafts (TEVGs) that promote and support endothelialization at their luminal surface to avoid thrombus formation (7). In addition, widespread implantation of TEVGs could minimize wound complications associated with peripheral graft harvesting.

For patients with advanced degenerative heart valve disease, mechanical or bioprosthetic valve implantation is chosen if the native valve is unsuitable for reconstructive surgery. Patients that receive mechanical implants require lifelong anticoagulation to avoid potential thrombogenic complications (8). After implantation of a xenogeneic bioprosthetic valve, guidelines recommend anticoagulation therapy for only 3 months, because thrombotic events usually occur within the first 3 months after implantation (9). However, leaflets of bioprosthetic valves can calcify and become fibrotic over time, leading to progressive stenosis. A biocompatible fully endothelialized tissue-engineered heart valve (TEHV) may prevent early thrombus formation, chronic degeneration and generally minimizes the duration of anticoagulation therapy and associated complications.

For patients with end-stage heart failure due to coronary artery disease, heart valve dysfunction or other causes, heart transplantation and VAD support are the only available therapeutic options. However, both have their limitations and due to the increasing lack of donor organs, there will be a higher need for VAD therapy in the future (10). Unfortunately, long-term VAD implantation dramatically increases the risk of thrombosis and hemorrhagic complications due to insufficient hemocompatibility (11).

Endothelialization of vascular stents, vascular grafts, valves or even VADs may minimize the major disadvantages associated with long-term implantation of CV implants, but is still a challenging goal. For example, a plethora of reviews have reported current and evolving strategies designed to aid in the mobilization of bone marrow endothelial progenitor cells, as well as cell-specific homing, adhesion, and activation for *in situ* endothelialization (12–16). Moreover, there are numerous reviews on innovative methods that are utilized for biomaterial biofunctionalization. While many reports mainly focus on chemical modification, less attention has been paid to physical modification of biomaterial surfaces (17, 18). In addition, most of the literature focusing on physical modifications is limited regarding the effect of different nanotopographic patterns or biomaterials on basic cell functions such as adhesion, orientation, or migration (19, 20). In the present review, we look back on the last three decades and report critically on important innovative steps toward the endothelialization of CV implants (6). Furthermore, we focus on physical modification of surfaces with the aim to describe sperically the influence of surface-induced biomechanical cues on complex endothelial cell (EC) functions such as proliferation, apoptosis, inflammatory activation or even regeneration. As endothelialization strategies will target more complex CV implants in the future, we also evaluate VAD endothelialization studies and endeavor to critically comment on challenges related to the complexity and cost-effectiveness, as well as the regulatory path and clinical utility of endothelialization in CV implants.

Function of the endothelial monolayer

ECs play an important role in hemostasis and blood-tissue barrier function, including: (i) control of vascular tone and permeability, (ii) control of coagulation and inflammation, and (iii) modulation of regenerative and anti-apoptotic pathways (21). In general, the endothelial monolayer covers the vascular luminal surface and acts as a selective barrier controlling the movement of water, proteins, metabolites and blood cells between the intravascular and interstitial space (22). Endothelial barrier functions are mainly ensured by junctional integrity, which is controlled by proteins that form the adherens junction (AJ) and tight junction (TJ) complexes, the focal adhesions (FAs) and the actin cytoskeleton. Adjacent ECs are laterally connected to their neighbors through AJs and TJs, both based on transmembrane adhesive proteins that promote homophilic interactions in a dynamic and plastic way (23, 24). Integrin-based FAs connect the basal side of ECs to the endothelial

basement membrane (EBM). In the cytoplasm, the dynamic organization of actin filaments anchored to regions of cell-to-cell or cell-to-EBM contact contributes to a super-cellular mechanosensitive and mechanotransducive molecular network (25). Moreover, vascular permeability is determined by the synthesis and release of a wide range of vasoactive molecules (26). Nitric oxide (NO), the most studied vasoactive molecule is generated from L-arginine by endothelial NO synthase. NO synthesis leads to vasodilation, increases vascular permeability, inhibits platelet aggregation and modulates smooth muscle cell proliferation (22, 27). Intriguingly, NO synthesis and release, as well as inter-cellular junctions, FAs, and cytoskeletal organization are all modulated under the impact of blood flow-mediated biomechanical cues (28). The endothelium senses these signals and converts them into biological responses *via* mechanotransduction pathways to maintain its physiological function (28, 29). Under steady laminar blood flow in straight arterial segments with high shear stress acting on the endothelial luminal surface, ECs orient parallel to the flow as actin filament elongation reduces parallel intercellular stresses in favor of stability of intercellular adherent junctions and improvement of the monolayer integrity (30, 31). In addition, the physiological activation of NO synthesis and release increases blood flow to areas of the body that are deprived of oxygen and nutrients (32, 33). In contrast, impaired multidirectional turbulent blood flow at specific anatomic sites (e.g., aortic bifurcation) due to low shear stress is associated with reduced NO production and a chronic, low-grade inflammatory process. This in turn leads to a predisposition to endothelial injury and activation of the blood clotting cascade, mainly in patients with common risk factors such as hypertension, hypercholesterolemia, smoking, and diabetes mellitus (34–36).

When endothelial injury occurs, extracellular matrix (ECM) components, such as collagen, exposed to blood lead to the accumulation of platelets, red blood cells and fibrin polymerization, resulting in thrombus formation (37). In general, this coagulation process occurs *via* two pathways: (i) the extrinsic pathway, which is primarily triggered by external trauma, and (ii) the intrinsic pathway, which is triggered by damage to the inner vessel wall. The extrinsic pathway consists of the transmembrane receptor tissue factor (TF), which binds to coagulation factor VII/VIIa and initiates the coagulation cascade. The intrinsic pathway consists of plasma coagulation factors XI, IX, and VIII (37). TF is mainly expressed by perivascular cells such as adventitia fibroblasts or even vascular smooth muscle cells and circulating monocytes in response to the initiation of the coagulation cascade (38). Interestingly, mechanical injury due to excessive stretching or excessive release of circulating pro-inflammatory molecules (e.g., lipopolysaccharide, tumor necrosis factor-α, interleukin-1β, thromboxane A2) leads to EC activation and enhanced expression of TF, mainly due to nuclear translocation of the nuclear factor kappa-light-chain-enhancer of activated B cells (NF-κB). In parallel, there is a down-regulation of anticoagulant factors [e.g., thrombomodulin, tissue plasminogen activator, tissue factor pathway inhibitor (TFPI), NO synthesis] and a decrease in heparan-sulfate containing the anticoagulant glycocalyx (39). Furthermore, in activated ECs, intracellular vesicles with preformed proteins (e.g., the Weibel–Palade bodies) accumulate at the plasma membrane and release von Willebrand factor (VWF), P/E-selectin, angiopoietin-2, VCAM-1, and ICAM-1, which enhance further platelet binding and leukocyte recruitment (40). Moreover, blood cell transmigration and the release of pro-inflammatory stimuli destabilize the intercellular junctions, contributing to a progressive disruption of the endothelial barrier and the propagation of inflammation and thrombus formation (41).

Whereas permeability, monolayer integrity, and anticoagulant properties of EC monolayers are controlled by flow- or inflammation-mediated biomechanical cues as described above. Biomechanical cues derived from the interplay between FAs and the EBM appear to play a fundamental role in monolayer connectivity as well as modulation of tissue repair pathways. Intriguingly, there is a growing body of literature expressing the hypothesis that cross-regulation between AJs and FAs contributes to the maintenance of vascular barrier function (42). Furthermore, recent experimental data recognize integrins as a major player in endothelialization during angiogenesis, which regulate fundamental cellular processes including not only anchoring, polarization, and migration, but also cell proliferation, differentiation, and regeneration (43, 44). Indeed, mechanosensing can be transmitted from the cell membrane through the actin cytoskeleton to the nucleoskeleton by cell-to-surface interaction, thereby modulating gene expression associated with regenerative, tissue repair and antiapoptotic pathways (45, 46).

Requirements for biomimetic surfaces and strategies for endothelialization

To develop a CV implant with a hemocompatible luminal surface, several key requirements must be met. The ideally biocompatible surface for endothelialization should (i) reduce or even eliminate non-specific protein adsorption (ii) enhance EC adhesion, polarization, flow-oriented elongation, and migration, leading to the establishment of an EC monolayer, (iii) prevent platelet adhesion and thrombus formation due to inflammatory EC activation and initiation of blood coagulation cascade, and (iv) activate regenerative and anti-apoptotic pathways without increasing the risk of uncontrolled proliferation and tumor growth. Considering the essential role of the EC monolayer in the homeostasis of the whole vascular wall, numerous research groups are

making immense efforts to develop innovative strategies for successful endothelialization of CV implants. Two of the most common approaches for the development of CV implant surfaces aimed at mimicking and adopting the properties of ECs are physical and chemical modification. Physical modification approaches aim to engineer physical properties of biomaterials, including stiffness, wetness and surface topography, at the micro- or nanoscale topography (47). Chemical modification strategies aim to adjust chemical and biological properties of biomaterials (47). The most studied type of chemical modification is the biofunctionalization of surfaces *via* chemical adsorption, surface grafting, plasma treatment, and control of protein adsorption. Protein adsorption is the first event that occurs after implantation of a CV implant, beginning a few seconds after blood–surface interaction (48). After binding on the surface, the protein molecules (e.g., albumin and fibrinogen) show a modification of their macromolecular conformation that tends to adopt unique biochemical and physicochemical behavior (49). The progressive degradation of biomaterials, chronic recurrent infection due to biofilm formation, deleterious inflammatory, and immune responses, as well as initiation of blood coagulation cascade due to the activation of circulating blood cells and blood coagulation factors are the main effects of excessive protein deposition on the surface of biomaterials (50). Several strategies have been developed to integrate stealth properties into the surface of biomaterials that prevent protein deposition. Highly hydrophilic water-binding molecules, such as hydrophilic polysaccharides (e.g., dextran, heparin, polyacrylates, phosphorylcholine, polyethylene glycol) have been used to cover the inert blood-contacting surface, as it is well-described that the increased surface wetness is associated with reduced protein adsorption (51). In contrast, superhydrophobic micro-structured surfaces with specific geometry have been also applied to prevent highly soluble protein molecules from penetrating into the cavities of the nanostructure (52).

While numerous strategies have been focused on blocking the surface-protein interplay and initiating the blood coagulation cascade, alternative strategies aim to develop hemocompatible CV implants by promoting the endothelialization of the inert surface. Since the 1980s, the two main strategies for forming a healthy and functional endothelium on the blood-contacting surfaces of CV implants have been *in vitro* and *in vivo* endothelialization (53). For *in vitro* endothelialization, the three basic steps are: (i) EC isolation after vascularized tissue harvesting (e.g., saphenous vein or umbilical cord), (ii) *in vitro* cell expansion, and (iii) cell seeding on CV implants before implantation. *In vivo* endothelialization can be achieved by EC migration from the intact endothelium (transanastomotic ingrowth) or by adhesion, proliferation, and differentiation of circulating endothelial progenitor cells (EPCs).

While the formation of an intact EC monolayer may enhance the hemocompatibility of CV implants due to the anticoagulant properties of an intact monolayer, it is of great importance to underscore that activated endothelium due to inflammatory signals or mechanical injury, even in fully confluent monolayers, procoagulant and inflammatory properties can occur, which must be avoided in any endothelialization strategy (39). In this direction, a growing number of tissue engineering groups target to modulate complex pathways of plasmatic coagulation and inflammation strongly associated with EC activation *via*: (i) inactivation of adenosine diphosphate, GPIIb/IIIA, or VWF-dependent platelet adhesion, (ii) upregulation of anti-coagulant factors such as thrombomodulin, activated protein C, tissue factor protein inhibitor, heparin (iii) downregulation of pro-coagulant factors such as thrombin, Factor Xa, (iv) direct activation of fibrinolytic pathways based on tissue type plasminogen activator, urokinase, streptokinase and active plasmin immobilization, or (v) immobilization of immunosuppressive drugs such as everolimus, tacrolimus, and paclitaxel. (54).

Parallel, alternative experimental studies modify biological properties of CV biomaterials trying to mimic the biomechanical and biochemical native environment of ECs in favor of tissue repair, regeneration and anti-apoptotic properties (14). This includes, for example, the coating or incorporation of biomaterials with various biomolecules (e.g., NO donors) as well as growth factors [e.g., vascular endothelial growth factor (VEGF)]. These strategies have already been evaluated by several *in vitro* and animal studies as well as human clinical trials which are further discussed below (**Table 1**) (14).

Endothelialization of cardiovascular stents

Over the last three decades, important steps toward the production of biocompatible vascular stents have been made. Since the first implantation of a bare metal stent in the mid-1980s, innovative stent technologies have contributed to the development of drug eluting stents (DESs), which hinder excessive proliferation of smooth muscle cells and prevent intima hyperplasia through the controlled release of cytostatic drugs (4). Indeed, according to numerous large-scale clinical trials, DESs significantly reduced the risk of gradual re-narrowing of the stented segment (in stent restenosis) that occurs mostly between 3 and 12 months after coronary intervention (55, 56). However, anti-proliferative agents also delay the formation of an endothelial monolayer across the stent surface and consequently increase the risk of late (after 1 month) and very late (after 1 year) stent thrombosis (5). Therefore, in addition to the gradual drug release from implants within

TABLE 1 Past attempts to facilitate endothelialization of cardiovascular (CV) implants.

Properties/name	Luminal surface	References
CV stents		
Paclitaxel release TAXUS Express	Non-biodegradable coating material: poly(styrene-block-isobutylene-block-styrene) SIBS	TAXUS Clinical Trial, Stone et al. (142)
Sirolimus release CYPHER	Non-biodegradable coating materials: Parylene C, poly (ethylene-vinyl acetate), Poly(butyl methacrylate)	SIRTAX Clinical trial, Yamaji et al. (143)
Sirolimus release MiStent	Biodegradable coating material: poly(lactic-co-glycolic acid)	Dissolve clinical trial, Winter et al. (144)
Sirolimus release Ultimaster	Biodegradable coating materials: poly(D,L-lactide) and polymer light-emitting electrochemical cell	Chisari et al. (145)
Sirolimus release and EPCs attachment Combo	Biodegradable coating materials: poly(D,L-lactide) and poly(lactic-co-glycolic acid) with anti-CD34	REMEDEE clinical trial, Kerkmeijer et al. (146)
Sirolimus release Medtronic, Santa Rosa	Polymer-free	RevEvolution clinical trial, Worthley et al. (147)
Everolimus release Xience	Non-biodegradable coating materials: poly(butyl methacrylate), poly(vinylidene fluoride-co-hexafluoropropylene)	SPIRIT III clinical trial, Gada et al. (148)
Everolimus release Synergy	Biodegradable coating material: poly(D,L-lactide)	EVOLVE II clinical trial, Kereiakes et al. (149)
Zotarolimus release Resolute	Non-biodegradable coating materials: BioLinks composition of 3 polymers (C10, C19, and polyvinyl pyrrolidon)	TWENTE clinical trial, Birgelen et al. (150)
Novolimus release DESyne Nx	Non-biodegradable coating material: poly(butyl methacrylate)	EXCELLA II randomized controlled trial, Iqbal et al. (151)
Nitride oxide release TiNo stent	Polymer-free bare metal stent with titanium-NO	TIDES-ACS clinical trial, Tonino et al. (152)
Nitride oxide release Titan2 stent	Polymer-free bare metal stent with titanium-NO	TITAX clinical trial, KARJALAINEN et al. (63)
Nitride oxide release	Mussel-inspired dopamine-Cu II-coated metal stents for sustained *in situ* generation of NO	Rabbit model, Feng Zhang et al. (62)
VEGF/hepatocyte growth factor-secreting umbilical cord blood-derived mesenchymal stromal cells	Biodegradable coating material polydopamine with stem cell-secreting angiogenic growth factors	Swine model, Chang et al. (64)
Paclitaxel release	Porous composite matrix synthesized from amorphous carbon nanoparticles embedded in glassy polymeric carbon	Porcine model, Balram Bhargava et al. (153)
Paclitaxel release	Polymer-free nano-porous polymer	Porcine model, Haibo Jia et al. (154)
Sirolimus release	Polymer-free nano-porous polymer	Porcine model, Chen et al. (155)
TEVGs		
Position	**Production of TEVG**	**References**
Extracardiac total cavopulmonary conduit	Bioresorbable scaffolds of poly-l-lactide acid or poly (glycolic acid) coated with poly(l-lactic-co-ε-caprolactone) seeded with autologous bone marrow mononuclear cells	Human clinical trial in 25 pediatric patients with univentricular physiology, Tadahisa Sugiura et al. (78)
Hemodialysis conduit	Bioengineered accellular grafts produced in custom bioreactors using pulsatile circulation with cyclic radial strain followed by decellularization	Human trial in hemodialysis patients, Kirkton et al. (84)
Coronary artery bypass	Allograft saphenous veins were deendothelialized and seeded with autologous endothelial cells	Human clinical trial in 12 patients undergoing Coronary artery bypass surgery, Hermann et al. (80)
Infrarenal aortic replacement model	Hybrid grafts with poly (lactide-co-epsilon-caprolactone), collagen, and elastin loaded with heparin and VEGF	Rabbit model, Hu et al. (87)
Carotid artery bypass	Heparin and VEGF biofunctionalization of cell- free vessels based on small intestinal submucosa	Ovine model, Koobatian et al. (89)
Carotid artery bypass	Local NO delivery in decellularized xenografts derived from porcine veins promotes vascular regeneration and attenuates intimal hyperplasia and vascular calcification	Rabbit and rat model, Fei Wang et al. (88)

(*Continued*)

TABLE 1 (Continued)

Position	Production of TEHV	References
TEHVs		
Pulmonary valve replacement	*In vitro* seeding of decellularized cryopreserved pulmonary allograft with autologous vascular endothelial cell	Case report of a 43 year old patient, Dohmen et al. (114)
Pulmonary valve replacement	Decellularized human pulmonary valve allografts were reseeded with peripheral EPCs isolated from human blood.	First clinical implantation of pulmonary heart valves into 2 pediatric patients, Cebotari et al. (111)
Pulmonary valve replacement	A pulmonary allograft or xenograft was decellularized, coated with fibronectin, and seeded with autologous vascular endothelial cells, isolated from a piece of forearm or saphenous vein	Human trial in 23 patients, Dohmen et al. (116)
Pulmonary valve replacement	Decellularized fresh allograft valves	Human trial in 23 patients, Cebotari et al. (115)
Pulmonary valve replacement	*In vitro* ECM production from autologous derived cells on fast biodegradable synthetic scaffolds following enzymatic decellularization	Ovine model, Driessen-Mol et al. (108)
Pulmonary valve replacement	Seeding of acellular ovine pulmonary valve scaffolds with differentiated ECs and fibroblasts after stem cell isolation from adipose tissue	Ovine model, Movileanu et al. (109)
Pulmonary valve replacement	Cell-free, slow degrading elastomeric valvular implant populated by endogenous cells	Ovine model, Kluin et al. (127)
Pulmonary valve replacement	Decellularized porcine pulmonary valves were reseeded with autologous EPCs conjugated with CD133 antibodies	Ovine model, Jordan et al. (110)
VADs		
Position	**Surface modification**	**References**
In-flow cannula	Totally sintered cannula	Tucanova et al. (137)
In-flow cannula	Totally sintered cannula	Ranjit et al. (140)
In-flow cannula	Partially sintered titanium microsphere surface	Selzman et al. (138)

the first 4–6 weeks, alternative surface biofunctionalization approaches were developed (57). In 2003, the first-in-man implantation of an EPC capture stent was reported. These stents attract circulating EPCs with a CD34-positive antibody-coated surface. While phase I clinical studies have demonstrated the safety and efficacy of these stents (58), data from the multi-center TRIAS HR (TRI-stent adjudication study-high risk of restenosis) clinical trial showed that EPC-capturing stents are inferior to established DESs (59). Based on these results, a biofunctionalized DES known as the COMBO stent was developed that aimed to combine the pro-endothelialization property of EPC capture technology with the abluminal elution of the anti-proliferating agent sirolimus (58). In the first human study comparing COMBO stents to paclitaxel-coated DESs, a lower rate of thrombosis was observed (60). This led the group of Caligiuri to study the role of a soluble synthetic peptide (P8RI) that acts as a CD31 agonist and increases EC adhesion, showing accelerated endothelialization upon transplantation in the swine model of female farm pigs (61).

In recent years, alternative surface biofunctionalization approaches have been also developed. In a small animal study (rabbit model), mussel-inspired dopamine-Cu II-coated metal stents improved *in situ* NO generation and decreased the risk of stent thrombosis and restenosis (62). In parallel, in 2013, the research group of Karjalainen presented the 5-year clinical outcome of the randomized control study TITAX-AMI with a total of 425 patients. Interestingly, bioactive stents coated with titanium-NO achieved greater reductions in serious cardiovascular adverse events compared to paclitaxel-eluting stents (63). In addition, in a small scale animal study (swine model), Chang et al. reported a significant pro-endothelialization effect of coronary stents seeded with vascular endothelial growth factor-secreting mesenchymal stromal cells (MSCs) (64). Large scale animal and clinical studies are needed to further investigate these endothelialization strategies.

Endothelialization of vascular grafts

In 1954, Michael DeBakey reported the first successful distal aortic aneurysm resection and replacement in humans using a synthetic vascular graft of polyethylene terephthalate (39). Since then, large-diameter grafts made of synthetic, non-biodegradable materials have been extensively studied (65, 66). These materials have been shown to exhibit suitable mechanical properties and increased long-term durability in aortoiliac regions and other large arteries with diameters greater than 6 mm where high velocity blood flow and increased wall shear stress are encountered. However, their implementation in vessels with smaller diameters of less than 6 mm showed

a significant risk of intima hyperplasia and occlusive stenosis (7). It is already known that synthetic materials are associated with high protein adsorption, which contributes to foreign body reaction and thrombus formation (67). In addition, the lack of integrin binding sites prevents attachment of circulating EPCs or expansion of adjacent cell populations such as ECs, thereby inhibiting endothelialization (68).

In the mid-1980s, Weinberg and Bell started developing TEVGs based on natural ECM components such as collagen (69). Increased biocompatibility, lower toxicity, as well as enhanced EC adhesion and proliferation were observed in small animal studies (69–72). However, the poor mechanical properties of natural polymers under the hemodynamic forces of arterial blood flow shifted the focus to the development of synthetic biodegradable polymers (e.g., polycal-prolactone, polylactic acid) (73, 74). Biodegradable polymers often act as a temporary scaffold of a blood vessel and showed promising results in many animal studies (75, 76). The group of Shin'oka published in 1998 the first attempt of TEVGs made of synthetic biodegradable materials pre-cultured *in vitro* with autologous EC as pulmonary artery autografts in sheep (74). The same group later reported the first use of TEVGs as pulmonary artery replacement after *in vitro* culture with autologous bone marrow-derived mononuclear cells in a long-term study examining 25 pediatric patients with single ventricular physiology (77, 78). Even after 7 and 11 years of follow-up, no evidence of aneurysm formation, graft rupture, graft infection, or ectopic calcification was observed. The main reason for graft failure, which occurred in a small number of patients, was graft stenosis (78, 79). These studies demonstrated for the first time that endothelialization of TEVGs is possible after implantation in the high-flow, low-pressure system of the human pulmonary artery. Whether this success can also be expected under high-pressure arterial flow in small diameter arteries still needs to be investigated. In this context, Hermann et al. presented long-term results of 12 patients undergoing coronary artery bypass surgery in 2019. Intriguingly, in de-endothelialized allograft saphenous veins seeded with autologous endothelial cells *in vitro*, graft patency was detected up to 32 months after surgery. Immunohistochemistry after death suggested that monocyte activation may lead to vessel remodeling with thickening of the vessel wall (80).

To better understand the importance of EC monolayer predisposition to the specific hemodynamical environment of small and medium diameter arteries, the research group of Niklason and Langer developed a novel bioreactor system for testing TEVGs. The bioreactor is capable of using biomimetic mechanical stimulation applying biaxial (circumferential and axial) stretching (81). First, cells seeded on the polymer scaffold produce the vessel structure according to characteristics of the native ECM during bioreactor culture. In a second step, a decellularization process removes all cells, leaving only their ECMs, onto which autologous ECs can then be seeded *in vitro* or *in vivo*, providing a ready-to-use graft solution with promising results in animal studies (82, 83). These recent achievements are expected to lead to pilot studies in humans aimed at testing the efficacy of human acellular grafts used, for instance, as arteriovenous fistulas for vascular access in patients with end-stage renal disease (84). This graft design has great potential for clinical utility but remains to be evaluated in a larger number of patients and other sites of the human circulatory system. Recently, Hermann et al. reported the first data from a small human study in which allograft saphenous veins were harvested from organ donors, cryopreserved, deendothelialized, and then seeded with autologous ECs prior to implantation in 12 patients. Immunohistochemistry revealed the presence of ECs and monocytes as well as graft patency detected up to 32 months after surgery (80). These observations highlight the importance of the ECM and natural polymer components as a promising surface for any endothelialization procedure. This motivated tissue engineering groups to focus on the development of biofunctionalized hybrid grafts with the aim to mimic the biological properties of an endothelial monolayer. In detail, coating of synthetic polymer scaffolds with natural polymers has been studied extensively to improve biocompatibility and cell adhesion (85, 86). Hu et al. investigated hybrid grafts with poly (lactide-co-epsilon-caprolactone) (PLCL), collagen, and elastin loaded with heparin and VEGF in a short-term animal study (rabbit model, follow-up of 28 days), which showed increased cell adhesion and a high EC proliferation rate (87). Similarly, Wang et al. reported enhanced vascular regeneration and inhibition of intimal hyperplasia and vascular calcification after implantation of bio-hybrid vascular grafts with local NO delivery in both rabbit and mouse models (88). In another large animal study (sheep model), an acellular tissue engineered vessel based on small intestinal submucosa functionalized with heparin and VEGF demonstrated impressive mechanical properties with concomitant successful endothelialization (89).

In conclusion, synthetic or natural non-biodegradable materials are already associated with poor clinical results due to the high risk of intima hyperplasia and occlusive stenosis or inferior mechanical properties. Since synthetic biodegradable polymers have shown encouraging results, especially in small pediatric studies, many researches are now focusing on the development of biofunctionalized hybrid grafts with biomimetic properties.

Endothelialization of heart valves

Most commercial bioprosthetic heart valves are manufactured using glutaraldehyde-fixed xenogeneic materials, which offer an improved hemodynamic profile and reduced thrombogenicity compared to mechanical valves, thereby reducing the need for anticoagulation therapy. However, glutaraldehyde treatment does not prevent a complete

antigenicity of bioprosthetic valves, contributing to a chronic immunologic response associated with calcification, progressive degeneration, and structural valve failure within 10–15 years (90). The formation of a long-living EC monolayer on the valve surface prior to implantation could minimize the risk of thrombus formation and promote tissue regeneration. It is already known that spontaneous endothelialization occurs after implantation of bioprosthetic valves, but only in a small number of patients. Additionally, if endothelialization occurs, it shows heterogenous patterns mainly close to the base of the leaflets (91). Moreover, endothelialization on surfaces pre-treated with glutaraldehyde is associated with significant cytotoxicity (92, 93). Based on *in vitro* and *in vivo* data, detoxification procedures such as treatment with L-glutamic acid promote the formation of endothelial monolayers on the surface of glutaraldehyde-preserved cardiac valves (93, 94). Therefore, from a translational perspective, less cytotoxic strategies that promote long-term EC proliferation are needed. The use of non-glutaraldehyde reagents, the application of biodegradable hydrogels, crosslinking with drug-loaded nanoparticle, the use of RGD peptides, and decellularization techniques are all tissue engineering strategies that have been developed to modify the surface of heart valves (95–101). Biomimetic acellular ECM-based TEHVs are manufactured from a polymer composite (PGA/P4HB) and an *in vitro* grown ECM, which are subsequently decellularized leaving a cell-free construct. Preclinical studies of such biomimetic valves have demonstrated their ability to undergo remodeling and recellularization, including endothelialization (102–109). Biofunctionalization of decellularized scaffolds with antibodies (e.g., CD133) to attract and capture circulating EPCs was also performed, displaying rapid *in situ* endothelialization within the first month after implantation (110, 111).

Recent clinical trials that tested human-derived pulmonary and aortic homografts showed excellent results. In detail, both the ARISE and the ESPOIR trials recently posted short term outcomes on their respective trials showing excellent outcomes for decellularized homografts. Especially the ESPOIR trial demonstrated the superiority of these grafts compared to traditional cryopreserved homografts or jugular vein conduits (112, 113). TEHVs have mostly been used as pediatric pulmonary valve replacements or as part of the Ross procedure, in which a diseased aortic valve is replaced with the patient's own pulmonary valve (114, 115). A study of two pediatric patients implanted with decellularized pulmonary allografts showed that pre-seeding with autologous EPCs is a feasible and safe method (111). In addition, a Ross procedure study of 23 patients confirmed previous results supporting the hypothesis that heart valve decellularization and seeding with autologous vascular ECs may minimize tissue degeneration and improve valve durability (116). In a larger pulmonary valve replacement study, 38 patients were followed up to 5 years after acellular graft implantation and showed improved freedom from explanation, low gradients in echocardiographic follow-up, and adaptive growth (115). Interestingly, histological valve examination in one patient who died from non-valve related reasons revealed partial *in vivo* repopulation of the decellularized graft with autologous cells. Decellularized aortic valve allografts also appeared to be a promising alternative for aortic valve replacement.

Additionally, a variety of other materials and cell source combinations are considered for heart valve tissue engineering and have been used primarily in sheep models with varying degrees of success (117–124). Due to their versatility in mechanical, chemical and geometrical properties, synthetic bioresorbable polymers are also currently under investigation as potential starting materials for TEHV applications (125, 126). The functionality and remodeling potential of such bioresorbable polymers have been studied in several large animal models (125–128), also in combination with one-step preseeding procedures using autologous bone marrow mononuclear cells (129–133).

Endothelialization of ventricular assist devices

Despite major technological advances, the risk of thromboembolic events on artificial surfaces that are in contact with blood limits the functionality of VADs. Various approaches have been proposed to accelerate endothelialization and thus improve VAD hemocompatibility. Texture modifications such as sintered titanium surfaces, different surface coatings (e.g., titanium nitride and heparin) and pre-seeding with engineered cells (e.g., fibroblasts) were investigated (134–136). In a small clinical study in 1987, Kurt and colleagues demonstrated how a texture modification at the luminal interface of HeartMate XVE supports endothelium formation. Since then, numerous research groups have developed innovative VADs with textured inflow cannulas (e.g., Jarvik 2000 Heart Mate II and HeartMate III) associated with low rates of apical thrombus formation and thromboembolic events (**Table 1**) (137–140).

However, endothelialization of the whole luminal VAD surface is very challenging, mainly due to the complex design and hemodynamic environment. To overcome these hurdles, Xi et al. recently developed a novel patterning method, harnessing the condensation and evaporation of water droplets on a curing liquid elastomer, aiming to ensure the maintenance of a protective autologous endothelium even on complex non-planar surfaces of CV implants (141). In addition, most research groups today focus on improving the physical characteristics of biomaterials such as the surface topography. Research in this field underscores the significant role of biomechanical cues generated throughout endothelialization and proposes innovative strategies to

accelerate endothelialization under normal laminar flow conditions with physiological wall shear stress (WSS), or even very high supraphysiological WSS levels.

Incorporation of biomechanical cues to enhance endothelialization

As previously described, several research groups attempted to increase the hemocompatibility of CV implants by developing biomimetic surfaces. Biological tissues in the body have a variety of physical characteristics (e.g., wetness and stiffness) as well as surface morphological features such as fibers, pores, and pits (roughness) which regulate cell behavior. For example, ECs tend to be rounder and less distributed on soft surfaces than on stiff surfaces (156). Increased pore size promotes rapid endothelialization of TEVGs, which affects not only EC adhesion, but more importantly transmural endothelialization (157). Moreover, a growing body of literature underscores that the implementation of micrometer or nanoscale surface modifications on known biomaterials enhance surface roughness and, as a result, the endothelialization of CV implants (20, 158–160). Physiologically, the formation of an EC monolayer in the native blood vessel wall requires an intact EC-EBM interplay to promote cell adhesion, cell elongation, migration and proliferation. The EC-EBM interplay starts with the formation of focal contacts. The ECs use these anchors to sense the substrate (mechanosensation) and generate a regulatory signal that is transmitted from the cytoskeleton to the nucleus (mechanotransduction) to optimize the cells' adaptation to the surface, a phenomenon known as contact guidance (161).

Topography engineering approaches are aiming at mimicking biomechanical signals originating from the EC-EBM-ECM interplay and directing them toward accelerating endothelialization of the CV implant surface. In a systematic screening of various micro-structured substrates, Kukumberg et al. demonstrated that the surface topography either promotes or inhibits cell adhesion and cell proliferation (162). In detail, isotropic topographies such as pillars or wells resulted in lower cell density and cell proliferation compared to anisotropic topographies such as gratings. In another study by Ding et al., microgrooves on coronary stent lumen surfaces promoted EC migration and proliferation, which has also been confirmed by several research groups in the past (163–165). It was also found that ECs cultivated under physiological WSS on electrospun scaffolds are more adherent with fully aligned nanofibers than with random or semi-aligned scaffold topography (166). This observation supports the hypothesis that surface engineering of electrospun scaffolds used for CV implants may promote endothelialization and improve hemocompatibility of TEVGs or TEHVs. Nevertheless, it is still not clear how various physical properties of anisotropic features such as depth or height affect EC performance. In this direction, Potthoff et al. studied EC adhesion and migration on gratings with different dimensions under laminar flow conditions (160). As mammalian cells do not sense grooves shallower than 50 nm, gratings from 100 to 1,000 nm were examined. According to the published data, the basement membrane only contacts the top of the deep gratings (800 nm or more) and the cell membrane bridges over grooves. This led to an increase in focal adhesion kinase (FAK) activity, which ultimately contributed to improved migratory ability. Previous studies under static conditions confirmed these findings (167). Conversely, on shallow gratings (100–400 nm), the cell basement membrane interacts with both the top of the ridges and the bottom of the grooves. This led to a maturation of the FA complex and an increase in cell-surface adhesion (160). While most previous studies have focused almost exclusively on investigating the EC properties under static conditions or laminar flow with physiological WSS, Robotti et al. further investigated how 1,000 nm grids contribute to endothelialization by using a custom-designed flow bioreactor capable of reproducing supraphysiological WSS values of up to 10 Pa (168). Compared to flat surfaces, the gratings have been shown to improve monolayer integrity and support maturation of intercellular AJs, even under a WSS of 10 Pa. This data suggests that in ECs cultivated on deep gratings with 1,000 nm, FAK activation can acquire an actomyosin contractility-based pro-migratory profile that supports adhesion under flow conditions. This could potentially even promote the stability of the EC monolayer in the complex VAD hemodynamic environment in which supraphysiological WSS occurs (169). Recently, Ferrari et al. tested endothelialization on a novel hybrid membrane VAD *in vivo* (ovine animal model) and showed that a hexagonal honeycomb topography can support the generation and maintenance of a fully connected and functional endothelium (170).

While previous studies mainly focus on analyzing EC performance during endothelialization in terms of adhesion, intercellular connectivity and migratory ability, other researchers are investigating the topographical influence on factors important for EC monolayer maintenance such as proliferative ability, apoptosis, inactivation of blood coagulation and thrombus formation as well as EC regeneration. For example, Bachman et al. introduced a surface topography comprising hexagonal honeycomb shelters. EC monolayers cultivated on this topography retained their monolayer integrity even under supraphysiological loads. Intriguingly, this topography also enhanced anti-apoptotic, pro-survival and proliferative signaling pathways (171). In another experimental study on human vascular endothelial cells, different sized micro-structured surfaces with parallel micro-stripes improved NO, PGI2, TFPI, E-selectin expression, and reduced VWF secretion.

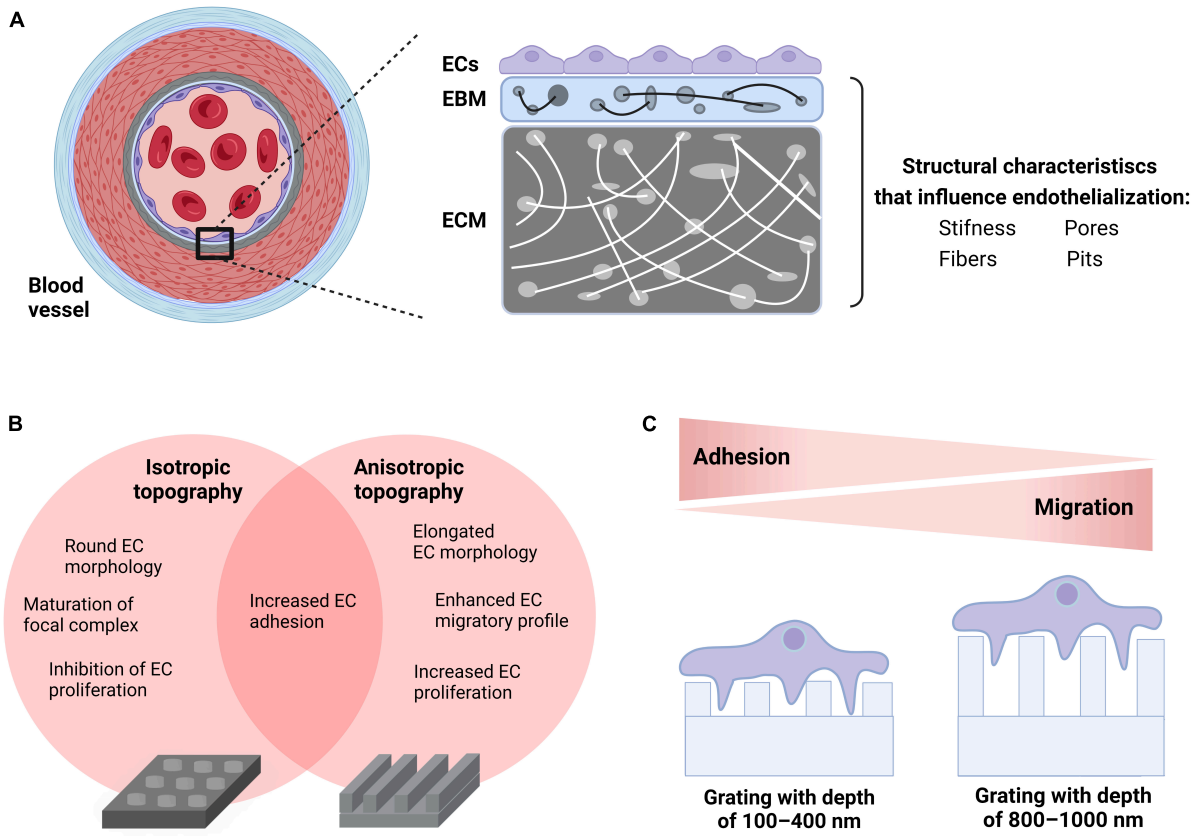

FIGURE 1
Incorporation of biomechanical cues to enhance endothelialization of CV implants. **(A)** Physiological properties of human vascular tissue such as physical (e.g., stiffness) and morphological (e.g., fibers, pores, and pits) characteristics dictate the EC-EBM-ECM interplay generating biomechanical cues that influence endothelialization. **(B)** Choice of surface geometry: ECs seeded on isotropic topographies (e.g., wells) obtain a round cellular morphology, migrate less due to the maturation of focal complexes into FAs and show low proliferation rate. In contrast, ECs seeded on anisotropic topographies such as gratings acquire an elongated cell morphology that enhances both migration and proliferation. Both surfaces increase cell adhesion under static and flow conditions. **(C)** Adjusting the surface topography: EC monolayers on shallow gratings (100–400 nm depth) interact with both the top of the ridges and the bottom of the grooves promoting FA complex maturation and enhancement of cell-surface adhesion, whereas EC monolayers on deep gratings (800–1,000 nm depth) bridge over grooves resulting in an increase in FAK activity due to enhanced phosphorylation as well as improved migratory ability. This figure was created with biorender.com.

Moreover, the platelet adhesion test and the whole blood clotting time test underscored the increasing anticoagulation property of elongated ECs (172). Consistent with a previous study, Huang et al. demonstrated that micropatterned and aligned nanofibrillar substrates promoted an atheroresistant EC phenotype by downregulating the expression of monocyte and platelet adhesion proteins and chemokines, supporting the hypothesis that micropatterned ECs have a unique transcriptional signature (173).

In summary, substrate stiffness, surface geometry as well as topography may play a significant role in the early phase of endothelialization by influencing adhesion, flow-oriented cell shape elongation and migration, as well as influencing the proliferative and regenerative capacity of ECs in the long-term phase (**Figure 1**). *In vivo* experiments as well as large-scale clinical trials are needed to further evaluate the survival of the endothelium and its long-term adaptation to biomimetic surfaces designed for the development of fully biocompatible CV implants.

Discussion

Passing through the "valley of death"

Despite the success in preclinical translational research, tissue engineered products are still lacking in the clinical market (174). Currently, only 12 tissue engineering products obtained market authorization for further commercialization (175). In particular, CV implants with engineered biomimetic surfaces differ dramatically from any other biotechnological or traditional medical product. Most regulatory agencies, such as the European Medicines Agency or the Food and Drug Administration allocate CV implants to a product class with

the highest safety risk classification. In addition to the safety-related engineering and physical aspects of the product, the combination with living tissue creates an additional regulatory burden. On the research and development level, it requires close cooperation between engineers, biomedical researchers and physicians. In addition to the safety and physical aspects of the product, the combination with living tissue creates an additional regulatory burden. At the research and development level, close cooperation is required between engineers, biomedical researchers and physicians. In addition, most CV implant modifications are based on existing designs, which would also require close cooperation with industry and patent holders, another major obstacle to translation and commercialization. This also explains why most bioengineered products to date are implantable valves and stents. The overall increasing demand for such products, as well as the lower "engineering" complexity, makes them easier targets for innovation and the promotion of new designs compared to more complex devices such as VADs.

Ex vivo or *in vivo* endothelialization approach? The one-billion-dollar question

Endothelialization on biomaterial surfaces was originally developed by *ex vivo* cell seeding. The fate of any *ex vivo* endothelialization strategy depends on the following factors: seeding efficiency, seeding technique and cell source (176). Seeding efficiency is mainly determined by patient characteristics (e.g., presence of cardiovascular risk factors), culture characteristics such as composition of culture media (e.g., concentration of amino acids and growth factors), as well as stimuli applied to the EC surface during *in vitro* expansion. In general, cultivation under the impact of shear stress or even circumferential dynamic forces is associated with enhanced EC performance during endothelialization (81). With regard to the seeding technique, a two-stage seeding approach has dominated in recent years. In the first step, isolated ECs are expanded *in vitro* for up to 4 weeks and in the second step, after reaching a sufficient cell number, scaffold seeding follows (177). While this approach is theoretically attractive, it also poses important regulatory issues. One the one hand, the development of good manufacturing practice-compatible standard operating procedures for harvesting and expansion of cells under ideally xeno-free culture conditions is more than necessary but an extremely time-consuming process. On the other, clean room conditions are required, which is associated with high production costs. Given the complexity of some CV devices such as VADs, seeding and maintaining an endothelial monolayer from production to implantation seems too costly and impractical. However, incorporating modifications to the luminal surfaces of CV implants may be a promising endothelialization strategy. On the one hand, physical modification of biomaterials, for example through imprintable topographies, is simple, inexpensive, safe and time-efficient as it would only add one production step during assembly of the device. However, the rapid degradation of coating biomaterials may lead to CV implant failure in the long term. On the other hand, chemical modification methods better reflect the conditions in the human body and are also characterized by a higher durability. However, they are significantly less cost-effective and very complex (178).

Struggling to jump on the biomimetic bandwagon

The fact that cell behavior can be changed by modulating the physical and/or biochemical properties of their respective surface may open a path to a faster and less expansive regulatory road to improve endothelialization and hence hemocompatibility of CV implants. Transanastomotic endothelialization was one of the first endothelialization mechanisms identified, but it only occurs in a small area approximately 2 cm distal to the anastomosis. Furthermore, spontaneous endothelialization *in vivo* from circulating EPCs at sites of vascular ischemia and endothelial injury has been reported in animal model studies (179). However, EPCs are mainly located in the bone marrow and the number of circulating EPCs that would adhere, migrate and proliferate to form an endothelium monolayer at sites where neovascularization occurs is very limited (24). Surface modification may promote attachment, migration as well as differentiation of circulating EPCs. However, EPCs do not refer to a single cell population with a specific identity. Many researchers suggest that bone and non-bone marrow-derived cell populations can be differentiated into ECs and therefore is difficult to define, characterize and identify the "true" EPCs and their primary role in endothelial regeneration (180). Recently, several studies also supported the hypothesis that age-related vascular inflammatory disease and oxidative stress may lead to significant EPC dysfunction and EPC pool depletion, impeding the potential of endothelialization in elderly CV patients who are the main recipients of CV implants (181). Novel approaches aim to combine more than one strategy, for example by expanding EPC populations *in vitro* for vascular or coronary stent tissue engineering applications (182, 183).

In summary, despite encouraging *in vivo* data, *ex vivo* endothelialization of CV implants is associated with a significant regulatory and hence financial burden. This makes a successful bench-to-bedside-to-market translation highly challenging. Surface modifications of CV implants such as imprintable topographies may have a higher chance of bridging this so-called valley of death.

Conclusion

Technological advances have revolutionized the design, development, and manufacturing of advanced implantable CV devices. However, due to insufficient hemocompatibility, they are still associated with devastating complications. Tissue engineering is an emerging field in contemporary health sciences aimed to optimize CV implants. This scope can be achieved through physical or biochemical surface modification of CV implants aimed to mimicking the physiological endothelial tissue function. The biochemical functionalization described above is difficult from economic and regulatory aspects. Microengineering of CV surface topography can be a promising cost-effective strategy.

Author contributions

VE: first draft and literature research. CG: first draft. EZ and HH: literature research. SN and ME: editing. SM: literature research and editing. TN-S: first draft and editing. All authors contributed to the article and approved the submitted version.

Acknowledgments

This work is part of the Zurich Heart project under the umbrella of University Medicine Zurich and was supported by the Stavros Niarchos Foundation (SNF). TN-S is a scholar in the BIH Charité Clinician Scientist Program funded by the Charité–Universitätsmedizin Berlin and the Berlin Institute of Health. The Program was initiated and led by Duska Dragun to enable resident physicians to pursue a career in academic medicine. Dragun passed away on December 28, 2020. This publication is dedicated to her memory as a mentor, role model, and stellar scientist. This study was also supported by the Swiss National Science Foundation, Grant SNF (205321_188828) (CG). We thank the Cleanroom Operations Team of the Binnig and Rohrer Nanotechnology Center (BRNC) for their help and support.

Conflict of interest

The authors declare that the research was conducted in the absence of any commercial or financial relationships that could be construed as a potential conflict of interest.

Publisher's note

All claims expressed in this article are solely those of the authors and do not necessarily represent those of their affiliated organizations, or those of the publisher, the editors and the reviewers. Any product that may be evaluated in this article, or claim that may be made by its manufacturer, is not guaranteed or endorsed by the publisher.

References

1. Roth GA, Mensah GA, Johnson CO, Addolorato G, Ammirati E, Baddour LM. Global burden of cardiovascular diseases and risk factors, 1990–2019: update from the GBD 2019 study. *J Am Coll Cardiol.* (2020) 76:2982–3021.

2. Bragazzi NL, Zhong W, Shu J, Much A. Abu, Lotan D, Grupper A. Burden of heart failure and underlying causes in 195 countries and territories from 1990 to 2017. *Eur J Prev Cardiol.* (2021) 28:1682–90. doi: 10.1093/eurjpc/zwaa147

3. Zhang S, Kriza C, Schaller S, Kolominsky-Rabas PL. Recalls of cardiac implants in the last decade: what lessons can we learn?. *PLoS One.* (2015) 10:e0125987. doi: 10.1371/journal.pone.0125987

4. Iqbal J, Gunn J, Serruys PW. Coronary stents: historical development, current status and future directions. *Br Med Bull.* (2013) 106:193–211. doi: 10.1093/bmb/ldt009

5. Räber L, Magro M, Stefanini GG, Kalesan B, van Domburg RT, Onuma Y. Very late coronary stent thrombosis of a newer-generation everolimus-eluting stent compared with early-generation drug-eluting stents: a prospective cohort study. *Circulation.* (2012) 125:1110–21. doi: 10.1161/CIRCULATIONAHA.111.058560

6. Pashneh-Tala S, MacNeil S, Claeyssens F. The tissue-engineered vascular graft-past, present, and future. *Tissue Eng Part B Rev.* (2016) 22:68–100. doi: 10.1089/ten.teb.2015.0100

7. Durán-Rey D, Crisóstomo V, Sánchez-Margallo JA, Sánchez-Margallo FM. Systematic Review of Tissue-Engineered Vascular Grafts. *Front Bioeng Biotechnol.* (2021) 9:771400. doi: 10.3389/fbioe.2021.771400

8. Catterall F, Ames PR, Isles C. Warfarin in patients with mechanical heart valves. *BMJ.* (2020) 371:m3956. doi: 10.1136/bmj.m3956

9. Carlin S, Eikelboom J. Advances in anticoagulation: patients with bioprosthetic heart valves. *Cardiovasc Res.* (2022) 118:e26–8. doi: 10.1093/cvr/cvab360

10. Garbade J, Barten MJ, Bittner HB, Mohr FW. Heart transplantation and left ventricular assist device therapy: two comparable options in end-stage heart failure?. *Clin Cardiol.* (2013) 36:378–82. doi: 10.1002/clc.22124

11. Potapov EV, Stepanenko A, Krabatsch T, Hetzer R. Managing long-term complications of left ventricular assist device therapy. *Curr Opin Cardiol.* (2011) 26:237–44. doi: 10.1097/HCO.0b013e328345af80

12. Smith RJ, Nasiri B, Kann J, Yergeau D, Bard JE, Swartz DD. Endothelialization of arterial vascular grafts by circulating monocytes. *Nat Commun.* (2020) 11:1622. doi: 10.1038/s41467-020-15361-2

13. Melchiorri AJ, Hibino N, Fisher JP. Strategies and techniques to enhance the in situ endothelialization of small-diameter biodegradable polymeric vascular grafts. *Tissue Eng Part B Rev.* (2013) 19:292–307. doi: 10.1089/ten.teb.2012.0577

14. Zhuang Y, Zhang C, Cheng M, Huang J, Liu Q, Yuan G. Challenges and strategies for in situ endothelialization and long-term lumen patency of vascular grafts. *Bioact Mater.* (2021) 6:1791–809. doi: 10.1016/j.bioactmat.2020.11.028

15. de Mel A, Jell G, Stevens MM, Seifalian AM. Biofunctionalization of biomaterials for accelerated in situ endothelialization: a review. *Biomacromolecules.* (2008) 9:2969–79. doi: 10.1021/bm800681k

16. Liu T, Liu S, Zhang K, Chen J, Huang N. Endothelialization of implanted cardiovascular biomaterial surfaces: the development from in vitro to in vivo. *J Biomed Mater Res A.* (2014) 102:3754–72. doi: 10.1002/jbm.a.35025

17. Ren X, Feng Y, Guo J, Wang H, Li Q, Yang J. Surface modification and endothelialization of biomaterials as potential scaffolds for vascular tissue engineering applications. *Chem Soc Rev.* (2015) 44:5680–742. doi: 10.1039/C4CS00483C

18. Jana S. Endothelialization of cardiovascular devices. *Acta Biomater.* (2019) 99:53–71. doi: 10.1016/j.actbio.2019.08.042

19. Bedair TM, ElNaggar MA, Joung YK, Han DK. Recent advances to accelerate re-endothelialization for vascular stents. *J Tissue Eng.* (2017) 8:2041731417731546. doi: 10.1177/2041731417731546

20. Zhao J, Feng Y. Surface engineering of cardiovascular devices for improved hemocompatibility and rapid endothelialization. *Adv Healthc Mater.* (2020) 9:2000920. doi: 10.1002/adhm.202000920

21. Pober JS, Sessa WC. Evolving functions of endothelial cells in inflammation. *Nat Rev Immunol.* (2007) 7:803–15. doi: 10.1038/nri2171

22. Rodrigues SF, Granger DN. Blood cells and endothelial barrier function. *Tissue Barriers.* (2015) 3:e978720. doi: 10.4161/21688370.2014.978720

23. Claesson-Welsh L, Dejana E, McDonald DM. Permeability of the endothelial barrier: identifying and reconciling controversies. *Trends Mol Med.* (2021) 27:314–31. doi: 10.1016/j.molmed.2020.11.006

24. Dejana E. Endothelial cell–cell junctions: happy together. *Nat Rev Mol Cell Biol.* (2004) 5:261–70. doi: 10.1038/nrm1357

25. Lampugnani MG. Endothelial adherens junctions and the actin cytoskeleton: an 'infinity net'?. *J Biol.* (2010) 9:16. doi: 10.1186/jbiol232

26. Laurindo FRM, Liberman M, Fernandes DC, Leite PF. Chapter 8 – Endothelium-dependent vasodilation: nitric oxide and other mediators. In: Da Luz PL, Libby P, Chagas ACP, Laurindo FRM editors. *Endothelium and Cardiovascular Diseases*. London: Academic Press (2018). p. 97–113. doi: 10.1016/B978-0-12-812348-5.00008-8

27. Durán WN, Breslin JW, Sánchez FA. The NO cascade, eNOS location, and microvascular permeability. *Cardiovasc Res.* (2010) 87:254–61. doi: 10.1093/cvr/cvq139

28. Sriram K, Laughlin JG, Rangamani P, Tartakovsky DM. Shear-induced nitric oxide production by endothelial cells. *Biophys J.* (2016) 111:208–21. doi: 10.1016/j.bpj.2016.05.034

29. Liu HB, Zhang J, Xin SY, Liu C, Wang CY, Zhao D. Mechanosensitive properties in the endothelium and their roles in the regulation of endothelial function. *J Cardiovasc Pharmacol.* (2013) 61:461–70. doi: 10.1097/FJC.0b013e31828c0933

30. Choi CK, Helmke BP. Short-term shear stress induces rapid actin dynamics in living endothelial cells. *Mol Cell Biomech.* (2008) 5:247–58.

31. Steward R Jr., Tambe D, Hardin CC, Krishnan R, Fredberg JJ. Fluid shear, intercellular stress, and endothelial cell alignment. *Am J Physiol Cell Physiol.* (2015) 308:C657–64. doi: 10.1152/ajpcell.00363.2014

32. Korenaga R, Ando J, Tsuboi H, Yang WD, Sakuma I, Toyooka T. Laminar flow stimulates ATP- and shear stress-dependent nitric oxide production in cultured bovine endothelial cells. *Biochem Biophys Res Commun.* (1994) 198:213–9. doi: 10.1006/bbrc.1994.1030

33. Tsao PS, Buitrago R, Chan JR, Cooke JP. Fluid flow inhibits endothelial adhesiveness. Nitric oxide and transcriptional regulation of VCAM-1. *Circulation.* (1996) 94:1682–9. doi: 10.1161/01.CIR.94.7.1682

34. Cybulsky MI, Marsden PA. Effect of disturbed blood flow on endothelial cell gene expression. *Arterioscler Thromb Vasc Biol.* (2014) 34:1806–8. doi: 10.1161/ATVBAHA.114.304099

35. Ferlito S. Cardiovascular diseases and nitric oxide in humans. *Minerva Cardioangiol.* (2000) 48:379–86.

36. Naseem KM. The role of nitric oxide in cardiovascular diseases. *Mol Aspects Med.* (2005) 26:33–65. doi: 10.1016/j.mam.2004.09.003

37. Yau JW, Teoh H, Verma S. Endothelial cell control of thrombosis. *BMC Cardiovasc Disord.* (2015) 15:130. doi: 10.1186/s12872-015-0124-z

38. Grover SP, Mackman N. Tissue Factor. *Arterioscler Thromb Vasc Biol.* (2018) 38:709–25. doi: 10.1161/ATVBAHA.117.309846

39. van Hinsbergh VW. Endothelium–role in regulation of coagulation and inflammation. *Semin Immunopathol.* (2012) 34:93–106. doi: 10.1007/s00281-011-0285-5

40. Valentijn KM, Sadler JE, Valentijn JA, Voorberg J, Eikenboom J. Functional architecture of Weibel-Palade bodies. *Blood.* (2011) 117:5033–43. doi: 10.1182/blood-2010-09-267492

41. Chistiakov DA, Orekhov AN, Bobryshev YV. Endothelial barrier and its abnormalities in cardiovascular disease. *Front Physiol.* (2015) 6:365. doi: 10.3389/fphys.2015.00365

42. Pulous FE, Petrich BG. Integrin-dependent regulation of the endothelial barrier. *Tissue Barriers.* (2019) 7:1685844. doi: 10.1080/21688370.2019.1685844

43. Streuli CH. Integrins and cell-fate determination. *J Cell Sci.* (2009) 122:171–7. doi: 10.1242/jcs.018945

44. Moreno-Layseca P, Streuli CH. Signalling pathways linking integrins with cell cycle progression. *Matrix Biol.* (2014) 34:144–53. doi: 10.1016/j.matbio.2013.10.011

45. Martino F, Perestrelo AR, Vinarský V, Pagliari S, Forte G. Cellular mechanotransduction: from tension to function. *Front Physiol.* (2018) 9:824. doi: 10.3389/fphys.2018.00824

46. Sun Z, Guo SS, Fässler R. Integrin-mediated mechanotransduction. *J Cell Biol.* (2016) 215:445–56. doi: 10.1083/jcb.201609037

47. Raval N, Kalyane D, Maheshwari R, Tekade RK. Chapter 17 – Surface modifications of biomaterials and their implication on biocompatibility. In: Tekade RK editor. *Biomaterials and Bionanotechnology*. London: Academic Press (2019). p. 639–74. doi: 10.1016/B978-0-12-814427-5.00017-2

48. Felgueiras HP, Antunes JC, Martins MCL, Barbosa MA. 1 – Fundamentals of protein and cell interactions in biomaterials. In: Barbosa MA, Martins MCL editors. *Peptides and Proteins as Biomaterials for Tissue Regeneration and Repair*. Sawston: Woodhead Publishing (2018). p. 1–27. doi: 10.1016/B978-0-08-100803-4.00001-2

49. Roach P, Farrar D, Perry CC. Interpretation of protein adsorption:? surface-induced conformational changes. *J Am Chem Soc.* (2005) 127:8168–73. doi: 10.1021/ja042898o

50. Jesmer AH, Wylie RG. Controlling experimental parameters to improve characterization of biomaterial fouling. *Front Chem.* (2020) 8:604236. doi: 10.3389/fchem.2020.604236

51. Kruk T, Bzowska M, Hinz A, Szuwarzyński M. Control of specific/nonspecific protein adsorption: functionalization of polyelectrolyte multilayer films as a potential coating for biosensors. *Materials.* (2021) 14:7629. doi: 10.3390/ma14247629

52. Zhang J, Li G, Man J, Qu Y, Guo Z, Zhang S. Mechanism of anti-proteins adsorption behavior on superhydrophobic titanium surface. *Surf Coat Technol.* (2021) 421:127421. doi: 10.1016/j.surfcoat.2021.127421

53. Bordenave L, Fernandez P, Rémy-Zolghadri M, Villars S, Daculsi R, Midy D. In vitro endothelialized ePTFE prostheses: clinical update 20 years after the first realization. *Clin Hemorheol Microcirc.* (2005) 33:227–34.

54. Maitz MF, Martins MCL, Grabow N, Matschegewski C, Huang N, Chaikof EL. The blood compatibility challenge. Part 4: surface modification for hemocompatible materials: passive and active approaches to guide blood-material interactions. *Acta Biomater.* (2019) 94:33–43. doi: 10.1016/j.actbio.2019.06.019

55. Kalesan B, Pilgrim T, Heinimann K, Räber L, Stefanini GG, Valgimigli M. Comparison of drug-eluting stents with bare metal stents in patients with ST-segment elevation myocardial infarction. *Eur Heart J.* (2012) 33:977–87. doi: 10.1093/eurheartj/ehs036

56. Buccheri D, Piraino D, Andolina G, Cortese B. Understanding and managing in-stent restenosis: a review of clinical data, from pathogenesis to treatment. *J Thorac Dis.* (2016) 8:E1150–62. doi: 10.21037/jtd.2016.10.93

57. Lansky AJ, Kereiakes DJ, Baumbach A, Windecker S, Hussain Y, Pietras C. Novel supreme drug-eluting stents with early synchronized antiproliferative drug delivery to inhibit smooth muscle cell proliferation after drug-eluting stents implantation in coronary artery disease: results of the PIONEER III randomized clinical trial. *Circulation.* (2021) 143:2143–54. doi: 10.1161/CIRCULATIONAHA.120.052482

58. Sethi R, Lee CH. Endothelial progenitor cell capture stent: safety and effectiveness. *J Interv Cardiol.* (2012) 25:493–500. doi: 10.1111/j.1540-8183.2012.00740.x

59. Kerkmeijer LSM, Woudstra P, Klomp M, Kalkman DN, Varma C, Koolen JJ, et al. P2798Final 5-year outcomes of the TRIAS high risk of restenosis; a multi-centre, randomized trial comparing endothelial progenitor cell capturing stent with drug-eluting stents. *Eur Heart J.* (2019) 40:ehz748.1111. doi: 10.1093/eurheartj/ehz748.1111

60. Woudstra P, Kalkman DN, den P, Heijer I.B. Menown, Erglis A, Suryapranata H. 1-year results of the REMEDEE registry: clinical outcomes after deployment of the abluminal sirolimus-coated bioengineered (combo) stent in a multicenter, prospective all-comers registry. *JACC Cardiovasc Interv.* (2016) 9:1127–34.

61. Diaz-Rodriguez S, Rasser C, Mesnier J, Chevallier P, Gallet R, Choqueux C. Coronary stent CD31-mimetic coating favours endothelialization and reduces local inflammation and neointimal development in vivo. *Eur Heart J.* (2021) 42:1760–9. doi: 10.1093/eurheartj/ehab027

62. Zhang F, Zhang Q, Li X, Huang N, Zhao X, Yang Z. Mussel-inspired dopamine-Cu(II) coatings for sustained in situ generation of nitric oxide for

prevention of stent thrombosis and restenosis. *Biomaterials.* (2019) 194:117–29. doi: 10.1016/j.biomaterials.2018.12.020

63. Tuomainen PO, Ylitalo A, Niemelä M, Kervinen K, Pietilä M, Sia J. Five-year clinical outcome of titanium-nitride-oxide-coated bioactive stents versus paclitaxel-eluting stents in patients with acute myocardial infarction: long-term follow-up from the TITAX AMI trial. *Int J Cardiol.* (2013) 168:1214–9. doi: 10.1016/j.ijcard.2012.11.060

64. Chang H-K, Kim P-H, Kim DW, Cho H-M, Jeong MJ, Kim DH. Coronary stents with inducible VEGF/HGF-secreting UCB-MSCs reduced restenosis and increased re-endothelialization in a swine model. *Exp Mol Med.* (2018) 50:1–14. doi: 10.1038/s12276-018-0143-9

65. Boretos JW, Pierce WS. Segmented polyurethane: a new elastomer for biomedical applications. *Science.* (1967) 158:1481–2. doi: 10.1126/science.158.3807.1481

66. Norton L, Eiseman B. Replacement of portal vein during pancreatectomy for carcinoma. *Surgery.* (1975) 77:280–4.

67. Zardeneta G, Mukai H, Marker V, Milam SB. Protein interactions with particulate Teflon: implications for the foreign body response. *J Oral Maxillofac Surg.* (1996) 54:873–8. doi: 10.1016/S0278-2391(96)90540-6

68. Radke D, Jia W, Sharma D, Fena K, Wang G, Goldman J. Tissue engineering at the blood-contacting surface: a review of challenges and strategies in vascular graft development. *Adv Healthc Mater.* (2018) 7:e1701461. doi: 10.1002/adhm.201701461

69. Weinberg CB, Bell E. A blood vessel model constructed from collagen and cultured vascular cells. *Science.* (1986) 231:397–400. doi: 10.1126/science.2934816

70. Copes F, Pien N, Vlierberghe S. Van, Boccafoschi F, Mantovani D. Collagen-based tissue engineering strategies for vascular medicine. *Front Bioeng Biotechnol.* (2019) 7:166. doi: 10.3389/fbioe.2019.00166

71. Zavan B, Vindigni V, Lepidi S, Iacopetti I, Avruscio G, Abatangelo G. Neoarteries grown in vivo using a tissue-engineered hyaluronan-based scaffold. *FASEB J.* (2008) 22:2853–61. doi: 10.1096/fj.08-107284

72. Swartz DD, Russell JA, Andreadis ST. Engineering of fibrin-based functional and implantable small-diameter blood vessels. *Am J Physiol Heart Circ Physiol.* (2005) 288:H1451–60. doi: 10.1152/ajpheart.00479.2004

73. McAllister T. The evolution of tissue engineered vascular grafts: from research to clinical practice. *Annu Int Conf IEEE Eng Med Biol Soc.* (2010) 2010:3589. doi: 10.1109/IEMBS.2010.5627457

74. Shinoka T, Shum-Tim D, Ma PX, Tanel RE, Isogai N, Langer R, et al. Creation of viable pulmonary artery autografts through tissue engineering. *J Thorac Cardiovasc Surg.* (1998) 115:536–45. doi: 10.1016/S0022-5223(98)70315-0

75. Hoerstrup SP, Cummings Mrcs I, Lachat M, Schoen FJ, Jenni R, Leschka S, et al. Functional growth in tissue-engineered living, vascular grafts: follow-up at 100 weeks in a large animal model. *Circulation.* (2006) 114:I159–66. doi: 10.1161/CIRCULATIONAHA.105.001172

76. Cummings I, George S, Kelm J, Schmidt D, Emmert MY, Weber B. Tissue-engineered vascular graft remodeling in a growing lamb model: expression of matrix metalloproteinases. *Eur J Cardiothorac Surg.* (2012) 41:167–72. doi: 10.1016/j.ejcts.2011.02.077

77. Shin'oka T, Matsumura G, Hibino N, Naito Y, Watanabe M, Konuma T. Midterm clinical result of tissue-engineered vascular autografts seeded with autologous bone marrow cells. *J Thorac Cardiovasc Surg.* (2005) 129:1330–8. doi: 10.1016/j.jtcvs.2004.12.047

78. Sugiura T, Matsumura G, Miyamoto S, Miyachi H, Breuer CK, Shinoka T. Tissue-engineered vascular grafts in children with congenital heart disease: intermediate term follow-up. *Semin Thorac Cardiovasc Surg.* (2018) 30:175–9. doi: 10.1053/j.semtcvs.2018.02.002

79. Hibino N, McGillicuddy E, Matsumura G, Ichihara Y, Naito Y, Breuer C, et al. Late-term results of tissue-engineered vascular grafts in humans. *J Thorac Cardiovasc Surg.* (2010) 139:431–6. doi: 10.1016/j.jtcvs.2009.09.057

80. Herrmann FEM, Lamm P, Wellmann P, Milz S, Hagl C, Juchem G. Autologous endothelialized vein allografts in coronary artery bypass surgery – Long term results. *Biomaterials.* (2019) 212:87–97. doi: 10.1016/j.biomaterials.2019.05.019

81. Huang AH, Lee Y-U, Calle EA, Boyle M, Starcher BC, Humphrey JD. Design and use of a novel bioreactor for regeneration of biaxially stretched tissue-engineered vessels. *Tissue Eng Part C Methods.* (2015) 21:841–51. doi: 10.1089/ten.tec.2014.0287

82. Pellegata AF, Dominioni T, Ballo F, Maestroni S, Asnaghi MA, Zerbini G. Arterial decellularized scaffolds produced using an innovative automatic system. *Cells Tissues Organs.* (2014) 200:363–73. doi: 10.1159/000439082

83. Quint C, Arief M, Muto A, Dardik A, Niklason LE. Allogeneic human tissue-engineered blood vessel. *J Vasc Surg.* (2012) 55:790–8. doi: 10.1016/j.jvs.2011.07.098

84. Kirkton RD, Santiago-Maysonet M, Lawson JH, Tente WE, Dahl SLM, Niklason LE, et al. Bioengineered human acellular vessels recellularize and evolve into living blood vessels after human implantation. *Sci Transl Med.* (2019) 11:eaau6934. doi: 10.1126/scitranslmed.aau6934

85. Lu G, Cui SJ, Geng X, Ye L, Chen B, Feng ZG. Design and preparation of polyurethane-collagen/heparin-conjugated polycaprolactone double-layer bionic small-diameter vascular graft and its preliminary animal tests. *Chin Med J.* (2013) 126:1310–6.

86. Wise SG, Byrom MJ, Waterhouse A, Bannon PG, Weiss AS, Ng MK. A multilayered synthetic human elastin/polycaprolactone hybrid vascular graft with tailored mechanical properties. *Acta Biomater.* (2011) 7:295–303. doi: 10.1016/j.actbio.2010.07.022

87. Hu YT, Pan XD, Zheng J, Ma WG, Sun LZ. In vitro and in vivo evaluation of a small-caliber coaxial electrospun vascular graft loaded with heparin and VEGF. *Int J Surg.* (2017) 44:244–9. doi: 10.1016/j.ijsu.2017.06.077

88. Wang F, Qin K, Wang K, Wang H, Liu Q, Qian M. Nitric oxide improves regeneration and prevents calcification in bio-hybrid vascular grafts via regulation of vascular stem/progenitor cells. *Cell Rep.* (2022) 39:110981. doi: 10.1016/j.celrep.2022.110981

89. Koobatian MT, Row S, Smith RJ Jr., Koenigsknecht C, Andreadis ST, Swartz DD. Successful endothelialization and remodeling of a cell-free small-diameter arterial graft in a large animal model. *Biomaterials.* (2016) 76:344–58. doi: 10.1016/j.biomaterials.2015.10.020

90. Manji RA, Zhu LF, Nijjar NK, Rayner DC, Korbutt GS, Churchill TA. Glutaraldehyde-fixed bioprosthetic heart valve conduits calcify and fail from xenograft rejection. *Circulation.* (2006) 114:318–27. doi: 10.1161/CIRCULATIONAHA.105.549311

91. Ishihara T, Ferrans VJ, Jones M, Boyce SW, Roberts WC. Occurrence and significance of endothelial cells in implanted porcine bioprosthetic valves. *Am J Cardiol.* (1981) 48:443–54. doi: 10.1016/0002-9149(81)90071-0

92. Bengtsson L, Radegran K, Haegerstrand A. In vitro endothelialization of commercially available heart valvebioprostheses with cultured adult human cells. *Eur J Cardiothorac Surg.* (1993) 7:393–8. doi: 10.1016/1010-7940(93)90001-R

93. Guldner NW, Jasmund I, Zimmermann H, Heinlein M, Girndt B, Meier V. Detoxification and endothelialization of glutaraldehyde-fixed bovine pericardium with titanium coating. *Circulation.* (2009) 119:1653–60. doi: 10.1161/CIRCULATIONAHA.108.823948

94. Lehner G, Fischlein T, Baretton G, Murphy JG, Reichart B. Endothelialized biological heart valve prostheses in the non-human primate model. *Eur J Cardiothorac Surg.* (1997) 11:498–504. doi: 10.1016/S1010-7940(96)01096-2

95. Yu T, Yang W, Zhuang W, Tian Y, Kong Q, Chen X. A bioprosthetic heart valve cross-linked by a non-glutaraldehyde reagent with improved biocompatibility, endothelialization, anti-coagulation and anti-calcification properties. *J Mater Chem B.* (2021) 9:4031–8. doi: 10.1039/D1TB00409C

96. Wu B, Zheng C, Ding K, Huang X, Li M, Zhang S. Cross-linking porcine pericardium by 3,4-dihydroxybenzaldehyde: a novel method to improve the biocompatibility of bioprosthetic valve. *Biomacromolecules.* (2021) 22:823–36. doi: 10.1021/acs.biomac.0c01554

97. Zhang S, Zheng C, Li M, Ding K, Huang X, Liang X. Sodium lignosulfonate cross-linked bioprosthetic heart valve materials for enhanced cytocompatibility, improved hemocompatibility, and reduced calcification. *Compos B Eng.* (2022) 234:109669. doi: 10.1016/j.compositesb.2022.109669

98. Nina V, Pomerantzeff P, Casagrande I, Chung D, Benvenuti L. In vivo endothelialization of cardiac bioprostheses : conventional versus non-aldehyde preservation. *Braz J Cardiovasc Surg.* (2004) 19:144–151. doi: 10.1590/S1678-97412004000200008

99. Lopez-Moya M, Melgar-Lesmes P. Optimizing glutaraldehyde-fixed tissue heart valves with chondroitin sulfate hydrogel for endothelialization and shielding against deterioration. *Biomacromolecule.* (2018) 19:1234–44. doi: 10.1021/acs.biomac.8b00077

100. Hu C, Luo R, Wang Y. Heart valves cross-linked with erythrocyte membrane drug-loaded nanoparticles as a biomimetic strategy for anti-coagulation, anti-inflammation, anti-calcification, and endothelialization. *ACS Appl Mater Interfaces.* (2020) 12:41113–26. doi: 10.1021/acsami.0c12688

101. Bellis SL. Advantages of RGD peptides for directing cell association with biomaterials. *Biomaterials.* (2011) 32:4205–10. doi: 10.1016/j.biomaterials.2011.02.029

102. Emmert MY, Schmitt BA. Computational modeling guides tissue-engineered heart valve design for long-term in vivo performance in a translational

sheep model. *Sci Transl Med.* (2018) 10:eaan4587. doi: 10.1126/scitranslmed.aan4587

103. Dijkman PE, Driessen-Mol A, Frese L, Hoerstrup SP, Baaijens FP. Decellularized homologous tissue-engineered heart valves as off-the-shelf alternatives to xeno- and homografts. *Biomaterials.* (2012) 33:4545–54. doi: 10.1016/j.biomaterials.2012.03.015

104. Motta SE, Fioretta ES, Dijkman PE, Lintas V, Behr L, Hoerstrup SP. Development of an off-the-shelf tissue-engineered sinus valve for transcatheter pulmonary valve replacement: a proof-of-concept study. *J Cardiovasc Transl Res.* (2018) 11:182–91. doi: 10.1007/s12265-018-9800-6

105. Motta SE, Fioretta ES, Lintas V, Dijkman PE, Hilbe M, Frese L. Geometry influences inflammatory host cell response and remodeling in tissue-engineered heart valves in-vivo. *Sci Rep.* (2020) 10:19882. doi: 10.1038/s41598-020-76322-9

106. Motta SE, Zaytseva P, Fioretta ES, Lintas V, Breymann C, Hoerstrup SP. Endothelial progenitor cell-based in vitro pre-endothelialization of human cell-derived biomimetic regenerative matrices for next-generation transcatheter heart valves applications. *Front Bioeng Biotechnol.* (2022) 10:867877. doi: 10.3389/fbioe.2022.867877

107. Motta SE, Lintas V, Fioretta ES, Hoerstrup SP, Emmert MY. Off-the-shelf tissue engineered heart valves for in situ regeneration: current state, challenges and future directions. *Expert Rev Med Devices.* (2018) 15:35–45. doi: 10.1080/17434440.2018.1419865

108. Driessen-Mol A. M.Y. Emmert, P.E. Dijkman, L. Frese, B. Sanders, B. Weber, et al., Transcatheter implantation of homologous "off-the-shelf" tissue-engineered heart valves with self-repair capacity: long-term functionality and rapid in vivo remodeling in sheep. *J Am Coll Cardiol.* (2014) 63:1320–9. doi: 10.1016/j.jacc.2013.09.082

109. Movileanu I, Harpa M, Al Hussein H, Harceaga L, Chertes A, Al Hussein H, et al. Preclinical testing of living tissue-engineered heart valves for pediatric patients, challenges and opportunities. *Front. Cardiovasc. Med.* (2021) 8:707–892. doi: 10.3389/fcvm.2021.707892

110. Jordan JE, Williams JK, Lee SJ, Raghavan D, Atala A, Yoo JJ. Bioengineered self-seeding heart valves. *J Thorac Cardiovasc Surg.* (2012) 143:201–8. doi: 10.1016/j.jtcvs.2011.10.005

111. Cebotari S, Lichtenberg A, Tudorache I, Hilfiker A, Mertsching H, Leyh R. Clinical application of tissue engineered human heart valves using autologous progenitor cells. *Circulation.* (2006) 114:I132–7. doi: 10.1161/CIRCULATIONAHA.105.001065

112. Horke A, Tudorache I, Laufer G, Andreas M, Pomar JL, Pereda D. Early results from a prospective, single-arm European trial on decellularized allografts for aortic valve replacement: the ARISE study and ARISE Registry data. *Eur J Cardiothorac Surg.* (2020) 58:1045–53. doi: 10.1093/ejcts/ezaa100

113. Boethig D, Horke A, Hazekamp M, Meyns B, Rega F, Van Puyvelde J. A European study on decellularized homografts for pulmonary valve replacement: initial results from the prospective ESPOIR Trial and ESPOIR Registry data†. *Eur J Cardiothorac Surg.* (2019) 56:503–9. doi: 10.1093/ejcts/ezz054

114. Dohmen PM, Lembcke A, Hotz H, Kivelitz D, Konertz WF. Ross operation with a tissue-engineered heart valve. *Ann Thorac Surg.* (2002) 74:1438–42. doi: 10.1016/S0003-4975(02)03881-X

115. Cebotari S, Tudorache I, Ciubotaru A, Boethig D, Sarikouch S, Goerler A, et al. Use of fresh decellularized allografts for pulmonary valve replacement may reduce the reoperation rate in children and young adults. *Circulation.* (2011) 124:S115–23. doi: 10.1161/CIRCULATIONAHA.110.012161

116. Dohmen PM, Lembcke A, Holinski S, Kivelitz D, Braun JP, Pruss A. Mid-term clinical results using a tissue-engineered pulmonary valve to reconstruct the right ventricular outflow tract during the Ross procedure. *Ann Thorac Surg.* (2007) 84:729–36. doi: 10.1016/j.athoracsur.2007.04.072

117. Hoerstrup SP, Sodian R, Daebritz S, Wang J, Bacha EA, Martin DP, et al. Functional living trileaflet heart valves grown in vitro. *Circulation.* (2000) 102:III44–9. doi: 10.1161/01.CIR.102.suppl_3.III-44

118. Syedain Z, Reimer J, Schmidt J, Lahti M, Berry J, Bianco R. 6-month aortic valve implantation of an off-the-shelf tissue-engineered valve in sheep. *Biomaterials.* (2015) 73:175–84. doi: 10.1016/j.biomaterials.2015.09.016

119. Reimer J, Syedain Z, Haynie B, Lahti M, Berry J, Tranquillo R. Implantation of a Tissue-Engineered Tubular Heart Valve in Growing Lambs. *Ann Biomed Eng.* (2017) 45:439–51. doi: 10.1007/s10439-016-1605-7

120. Syedain ZH, Haynie B, Johnson SL. Pediatric tri-tube valved conduits made from fibroblast-produced extracellular matrix evaluated over 52 weeks in growing lambs. *Sci Transl Med.* (2021) 13:eabb7225. doi: 10.1126/scitranslmed.abb7225

121. Capulli AK, Emmert MY, Pasqualini FS, Kehl D, Caliskan E, Lind JU. JetValve: rapid manufacturing of biohybrid scaffolds for biomimetic heart valve replacement. *Biomaterials.* (2017) 133:229–41. doi: 10.1016/j.biomaterials.2017.04.033

122. Fioretta ES, Motta SE, Lintas V, Loerakker S, Parker KK, Baaijens FPT. Next-generation tissue-engineered heart valves with repair, remodelling and regeneration capacity. *Nat Rev Cardiol.* (2021) 18:92–116. doi: 10.1038/s41569-020-0422-8

123. Weber B, Emmert MY, Hoerstrup SP. Stem cells for heart valve regeneration. *Swiss Med Wkly.* (2012) 142:w13622. doi: 10.4414/smw.2012.13622

124. Fioretta ES, Dijkman PE, Emmert MY, Hoerstrup SP. The future of heart valve replacement: recent developments and translational challenges for heart valve tissue engineering. *J Tissue Eng Regen Med.* (2018) 12:e323–35. doi: 10.1002/term.2326

125. Bennink G, Torii S, Brugmans M, Cox M, Svanidze O, Ladich E, et al. A novel restorative pulmonary valved conduit in a chronic sheep model: mid-term hemodynamic function and histologic assessment. *J Thorac Cardiovasc Surg.* (2018) 155:2591–601.e3. doi: 10.1016/j.jtcvs.2017.12.046

126. Coyan GN, D'Amore A, Matsumura Y, Pedersen DD, Luketich SK, Shanov V. In vivo functional assessment of a novel degradable metal and elastomeric scaffold-based tissue engineered heart valve. *J Thorac Cardiovasc Surg.* (2019) 157:1809–16. doi: 10.1016/j.jtcvs.2018.09.128

127. Kluin J, Talacua H, Smits AI, Emmert MY, Brugmans MC, Fioretta ES. In situ heart valve tissue engineering using a bioresorbable elastomeric implant – From material design to 12 months follow-up in sheep. *Biomaterials.* (2017) 125:101–17. doi: 10.1016/j.biomaterials.2017.02.007

128. Soliman OI, Miyazaki Y, Abdelghani M, Brugmans M, Witsenburg M, Onuma Y. Midterm performance of a novel restorative pulmonary valved conduit: preclinical results. *EuroIntervention.* (2017) 13:e1418–27. doi: 10.4244/EIJ-D-17-00553

129. Weber B, Scherman J, Emmert MY, Gruenenfelder J, Verbeek R, Bracher M. Injectable living marrow stromal cell-based autologous tissue engineered heart valves: first experiences with a one-step intervention in primates. *Eur Heart J.* (2011) 32:2830–40. doi: 10.1093/eurheartj/ehr059

130. Emmert MY, Weber B, Behr L, Frauenfelder T, Brokopp CE, Grünenfelder J. Transapical aortic implantation of autologous marrow stromal cell-based tissue-engineered heart valves: first experiences in the systemic circulation. *JACC Cardiovasc Interv.* (2011) 4:822–3. doi: 10.1016/j.jcin.2011.02.020

131. Emmert MY, Weber B, Wolint P, Behr L, Sammut S, Frauenfelder T. Stem cell-based transcatheter aortic valve implantation: first experiences in a pre-clinical model. *JACC Cardiovasc Interv.* (2012) 5:874–83. doi: 10.1016/j.jcin.2012.04.010

132. Emmert MY, Weber B, Behr L, Sammut S, Frauenfelder T, Wolint P. Transcatheter aortic valve implantation using anatomically oriented, marrow stromal cell-based, stented, tissue-engineered heart valves: technical considerations and implications for translational cell-based heart valve concepts. *Eur J Cardiothorac Surg.* (2014) 45:61–8. doi: 10.1093/ejcts/ezt243

133. Fioretta ES, Lintas V, Mallone A, Motta SE, von Boehmer L, Dijkman PE. Differential leaflet remodeling of bone marrow cell pre-seeded versus nonseeded bioresorbable transcatheter pulmonary valve replacements. *JACC Basic Transl Sci.* (2020) 5:15–31. doi: 10.1016/j.jacbts.2019.09.008

134. Noviani M, Jamiolkowski RM, Grenet JE, Lin Q, Carlon TA, Qi L. Point-of-care rapid-seeding ventricular assist device with blood-derived endothelial cells to create a living antithrombotic coating. *ASAIO J.* (2016) 62:447–53. doi: 10.1097/MAT.0000000000000351

135. Sin DC, Kei HL, Miao X. Surface coatings for ventricular assist devices. *Expert Rev Med Devices.* (2009) 6:51–60. doi: 10.1586/17434440.6.1.51

136. Scott-Burden T, Tock CL, Bosely JP, Clubb FJ, Parnis SM, Schwarz JJ, et al. Nonthrombogenic, adhesive cellular lining for left ventricular assist devices. *Circulation.* (1998) 98:Ii339–45.

137. Tucanova Z, Ivak P, Konarik M, Szarszoi O, Fabian O, Melenovsky V, et al. Systematic evaluation of heartmate 3 inflow cannula at transplant and the association with reduced anticoagulation. *J Heart Lung Transplant.* (2022) 41:S487. doi: 10.1016/j.healun.2022.01.1231

138. Selzman CH, Koliopoulou A, Glotzbach JP, McKellar SH. evolutionary improvements in the Jarvik 2000 left ventricular assist device. *ASAIO J.* (2018) 64:827–30. doi: 10.1097/MAT.0000000000000743

139. Kurtyka P, Kustosz R, Kaczmarek M, Gonsior M, Tokarska K. Surface modifications for inflow cannulas of ventricular assist devices – comparison of latest solutions. *Eng Biomater.* (2019) 22:17–23.

140. John R, Kamdar F, Liao K, Colvin-Adams M, Miller L, Joyce L. Low thromboembolic risk for patients with the Heartmate II left ventricular assist

device. *J Thorac Cardiovasc Surg.* (2008) 136:1318–23. doi: 10.1016/j.jtcvs.2007.12.077

141. Wu X, Moimas S, Hopf R, Giampietro C, Kourouklis A, Falk V. A free-form patterning method enabling endothelialization under dynamic flow. *Biomaterials.* (2021) 273:120816. doi: 10.1016/j.biomaterials.2021.120816

142. Stone GW, Ellis SG, Colombo A, Grube E, Popma JJ, Uchida T. Long-term safety and efficacy of paclitaxel-eluting stents final 5-year analysis from the TAXUS clinical trial program. *JACC Cardiovasc Interv.* (2011) 4:530–42. doi: 10.1016/j.jcin.2011.03.005

143. Yamaji K, Räber L, Zanchin T, Spitzer E, Zanchin C, Pilgrim T. Ten-year clinical outcomes of first-generation drug-eluting stents: the Sirolimus-Eluting vs. paclitaxel-eluting stents for coronary revascularization (SIRTAX) VERY LATE trial. *Eur Heart J.* (2016) 37:3386–95. doi: 10.1093/eurheartj/ehw343

144. de Winter RJ, Katagiri Y, Asano T, Milewski KP, Lurz P, Buszman P. A sirolimus-eluting bioabsorbable polymer-coated stent (MiStent) versus an everolimus-eluting durable polymer stent (Xience) after percutaneous coronary intervention (DESSOLVE III): a randomised, single-blind, multicentre, non-inferiority, phase 3 trial. *Lancet.* (2018) 391:431–40. doi: 10.1016/S0140-6736(17)33103-3

145. Chisari A, Pistritto AM, Piccolo R, Manna A. La, Danzi GB. The ultimaster biodegradable-polymer sirolimus-eluting stent: an updated review of clinical evidence. *Int J Mol Sci.* (2016) 17:1490. doi: 10.3390/ijms17091490

146. Kerkmeijer LSM, Chandrasekhar J. Final five-year results of the REMEDEE registry: real-world experience with the dual-therapy COMBO stent. *Catheter Cardiovasc Interv.* (2021) 98:503–10. doi: 10.1002/ccd.29305

147. Worthley SG, Abizaid A, Kirtane AJ, Simon DI, Windecker S, Brar S. First-in-human evaluation of a novel polymer-free drug-filled stent: angiographic, IVUS, OCT, and clinical outcomes from the revelution study. *JACC Cardiovasc Interv.* (2017) 10:147–56.

148. Gada H, Kirtane AJ, Newman W, Sanz M, Hermiller JB, Mahaffey KW. 5-year results of a randomized comparison of XIENCE V everolimus-eluting and TAXUS paclitaxel-eluting stents: final results from the SPIRIT III Trial (clinical evaluation of the XIENCE V everolimus eluting coronary stent system in the treatment of patients with de novo native coronary artery lesions). *JACC Cardiovasc Interv.* (2013) 6:1263–6. doi: 10.1016/j.jcin.2013.07.009

149. Kereiakes DJ, Windecker S, Jobe RL, Mehta SR, Sarembock IJ, Feldman RL. Clinical outcomes following implantation of thin-strut, bioabsorbable polymer-coated, everolimus-eluting SYNERGY stents. *Circ Cardiovasc Interv.* (2019) 12:e008152. doi: 10.1161/CIRCINTERVENTIONS.119.008152

150. von Birgelen C, van der Heijden LC, Basalus MWZ, Kok MM, Sen H, Louwerenburg HW. Five-year outcome after implantation of zotarolimus- and everolimus-eluting stents in randomized trial participants and nonenrolled eligible patients: a secondary analysis of a randomized clinical trial. *JAMA Cardiol.* (2017) 2:268–76. doi: 10.1001/jamacardio.2016.5190

151. Iqbal J, Verheye S, Abizaid A, Ormiston J, de Vries T, Morrison L. DESyne novolimus-eluting coronary stent is superior to Endeavor zotarolimus-eluting coronary stent at five-year follow-up: final results of the multicentre EXCELLA II randomised controlled trial. *EuroIntervention.* (2016) 12:e1336–42. doi: 10.4244/EIJY15M10_04

152. Tonino PAL, Pijls NHJ, Collet C, Nammas W, Van der Heyden J, Romppanen H. Titanium-nitride-oxide-coated versus everolimus-eluting stents in acute coronary syndrome: the randomized TIDES-ACS trial. *JACC Cardiovasc Interv.* (2020) 13:1697–705. doi: 10.1016/j.jcin.2020.04.021

153. Bhargava B, Reddy NK, Karthikeyan G, Raju R, Mishra S, Singh S. A novel paclitaxel-eluting porous carbon-carbon nanoparticle coated, nonpolymeric cobalt-chromium stent: evaluation in a porcine model. *Catheter Cardiovasc Interv.* (2006) 67:698–702. doi: 10.1002/ccd.20698

154. Jia H, Liu H, Kong J, Hou J, Wu J, Zhang M. A novel polymer-free paclitaxel-eluting stent with a nanoporous surface for rapid endothelialization and inhibition of intimal hyperplasia: comparison with a polymer-based sirolimus-eluting stent and bare metal stent in a porcine model. *J Biomed Mater Res A.* (2011) 98:629–37. doi: 10.1002/jbm.a.33151

155. Chen M, Zheng B, Wu Z, Peng HY, Wang XG, Zhang B. Efficacy and safety of a novel nano-porous polymer-free sirolimus-eluting stent in pigs. *Chin Med J.* (2013) 126:4731–5.

156. Yi B, Shen Y, Tang H, Wang X, Zhang Y. Stiffness of the aligned fibers affects structural and functional integrity of the oriented endothelial cells. *Acta Biomater.* (2020) 108:237–49. doi: 10.1016/j.actbio.2020.03.022

157. O'Brien FJ, Harley BA, Waller MA, Yannas IV, Gibson LJ, Prendergast PJ. The effect of pore size on permeability and cell attachment in collagen scaffolds for tissue engineering. *Technol Health Care.* (2007) 15:3–17. doi: 10.3233/THC-2007-15102

158. Stolberg S, McCloskey KE. Can shear stress direct stem cell fate?. *Biotechnol Prog.* (2009) 25:10–9. doi: 10.1002/btpr.124

159. Karki P, Birukova AA. Substrate stiffness-dependent exacerbation of endothelial permeability and inflammation: mechanisms and potential implications in ALI and PH (2017 Grover Conference Series). *Pulm Circ.* (2018) 8:2045894018773044. doi: 10.1177/2045894018773044

160. Potthoff E, Franco D, D'Alessandro V, Starck C, Falk V, Zambelli T. Toward a rational design of surface textures promoting endothelialization. *Nano Lett.* (2014) 14:1069–79. doi: 10.1021/nl4047398

161. Almonacid Suarez AM, van der Ham I, Brinker MGL, van Rijn P, Harmsen MC. Topography-driven alterations in endothelial cell phenotype and contact guidance. *Heliyon.* (2020) 6:e04329. doi: 10.1016/j.heliyon.2020.e04329

162. Kukumberg M, Yao Y, Goh SH, Neo DJ, Yao JY, Yim EK. Evaluation of the topographical influence on the cellular behavior of human umbilical vein endothelial cells. *Adv Biosyst.* (2018) 2:1700217. doi: 10.1002/adbi.201700217

163. Ding Y, Yang Z, Bi CW, Yang M, Xu SL, Lu X. Directing vascular cell selectivity and hemocompatibility on patterned platforms featuring variable topographic geometry and size. *ACS Appl Mater Interfaces.* (2014) 6:12062–70. doi: 10.1021/am502692k

164. Sprague EA, Tio F, Ahmed SH, Granada JF, Bailey SR. Impact of parallel micro-engineered stent grooves on endothelial cell migration, proliferation, and function. *Circ Cardiovasc Interv.* (2012) 5:499–507. doi: 10.1161/CIRCINTERVENTIONS.111.967901

165. Tan J, Bai J, Yan Z. An aligned patterned biomimetic elastic membrane has a potential as vascular tissue engineering material. *Front Bioeng Biotechnol.* (2020) 8:704. doi: 10.3389/fbioe.2020.00704

166. Whited BM, Rylander MN. The influence of electrospun scaffold topography on endothelial cell morphology, alignment, and adhesion in response to fluid flow. *Biotechnol Bioeng.* (2014) 111:184–95. doi: 10.1002/bit.24995

167. Franco D, Klingauf M, Bednarzik M, Cecchini M, Kurtcuoglu V, Gobrecht J. Control of initial endothelial spreading by topographic activation of focal adhesion kinase. *Soft Matter.* (2011) 7:7313–24. doi: 10.1039/c1sm05191a

168. Robotti F, Franco D, Bänninger L, Wyler J, Starck CT, Falk V. The influence of surface micro-structure on endothelialization under supraphysiological wall shear stress. *Biomaterials.* (2014) 35:8479–86. doi: 10.1016/j.biomaterials.2014.06.046

169. Mierke CT, Fischer T, Puder S, Kunschmann T, Soetje B, Ziegler WH. Focal adhesion kinase activity is required for actomyosin contractility-based invasion of cells into dense 3D matrices. *Sci Rep.* (2017) 7:42780. doi: 10.1038/srep42780

170. Ferrari A, Giampietro C, Bachmann B, Bernardi L, Bezuidenhhout D, Ermanni P. A novel hybrid membrane VAD as first step toward hemocompatible blood propulsion. *Ann Biomed Eng.* (2021) 49:716–31. doi: 10.1007/s10439-020-02590-1

171. Bachmann BJ, Giampietro C, Bayram A, Stefopoulos G, Michos C, Graeber G. Honeycomb-structured metasurfaces for the adaptive nesting of endothelial cells under hemodynamic loads. *Biomater Sci.* (2018) 6:2726–37. doi: 10.1039/C8BM00660A

172. Li J, Zhang K, Yang P, Qin W, Li G, Zhao A. Human vascular endothelial cell morphology and functional cytokine secretion influenced by different size of HA micro-pattern on titanium substrate. *Colloids Surf B Biointerfaces.* (2013) 110:199–207. doi: 10.1016/j.colsurfb.2013.04.048

173. Huang NF, Lai ES, Ribeiro AJ, Pan S, Pruitt BL, Fuller GG. Spatial patterning of endothelium modulates cell morphology, adhesiveness and transcriptional signature. *Biomaterials.* (2013) 34:2928–37. doi: 10.1016/j.biomaterials.2013.01.017

174. O'Donnell BT, Ives CJ, Mohiuddin OA, Bunnell BA. Beyond the present constraints that prevent a wide spread of tissue engineering and regenerative medicine approaches. *Front Bioeng Biotechnol.* (2019) 7:95. doi: 10.3389/fbioe.2019.00095

175. Oberweis CV, Marchal JA, López-Ruiz E, Gálvez-Martín P. A worldwide overview of regulatory frameworks for tissue-based products. *Tissue Eng Part B Rev.* (2020) 26:181–96. doi: 10.1089/ten.teb.2019.0315

176. Sánchez PF, Brey EM, Briceño JC. Endothelialization mechanisms in vascular grafts. *J Tissue Eng Regen Med.* (2018) 12:2164–78. doi: 10.1002/term.2747

177. de Valence S, Tille JC, Mugnai D, Mrowczynski W, Gurny R, Möller M. Long term performance of polycaprolactone vascular grafts in a rat abdominal aorta replacement model. *Biomaterials.* (2012) 33:38–47. doi: 10.1016/j.biomaterials.2011.09.024

178. Kurpanik R, Stodolak-Zych E. Chemical and physical modifications of electrospun fibers as a method to stimulate tissue regeneration – minireview. *Eng Biomater.* (2021) 159:31–41.

179. Asahara T, Murohara T, Sullivan A, Silver M, Zee RVD, Li T. Isolation of putative progenitor endothelial cells for angiogenesis. *Science.* (1997) 275:964–6. doi: 10.1126/science.275.5302.964

180. Urbich C, Dimmeler S. Endothelial progenitor cells. *Circ Res.* (2004) 95:343–53. doi: 10.1161/01.RES.0000137877.89448.78

181. Balistreri CR, Buffa S, Pisano C, Lio D, Ruvolo G, Mazzesi G. Are endothelial progenitor cells the real solution for cardiovascular diseases? focus on controversies and perspectives. *Biomed Res Int.* (2015) 2015:835934. doi: 10.1155/2015/835934

182. Tsukada J, Wolf F, Vogt F, Schaaps N, Thoröe-Boveleth S, Keijdener H. Development of in vitro endothelialized drug-eluting stent using human peripheral blood-derived endothelial progenitor cells. *J Tissue Eng Regen Med.* (2020) 14:1415–27. doi: 10.1002/term.3107

183. Melchiorri AJ, Bracaglia LG, Kimerer LK, Hibino N, Fisher JP. In vitro endothelialization of biodegradable vascular grafts via endothelial progenitor cell seeding and maturation in a tubular perfusion system bioreactor. *Tissue Eng Part C Methods.* (2016) 22:663–70. doi: 10.1089/ten.tec.2015.0562

frontiers | Frontiers in Cardiovascular Medicine

TYPE Original Research
PUBLISHED 05 October 2022
DOI 10.3389/fcvm.2022.953582

OPEN ACCESS

EDITED BY
Ellen T. Roche,
Massachusetts Institute of Technology, United States

REVIEWED BY
Andrei Ivanov,
Cleveland Clinic, United States
Yiling Fan,
Massachusetts Institute of Technology, United States

*CORRESPONDENCE
Timo Z. Nazari-Shafti
nazari@dhzb.de

SPECIALTY SECTION
This article was submitted to General Cardiovascular Medicine, a section of the journal Frontiers in Cardiovascular Medicine

RECEIVED 26 May 2022
ACCEPTED 31 August 2022
PUBLISHED 05 October 2022

CITATION
Exarchos V, Neuber S, Meyborg H, Giampietro C, Chala N, Moimas S, Hinkov H, Kaufmann F, Pramotton FM, Krüger K, Rodriguez Cetina Biefer H, Cesarovic N, Poulikakos D, Falk V, Emmert MY, Ferrari A and Nazari-Shafti TZ (2022) Anisotropic topographies restore endothelial monolayer integrity and promote the proliferation of senescent endothelial cells.
Front. Cardiovasc. Med. 9:953582.
doi: 10.3389/fcvm.2022.953582

Anisotropic topographies restore endothelial monolayer integrity and promote the proliferation of senescent endothelial cells

Vasileios Exarchos[1,2], Sebastian Neuber[1,2], Heike Meyborg[1,2], Costanza Giampietro[3,4], Nafsika Chala[5], Silvia Moimas[5], Hristian Hinkov[1,2], Friedrich Kaufmann[1], Francesca M. Pramotton[3,4], Katrin Krüger[1,2,6], Hector Rodriguez Cetina Biefer[1,2,7], Nikola Cesarovic[1,8], Dimos Poulikakos[5], Volkmar Falk[6,8,9], Maximilian Y. Emmert[1,2,6,8,10], Aldo Ferrari[3,4,5] and Timo Z. Nazari-Shafti[1,2,11]*

[1]Cardiosurgical Research Group, Department of Cardiothoracic and Vascular Surgery, German Heart Center Berlin, Berlin, Germany, [2]Translational Cardiovascular Regenerative Technologies Group, BIH Center for Regenerative Therapies, Berlin Institute of Health at Charité—Universitätsmedizin Berlin, Berlin, Germany, [3]Experimental Continuum Mechanics, Empa Swiss Federal Laboratories for Materials Science and Technology, Dübendorf, Switzerland, [4]Department of Mechanical and Process Engineering, Institute for Mechanical Systems, ETH Zürich, Zurich, Switzerland, [5]Laboratory of Thermodynamics in Emerging Technologies, Department of Mechanical and Process Engineering, ETH Zürich, Zurich, Switzerland, [6]Clinic for Cardiovascular Surgery, Charité—Universitätsmedizin Berlin, Berlin, Germany, [7]Department of Cardiac Surgery, City Hospital of Zürich, Site Triemli, Zurich, Switzerland, [8]Department of Health Sciences and Technology, ETH Zürich, Zurich, Switzerland, [9]Department for Cardiovascular and Thoracic Surgery, German Heart Center Berlin, Berlin, Germany, [10]Institute for Regenerative Medicine, University of Zurich, Zurich, Switzerland, [11]BIH Biomedical Innovation Academy, BIH Charité (Junior) (Digital) Clinician Scientist Program, Berlin Institute of Health at Charité—Universitätsmedizin Berlin, Berlin, Germany

Thrombogenicity remains a major issue in cardiovascular implants (CVIs). Complete surficial coverage of CVIs by a monolayer of endothelial cells (ECs) prior to implantation represents a promising strategy but is hampered by the overall logistical complexity and the high number of cells required. Consequently, extensive cell expansion is necessary, which may eventually lead to replicative senescence. Considering that micro-structured surfaces with anisotropic topography may promote endothelialization, we investigated the impact of gratings on the biomechanical properties and the replicative capacity of senescent ECs. After cultivation on gridded surfaces, the cells

showed significant improvements in terms of adherens junction integrity, cell elongation, and orientation of the actin filaments, as well as enhanced yes-associated protein nuclear translocation and cell proliferation. Our data therefore suggest that micro-structured surfaces with anisotropic topographies may improve long-term endothelialization of CVIs.

KEYWORDS

endothelial cells, monolayer integrity, proliferation, topography, anisotropy, senescence, telomere, aging

Introduction

Despite technological advances, the use of cardiovascular implants (CVIs) such as left ventricular assist devices (LVADs) or heart valves is associated with adverse events, including thromboembolic complications that may lead to stroke or systemic embolism (1, 2). Thrombus formation occurs predominantly on foreign or xenograft surfaces exposed to low flow, e.g., the inflow cannula of LVADs (**Figure 1**) or the aorta facing surfaces of bioprosthetic or mechanical heart valves (3–5). Hence, the formation of a monolayer of endothelial cells (ECs) on these surfaces could reduce the contact area between blood and synthetic components, thereby improving the hemocompatibility of CVIs and thus reducing thromboembolic events (6, 7).

In general, there are two strategies for achieving endothelialized CVIs: (i) *in vitro* endothelialization and (ii) *in vivo* endothelialization. *In vitro* endothelialization requires the *ex vivo* seeding of ECs on CVI surfaces from either autologous vascular tissue (e.g., saphenous vein) or allogeneic sources (e.g., umbilical cord), whereas *in vivo* endothelialization involves EC migration from the intact endothelium or by adhesion, proliferation, and differentiation of circulating endothelial progenitors (8). Both approaches require chemical and/or biological functionalization of the luminal surfaces of CVIs to support cell recruitment and adhesion (7, 9). For example, surface textures produced by nanotechnology modulate the dynamics of cell protrusion (i.e., the establishment of initial adhesions and their interaction with the cytoskeleton), thus contributing to fundamental steps in the initial phase of the endothelialization process (10, 11).

Overall, patients who could benefit from CVI endothelialization usually have multiple co-morbidities and are of old age. However, these factors are directly linked to premature EC inflammatory and replicative senescence (RS), a major challenge in the formation of intact EC monolayers when using autologous cells (12). In general, senescence is a cellular state of hibernation characterized by a typical irreversible cell cycle arrest, coupled with changes at the transcriptional, metabolic, and secretory levels as well as a modified cell morphology. As the percentage of senescent ECs in a monolayer will greatly impact its functionality (13, 14), it is necessary to develop strategies that promote the maintenance of a functional EC monolayer not only for young and healthy ECs, but also for aged and senescent ECs. Biochemical changes during the transition from proliferating to senescent ECs are well characterized, but associated biomechanical changes are relatively unknown. As it has been observed that micro-structured surfaces with gratings can enhance EC alignment and improve the integrity of cell-to-cell junctions (15), we hypothesized that surfaces with gratings may not only improve the biomechanical properties of senescent ECs, but also increase their replication capacity.

Materials and methods

Cell isolation and cell culture

Human umbilical cord vein endothelial cells (HUVECs) and human umbilical cord mesenchymal stems cells (HUMSCs) were isolated from umbilical cords that were obtained from the Department of Obstetrics and Gynecology at the Charité-Universitätsmedizin Berlin. The collection and use of the samples was approved by the institutional ethics board under application number EA2/178/13. In total, three different healthy donors were included in this study. All cells were cultured in Medium 200 (Thermo Fisher Scientific, Waltham, MA, USA) supplemented with low-serum growth supplement (Thermo

Abbreviations: AJ, adherens junction; AT, anisotropic topography; BSA, bovine serum albumin; CI, connectivity index; COC, cyclic olefin copolymer; CV, cardiovascular; CVI, cardiovascular implant; DAPI, 4′,6-diamidino-2-phenylindole; EC, endothelial cell; EdU, ethynyl-2′-deoxyuridine; FA, focal adhesion; HUMSC, human umbilical cord mesenchymal stems cell; HUVEC, human umbilical cord vein endothelial cell; LVAD, left ventricular assist device; RS, replicative senescence; PBS, phosphate-buffered saline; PCR, polymerase chain reaction; PD, population doubling; PDT, population doubling time; PDMS, polydimethylsiloxane; PFA, paraformaldehyde; SA-β-gal, senescence-associated β-galactosidase; VEC, vascular endothelial cadherin; WSS, wall shear stress; YAP, yes-associated protein.

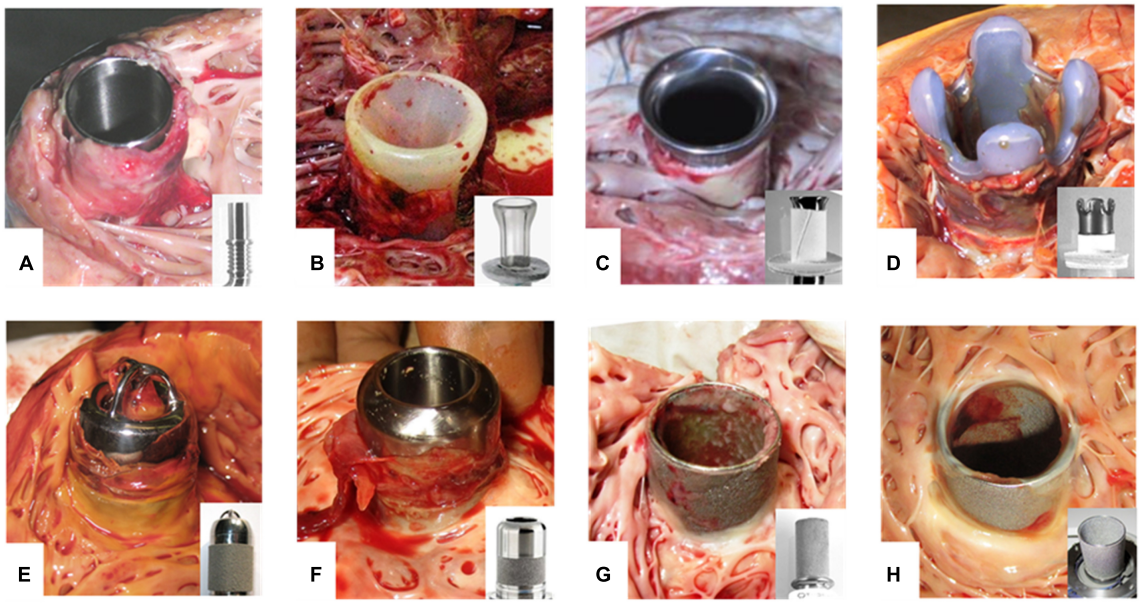

FIGURE 1
Thrombus formation at LVAD inflow cannulas. **(A–H)** Inflow cannulas of various LVADs after explanation. Cannulas without any textured surface are prone to thrombus development of unhindered growth **(A,B)**. Textured cannulas show scar tissue at the well healed myocardial wound of the entry site covering the lower section with a textured surface consisting of woven polyester cuff **(C,D)** or sintered titanium microspheres **(E–H)**. Intracaval sintered parts of the cannula frequently are covered by fibrin layers of various thickness **(G,H)**. Especially at intraluminal parts these layers may form patchy structures or increased thickness with the risk of constricting the flow path or peeling off. Thrombus formation often is originating from the transition to the polished tip with uncontrolled growth. EC lining should prevent thrombus formation and propagation. **(A)** DuraHeart (Terumo Heart, Inc., Ann Arbor, MI, USA), totally polished titanium inflow cannula. **(B)** VentrAssist (Ventracor, Chatswood, NSW, Australia), smooth silicone cannula without texturing. **(C)** DeBakey pump (MicroMed Cardiovascular, Inc., Houston, TX, USA), lower part textured with Dacron cuff, polished titanium cannula. **(D)** INCOR (BerlinHeart, Berlin, Germany) with Dacron cuff and smooth silicone tip. **(E)** Jarvik-2000 (Jarvik Heart, New York, NY, USA). **(F)** HVAD (Medtronic Inc., USA) inflow cannula featuring about 50% sintered surface length. **(G)** Heartmate-II (Abbott, Pleasanton, CA, USA). **(H)** HeartMate-3 with totally sintered cannula sparing about 1 mm at the cannula brim.

Fisher Scientific, Waltham, MA, USA) at 37°C with 5% CO_2. The final concentrations of supplements were 2% fetal bovine serum, 1 μg/ml hydrocortisone, 10 ng/ml human epidermal growth factor, 3 ng/ml basic fibroblast growth factor, and 10 μg/ml heparin. During *in vitro* expansion, cells were either seeded on plates at a density of 20,000 cells/cm^2, coated with 1.5% gelatine solution (Millipore Sigma, Burlington, MA, USA) or on a surface with gratings (described below) at a density of 5 × 10^3 cells/cm^2 coated with glutaraldehyde cross-linked gelatin to increase cell adhesion. When cells were grown on the gratings, the medium was supplemented with a higher serum concentration of 10% fetal bovine serum. For both conditions, the medium was changed every 2–3 days and the cells were passaged at 80–90% confluence.

Flow cytometry analysis

Cells were harvested after reaching 70–80% confluence and approximately 1 × 10^6 cells were suspended in 1 ml flow cytometry buffer containing phosphate-buffered saline (PBS) with 5 mM EDTA, 25 mM HEPES, 1% fetal bovine serum, and 1% penicillin/streptomycin at pH 7.6. After centrifugation at 300 × g for 5 min, the cell pellets were incubated with the following antibodies for 30 min at 4°C in the dark: anti-human CD31/PE-Cy7 (clone WM59, BioLegend, San Diego, CA, USA), anti-human CD105/PE (clone 43A3, BioLegend, San Diego, CA, USA), or anti-human CD90/FITC (clone 5E10, Invitrogen, Carlsbad, CA, USA), each at a concentration of 5 μg/ml in PBS containing 5% bovine serum albumin (BSA). The samples were washed twice with flow cytometry buffer, fixed with flow cytometry buffer supplemented with 0.5% paraformaldehyde (PFA) and stored at 4°C until measurement using a FACS Canto II Flow Cytometer (BD Biosciences, USA). Analysis was performed using FlowJo version 10.6.1 (Tree Star, Ashland, OR, USA).

Cell proliferation and population doubling analysis

Cell proliferation rate was determined using a cell proliferation kit (Click-iT EdU Cell Proliferation Kit for Imaging, Alexa Fluor 555 dye) according to the manufacturer's instructions. Images were taken with the Keyence BZ-X710 fluorescence microscope (Keyence, Itasca, IL, USA) and the number of 5-ethynyl-2'-deoxyuridine (EdU)-positive cells

was analyzed using Imaris software (version 9.6.0, Oxford Instruments, Abingdon, UK).

The population doubling time (PDT) was calculated using the following equation: PDT = t·log2/[log(Nf)-log(N0)], where t is the culture duration, Nf is the number of harvested cells and N0 is the number of seeded cells.

Senescence-associated β-galactosidase assay

Senescence-associated β-galactosidase (SA-β-gal) activity was measured using a histochemical senescence detection kit (Cell Signaling Technology, MA, USA, catalog no. 9860) according to the manufacturer's instructions. Briefly, 2–3 × 10^5 HUVECs per well were seeded in a 48-well plate and cultured for 24 h. Cells were washed twice with PBS at pH 7.4 and fixed with the fixative solution for 15 min at room temperature. After two washes with PBS, cells were incubated at 37°C without CO_2 supply in freshly prepared SA-β-gal staining solution. After 12 h, the reaction was stopped by removing the SA-β-gal staining solution and cells were washed twice with PBS. To ensure a representative count, each tissue culture dish was divided into four quarters and at least one image was obtained from each quarter. The percentage of SA-β-gal-positive cells was determined by counting all SA-β-gal-positive cells under bright field illumination. The total number of cells was determined by 4′, 6-diamidino-2-phenylindole (DAPI) counterstaining (0.1 μg/ml in PBS, 15 min) and subsequent fluorescence microscopy (BZ-X710, Keyence, USA). Data analysis was performed using ImageJ software (version 1.52p, National Institutes of Health, USA) (16).

Telomere length measurement

Relative telomere length was measured using a modified version of the monochrome multiplex quantitative polymerase chain reaction (PCR) protocol as previously described (17, 18). In brief, total DNA was isolated from HUVECs using Direct PCR Lysis Buffer (Viagen Biotech, Inc., CA, USA) and the DNA equivalent of 100,000 cells was added to each PCR reaction. The PCR reaction was performed in technical triplicates using a LightCycler 480 PCR system (Roche, Basel, Switzerland). A serial dilution of DNA from low passage HUVECs (passage 2) ranging from 10 to 1,200 pg was included in each assay to create a standard curve for sample DNA quantification. Reaction mixtures (10 μl) contained 20 mM Tris-HCl (pH 8.4), 50 mM KCl, 3 mM $MgCl_2$, 0.2 mM of each deoxyribonucleotide triphosphate, 1 mM dithiothreitol, 1 M betaine (Affymetrix, Santa Clara, CA, USA), 0.5 × SYBR Green I (Thermo Fisher Scientific, Waltham, MA, USA), 0.1875 U Platinum Taq DNA polymerase (Thermo Fisher Scientific, Waltham, MA, USA), 0.0625 × Titanium Taq DNA polymerase (Clontech Laboratories, Mountain View, CA, USA), and 900 nM of each primer (telg, telc, hbgu, and hbgd). Primer sequences are given in Cawthon (19). Amplification conditions were as follows: 2 min at 95°C, followed by 6 cycles for 15 s at 95°C, and 15 s at 49°C, followed by 40 cycles for 15 s at 95°C, 10 s at 62°C, and 15 s at 72°C with signal acquisition, followed by 15 s at 84°C and 10 s at 88°C with signal acquisition. Roche LightCycler 480 software (version 1.5, Roche, Basel, Switzerland) was used to generate standard curves and to calculate DNA concentrations of telomeres and single-copy genes for each sample. The relative telomere lengths (T/S ratios) were calculated for each sample replicate.

Cyclic olefin copolymer-slide preparation and flow experiments

Cyclic olefin copolymer (COC)-coated surfaces were obtained from Ibidi GmbH (Gräfelfing, Germany) and cut into rectangular slides of 3 cm × 1.5 cm. The slides were cleaned with 70% ethanol, washed three times with PBS, and coated with glutaraldehyde cross-linked gelatin to increase cell adhesion (20). In detail, COC slides were incubated with 1.5% gelatin solution for 1 h at 37°C, followed by cross-linking with 2% glutaraldehyde solution (Sigma Aldrich, St. Louis, MO, USA) for 15 min at room temperature. Glutaraldehyde was removed and the COC slides were incubated with 70% ethanol for 1 h at room temperature. After five washes with PBS followed by overnight incubation with PBS containing 2 mM glycine, the COC slides were washed five times with PBS and stored at 4°C prior to cell seeding.

All flow experiments were performed using a specifically designed parallel plate flow chamber to apply a constant shear stress to the monolayer of HUVECs (10). The shear stress (τ) applied to the monolayers can be expressed as a function of the channel dimension (width, w and height, h), medium property (viscosity, μ) and volumetric flow rate (Q) using the following formula for wall shear stress (WSS) in a rectangular channel: $\tau = (6 \cdot Q \cdot \mu)/(w \cdot h^2)$. While the channel dimension and medium property were fixed in our experimental setup (w = 20 mm, h = 0.3 mm, $\mu = 8.4 \times 10^{-4}$ Pa·s), the flow rate was controlled using a peristaltic roller pump (Model 66, Harvard Apparatus, Holliston, MA, USA) to apply a WSS of 1.4 Pa to the endothelial monolayer. A compliance element was inserted between the roller pump and the flow chamber to dampen flow pulsation. The flow chamber was connected to the pump with Tygon tubing (Radnor, PA, USA) certified for low cytotoxicity. The COC slides containing a cell monolayer with a density of 4–5 × 10^4 cells/cm^2 was placed in the flow chamber, which was then filled with medium and connected to the hydraulic circuit. The flow bioreactor and the medium reservoir were allocated in a chamber in which the environment was maintained at 37°C and 5% CO_2. The cell monolayer was then exposed to the flow generating the desired shear stress conditions for 16 h.

Preparation of surfaces with anisotropic topography

To produce surfaces with gratings, template wafers with gratings of 1 μm depth and height were first fabricated at the cleanroom facilities of the Binnig and Rohrer Nanotechnology Center by a standard nanoimprint lithography process as previously reported (10). At the end of the fabrication process, the wafers were rinsed with acetone and 2-propanol, followed by immersion in dimethyldichlorosilane for 15 min to facilitate silanization. To transfer the same geometries to silicone elastomers, the template wafer was used as a direct form. Polydimethylsiloxane (PDMS) components A and B (Sylgard 184 Silicone Elastomer, Dow Chemical Company, MI, USA) were mixed in a ratio of 1:10 and poured onto the template, while elastomeric substrates were mixed in a ratio of 1:10. Silicone membranes with the desired topography were then cured for 1 h at 80°C and carefully removed from the wafer. For a direct comparison within each experiment, silicones with unstructured (flat) and topographically modified (grating) surfaces were produced. Up to six imprinted PDMS substrates were sealed in a well of a 6-well plate and cleaned by treatment with ethanol overnight. After washing three times with PBS, the surfaces were coated with glutaraldehyde cross-linked gelatin as described above and stored at 4°C prior to cell seeding.

Immunofluorescence microscopy

At the end of each experiment, cells were fixed with 4% paraformaldehyde (PFA) for 20 min, washed with PBS, permeabilized with 0.5% Triton-X100 for 10 min and blocked with 5% BSA in PBS for 1 h. For the biomechanical characterization of senescent HUVECs under flow conditions, the samples were incubated with the following primary antibodies overnight at 4°C: rabbit anti-vascular endothelial cadherin (VEC) antibody (catalog no PA5-19612, Abcam, Cambridge, UK, 1:100) and rabbit anti-GOLM1 antibody (catalog no HPA010638, Sigma Aldrich, St. Louis, MO, USA, 1:100). After washing three times with PBS, cells were incubated with Alexa Fluor 568-labeled donkey anti-rabbit antibody (catalog no A-21206, Thermo Fisher, Waltham, MA, USA, 1:200) for 1 h at room temperature protected from light. To visualize cytoskeleton, F-actin fibers were directly stained with Alexa Fluor 555-labeled phalloidin (catalog no A34055, Thermo Fisher, Waltham, MA, USA, 1:200). For the biomechanical characterization of senescent HUVECs after cultivation on anisotropic topography with gratings, in addition to the staining for VEC protein and F-actin fibers, the samples were incubated overnight at 4°C with mouse anti-yes-associated protein (YAP) primary antibody (catalog no sc-101199, Santa Cruz, Dallas, TX, USA, 1:100), and after washing three times with PBS, the cells were incubated with Alexa Fluor 555-labeled donkey anti-mouse antibody (catalog no A31570, Thermo Fisher, Waltham, MA, USA, 1:100). To visualize focal adhesions (FAs), the samples were stained with the following primary antibodies overnight at 4°C: mouse anti-paxillin antibody (catalog no 610051, BD Bioscience, USA, 1:100) and rabbit anti-p-paxillin Tyr118 antibody (catalog no 2541S, Cell Signaling Technology, USA, 1:100). After washing three times with PBS, the cells were incubated with the following secondary antibodies: Alexa Fluor 488-labeled donkey anti-mouse antibody (catalog no A-21202, Thermo Fisher, Waltham, MA, USA, 1:100) and Alexa Fluor 555-labeled donkey anti-rabbit antibody (catalog no A-32794, Thermo Fisher, Waltham, MA, USA, 1:100), respectively. After washing three times in PBS, samples were mounted with medium containing DAPI (0.1 μg/ml). Images were taken with the Keyence BZ-X710 fluorescence microscope (Keyence, Itasca, IL, USA) and analyzed using ImageJ (version 1.52p) and MATLAB (version 7.0, MathWorks, USA) (16).

Image analysis

To quantify the number of phosphorylated histone H2AX (γ-H2AX) foci per nucleus, images were analyzed and processed using the FoCo algorithm (21). A nuclear mask was created based on the DAPI fluorescent signal using MATLAB (MathWorks, USA) and ImageJ (version 1.52p, National Institute of Health, USA). The distribution of the γ-H2AX signal in nucleus was then analyzed to count the number of foci. Cells were categorized in three groups based on the number of detected foci (0, 1–3, and > 4). Quantitative analysis of FAs in the peripheral region of the cell was based on a previously reported protocol (22). Both the number of FAs divided to the cell perimeter, known as linear FA density, as well as the FA size were obtained by analyzing the number of FAs after excluding the nuclear and perinuclear fields in the cell center. To assess the polarization of HUVECs in relation to the flow, the nucleus and the Golgi apparatus of cells were marked and saved as separate files using the Imaris software. The position of the nucleus was calculated in relation to the Golgi apparatus using MATLAB software. The connectivity index (CI) was calculated from the average skewness (Rsk) of the VEC signal profile along four directions according to the following formula: CI = average [Rsk(north), Rsk(west), Rsk(south), Rsk(east)]. Each CI value was normalized according to the maximum value. CI values close to 1 indicate a monolayer with a fully preserved network of cell-to-cell junctions typical for long confluent EC monolayers, while values close to 0 indicate a diffuse VEC signal in the cytoplasm, which is typical for EC monolayers with disassembled or immature junctions. A connectivity threshold was established by measuring the VEC-CI in recently confluent monolayers, i.e., after 12–16 h of cultivation (23, 24).

The tortuosity of endothelial adherent junctions was obtained from the VEC signal. Briefly, the VEC adherent junctions were traced in ImageJ (version 1.52p), and for each junction, the contour length of the junction, *L*, and the end-to-end distance, *D*, were measured. The tortuosity was then computed as the ratio of *L*/*D*. Tortuosity index values close to 1 indicate a straight junction, while higher values indicate highly convoluted junction topology (15). A measure of average cell orientation was obtained from the VEC trace or the F-actin signal using the freehand selection tool of ImageJ. In detail, the cell profile was manually drawn and the cell orientation angle along with additional shape features of the cell were obtained using the "Fit ellipse" option in the "Measurements" tool. The range of possible alignment angles between cells and the direction of flow was 0–90 degrees; a value close to 0° indicates parallel alignment, a value close to 45° indicates no alignment and a value close to 90° indicates perpendicular alignment. The aspect ratio of cells was calculated as the ratio of the length of the major axis to the length of the minor axis.

To quantify the level of cytoplasmic-to-nuclear YAP translocation, the ratio between the cytoplasmic and nuclear YAP mean signal intensity was calculated using MATLAB (MathWorks, USA) and ImageJ (version 1.52p, National Institute of Health, USA) (25).

Statistical analysis

GraphPad Prism 9.0 (San Diego, CA, USA) was used for performing data analysis and generating graphs. The comparison of population means was done using a two-way analysis of variance and a *p*-value of less than 0.05 was considered significant. All quantitative measurements reported are expressed as average values plus standard errors of the mean. Analysis was always based on three or more independent experiments, as specified in each figure legend. For box plots, the size depicts the measured standard error of the mean and the whiskers indicate 5% and 95% confidence intervals.

Results

Replicative senescence in human umbilical cord vein endothelial cells compromises monolayer integrity

In our study, we used HUVECs that were freshly isolated form umbilical cords and showed a typical cobblestone morphology and classical endothelial surface markers such as CD31 and CD105 under *in vitro* conditions on population doubling level (PDL) 3 (**Supplementary Figure 1**). RS was induced by extended *in vitro* culture, resulting in cells with significant formation of DNA double-strand breaks, increased senescence-associated β-galactosidase (SA-β-gal) activity, and significantly shortened relative telomere lengths (**Supplementary Figure 2**), three typical markers of RS (26, 27). Furthermore, *in vitro* cell expansion affected not only cell growth characteristics such as PDT and replication capacity, but also the cell density of the EC monolayer and cell morphology, as also described by others (**Supplementary Figures 2, 3**) (28, 29). Next, we characterized the following biomechanical properties of young [3 population doublings (PDs)] and senescent (17 PDs) HUVECs that are considered to play an important role in the formation of a stable and functional monolayer on foreign surfaces under physiological flow:

a. the polarization of cells through the interplay between the Golgi apparatus and the nucleus (**Figure 2A**).
b. the formation of mature cell-to-cell adherens junctions (AJs) according to the distribution of VEC signal across the cell outer membrane, measured through the CI (**Figures 2B,C**), and
c. the orientation and elongation of ECs according to the actin filament reorganization (**Figures 2D–G**),

Under flow conditions, both low-passage HUVECs (3 PDs) and high-passage HUVECs (17 PDs) achieved counterflow polarization (**Figure 2A**). Under both static and flow conditions, immunostaining of VEC protein revealed a significant loss in connectivity, ranging from 0.9 ± 0.05 (3 PDs) to 0.6 ± 0.05 (17 PDs) under static conditions (p = 0.001) and from 1.0 ± 0.1 (3 PDs) to 0.5 ± 0.03 (17 PDs) under flow conditions (p = 0.0001), respectively (**Figures 2B,C**). At 3 PDs, HUVECs aligned their shape along the direction of flow, whereas high-passage HUVECs lost the ability to form a monolayer with well-organized elongated and aligned actin stress fibers (**Figure 2D**). The aspect ratio changed significantly for HUVECs at low passage from 1.5 ± 0.1 under static conditions to 3.3 ± 0.3 under flow conditions (p = 0.0001), but was similar to HUVECs at high passage with values of 1.96 ± 0.1 under static conditions and 1.76 ± 0.1 under flow conditions (**Figure 2E**). Similarly, the average directionality of actin filaments for low-passage HUVECs was 45 ± 8° under static conditions and 16 ± 4° under flow conditions (p = 0.01). At 17 PDs, there was no significant difference in directionality under both static and flow conditions (**Figures 2D,F**). Our data also showed that low-passage HUVECs aligned with the direction of flow, a property that was lost at high passage (11 ± 1.7° vs. 44 ± 2°, respectively; p = 0.004) (**Figure 2G**). In conclusion, highly passaged HUVECs maintained their ability to achieve counterflow polarization. However, they lost their connectivity as well as their ability to elongate and orient in

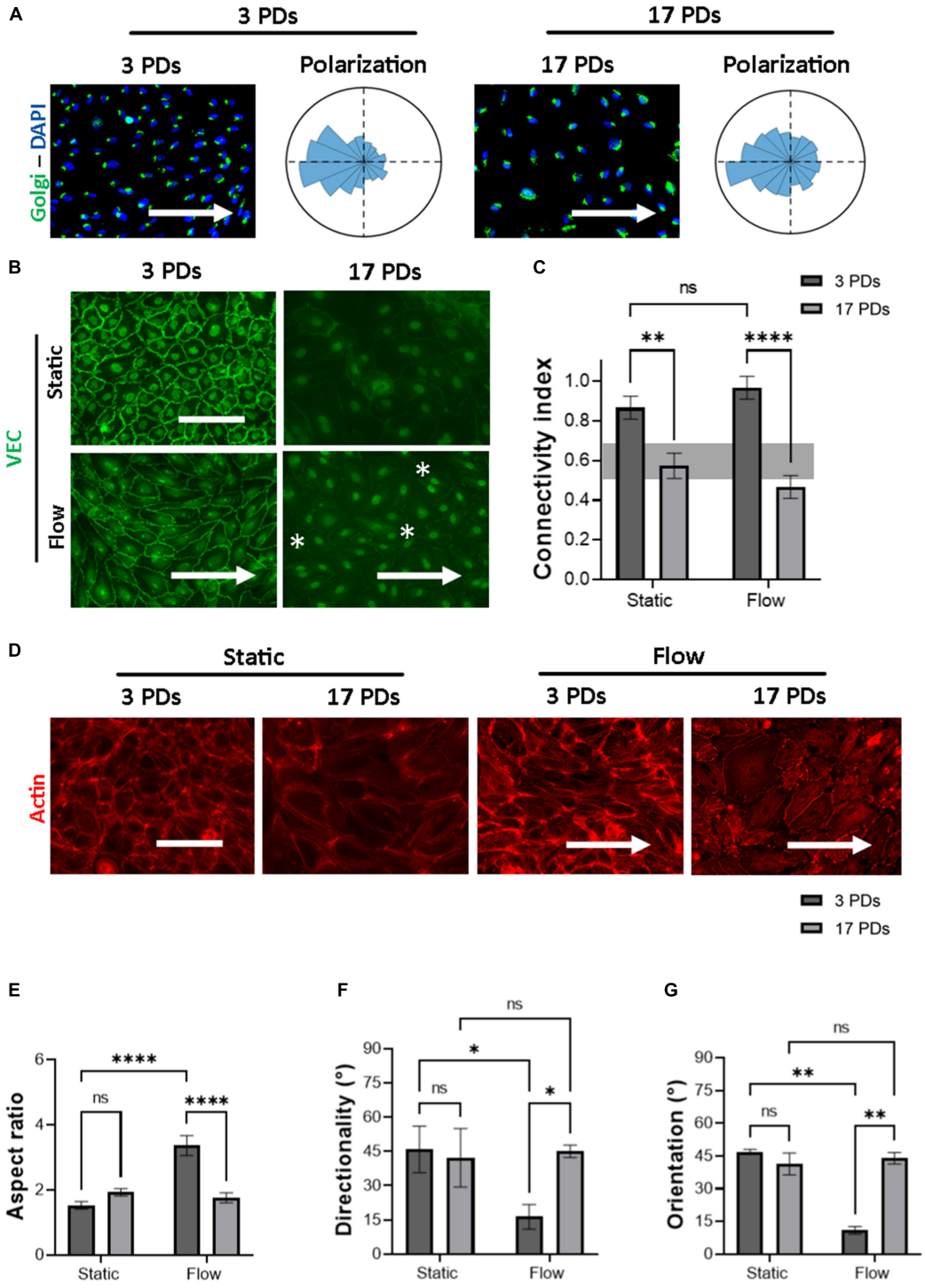

FIGURE 2
Highly passaged HUVECs lose their monolayer integrity under physiological flow of 1.4 Pa. Representative immunofluorescence microscopy images for analysis of HUVECs cultured under flow conditions generating a WSS value of 1.4 Pa for 16 h; **(A)** cells stained with an antibody against the Golgi apparatus (green), the nuclei were stained with DAPI (blue). Histograms indicate the assessment of cell polarity. **(B)** Cells stained with an antibody against VEC (green), white asterisks indicate signs of monolayer disruption. **(C)** Measure of normalized VEC-CI values in non-senescent (3 PDs) and senescent (17 PDs) HUVEC monolayers grown under static and flow conditions with a WSS value of 1.4 Pa. **(D)** Cells stained with an antibody against Phalloidin (red). In **(A,B,D)** arrows indicate the direction of flow. Scale bars, 100 μm. **(E)** Aspect ratio of cells defined as the ratio of major- to minor-axis length. **(F)** Average directionality of actin filaments in degrees according to the direction of the flow. **(G)** Average cell orientation in degrees according to the direction of the flow. In **(C,E–G)**, data represent the mean and standard error of the mean of 3 donors with more than 100 cells per condition. $^{*}p < 0.05$; $^{**}p \leq 0.01$; $^{****}p \leq 0.0001$; ns, not significant.

response to actin filament reorganization under parallel flow with physiological WSS.

Cultivation on a micro-structured surface with gratings restores the monolayer integrity of senescent human umbilical cord vein endothelial cells

As it has been observed that micro-structured surfaces with gratings can enhance EC alignment and improve the integrity of cell-to-cell junctions (15), we produced surfaces with an anisotropic topography with gratings of 1 μm width and height (**Supplementary Figure 4**) and tested under static conditions whether these topographies have a positive impact on the biomechanical properties of both non-senescent and senescent HUVECs. At first, we investigated the cell anchoring to the surface (flat vs. grating) by imaging paxillin and its phosphorylated form as important regulators of FA assembly and disassembly (**Figures 3A,B**) (30). On the flat surface, senescent HUVECs (17 PDs) exhibited a significant increase in the linear density of inactivated FAs in relation to non-senescent HUVECs (3 PDs) from 0.15 ± 0.01 to 0.21 ± 0.01 FA/μm (**Figure 3A** left panel and **Figure 3C**, $p = 0.04$). The linear density of activated FAs was also increased significantly after 17 PDs, from 0.12 ± 0.01 to 0.17 ± 0.02 FA/μm (**Figure 3B** left panel and **Figure 3D**, $p = 0.006$). A concomitant increase in the size of inactivated and activated FAs was not observed (**Figures 3E,F**). Compared to cultivation on a flat surface, HUVECs cultured on gratings also displayed a significant increase in linear FA density from 0.15 ± 0.01 to 0.24 ± 0.01 FA/μm after 3 PDs and from 0.21 ± 0.01 to 0.32 ± 0.02 FA/μm after 17 PDs (**Figure 3A** right panel and **Figure 3C**, $p = 0.01$ for both conditions). Similarly, the activated linear FA density increased from 0.12 ± 0.1 to 0.19 ± 0.02 FA/μm after 3 PDs and from 0.17 ± 0.02 to 0.3 ± 0.03 FA/μm after 17 PDs (**Figure 3D**, $p = 0.001$ and $p < 0.001$ respectively) when cultured on a surface with gratings. Accordingly, the inactivated FA size increased from 2.51 ± 0.1 to 3.2 ± 0.2 μm^2 after 3 PDs and from 2.6 ± 0.1 to 3.1 ± 0.2 μm^2 after 17 PDs (**Figures 3E,F**, $p = 0.008$ and $p = 0.03$ respectively). In summary, our data suggests that both senescence and cultivation on topographies lead to formation and maturation of FAs in HUVECs. In addition, HUVEC monolayers cultured on the micro-structured surface with gratings adopted elongated shape with no evidence of monolayer disruption and formed mainly linear AJs parallel to the grating axis with tortuosity index values close to 1. In contrast, HUVECs cultured on the flat surface mainly formed zipper-like AJs with no preferred orientation and resulted in an increase in tortuosity index values after 3 PDs (1.41 ± 0.05 for a surface with gratings vs. 2.31 ± 0.03 on a flat surface, $p < 0.0001$) and after 17 PDs (1.51 ± 0.02 for a surface with gratings vs. 2.34 ± 0.1 on a flat surface, < 0.0001) (**Figures 4A,C**). To quantify further the improved cell elongation on gratings in relation to the flat surface (**Figures 4A,D**), analysis of aspect ratio, actin filament directionality and cell orientation were performed. HUVECs showed an increase in the aspect ratio from 1.8 ± 0.05 to 5 ± 0.4 ($p < 0.001$) at 3 PDs, as well as after 17 PDs from 1.9 ± 0.06 to 3.7 ± 0.14 ($p < 0.001$) (**Figure 4E**). Intriguingly, cultivation on the gratings improved elongation of both cell groups, but not in the same extent as non-senescent HUVECs, which displayed a higher extent of elongation (**Figure 4E**, aspect ratio on gratings 5 ± 0.4 after 3 PDs and 3.7 ± 0.14 after 17 PDs, $p \leq 0.001$). The average actin filament directionality of HUVECs after 3 PDs was 36 ± 11° on the flat surface and 3 ± 0.04° on the gratings ($p = 0.002$). A similar change from baseline was observed for HUVECs after 17 PDs; the average directionality of actin filaments was changed from 36 ± 3° on a flat surface to 7 ± 1° on a surface with gratings ($p = 0.005$) (**Figure 4F**). This data is in line with measurements on the average cell orientation, namely 39 ± 8° on the flat surface and 6 ± 0.6° on the gratings ($p < 0.001$). A similar change was observed for HUVECs after 17 PDs: from 47 ± 6° on a flat surface to 10 ± 0.6° on a surface with gratings ($p < 0.001$) (**Figure 4G**). There was no significant difference of average cell orientation on either surface (**Figure 4G**). Overall, **Figure 4** demonstrates that anisotropic topographies increase VEC-CI, promote formation of linear VEC AJs as well as alignment and orientation of HUVECs.

Cultivation of human umbilical cord vein endothelial cells on gratings enhanced the cytoplasmic-to-nuclear translocation of yes-associated protein

It is known that surface-mediated cues may not only dictate FA formation and activation, cell-to-cell adhesion, and actin filament reorganization, but also cell proliferation (31). The latter is regulated through several mechanosensitive transcription factors such as the YAP (32). For this reason, we investigated under static conditions the impact of gratings on the activation of YAP. When cultured on flat surfaces, we observed that the majority of non-senescent HUVECs revealed a homogenous YAP signal equally distributed between the nucleus and the cytoplasm with a nucleus-to-cytoplasm ratio (NtCR) of 1.9 ± 0.1 (**Figures 5A,E**). In contrast, cultivation on the gratings resulted in a significant YAP translocation from the cytoplasm to the nucleus (NtCR of 2.6 ± 0.1, $p < 0.001$) (**Figures 5B,E**). Senescent HUVECs formed a heterogeneous monolayer on flat surfaces with an average NtCR of 2.8 ± 0.1 (**Figure 5E**). Cells with weak cell-to-cell contacts (**Figure 5C**) revealed an enhanced YAP

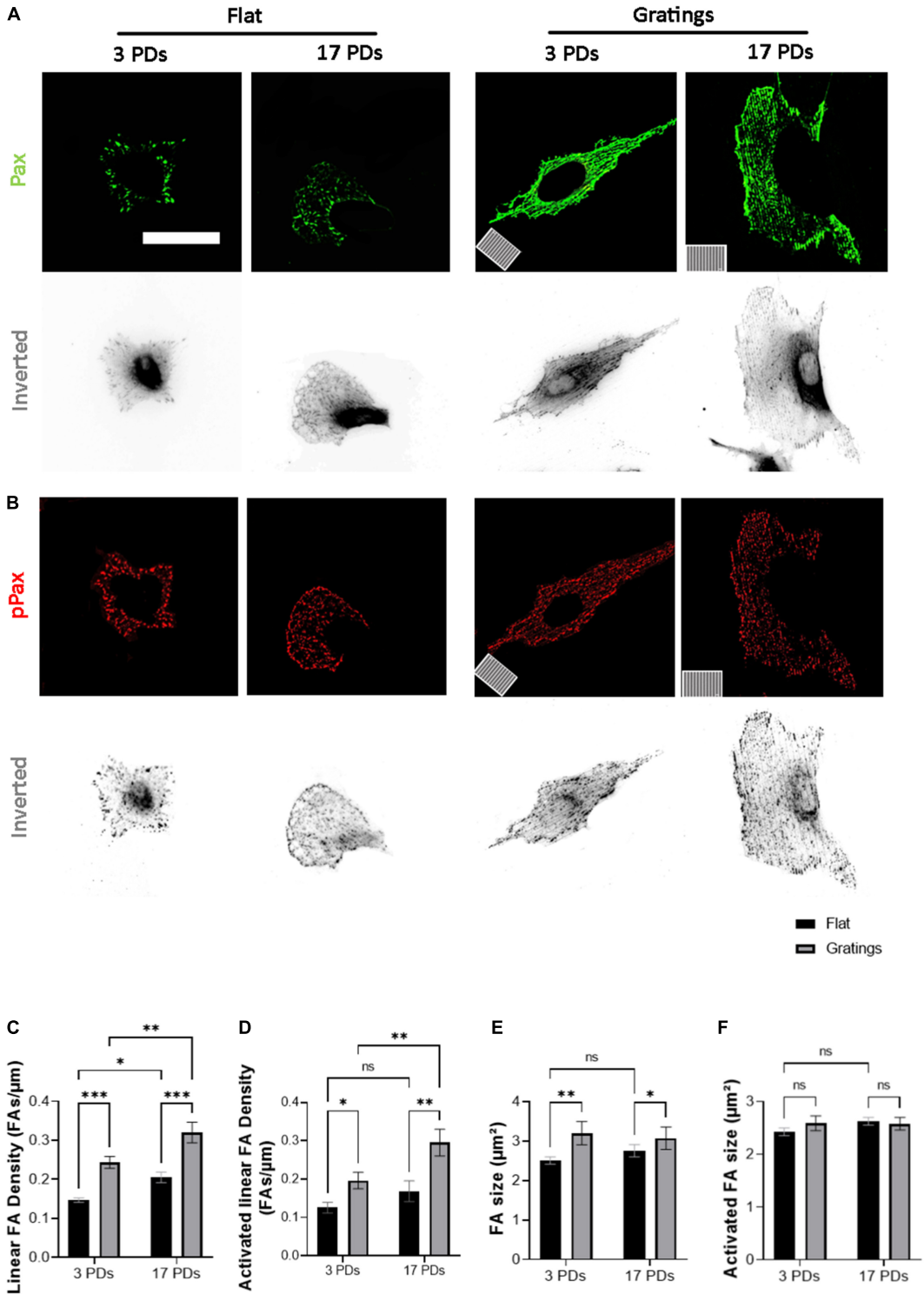

FIGURE 3

Gratings enhance the establishment of FA and promote FA activation. **(A,B)** Representative immunofluorescence analysis of HUVECs cultured under static conditions on a flat surface and a micro-structured surface with gratings; cells were stained with **(A)** an antibody against paxillin (Pax, green) and **(B)** an antibody against phosphorylated paxillin (pPax, red). The orientation of the gratings is indicated on the panels in the lower left corner. Scale bars are 100 µm. **(C)** Linear density of FA analyzed in HUVECs after 3 and 17 PDs on a flat surface and a surface with gratings. The number of FAs is normalized to the cell perimeter. **(D)** Linear density of activated FAs. **(E)** FA size after 3 and 17 PDs. **(F)** Activated FA size after 3 and 17 PDs. Data represent the mean and standard error of the mean of 3 donors with more than 360 FAs per condition. $^{*}p < 0.05$; $^{**}p \leq 0.01$; $^{***}p \leq 0.001$; ns, not significant.

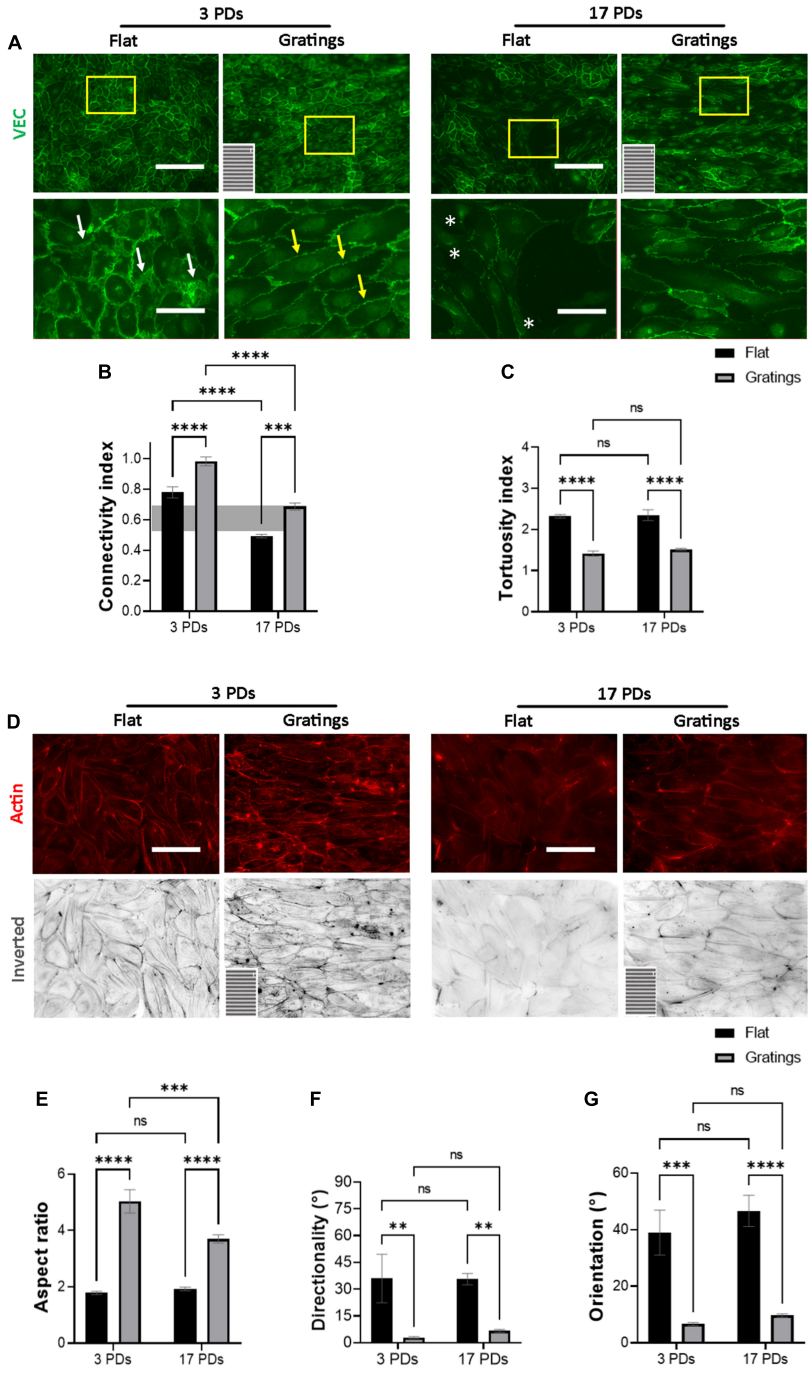

FIGURE 4
Gratings restore the monolayer integrity of HUVECs. Representative immunofluorescence microscopy images for the analysis of monolayers of HUVECs after 3 and 17 PDs cultured either on a flat surface or on a micro-structured surface with gratings. **(A)** Cells stained with an antibody against VEC (green), white arrows indicate zipper-like junctions on a flat surface, while yellow arrows indicate linear junctions on a surface with gratings. White asterisks indicate signs of monolayer disruption on the flat surface. **(B)** Measure of normalized VEC-CI values in non-senescent (3 PDs) and senescent confluent monolayers (17 PDs) grown on a flat surface or on a surface with gratings. A horizontal gray bar indicates the threshold value that defines differentiated ECs and was measured in recently confluent endothelial monolayers after 3 PDs. **(C)** Tortuosity index in non-senescent (3 PDs) and senescent confluent monolayers (17 PDs) of ECs grown on a flat surface or on a surface with gratings. **(D)** Cells stained with an antibody against phalloidin (red). The orientation of the gratings is indicated on the panels in the lower left corner. Scale bars are 200 μm **(A)** and 100 μm **(B)**. **(E)** Aspect ratio of HUVECs defined as the ratio of major- to minor-axis length. **(F)** Average directionality of actin filaments in degrees relative to the orientation of the gratings. **(G)** Average cell orientation relative to the orientation of the gratings. In **(B,C,E–G)**, data represent the mean and standard error of the mean of 3 donors with more than 100 cells per condition. $^{*}p < 0.05$; $^{**}p \leq 0.01$; $^{***}p \leq 0.001$; $^{****}p \leq 0.0001$; ns, not significant.

signal in the nucleus compared to the cytoplasm. However, cells with high VEC signal at the cell junctions showed homogeneously distributed YAP signal in the nucleus and cytoplasm (**Figures 5C,D**). Interestingly, senescent HUVECs that were cultured on gratings formed a more homogenous monolayer with a high signal of YAP in the nucleus (NtCR of 2.8 ± 0.1 to 3.2 ± 0.1, respectively; $p < 0.001$) (**Figures 5D,E**).

Cultivation of human umbilical cord vein endothelial cells on gratings enhances cell proliferation without increasing DNA damage or inducing an early onset of senescence

These observations led us to hypothesize that modulating the surface topography could aid senescent cells not only improve their cytoskeletal organization, but also increase their proliferation rate and even enhance their replication capacity. Culture of HUVECs on a surface with gratings under static conditions not only resulted in a significantly increased YAP nuclear translocation compared to cultivation on a flat surface, but also significantly improved the proliferative capacity of HUVECs. In fact, **Figures 6A,B** show a higher number of EdU-positive HUVECs after short-term cultivation on gratings for 16 h. At 3 PDs, 22 ± 0.6% EdU-positive cells were detected on flat surfaces vs. 28 ± 1% EdU-positive cells on gratings ($p = 0.003$). At 10 PDs, the number of EdU-positive cells decreased to 12 ± 1.2% on flat surfaces vs. 16 ± 0.6% EdU-positive cells on gratings ($p = 0.02$). Finally at 17 PDs, 6 ± 0.5% of cells were EdU-positive on flat surfaces vs. 11 ± 0.6% on gratings ($p = 0.006$, **Figures 6A,B**). To investigate the positive impact of gratings on cell proliferation, we expanded HUVECs *in vitro* on a polydimethylsiloxane surface with gratings. After a total period of 43 days, HUVECs underwent cumulatively 22 ± 1 PDs on flat surface and 25 ± 1 PDs on the gratings (**Figures 6C,D**, $p < 0.05$). The mean PDT was 48 ± 3 h on the flat surface and 43 ± 2 h on the surface with the gratings (**Figures 6E,F**, $p < 0.05$). More interestingly, after 10 and 17 PDs, cells cultured on the flat surface as well as on the surface with gratings displayed the same level of SA-β-gal activity (**Figure 6G**). In addition, the enhanced proliferation on the gratings did not lead to increased accumulation of γ-H2AX and significant telomere attrition (**Figures 6H,I**). The percentage of cells with 1–3 γ-H2AX foci was 27 ± 3% on the flat surface and 26 ± 4% on the gratings (**Figure 6H**, $p > 0.05$). On both surfaces after 17 PDs, an up to 40% decrease of telomeres initial length was observed (**Figure 6I**). The relative telomere length decreased from 1.0 ± 0.03 to 0.58 ± 0.01 on the flat surface ($p < 0.001$) and from 1.1 ± 0.1 to 0.59 ± 0.03 ($p < 0.001$) on the topographies (**Figure 6I**).

Discussion

Endothelial monolayer integrity is disrupted by senescent endothelial cells and loses the ability of mechanosensation and mechanotransduction

Long-term endothelialization of foreign body surfaces is a large unmet need for CVIs to improve their hemocompatibility (33). A promising approach to promoting endothelialization of artificial materials is to structure their luminal surfaces, as it enhances the biomechanical reorganization of ECs in the early stage of endothelialization (24, 34). However, while many studies have focused on the use of low-passage and proliferating HUVECs, in a clinically relevant setting of elderly patients with co-morbidities receiving CVIs, autologous endothelial progenitors and ECs required for endothelialization are most likely functionally impaired, have limited replicative capacity and enter RS (35, 36). Biochemical changes during the transition from proliferating to senescent ECs are well characterized, but associated biomechanical changes are relatively unknown. To gain further insights, we induced replicative senescence in HUVECs by extended *in vitro* culture, resulting in cells with increased SA-β-gal activity, significant formation of DNA double-strand breaks and significantly shortened relative telomere length, three typical markers of RS. These observations are consistent with previously published data (26, 27). In addition, *in vitro* cell expansion affected not only cell growth characteristics such as PDT, cell density, and replication capacity, but also cell morphology and the integrity of the EC monolayer. High-passage HUVECs lost their typical cobblestone morphology, another hallmark of senescent ECs that has also been described by others (28, 29). Next, we analyzed how a monolayer of senescent ECs behaves under physiological flow and shear stress conditions, as this is of great importance for successful endothelialization of CVIs. Physiologically in response to the laminar flow, the Golgi of ECs is located upstream of the nucleus, pointing against the flow direction (37). Furthermore, VEC protein is mainly organized along the major cell axis in the form of linear, continuous AJs between cells and is supported by cortical F-actin bundles parallel to the flow. Perpendicular to the direction of flow across the minor cell axis, VEC-AJs obtain a discontinuous, zipper-like morphology (38). In addition, the formation of F-actin stress fibers parallel to the linear AJs and localized along the edges of zipper-like AJs enhance ECs connectivity, promote EC elongation and

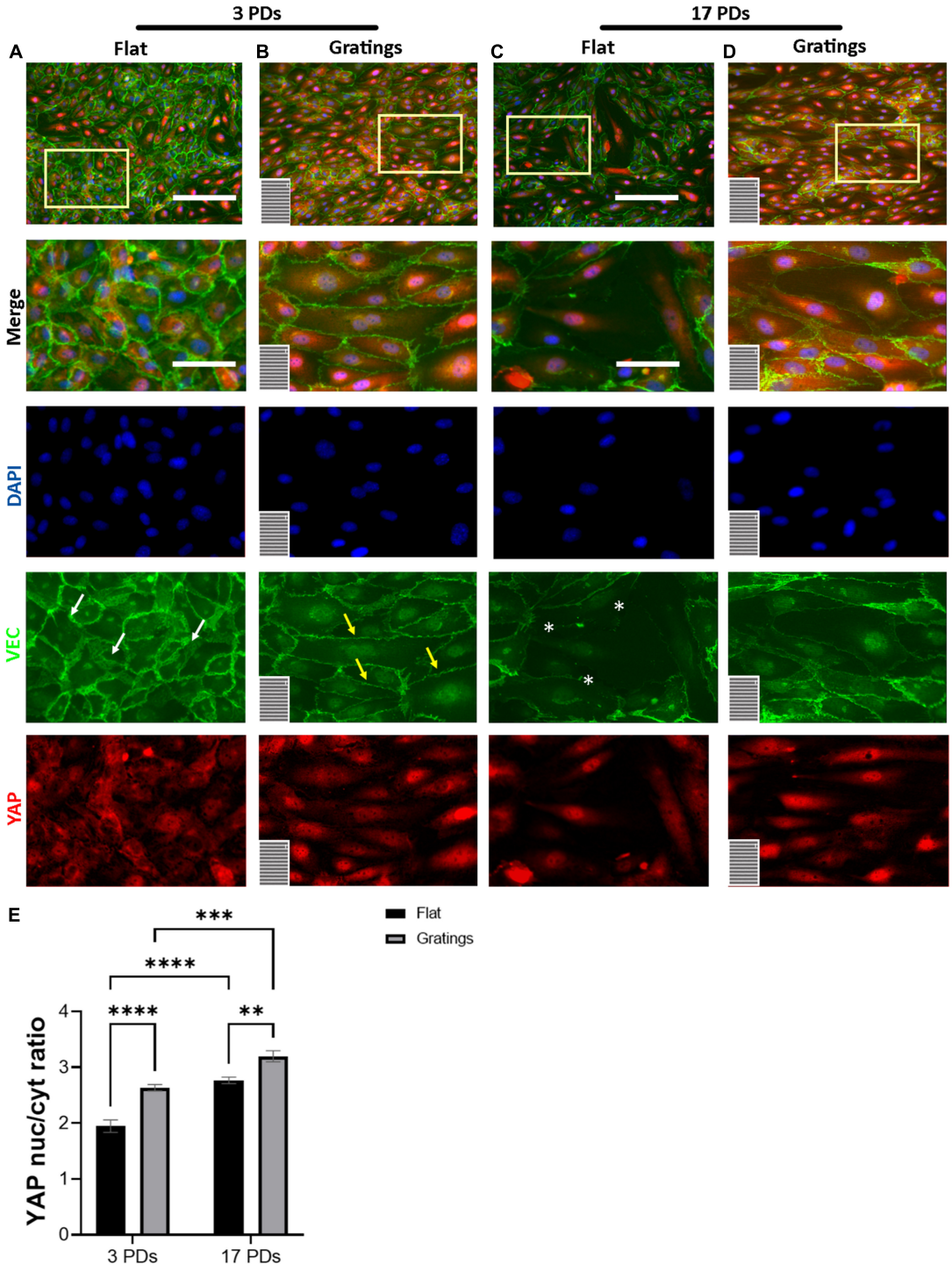

FIGURE 5
YAP nuclear translocation after HUVECs culture on gratings. **(A–D)** Immunofluorescence analysis of monolayers of HUVECs after 3 or 17 PDs cultured either on a flat surface or on a micro-structured surface with gratings. Cells were stained with an antibody against YAP (red), DAPI (blue), and VEC (green). The orientation of the gratings is indicated in the lower left corner. Yellow rectangles indicate the zoom-in areas. White arrows indicate zipper-like junctions on flat surface, while yellow arrows linear junctions on a surface with gratings. White asterisks indicate monolayer disruption on the flat surface. Scale bars, 200 μm; scale bars of zoomed images, 100 μm. **(E)** Quantification of YAP nuclear translocation as a ratio of YAP nuclear signal to YAP cytoplasmic signal. Data represent the mean and standard error of the mean 3 donors with more than 1,500 cells per condition. $^{**}p \leq 0.01$; $^{***}p \leq 0.001$; $^{****}p \leq 0.0001$.

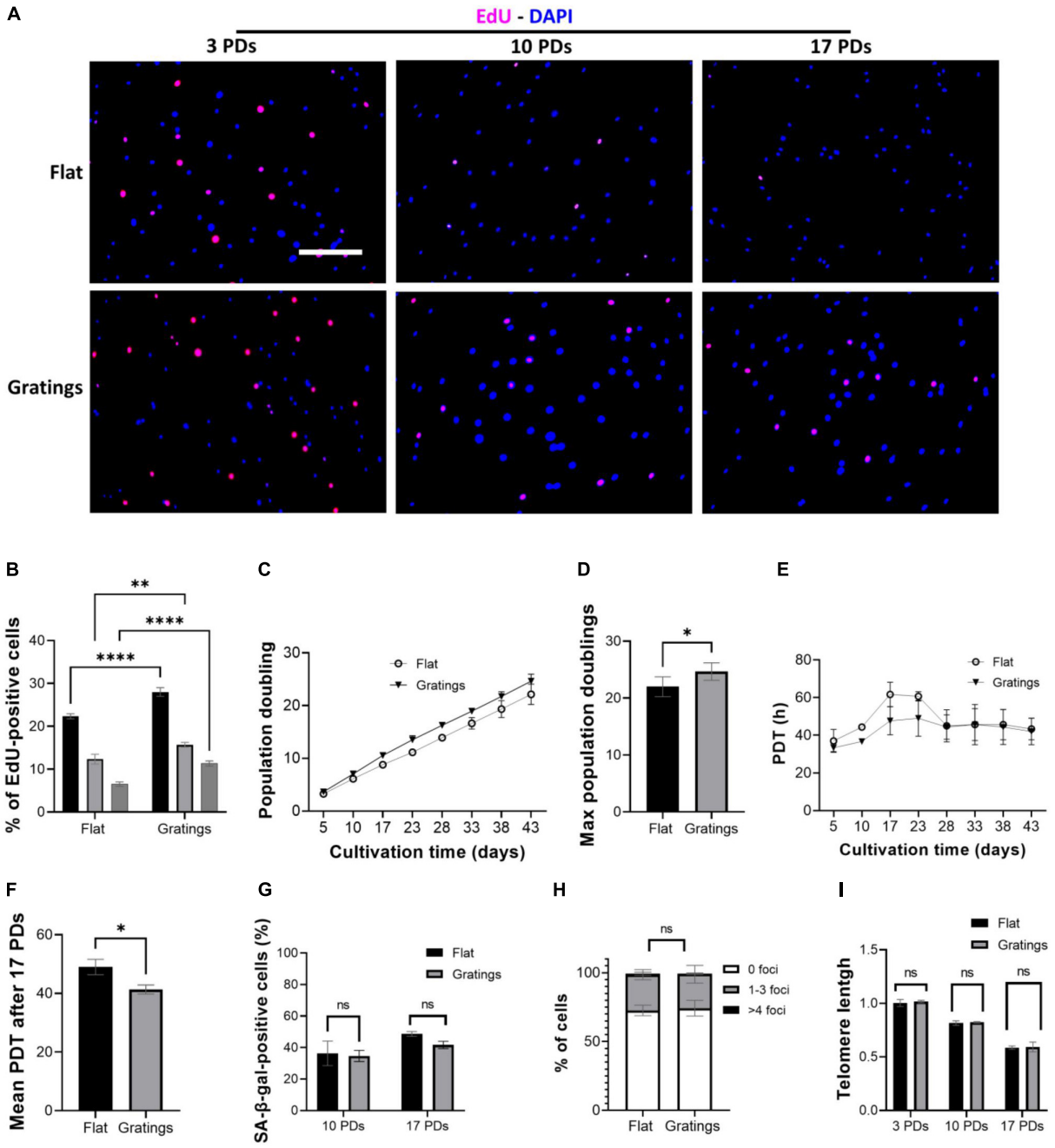

FIGURE 6
Gratings increase HUVEC proliferation without inducing an early onset of senescence or DNA damage. **(A)** EdU proliferation assay with cells after 3, 10, and 17 PDs, which were cultured on a flat surface (upper panel) or on a surface with gratings (lower panel). Blue, DAPI; Red, EdU. Scale bar, 400 μm. **(B)** Percentage of EdU-positive cells after 3, 10, and 17 PDs. **(C)** Cumulative growth curve during expansion of HUVECs isolated from three different umbilical cords on a flat surface and a micro-structured surface with gratings. **(D)** PDT of HUVECs during *in vitro* expansion on a flat surface and a micro-structured surface with gratings. **(E)** Maximum PDs achieved after cultivation on a flat surface or on a surface with gratings for a total period of 43 days. **(F)** Calculation of mean PDT after 17 PDs on a flat surface or on a surface with gratings. **(G)** Percentage of SA-β-gal-positive cells after 10 and 17 PDs on a flat surface or on a surface with gratings. **(H)** Percentage of cells presenting multiple γ-H2AX foci after 17 PDs on a flat surface or a surface with gratings. **(I)** Relative telomere length in relation to the number of PDs of HUVECs during *in vitro* expansion on a flat surface and a surface with gratings. Data represent the mean and standard error of the mean of 3 donors, for **(A,B)** more than 600 cells per condition, for **(E)** more than 2,500 cells per condition, for **(F)** more than 276 cells and for **(G)** more than 100,000 cells per condition were analyzed, $^{*}p < 0.05$; $^{**}p \leq 0.01$; $^{****}p \leq 0.0001$; ns, not significant.

orientation parallel to the flow, contributing to increased stress resistance (39). Both low-passage and senescent HUVECs showed counterflow polarization of the Golgi apparatus, but senescent HUVECs failed to achieve flow-dependent actin cytoskeleton organization. These findings are consistent with studies describing dramatic morphological changes due to RS or senescence induced by inflammatory stress (40, 41). There is evidence that senescent cells acquire significantly enlarged morphology due to the continued stimulation of cell growth pathways, such as mitogen-activated protein kinase and mammalian target of rapamycin pathways (42). Furthermore, RS is known to correlate with increased monolayer permeability due to impaired AJs (43). Consequently, the expansion of senescent HUVECs is associated with impaired intracellular transport of VEC protein at the site of cell-cell contacts and with reduced VEC protein expression (28) which is also shown in our study. Overall, our results support the fact that the increase in cell volume, the dysfunctional organization of AJs and the low extent of cell shape adaptation under physiological flow conditions due to RS negatively affect the ability of cells to sense mechanical cues (mechanosensation) and to transduce them into biochemical signals (mechanotransduction).

Gratings of 1 μm height and width restore the monolayer integrity in senescent human umbilical cord vein endothelial cell monolayers

Several studies have proposed that surface modulation with defined periodic topographies can have great potential for stabilizing healthy EC monolayers under static and flow conditions (11, 24, 33). In fact, there is a positive impact of anisotropic-pattered topographies with gratings on cell-surface and cell-cell interactions as well as cell shape adaptation during endothelialization (44, 45). For example, Gorji et al. showed that ECs cultivated under static conditions on a micro-scale grating topography respond similarly to the AJs and actin cytoskeleton remodeling that occurs under laminar flow conditions. In particular, EC cultivation on gratings promote their shape elongation due to F-actin stress fibers and the formation of linear VEC AJs, as shown by the increase in EC aspect ratio and tortuosity index, respectively (46). In line with these results, Franco et al. demonstrated a 40% increase in endothelial spreading on gratings with groove width and depth of 1 μm due to focal adhesion kinase (FAK) activation, as well as enhanced FA maturation and myosin-II dependent cell contractility (47). Robotti et al. showed that HUVECs retained their monolayer connectivity and AJ integrity under flow conditions when cultured on micro-sized gratings with 1 μm height and width under both physiological WSS values (1.4 Pa) as well as supra-physiological WSS values of LVAD luminal surfaces (up to 10 Pa) (24). While our data confirm these observations in low-passage HUVECs, we also show for the first time that gratings with 1 μm height and width improve essential biomechanical properties such as maturation of FAs and AJs, as well as cell elongation and alignment in senescent HUVECs.

Microtopographical guidance on a surface with gratings increases yes-associated protein nuclear translocation

Previous works have shown that surface modulation may impact cellular behavior beyond cell adhesion and biomechanical organization (48). In fact, topography also dictates the spatial organization and maturation of FAs, which promotes the assembly and activation of multiple proteins. For example, FAK-mediated paxillin phosphorylation induces the recruitment of vinculin at the adhesion site, which is responsible for the formation of actin stress fibers and enhanced cell elongation (49). These observations are consistent with our data showing significant FA maturation and reorganization of actin stress fibers after cultivation on gratings. Recent studies have also highlighted the involvement of YAP, a key mechanosensor and mechanotransducer of the Hippo signaling pathway that plays a critical role in correlating external mechanical stimuli with changes in gene expression. More specifically when the Hippo pathway is active, YAP becomes phosphorylated, resulting in cytoplasmic retention. However, when the Hippo pathway is inactive, YAP translocates into the nucleus and promotes cell proliferation (50, 51). It was previously reported that in confluent EC monolayers the VEC protein retains YAP in the cytoplasm by interacting with its cytoplasmic tail (52, 53). However, AJs do not simply provide sites for YAP inactivation, but they can further modulate Hippo pathway activity in response to mechanical stress signals (54). In the present study, when grown on a flat surface, ECs with cobblestone shape formed mature monolayers characterized by discontinuous, zipper-like AJs and junctional actin (55). In contrast, ECs cultivated on gratings exhibited an elongated shape, continuous, linear AJs and a strong YAP nuclear translocation.

This finding can be explained by the fact that the engagement of integrin on the grating surface has been proved to relocalize YAP in the nucleus, supporting the hypothesis that after cultivation on gratings, FA maturation is responsible for enhanced YAP shuttling in the nucleus (25). Parallel, the spatial reorganization of F-actin filaments in form of elongated stress fibers as well as the VEC protein in form of linear VEC AJs may also be in part responsible for the YAP nuclear translocation (56). In conclusion, EC shape elongation due to FA maturation and the formation of actin stress fibers and linear AJs are mainly responsible for the enhanced YAP shuttling in the nucleus.

The gratings improve the proliferative capacity of endothelial cells without inducing an early onset of senescence

Based on the aforementioned observations, we hypothesized that modulating the surface topography could aid senescent cells not only improve their cytoskeletal organization, but also increase their proliferation rate and even enhance their replicative capacity. In a study that compared the impact of patterned anisotropic topographies with different groove sizes decreasing in width from 50 to 0.5 μm revealed a significant increase in cell proliferation after cultivation on gratings over a total period of 5 days relative to the flat surface (57). In our study, we observed an improved proliferation rate of ECs on anisotropic topographies, as evidenced by EdU staining after 16 h. In addition, we found that long-term cultivation of ECs on a surface with gratings has a positive impact on the overall replicative capacity and the proliferation rate, while it did not lead to an increase in DNA damage, SA-β-gal accumulation or telomere shortening.

Conclusion and translational implications

In summary, we confirmed the negative effects of RS on the formation of a stable and mature EC monolayer. In addition, we found that extended *in vitro* cell expansion on micro-structured surfaces with gratings improves the impaired integrity of senescent endothelial monolayers and increases their proliferative capacity without inducing an early onset of senescence. This is a new and important insight into the field of endothelial senescence and could represent a potential strategy to improve the endothelialization of foreign surfaces and biointegration. Indeed, the clinical translation of such topographies to luminal surfaces is feasible from both a manufacturing and regulatory perspective, thus the implementation of specific textures on cardiovascular devices could be beneficial.

Limitations

Senescence protects against malignant transformation because it coordinates tissue morphogenesis and prevents further proliferation of dysfunctional cells. Consequently, reversal of senescence can increase the risk of tumor growth. In addition, given the heterogeneity of senescent EC monolayers, the morphological alterations that occur due to RS affect a number, but not all, of the cells of a monolayer. It is therefore possible that the increase of VEC connectivity or the decrease of tortuosity index due to AJs remodeling after cultivation on the micro-structure surface with gratings mainly occur in non-senescent ECs. Moreover, due to cytoskeletal tension after cultivation on gratings, YAP nuclear translocation may only enhance proliferation of cells that do not have the typical flattened and enlarged phenotype of senescent cells. We have shown that senescent cells exhibit a significantly increased YAP nuclear signaling when cultured on a flat surface, but this did not affect their proliferation capacity. Future studies are needed to further investigate the rejuvenating impact of anisotropic topographic structures. It is well known that proteins in the culture medium play a key role in mediating cell-surface interactions. This may be important in the case of ECs interacting with flat vs. textured surfaces. This suggests that the positive impact of the gratings on EC proliferation may only result from increased protein adsorption and enhanced protein-substrate interaction, leading to further stabilization of the monolayer. Further studies to quantify protein adsorption are needed.

Data availability statement

The raw data supporting the conclusions of this article will be made available by the authors, without undue reservation.

Ethics statement

The studies involving human participants were reviewed and approved by the Institutional Ethics Board of Charité—Universitätsmedizin Berlin (EA2/178/13). The patients/participants provided their written informed consent to participate in this study.

Author contributions

TN-S, CG, AF, NCh, and ME: scientific oversight. TN-S, VE, CG, and AF: experimental design. VE, NCe, TN-S, CG, HM, KK, HR, SM, FP, and FK: experimentation. VE, TN-S, and SN: manuscript writing. All authors: interpretation of data and critical revision.

Funding

This work was part of the Zurich Heart project under the umbrella of University Medicine Zurich and was supported by the Stavros Niarchos Foundation (SNF). TN-S was a scholar in the BIH Charité Clinician Scientist Program funded by the Charité—Universitätsmedizin Berlin and the Berlin Institute of Health. The Program was initiated and lead by Duska Dragun to enable resident physicians to pursue a career in academic medicine. Dragun passed away on December

28th of 2020. This publication is dedicated to her memory as a mentor, role model, and stellar scientist. This study was also supported by Swiss National Science Foundation, Grant SNF (205321_188828) (CG).

Acknowledgments

We thank the Cleanroom Operations Team of the Binnig and Rohrer Nanotechnology Center (BRNC) for their help and support.

Conflict of interest

Outside the submitted work: VF has relevant (institutional) financial activities with following commercial entities: Medtronic GmbH, Biotronik SE & Co., Abbott GmbH & Co. KG, Boston Scientific, Edwards Lifesciences, Berlin Heart, Novartis Pharma GmbH, JOTEC GmbH and Zurich Heart in relation to educational grants (including travel support), fees for lectures and speeches, fees for professional consultation and research and study funds. ME was a shareholder at LifeMatrix Technologies AG.

The remaining authors declare that the research was conducted in the absence of any commercial or financial relationships that could be construed as a potential conflict of interest.

Publisher's note

Supplementary material

The Supplementary Material for this article can be found online at: https://www.frontiersin.org/articles/10.3389/fcvm.2022.953582/full#supplementary-material

References

1. Kilic A, Acker MA, Atluri P. Dealing with surgical left ventricular assist device complications. *J Thoracic Dis.* (2015) 7:2158–64.

2. Rosseel L, De Backer O, Søndergaard L. Clinical valve thrombosis and subclinical leaflet thrombosis following transcatheter aortic valve replacement: is there a need for a patient-tailored antithrombotic therapy? *Front Cardiovasc Med.* (2019) 6:44. doi: 10.3389/fcvm.2019.00044

3. Yanagisawa R, Tanaka M, Yashima F, Arai T, Jinzaki M, Shimizu H, et al. Early and late leaflet thrombosis after transcatheter aortic valve replacement. *Circ Cardiovasc Interv.* (2019) 12:e007349.

4. Kaufmann F, Hörmandinger C, Knosalla C, Falk V, Potapov E. Thrombus formation at the inflow cannula of continuous-flow left ventricular assist devices—A systematic analysis. *Artif Organs.* (2022) 46:1573–84. doi: 10.1111/aor.14222

5. Ghodrati M, Maurer A, Schlöglhofer T, Khienwad T, Zimpfer D, Beitzke D, et al. The influence of left ventricular assist device inflow cannula position on thrombosis risk. *Artif Organs.* (2020) 44:939–46.

6. Baiguera S, Ribatti D. Endothelialization approaches for viable engineered tissues. *Angiogenesis.* (2013) 16:1–14.

7. Lopez-Moya M, Melgar-Lesmes P. Optimizing glutaraldehyde-fixed tissue heart valves with chondroitin sulfate hydrogel for endothelialization and shielding against deterioration. *Biomacromolecules.* (2018) 19:1234–44. doi: 10.1021/acs.biomac.8b00077

8. Liu T, Liu S, Zhang K, Chen J, Huang N. Endothelialization of implanted cardiovascular biomaterial surfaces: the development from in vitro to in vivo. *J Biomed Mater Res A.* (2014) 102:3754–72.

9. de Mel A, Jell G, Stevens MM, Seifalian AM. Biofunctionalization of biomaterials for accelerated in situ endothelialization: a review. *Biomacromolecules.* (2008) 9:2969–79. doi: 10.1021/bm800681k

10. Franco D, Milde F, Klingauf M, Orsenigo F, Dejana E, Poulikakos D, et al. Accelerated endothelial wound healing on microstructured substrates under flow. *Biomaterials.* (2013) 34:1488–97. doi: 10.1016/j.biomaterials.2012.10.007

11. Potthoff E, Franco D, D'Alessandro V, Starck C, Falk V, Zambelli T, et al. Toward a rational design of surface textures promoting endothelialization. *Nano Lett.* (2014) 14:1069–79. doi: 10.1021/nl4047398

12. Chala N, Moimas S, Giampietro C, Zhang X, Zambelli T, Exarchos V, et al. Mechanical fingerprint of senescence in endothelial cells. *Nano Lett.* (2021) 21:4911–20. doi: 10.1021/acs.nanolett.1c00064

13. Ghodrati M, Maurer A, Schlöglhofer T. The influence of left ventricular assist device inflow cannula position on thrombosis risk. *Artif Organs.* (2020) 44:939–46.

14. Katsuumi G, Shimizu I, Yoshida Y, Minamino T. Vascular senescence in cardiovascular and metabolic diseases. *Front Cardiovasc Med.* (2018) 5:18. doi: 10.3389/fcvm.2018.00018

15. Gorji A, Toh PJY, Toh Y-C, Toyama Y, Kanchanawong P. Enhancement of endothelialization by topographical features is mediated by PTP1B-dependent endothelial adherens junctions remodeling. *bioRxiv[Preprint].* (2019) Available online at: https://www.biorxiv.org/content/10.1101/766816v1 (accessed on September 16, 2019).

16. Schneider CA, Rasband WS, Eliceiri KW. NIH Image to ImageJ: 25 years of image analysis. *Nat Methods.* (2012) 9:671–5.

17. Ramunas J, Yakubov E, Brady JJ, Corbel SY, Holbrook C, Brandt M, et al. Transient delivery of modified mRNA encoding TERT rapidly extends telomeres in human cells. *Faseb J.* (2015) 29:1930–9. doi: 10.1096/fj.14-259531

18. Yepuri G, Sukhovershin R, Nazari-Shafti TZ, Petrascheck M, Ghebre YT, Cooke JP. Proton pump inhibitors accelerate endothelial senescence. *Circ Res.* (2016) 118:e36–42.

19. Cawthon RM. Telomere length measurement by a novel monochrome multiplex quantitative PCR method. *Nucleic Acids Res.* (2009) 37:e21.

20. Orsenigo F, Giampietro C, Ferrari A, Corada M, Galaup A, Sigismund S, et al. Phosphorylation of VE-cadherin is modulated by haemodynamic forces and contributes to the regulation of vascular permeability in vivo. *Nat Commun.* (2012) 3:1208. doi: 10.1038/ncomms2199

21. Lapytsko A, Kollarovic G, Ivanova L, Studencka M, Schaber J. FoCo: a simple and robust quantification algorithm of nuclear foci. *BMC Bioinformatics.* (2015) 16:392. doi: 10.1186/s12859-015-0816-5

22. Horzum U, Ozdil B, Pesen-Okvur D. Step-by-step quantitative analysis of focal adhesions. *MethodsX.* (2014) 1:56–9.

23. Lampugnani M, Corada M, Andriopoulou P, Esser S, Risau W, Dejana E. Cell confluence regulates tyrosine phosphorylation of adherens junction components in endothelial cells. *J Cell Sci.* (1997) 110(Pt 17):2065–77. doi: 10.1242/jcs.110.17.2065

24. Robotti F, Franco D, Bänninger L, Wyler J, Starck CT, Falk V, et al. The influence of surface micro-structure on endothelialization under supraphysiological wall shear stress. *Biomaterials.* (2014) 35:8479–86. doi: 10.1016/j.biomaterials.2014.06.046

25. Pramotton FM, Robotti F, Giampietro C, Lendenmann T, Poulikakos D, Ferrari A. Optimized topological and topographical expansion of epithelia. *ACS Biomater Sci Eng.* (2019) 5:3922–34. doi: 10.1021/acsbiomaterials.8b01346

26. Spazzafumo L, Mensà E, Matacchione G, Galeazzi T, Zampini L, Recchioni R, et al. Age-related modulation of plasmatic beta-Galactosidase activity in healthy subjects and in patients affected by T2DM. *Oncotarget.* (2017) 8:93338–48. doi: 10.18632/oncotarget.21848

27. Bernadotte A, Mikhelson VM, Spivak IM. Markers of cellular senescence. Telomere shortening as a marker of cellular senescence. *Aging.* (2016) 8:3–11.

28. Krouwer VJ, Hekking LH, Langelaar-Makkinje M, Regan-Klapisz E, Post JA. Endothelial cell senescence is associated with disrupted cell-cell junctions and increased monolayer permeability. *Vasc Cell.* (2012) 4:12.

29. Yi S, Lin K, Jiang T, Shao W, Huang C, Jiang B, et al. NMR-based metabonomic analysis of HUVEC cells during replicative senescence. *Aging.* (2020) 12:3626–46. doi: 10.18632/aging.102834

30. Zaidel-Bar R, Milo R, Kam Z, Geiger B. A paxillin tyrosine phosphorylation switch regulates the assembly and form of cell-matrix adhesions. *J Cell Sci.* (2007) 120:137–48. doi: 10.1242/jcs.03314

31. Chaudhary JK, Rath PC. Microgrooved-surface topography enhances cellular division and proliferation of mouse bone marrow-derived mesenchymal stem cells. *PLoS One.* (2017) 12:e0182128. doi: 10.1371/journal.pone.0182128

32. Dasgupta I, McCollum D. Control of cellular responses to mechanical cues through YAP/TAZ regulation. *J Biol Chem.* (2019) 294:17693–706.

33. Zhao J, Feng Y. Surface engineering of cardiovascular devices for improved hemocompatibility and rapid endothelialization. *Adv Healthc Mater.* (2020) 9:2000920.

34. Bachmann B, Giampietro C, Bayram A, Stefopoulos G, Michos C, Graeber G, et al. Honeycomb-structured metasurfaces for the adaptive nesting of endothelial cells under hemodynamic loads. *Biomater Sci.* (2018) 6:2726–37. doi: 10.1039/c8bm00660a

35. Donato AJ, Morgan RG, Walker AE, Lesniewski LA. Cellular and molecular biology of aging endothelial cells. *J Mol Cell Cardiol.* (2015) 89(Pt B):122–35.

36. Paneni F, Diaz Cañestro C, Libby P, Lüscher TF, Camici GG. The aging cardiovascular system: understanding it at the cellular and clinical levels. *J Am Coll Cardiol.* (2017) 69:1952–67.

37. Vion AC, Perovic T, Petit C, Hollfinger I, Bartels-Klein E, Frampton E, et al. Endothelial cell orientation and polarity are controlled by shear stress and VEGF through distinct signaling pathways. *Front Physiol.* (2020) 11:623769. doi: 10.3389/fphys.2020.623769

38. Dorland YL, Huveneers S. Cell-cell junctional mechanotransduction in endothelial remodeling. *Cell Mol Life Sci.* (2017) 74:279–92.

39. Fernández-Martín L, Marcos-Ramiro B, Bigarella CL, Graupera M, Cain RJ, Reglero-Real N, et al. Crosstalk between reticular adherens junctions and platelet endothelial cell adhesion molecule-1 regulates endothelial barrier function. *Arterioscler Thromb Vasc Biol.* (2012) 32:e90–102. doi: 10.1161/ATVBAHA.112.252080

40. Herranz N, Gil J. Mechanisms and functions of cellular senescence. *J Clin Invest.* (2018) 128:1238–46.

41. Carracedo J, Ramírez-Carracedo R, Alique M, Ramírez-Chamond R. Endothelial cell senescence in the pathogenesis of endothelial dysfunction. In: Lenasi H editor. *Endothelial Dysfunction - Old Concepts and New Challenges.* London: intechopen (2018).

42. Xu S, Cai Y, Wei Y. mTOR signaling from cellular senescence to organismal aging. *Aging Dis.* (2014) 5:263–73.

43. Jia G, Aroor AR, Jia C, Sowers JR. Endothelial cell senescence in aging-related vascular dysfunction. *Biochim Biophys Acta Mol Basis Dis.* (2019) 1865:1802–9.

44. Bettinger CJ, Langer R, Borenstein JT. Engineering substrate topography at the micro- and nanoscale to control cell function. *Angew Chemie Int Ed Engl.* (2009) 48:5406–15.

45. Tay CY, Irvine SA, Boey FYC, Tan LP, Venkatraman S. Micro-/nano-engineered cellular responses for soft tissue engineering and biomedical applications. *Small.* (2011) 7:1361–78. doi: 10.1002/smll.201100046

46. Gorji A, Toh PJY, Ong HT, Toh YC, Toyama Y, Kanchanawong P. Enhancement of endothelialization by topographical features is mediated by PTP1B-dependent endothelial adherens junctions remodeling. *ACS Biomater Sci Eng.* (2021) 7:2661–75. doi: 10.1021/acsbiomaterials.1c00251

47. Franco D, Klingauf M, Bednarzik M, Cecchini M, Kurtcuoglu V, Gobrecht J, et al. Control of initial endothelial spreading by topographic activation of focal adhesion kinase. *Soft Matter.* (2011) 7:7313–24.

48. Wong SY, Soto J, Li S. Biophysical regulation of cell reprogramming. *Curr Opin Chem Eng.* (2017) 15:95–101.

49. Katoh K. FAK-dependent cell motility and cell elongation. *Cells.* (2020) 9:192. doi: 10.3390/cells9010192

50. Boopathy GTK, Hong W. Role of hippo pathway-YAP/TAZ signaling in angiogenesis. *Front Cell Dev Biol.* (2019) 7:49. doi: 10.3389/fcell.2019.00049

51. McDonald AI, Shirali AS, Aragón R, Ma F, Hernandez G, Vaughn DA, et al. Endothelial regeneration of large vessels is a biphasic process driven by local cells with distinct proliferative capacities. *Cell Stem Cell.* (2018) 23:210–225.e6. doi: 10.1016/j.stem.2018.07.011

52. Giampietro C, Disanza A, Bravi L, Barrios-Rodiles M, Corada M, Frittoli E, et al. The actin-binding protein EPS8 binds VE-cadherin and modulates YAP localization and signaling. *J Cell Biol.* (2015) 211:1177–92. doi: 10.1083/jcb.201501089

53. Choi H-J, Zhang H, Park H, Choi K-S, Lee H-W, Agrawal V, et al. Yes-associated protein regulates endothelial cell contact-mediated expression of angiopoietin-2. *Nat Commun.* (2015) 6:6943. doi: 10.1038/ncomms7943

54. Benham-Pyle BW, Pruitt BL, Nelson WJ. Cell adhesion. Mechanical strain induces E-cadherin-dependent Yap1 and β-catenin activation to drive cell cycle entry. *Science.* (2015) 348:1024–7.

55. Zhang J, Betson M, Erasmus JC, Zeikos K, Bailly M, Cramer LP, et al. Actin at cell-cell junctions is composed of two dynamic and functional populations. *J Cell Sci.* (2005) 118:5549–62.

56. Wada K-I, Itoga K, Okano T, Yonemura S, Sasaki H. Hippo pathway regulation by cell morphology and stress fibers. *Development.* (2011) 138:3907–14.

57. Vandrangi P, Gott SC, Kozaka R, Rodgers VGJ, Rao MP. Comparative endothelial cell response on topographically patterned titanium and silicon substrates with micrometer to sub-micrometer feature sizes. *PLoS One.* (2014) 9:e111465. doi: 10.1371/journal.pone.0111465

Frontiers in
Cardiovascular Medicine

Innovations and improvements in cardiovascular treatment and practice

Focuses on research that challenges the status quo of cardiovascular care, or facilitates the translation of advances into new therapies and diagnostic tools.

Discover the latest Research Topics

See more →

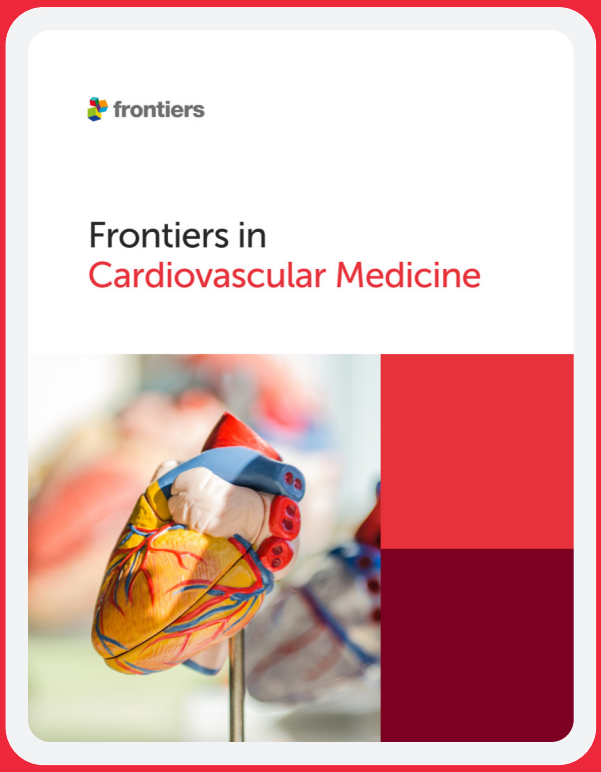

Frontiers

Avenue du Tribunal-Fédéral 34
1005 Lausanne, Switzerland
frontiersin.org

Contact us

+41 (0)21 510 17 00
frontiersin.org/about/contact